# The Role of Molecular Scaffolds at the Active Zone in Synaptic Vesicle Distribution and Release Probability

DISSERTATION

To obtain the academic degree

Doctor rerum naturalium (Dr. rer. nat.)

submitted to the

Department of Biology, Chemistry and Pharmacy

Freie Universität Berlin

Berlin, 2016

by

Christina Beis (née Hollmann)

This thesis was completed under the supervision of Prof. Dr. Stephan Sigrist from February 2011 to June 2016 at the Institute for Biology/ Genetics of Freie Universität Berlin, Germany.

1st reviewer: Prof. Dr. Stephan Sigrist

2nd reviewer: Prof. Dr. Hans-Joachim Pflüger

Date of Defense: 21.11.2016

## Statement of Authorship

I hereby declare that the work presented in this thesis has been written independently and without inappropriate support. All sources of information are referenced. I hereby declare that this thesis has not been submitted, either in the same or in a different form, to this or any other university for a degree.

_____

Christina Beis

# Contents

# 1. Summary / Zusammenfassung

## Summary

At neuronal cell-cell-contacts called synapses, transmitter is released from the synaptic vesicles (SVs) into the synaptic cleft at specialized areas of the plasma membrane, so-called Active Zones (AZs). Here, upon arrival of an action potential, $Ca^{2+}$ flows into the cell through voltage-gated $Ca^{2+}$ channels and triggers SV fusion; the $Ca^{2+}$ sensor is located on the SV membrane. At the postsynapse, the transmitter binds to membrane-residing receptors and causes a change in membrane potential. At the AZ, few SVs are in direct contact with the cell membrane (docked SV) which partially serve as an immediately release-ready pool for efficient and reliable synaptic transmission upon stimulation. Due to a limitation in the number of $Ca^{2+}$ channels, the change in presynaptic $Ca^{2+}$ concentration is locally restricted and forms a so-called nanodomain. A fast and direct SV fusion upon $Ca^{2+}$ influx is accomplished by SV placement in a sufficiently small distance to the $Ca^{2+}$ source to obtain tight coupling.

In my thesis, I studied the role of AZ components in SV distribution and the functional consequences of SV rearrangements at the neuromuscular junction (NMJ) of *Drosophila melanogaster* larvae. I focused my work in particular on the priming factor Unc13; additionally, the roles of the AZ components BRP (a large scaffold protein), Phosphatidylinositol-4 kinase PI4KIIIα (which influences lipid composition at the AZ), and Rabconnectin3B and Spinophilin (regulatory proteins) in synaptic transmission were analyzed. To unveil aspects of SV docking and priming, I characterized mutant larvae mainly in electron microscopy (EM) and electrophysiological recordings, partly with $Ca^{2+}$ buffer treatment. In these investigations, I focused specifically on SV placement, vesicle release probabilities, and the $Ca^{2+}$ dependence of release.

Two Unc13 isoforms are expressed in *Drosophila*, namely Unc13A and Unc13B. In this work it was found that the two Unc13 variants are localized in an isoform-specific pattern at the AZ. Unc13A is located in ~60 nm distance to the AZ center. I could show that Unc13A is the essential isoform for synaptic transmission and responsible for tight coupling of SVs to the $Ca^{2+}$ channels. Unc13B is located in ~120 nm distance to the $Ca^{2+}$ channels, and was not found to be especially relevant for signal transduction at the NMJ. Furthermore, the Unc13 N-term was found to be crucial in restricting the protein localization to the aforementioned sites at the AZ. Thus, Unc13

is the only identified protein of the core fusion machinery (additionally consisting of SNAREs and Unc18) which is not distributed over the whole neuronal membrane, but whose specific localization determines the sites of release.

Via the BRP C-term, SVs tether to the T-Bar, an electron-dense structure at the AZs of *Drosophila*. Upon loss of the last 17 amino acids of BRP, the T-Bar is devoid of SVs, and the brp allele is thus called $brp^{nude}$. I could show that the altered SV distribution in $brp^{nude}$ leads to a decreased SV replenishment rate at the release sites.

Furthermore, I established *in vivo* $Ca^{2+}$ imaging to investigate the participation of single AZs in spontaneous and evoked release at the NMJ. Here, I could show a profound heterogeneous distribution between individual AZs concerning the probability to participate in evoked and/or spontaneous release. Additionally it was found that evoked SV fusion is not only dependent on the BRP level the AZ, where with increasing BRP levels the participation in evoked release was proportionally elevated, but that evoked release is furthermore affected by the presence of Spinophilin.

In addition, the lipid composition at the plasma membrane alters SV release probability. In this work, I could show that the AZ component PI4KIIIα altered synaptic transmission properties.

In summary, I discovered that SV release probability is highly influenced by the spatial arrangement of SVs at the AZ, which in turn is altered by a number of AZ proteins I characterized and describe in this work. The location of docked SVs is determined by Unc13, which in turn defines the sites of SV fusion. An altered distribution of T-Bar associated SVs, as observed in $brp^{nude}$, leads to a diminished rate of SV recruitment rate to the fusion sites at the AZ. Furthermore, the composition of the protein matrix and the plasma membrane at the AZ influences synaptic transmission in general, and alters the probability to participate in evoked release already at the level of individual AZs in particular.

## Zusammenfassung

Neurone haben besondere Zell-Zell-Kontakte namens Synapsen, wo synaptische Vesikel (SV) an spezialisierten Bereichen der Plasmamembran, sog. Aktiven Zonen (AZ), fusionieren und ihren Inhalt in den synaptischen Spalt freisetzen. Bei Eintreffen eines Aktionspotentials an der Präsynapse strömt durch spannungsgesteuerte $Ca^{2+}$-Kanäle $Ca^{2+}$ ein und löst innerhalb von Millisekunden die Transmitterauschüttung aus. Der Transmitter bindet an Rezeptoren auf der postsynaptischen Zelle und verursacht dort wiederum eine Veränderung des Membranpotentials. Die SV sind teilweise schon direkt an der AZ angelagert (diese SV sind "gedockt"). Bei $Ca^{2+}$ Einstrom können gedockte, fusionskompetente SV unverzüglich mit der Plasmamembran fusionieren. Der $Ca^{2+}$ Sensor befindet sich auf den SV. Durch die begrenzte Anzahl an $Ca^{2+}$ Kanälen bildet sich nur ein lokaler $Ca^{2+}$ Konzentrationsgradient mit kleiner Reichweite aus, die sog. $Ca^{2+}$ Nanodomäne. Eine schnelle und unvermittelte SV-Fusion ist gewährleistet, wenn die SV sich in ausreichend kleiner Distanz zur $Ca^{2+}$ Quelle befinden, man spricht auch von enger Kopplung.

In meiner Doktorarbeit habe ich die Funktion einzelner AZ-Proteine bei der Verteilung der SV an der Synapse untersucht. In diesem Zusammenhang wurde an der Modellsynapse der neuromuskulären Endplatte (*neuromuscular junction*, NMJ) in *Drosophila melanogaster* Larven die Auswirkung von veränderter Vesikelanordung auf die Freisetzungswahrscheinlichkeit von synaptischen Vesikeln ermittelt. Meine Arbeit fokussierte sich dabei vor allem auf den Primingfaktor Unc13; außerdem wurde die Rolle des Gerüstproteins BRP, der Phosphatidylinositol-4 Kinase PI4KIIIα, die die Lipidzusammensetzung der Plasmamembran verändert, und den Regulatorproteinen Rabconnectin3B und Spinophilin in der synaptischen Transmission untersucht. Dafür wurden transgene Larven hauptsächlich elektronenmikroskopisch analysiert und elektrophysiologischen Messungen unterzogen, teilweise unter Anwendung von $Ca^{2+}$ Puffern. Hierbei konzentrierte ich mich im Speziellen auf die Analyse der Platzierung der SV relativ zur $Ca^{2+}$ Quelle, ihre Freisetzungswahrscheinlichkeit und die $Ca^{2+}$-Abhängigkeit der Freisetzung.

In *Drosophila* sind zwei Isoformen von Unc13 bekannt, Unc13A und Unc13B. In dieser Arbeit wurde festgestellt, dass die beiden Varianten an isoformspezifischen Positionen an der AZ verteilt sind. Unc13A, das in ca. 60 nm Entfernung zum Zentrum der AZ lokalisiert ist, wurde als die essentielle Isoform für synaptische Transmission identifiziert. Sie ist verantwortlich für eine enge Kopplung der SV zu $Ca^{2+}$ Kanälen und gewährleistet schnelle und zuverlässige Transmitterausschüttung. Unc13B befindet sich in ca. 120 nm Entfernung zum AZ-Zentrum und hat nur eine untergeordnete Rolle in der Signalübertragung an der NMJ. Darüber hinaus wurde der N-Term von Unc13 als notwendige Lokalisierungseinheit identifiziert, die die Lage des Protein an die o.g. Stellen an der AZ begrenzt. Dadurch wurde Unc13 als einziges Mitglied der Kern-

Fusionsmaschinerie (neben den SNARE-Proteinen und Unc18) ermittelt, das nicht über die gesamte neuronale Membran verteilt ist, sondern dessen Lokalisierung die physikalischen Fusionsnischen in AZ determiniert.

Über den BRP C-Term binden SV an den T-Bar, die elektronendichte Struktur, die an der präsynaptischen Membran angelagert ist. Bei Verlust der letzten 17 Aminosäuren des C-Terms ist der T-Bar frei von SV, das entsprechende Allel heißt *brp*$^{nude}$. Es konnte gezeigt werden, dass in *brp*$^{nude}$ die veränderte Verteilung der T-Bar-assoziierten SV ihre Rekrutierung zur AZ beeinträchtigt.

Weiterhin habe ich *in vivo* $Ca^{2+}$ imaging im Labor etabliert, um die Beteiligung einzelner AZ in spontaner und evozierter Vesikelfusion zu untersuchen. Dabei wurde festgestellt, dass die Teilnahme an einem oder beiden Modi (spontan oder evoziert) unter den AZ einer NMJ hochgradig heterogen verteilt ist. Außerdem konnte gezeigt werden, dass die Vesikelfusion nicht nur vom BRP-Level an der AZ abhängt, denn je mehr BRP vorhanden ist, desto größer ist die Wahrscheinlichkeit der AZ an evozierter SV-Fusion beteiligt zu sein; weiterhin wurde gezeigt, dass auch Spinophilin für evozierte Vesikelfusion relevant ist.

Doch nicht nur die Anwesenheit bestimmter Proteine an der AZ ist relevant für die synaptische Transmission, auch die Lipidkomposition der Plasmamembran wirkt sich auf die Fusionswahrscheinlichkeit aus. Es konnte in dieser Arbeit gezeigt werden, dass auch die an der AZ befindliche PI4KIIIα die synaptische Transmission beeinflusst.

Zusammenfassend konnte ich zeigen, dass Verteilung der SV an der AZ maßgebliche Bedeutung für ihre Freisetzungswahrscheinlichkeit hat. Ich habe mehrere Komponenten der Proteinmatrix der AZ identifiziert und charakterisiert, die die SV Verteilung beeinflussen. Der Ort gedockter SV wird von Unc13 festgelegt; Unc13 determiniert somit die Orte der SV-Fusion und hat damit einen direkten und maßgeblichen Einfluss auf die Freisetzungswahrscheinlichkeit von SV. Ist die Verteilung der T-Bar-assoziierten SV verändert wie in *brp*$^{nude}$, ist die Rekrutierung der SV zu den Fusionsstellen eingeschränkt. Darüber hinaus bestimmen sowohl die Komposition der Proteinmatrix als auch Lipide der Plasmamembran an der Aktiven Zone ganz generell die Wahrscheinlichkeit der evozierten und spontanen Transmitterausschüttung schon innerhalb einer einzelnen NMJ (wie in Fall von Spinophilin gezeigt wurde).

# 2. Introduction

## 2.1. The Chemical Synapse

In the nervous system, signals are travelling in form of action potentials (APs) along the axons of neuronal cells. At specialized contact sites called synapses, the signal is transmitted to the next cell. At the electrical synapse, cell contacts are formed by gap junctions, which can conduct current. Thereby, voltage changes can easily pass from one the cell to the other.

At the chemical synapse, the electrical signal is converted to a chemical one. Here, the plasma membrane of the signal transmitting presynaptic cell is in close proximity to the postsynaptic cell, only separated by the synaptic cleft (Fig. 1). At the presynaptic site, neurotransmitter molecules are stored in synaptic vesicles (SV), spherical organelles that cluster at the site of release, and which release their content when $Ca^{2+}$ enters the cell through voltage-gated $Ca^{2+}$ channels (VGCC). The opening of VGCCs is triggered by the arrival of an AP at the terminal, leading to a change of the membrane potential. $Ca^{2+}$ triggers the fusion of SVs with the plasma membrane at specialized areas of the plasma membrane called active zones (AZs) (Fig. 2). The understanding of the coupling between $Ca^{2+}$ influx and SVs is essential to comprehend i) the relationship between factors shaping the efficacy and speed of synaptic transmission, ii) the mechanism behind different forms of synaptic plasticity (which is the ability of synapses to adapt to changing conditions), and iii) the mechanisms underlying information coding and processing in the brain (Eggermann et al., 2011). It is essential to know on one side how many $Ca^{2+}$ channel are necessary to trigger fusion, and on the other side how many VGCC in general are participating in the fusion process, in order to understand the causal relationships between channel kinetics and transmitter release. These aspects have been extensively studied, mostly at the easily accessible model synapse in the mammalian auditory system Calyx of Held. Here, it was shown that the opening of a single $Ca^{2+}$ channel can already trigger SV fusion (Stanley, 1993). However, with smaller amounts of participating $Ca^{2+}$ channels, the volume in which the local $Ca^{2+}$ concentration changes is decreased (=*$Ca^{2+}$ nanodomain*). $Ca^{2+}$ nanodomains are defined as domains of elevated $Ca^{2+}$ concentrations that extend over less than 100 nm, and are differentiated from the so-called *$Ca^{2+}$ microdomain*, which extends over more than 100 nm.

The $Ca^{2+}$ -triggered quantal release of neurotransmitter in discrete packets (one packet = one SV = 1 quantum) was described by Fatt and Katz in 1952. The transmitter molecules are released into the synaptic cleft, bind to ligand-gated ion channel receptors located in the plasma membrane of the postsynaptic compartment, and evoke de- or hyperpolarization of the postsynaptic cell, depending on whether the synapse type is excitatory or inhibitory. In the postsynaptic cell, membrane-incorporated receptors convert the chemical signal back to an electric signal. At e.g. an excitatory glutamatergic synapse, the cytosolic part of the receptors is embedded in a mesh of intracellular scaffold proteins including PSD-95, Shank, GKAP, and Homer (MacGillavry et al., 2011).

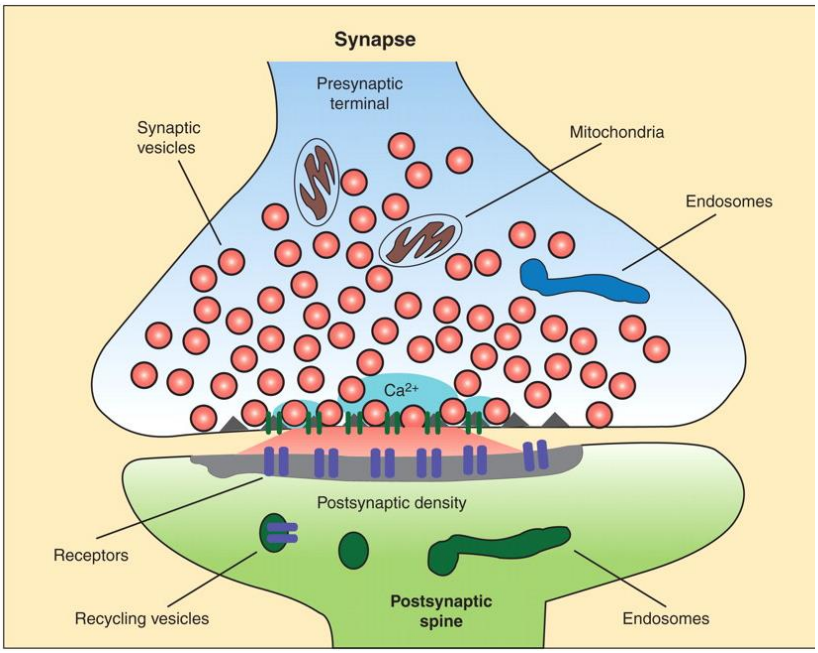


Figure 1 **Schematic Representation of a Central Vertebrate Synapse.** The presynaptic compartment is highlighted in light blue, the postsynaptic compartment in green. The postsynaptic density is marked as a dark shadow at the postsynaptic plasma membrane. The localized influx of $Ca^{2+}$ at the active zone (= blue area) over the $Ca^{2+}$ channels (green, in presynaptic plasma membrane) leads to neurotransmitter release (red = secreted neurotransmitters). The receptor field at the postsynapse is represented by purple ion channels.
Modified from (Südhof, 2012)

This network is called postsynaptic density (PSD) and serves i) via multiple protein interaction domains of the scaffold proteins as an intracellular framework to ensure local enrichment of receptors, ii) as a link to cell adhesion molecules like Neuroligins, LRRTMs (leucine rich repeat transmembrane protein family), and SALMs (synaptic cell adhesion-like molecule protein family), and iii) as the connection to the highly ordered Actin network which stabilizes the post-synaptic molecular architecture. In mammals, prominent receptor types for the neurotransmitter glutamate are AMPA (α-amino-3-hydroxy-5-methyl-4-isoxazolepropionic acid)- and NMDA (N-methyl-D-aspartate)- receptors. In *Drosophila melanogaster*, well-studied glutamatergic model synapses are found at the neuromuscular junction (NMJ). Here, glutamate receptors (GluRs) are heteromeric tetramers consisting of the essential subunits GluRIIC, GluRIID, and GluRIIE, and either GluRIIA or GluRIIB. They have different gating kinetics and their composition changes during the maturation of the synapse (Marrus et al., 2004; Qin et al., 2005).

In the postsynaptic cell, the local change of membrane potential propagates along the membrane as a newly formed electrical signal. The input from multiple contact sites (e.g. at different dendrites) are integrated at a specialized structure at the base of the axon, called axon hillock. According to a binary all-or-none response, a new AP is formed in the axon if the summated membrane depolarization exceeds a specific threshold.

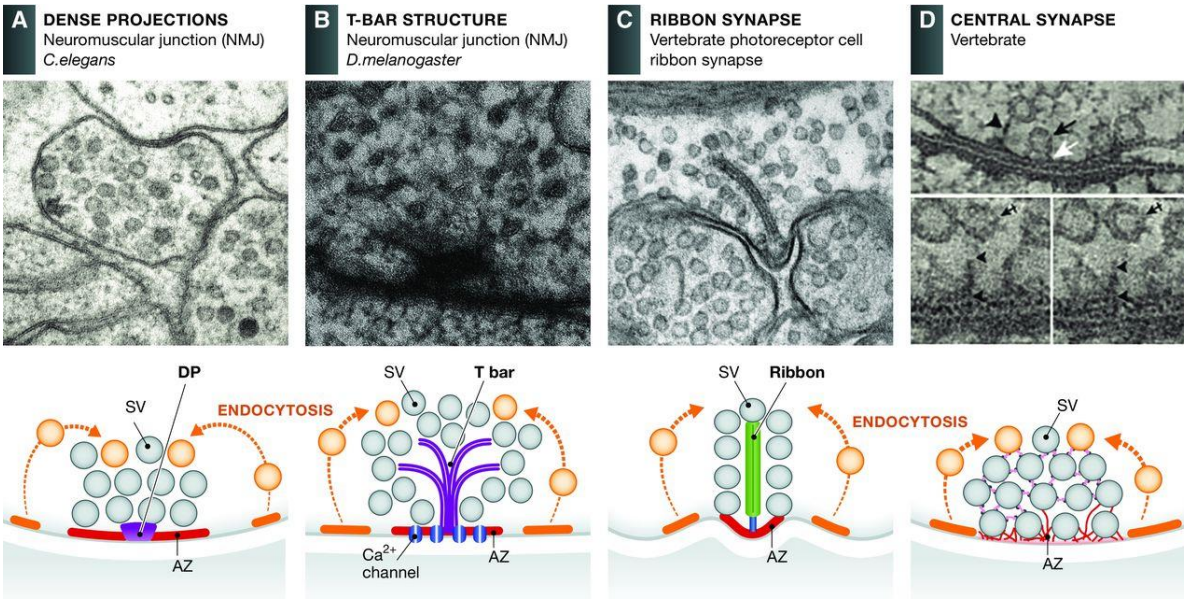


Figure 2 **Active Zones Display Different Morphologies.**
Electron micrographs and schematic drawings reveal that AZs can be divided into morphologically distinct groups: those with elaborate electron-dense projections such as T-Bars and ribbons, those with less prominent dense projections including *C. elegans* AZ, and those present at most vertebrate central nervous system synapses. (A) AZ from a *C. elegans* neuromuscular junction (NMJ). In general, these AZs are quite simple and generally characterized as a broad surface of plasma membrane situated between electron-dense projections and flanking cellular tight junctions. (B) AZs present at the NMJ of the fruit fly *Drosophila melanogaster*. These structures are more elaborate, forming a platform consisting of a meshwork of filaments overlaying a pedestal, which gave them the name T-Bars. (C) Vertebrate photoreceptor cell ribbon synapse. These synapses are characterized by a large AZ with a specialized organelle, the synaptic ribbon, which tethers large numbers of SVs near the AZ, facilitating fast-sustained synaptic transmission. (D) AZs of vertebrate central synapses are less complex than at sensory synapses, exhibiting fine filamentous projections that connect proximally (docked vesicles) and more distally located SVs, up to 100 nm, to the plasma membrane holding them close to the release sites. In schematic drawing, active and endocytic (not shown in electron microscopy micrograph) zones are marked as red and orange, respectively.
Figure and corresponding legend modified from (Ackermann et al., 2015)

Signal transduction at chemical synapses is a very fast but highly regulated process. Activity-dependent plasticity of synaptic transmission is a key property of brain function and the basis for learning and memory. On a short-term scale, the synapse can dynamically adapt to variable transmission intensities (so-called short-term plasticity, STP), but also long-term plasticity (long-term potentiation, LTP, increases synaptic strength, while long-term depression, LTD, reduces synaptic strength) has been described which results in lasting molecular rearrangements at the synapse. These adaptations occur at both the pre- and postsynaptic side, and include the regulation of the efficacy of transmitter release at the presynaptic terminal (Bear & Malenka, 1994), or

postsynaptic changes in receptor number or receptor open probability (Banke et al., 2000; Scannevin & Huganir, 2000; reviewed in Choquet & Triller, 2013)

A specialized set of proteins is involved in SV fusion in the presynaptic compartment. The relevant proteins for the SV fusion and recycling process are under investigation, and in the last years progress has been made in the identification of necessary steps and interactions during the process. Nonetheless, not all relevant components involved in synaptic transmission are identified yet, and it is influenced by plenty of parameters like the lipid composition in the membrane (Puchkov & Haucke, 2013) or $Ca^{2+}$-induced adaptations (R Schneggenburger & Rosenmund, 2015). Thus, SV dynamics are still intensely studied. Fortunately, the structure and function of most synaptic proteins are evolutionary conserved, and *Drosophila melanogaster* comprises orthologues of all major release proteins (Bruckner et al., 2012; Graf et al., 2012; Kaufmann et al., 2002; Liu et al., 2011; Wagh et al., 2006), which make the fruit fly a utile model to investigate the involved molecular players.

## 2.2. The Synaptic Vesicle Cycle

At the presynapse, a coupled process of exo- and endocytosis of SVs called the synaptic vesicle cycle ensures successful transmitter release (Fig. 3). The synaptic vesicle cycle starts with the recruitment of SVs to AZ, where they are tethered and docked at the AZ close to VGCCs, and subsequently molecularly primed. Molecular priming is a process involving several steps that lead to a fusion-competent SV. The total amount of fusion-competent SVs at a synapse is called the readily releasable pool (RRP). Upon $Ca^{2+}$-influx caused by an AP, the $Ca^{2+}$ sensor on a SV induces its fusion with the plasma membrane at so-called release sites, and its content diffuses into the synaptic cleft. Endocytosis recovers membrane and SV proteins, which are recycled and provided for following fusion events. At almost all steps of the synaptic vesicle cycle $Ca^{2+}$, or more precisely the local $Ca^{2+}$ concentration, has an essential role in controlling SV dynamics. Local $Ca^{2+}$ concentration regulates the dynamic equilibrium between different states of SVs during the recruitment and priming process. Additionally, elevated $Ca^{2+}$ concentrations in the presynapse also increase the rate of endocytosis; though it is not mandatory, $Ca^{2+}$ facilitates endocytosis after SV fusion (Deák et al., 2004; Gad et al., 1998).

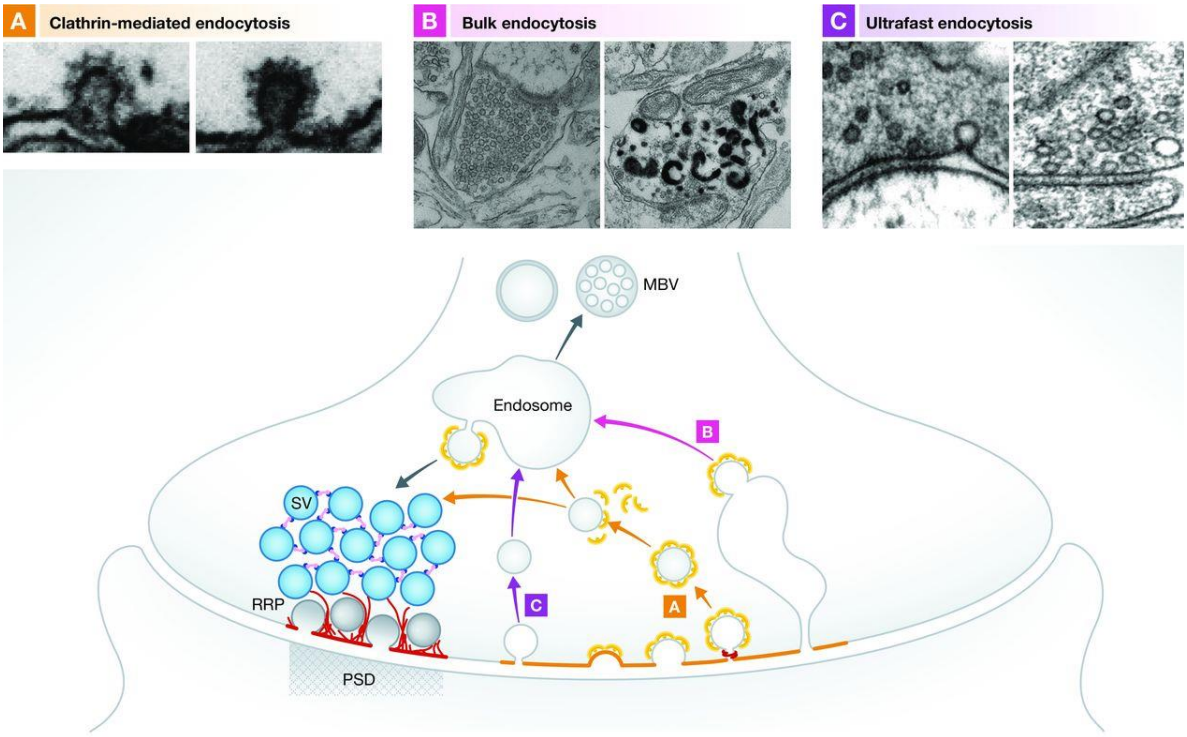


Figure 3 **Synaptic Vesicle Cycle at the Presynaptic Terminal.**
The presynaptic AZ functionally defines the space within boutons where, upon $Ca^{2+}$ influx, SV fusion and neurotransmission takes place (lower panel). It is the center of the SV life cycle. Vesicles are recruited from the vesicle cluster toward the AZ where they undergo maturation steps such as docking and priming, and finally fuse with the plasma membrane upon AP stimulation. After exocytosis, SV protein and membrane retrieval occurs through endocytosis in a region spatially adjacent to the AZ, the periactive zone. It is an important compensatory reaction to recapture excess membrane and generate new SVs. Different endocytosis pathways are known and can be visualized by electron microscopy following evoked stimulation (top panels). Clathrin-mediated endocytosis (A) is a slow form of membrane retrieval. SV proteins and membrane are taken up through the formation of Clathrin-coated pits, which are later pinched off from the membrane through the GTPase Dynamin. After uncoating, the newly formed vesicles either join the vesicle cluster or pass an additional sorting step through an early endosome. Bulk endocytosis (B) is a second form of endocytosis that mainly takes place during strong stimulation. Large membrane fractions are collected in big invaginations and pinched off from the plasma membrane. New vesicles are then formed via Clathrin-mediated budding from these structures. Most recently, a new mode of endocytosis has been described, termed ultrafast endocytosis (C). It is a very fast retrieval mechanism as it can take place within 50–100 ms after stimulation. Vesicles are pinched off from the plasma membrane at the edge of the AZ. Free vesicles fuse with a sorting endosome from which new synaptic vesicles are formed in a Clathrin-dependent manner. Top panels, EM micrographs of Clathrin-mediated (A), bulk (B), and ultrafast (C) endocytosis. Reproduced with permission from Frauke Ackermann, Joshua A. Gregory, and Lennart Brodin (A); [156] (B); [100] (C).
Figure and corresponding legend from Ackermann et al., 2015.

### 2.2.1. Synaptic Vesicle Fusion

Fusion of biological membranes is generally conducted by SNARE proteins (soluble N-ethylmaleimide-sensitive factor attachment receptor proteins). In neurons, the vesicular SNARE (vSNARE) protein is Synaptobrevin (or VAMP, vesicle-associated membrane protein); the target-SNARE (tSNARE) proteins in the plasma membrane are SNAP-25 (synaptosomal-associated protein 25) and syntaxin-1 (Fig. 4). Prior to fusion, the priming factor (M)Unc13 (mammalian homolog of C*. elegans* Uncoordinated-13 protein) catalyzes the opening of Syntaxin-1 from a closed into an activated open conformation. The three SNARE proteins form a *trans*-complex, where

their coiled-coil regions form a helix, twisting around each other and thereby forcing both membranes (of the vesicle and the plasma membrane, respectively) into close proximity. The SV is now primed (i.e. fusion-competent), but not yet fusing with the plasma membrane. This requires the influx of $Ca^{2+}$ ions through VGCC upon the arrival of an AP. The increase in $Ca^{2+}$ concentration is locally very restricted, and sensed by a protein on the SV called Synaptotagmin-1 that triggers the fusion. This reaction needs Complexin a as cofactor (Fig. 4). (M)Unc-18 (mammalian homolog of *C. elegans* uncoordinated 18, unrelated to (M)Unc13) is bound to Syntaxin-1 already in the closed conformation and stays bound to the assembled SNARE complex until the neurotransmitter is released. Its presence is crucial for the fusion process (Deák et al., 2009; Gerber et al., 2008; Khvotchev et al., 2007; M. Verhage et al., 2000). After fusion, the SNARE proteins are recycled; before that, the SNARE complex must dissociate again. This reaction is mediated by an evolutionarily conserved ATPase called NSF (N-ethylmaleimide-sensitive factor) (Söllner et al., 1993). In summary, many proteins are involved in SV recruitment and fusion, but essential for release are only Unc18, Unc13 and the SNARE proteins. However, which factor(s) finally determine the site of release still needs to be elucidated.

For the spatial organization of SVs at the AZ, several additional proteins are required (Fig. 4). Among these are RIM (Rab3-interacting molecule), Bruchpilot (BRP, the ortholog of ELKS/ CAST/ ERC in *D. melanogaster*), RIM-binding protein (RBP), Syd-1 (synapse defective), Rab3, Neurexin (Nrx) and Neuroligin (Nlg). Their structure and function are explained in detail in section 6.1 "The Cytomatrix at the AZ: structure and function of key components" in the appendix.

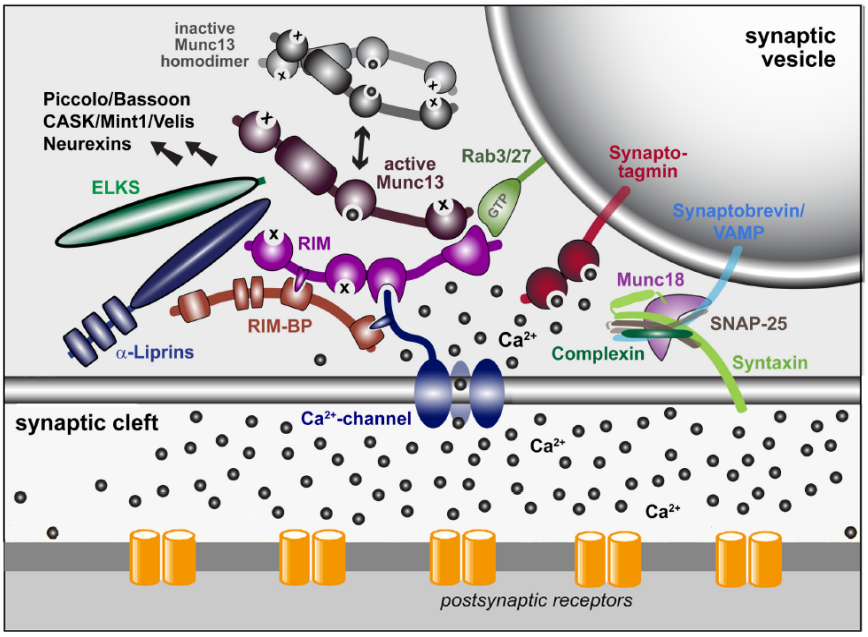


Figure 4 **Molecular Model of the Active Zone Protein Complex and Its Relation to the Synaptic Vesicle Fusion Machinery, $Ca^{2+}$ Channels, and Synaptic Cell-Adhesion Molecules.** For reliable and efficient fusion of a SV the $Ca^{2+}$ sensor Synaptotagmin is located in the SV's membrane and it is primed in close proximity to the $Ca^{2+}$ channels at the AZ. SV fusion is achieved via the SNARE machinery containing Synaptobrevin, Syntaxin and SNAP-25, supported by Complexin and Munc18. Several additional proteins are involved in the spatial organization of SVs at the AZ, like RIM, RIM-BP, Bruchpilot (the homologue of ELKS/ CAST/ ERC), Liprin-α and Munc13. Figure is adapted from Südhof, 2012; Südhof, 2013.

### 2.2.2. Synaptic Vesicle Endocytosis

SV proteins need to be recycled, as their number is limited and physiological AP firing frequencies can be as high as 100 Hz, e.g. in the auditory system (Taschenberger & von Gersdorff, 2000; S. Wu & Kelly, 1993). Furthermore, the increase in cell surface area by the addition of membrane with each fusion must be constrained. In this context, four different ways of endocytosis have been described, and all of them depend on Dynamin, a large GTPase necessary for pinching off endocytic vesicles. The different forms of endocytosis exhibit specific properties and are subdivided into the classes (1) kiss-and-run, (2) Clathrin-mediated endocytosis, (3) bulk endocytosis and (4) ultrafast endocytosis (reviewed in Kononenko & Haucke, 2015).

*(1) Kiss and Run* is a fast form of endocytosis, where the fusion pore opens only transiently at the AZ. The SVs do not collapse into the plasma membrane, all SV molecules are maintained. Thus, extensive protein sorting for later re-use of the SVs is avoided. Despite, or rather because of the fact that this mechanism was investigated in several subtypes of synapses with various techniques (reviewed in Alabi & Tsien, 2013), conflicting interpretations have emerged. There is no consensus in the research field whether kiss-and-run mechanism occurs during normal synaptic activity at all.

*(2) Clathrin-mediated endocytosis* (Fig. 3A) is a very well characterized process and definitely observed in various types of neurons at physiological conditions. It is rather slow in comparison (~ 20-30 s) and involves a variety of proteins like Endophilins, Amphiphysin, Synaptojanin, and Auxilin. Major cargos in this recycling mechanism are SV proteins, which accumulate at the periactive zones (lateral to the AZ), where they are sorted into Clathrin-coated pits and finally internalized. Detailed information about this process can be found in McMahon & Boucrot, 2011.

*(3) Bulk endocytosis* (Fig. 3B) is characterized by large invaginations of the plasma membrane lateral to the AZ and is mainly observed after very strong stimulation. Here, large vacuole-like structures are formed, which in later stages are processed into SVs, possibly with involvement of Clathrin (Heerssen, Fetter, & Davis, 2008).

*(4) Ultrafast endocytosis* (Fig. 3C) is, as the name suggests, a very rapid form of endocytosis (~100-300 ms) where SVs fully collapse into the plasma membrane (Watanabe, Liu, et al., 2013; Watanabe, Rost, et al., 2013). Peripheral to the AZ or directly close to the dense-projection, membrane invaginations and subsequent formation of large vesicles (80-100 nm diameter) were observed. This first step of the process is Clathrin-independent, but requires Actin (Watanabe et al., 2014). The endocytic vesicles are further converted into SVs, possibly under the involvement of Clathrin in these later steps (N. L. Kononenko & Haucke, 2015).

All described recycling pathways are Dynamin-dependent, and the terminal seems to be able to switch between slow and ultrafast endocytosis mode, dependending on the requirements of transmission like neuronal activity (N. L. Kononenko & Haucke, 2015; Watanabe et al., 2014).

## 2.3. Short-Term Plasticity (STP), SV Release Probability ($P_r$ and $P_{ves}$) and Synaptic Strength

The expression *short-term plasticity* (STP, reviewed in Alabi & Tsien, 2012; Hallermann et al., 2010; Körber & Kuner, 2016) describes a set of reversible changes in *synaptic strength* which happen on a short timescale (milliseconds to minutes). Preceding stimulation of release at a synapse will affect the amount of released neurotransmitter in a subsequent stimulation in a particular manner. The term *synaptic depression* describes a reduction in neurotransmission following single or repetitive (train) stimulation. It occurs when the limited pool of readily releasable SVs is depleted faster than fresh transmitter-filled SVs are replenished (refilling rate) (Zucker & Regehr, 2002). Additional factors influence synaptic depression, including use-dependent decrease of $Ca^{2+}$ currents (Jianhua Xu & Wu, 2005), release site inactivation (Armitage & Siegelbaum, 1998), and postsynaptic receptor desensitization or saturation (Neher & Sakaba, 2008). The term *synaptic facilitation* describes an increase in neurotransmission following a single or train stimulation. It is observed because the locally restricted elevated $Ca^{2+}$ concentration expands under repeated stimulation and triggers fusion of readily releasable vesicles in a larger distance from the $Ca^{2+}$ source (Katz & Miledi, 1967). Depression and facilitation are two counteracting processes that influence the efficacy of neurotransmitter release. However, the relationship between synaptic depression, facilitation, and the depletion of SVs with heterogeneous release properties is very complex and differs among different synapse types (Kraushaar & Jonas, 2000; Ralf Schneggenburger, Sakaba, & Neher, 2002).

The *release probability* ($P_r$) is a measure for synaptic reliability, and reflects the likelihood of at least one SV fusion upon the trigger of an AP (Alabi & Tsien, 2012). If a synapse shows depression in paired pulse recordings, the $P_r$ at this synapse is as high, as the likelihood of fusion upon first stimulation was high. Vice versa, the initial $P_r$ is low at a synapse when facilitation is observed in paired pulse recordings. $P_r$ has to be distinguished from the release probability of a single SV ($P_{ves}$). Synaptic reliability is additionally influenced by the number of release-ready SV (N), which equals the size of the RRP, however N sometimes also represents the number of fusion sites.

Synaptic strength, indicated by the size of the evoked excitatory junctional current (eEJC, I), is influenced by several factors that can be summarized in the following formula:

$I = N*P_{ves}*q$

(del Castillo & Katz, 1954)

It is dependent on the number of release sites (or readily-releasable SVs) (N), the average release probability ($P_{ves}$) of a single SV, and the quantal size (q) (i.e. the current, or charge, elicited by an average mEJC, representing spontaneous fusion events of single SVs as a measure of the quantal size). Changes in synaptic strength can principally arise from alterations of any of these factors. The level of depression during long-term stimulation and the recovery of it to former synaptic strength afterwards depends on the speed of recruitment of release-ready vesicles (Haucke, Neher, & Sigrist, 2011; Takahashi, 2015). Rate-limiting in this process might be the clearance of release sites (Neher, 2010), while an elevated $Ca^{2+}$ concentration has been reported to increase speed of the refilling rate and release site clearance (Henkel & Betz, 1995; Kuromi et al., 2010; Kuromi et al., 2004; Kuromi & Kidokoro, 2002; Zefirovet al., 2006).

## 2.4. Synaptic Transmission Modes: Synchronous, Asynchronous and Spontaneous Release; Tight and Loose Coupling

In the process of neurotransmitter release, three primary modes are distinguished: synchronous release, asynchronous release and spontaneous release. Synchronous release is the rapid and immediate transmitter release upon stimulation (Fig. 5A) and occurs within several milliseconds after an AP reaches the presynaptic terminal, while asynchronous release persists after the stimulus for tens of milliseconds up to tens of seconds after an AP or a series of APs (Fig. 5B). Spontaneous release is the fusion of a single SV independently of an AP (Fig. 5C) (Kaeser & Regehr, 2014; Neher & Sakaba, 2008; R Schneggenburger & Rosenmund, 2015). In a train of stimuli the $Ca^{2+}$ nanodomain increases and residual $Ca^{2+}$ builds up, thereby reaching readily releasable SVs in a higher distance from the $Ca^{2+}$ source and triggering their fusion. However, SVs in a larger distance to the $Ca^{2+}$ source are more likely to fuse in an asynchronous manner. This is only in part due to the diffusion time of the $Ca^{2+}$ ions, while the main cause is the intrinsic variability in kinetics of interleaved reactions of the fusion process and complex $Ca^{2+}$ dynamics at the presynaptic terminal under repetitive stimulation.

SVs with a high $P_{ves}$ are more likely fusing in a synchronous manner. The timing of SV fusion (synchronous/asynchronous mode) and its fusion probability $P_{ves}$ is directly dependent on the spatial

arrangement of the SVs with $Ca^{2+}$ channels (Fig. 6A), and can be measured in $Ca^{2+}$ buffering experiments with $Ca^{2+}$ chelators, such as *EGTA* (ethylene glycol-bis(2-aminoethylether)-N,N,N',N'-tetraacetic acid) and *Bapta* (1,2-bis(2-aminophenoxy)ethane -N,N,N',N'-tetraacetic acid). These two commonly used $Ca^{2+}$ buffers have different on-rates ($k_{on}$), but comparable affinities ($K_D$) (Fig. 6B). In several studies it was shown that the slow $Ca^{2+}$ chelator EGTA eliminates asynchronous release, but has minimal effect on synchronous release (Atluri & Regehr, 1998; Cummings, Wilcox, & Dichter, 1996). This implicates that the $Ca^{2+}$ sensor for asynchronous release is in a larger distance from the $Ca^{2+}$ source (Fig. 6B), likely based on positional heterogeneity in the SVs of the readily releasable pool (Meinrenken, Borst, & Sakmann, 2002).

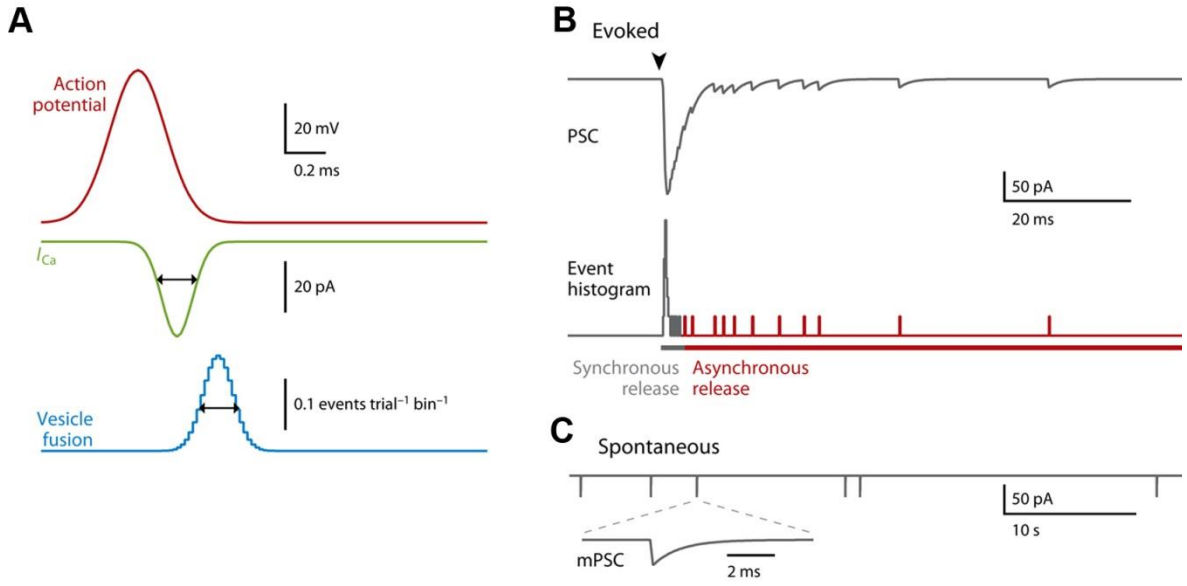


Figure 5 **Exemplary Scheme of Synaptic Transmission Modes, and Synchronous and Asynchronous Release.**
Different types of synaptic transmission illustrated with simulated data. (A) Stimulation (*arrowhead*) evokes synchronous and asynchronous release. (B) Spontaneous neurotransmitter release is shown on a different timescale. The inset shows a miniature postsynaptic current on an expanded timescale. Abbreviations: mPSC, miniature PSC; PSC, postsynaptic current. (C) Precision of synchronous release relies on brief $Ca^{2+}$ channel signals and on the rapid kinetics of the $Ca^{2+}$ sensor. The schematic illustrates the rapid depolarization and repolarization of an AP, and the speed of the resulting $Ca^{2+}$ current ($I_{Ca}$) and vesicle fusion.
Figure and figure legend modified from (Kaeser & Regehr, 2014)

Some studies even suggest a specialized $Ca^{2+}$ sensor with a less steep $Ca^{2+}$ dependence with lower $Ca^{2+}$ cooperativity that mediates asynchronous release. Highly controversially discussed candidates for this alternative sensor are Syt7 and Doc2, which themselves are specific to distinct synapse types (Kaeser & Regehr, 2014). However, it should be pointed out that the biophysical properties of the $Ca^{2+}$ signal alone are complex enough to produce synchronous and asynchronous release with just a single sensor (Xu-Friedman & Regehr, 1999, reviewed in Neher & Sakaba, 2008).

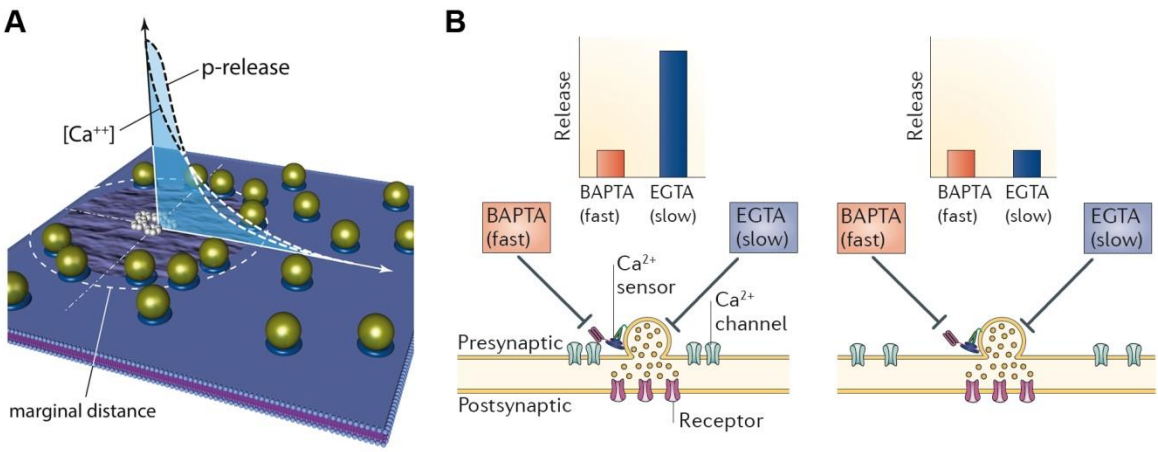


Figure 6 **The Coupling Distance Determines the Release Probability.**
A cluster of five VGCCs is assumed to be surrounded by ''fast'' vesicles at a certain perimeter. Some more ''slow'' vesicles are spread at larger distances. Local $Ca^{2+}$ concentration during an action potential ($[Ca^{2+}]$) is assumed (for simplicity) to decay inversely with distance. Release probability (p-release) decays as a power function of the latter. The strength of stimulation, as drawn, is such that p-release reaches the marginal value at a radius (marginal distance) that includes most of the fast vesicles. According to the simulations (Neher, 2015), these fast vesicles, but not slow ones, would show up in RRP estimates. For stronger stimulation (larger $[Ca^{2+}]$ and p-release), the marginal distance would be larger, and more vesicles would be included in the estimated pool. The drawing shows more vesicles per VGCC clusters than are actually present at the Calyx of Held, for better visualization of the vesicle distribution. (B) $Ca^{2+}$ chelators with different on-rates are used to probe the distance between $Ca^{2+}$ channels and sensors. In a tight coupling regime (left), only the fast $Ca^{2+}$ chelator BAPTA, but not the slow $Ca^{2+}$ chelator EGTA, will capture the $Ca^{2+}$ on its way from the source to the sensor. By contrast, in a loose coupling regime (right), both chelators will be effective, according to their affinity values, which are comparable.
Figure and figure legend modified from Neher, 2015 (A) and Eggermann et al., 2011 (B).

Whether spontaneous release has a relevant physiological function, or simply is a failure in the suppression of spontaneous SV fusion is under discussion since mEPSCs were discovered. Several functional roles for spontaneous SV fusion have been proposed, e.g. in the regulation of the excitability of neurons (Kombian et al., 2000) or in the synaptic stabilization, synaptic strength (Sutton et al., 2004) and long-term forms of synaptic plasticity (Frank et al., 2006; Zhang et al, 2009). Several proteins of the cytomatrix at the AZ (CAZ) have been proposed to "clamp" SVs at AZs thereby preventing their spontaneous vesicle fusion, e.g. Complexin (Huntwork & Littleton, 2007) and BRP (Peled & Isacoff, 2011).

The suggested prerequisites for spontaneous release are numerous and not consistent. The molecular machinery for evoked release might be the same as or different from the ones required for spontaneous SV fusion. Furthermore, $Ca^{2+}$ independent spontaneous release is possible, but the reduction of $Ca^{2+}$ influx tremendously decreased the spontaneous event rate at most synapse types (Goswami et al, 2012; Williams et al., 2012; Xu et al, 2009). However, it should be kept in mind that although the frequency of spontaneous events is mostly $Ca^{2+}$ dependent, the size of an average mEPSC, which equals to one quantum, is unaffected by the external $Ca^{2+}$ concentration. This is due to the fact that transient changes in the $Ca^{2+}$ concentration, like in a $Ca^{2+}$

nano- or microdomain, do not alter the amount of stored neurotransmitter in a single SV. It can be summarized that the supposed mechanisms for spontaneous SV fusion are not fully understood and controversially debated (reviewed in Kaeser & Regehr, 2014; R Schneggenburger & Rosenmund, 2015).

The terms "tight" and "loose coupling" describe the spatial arrangement between SVs and the $Ca^{2+}$ source at an AZ and are thus directly related to $P_{ves}$. Tightly coupled SVs are located in close proximity to the $Ca^{2+}$ source and in consequence have a high $P_{ves}$, are fusing in a synchronous manner and their fusion is insensitive to EGTA treatment. In contrast, loosely coupled SV are located in higher distance to the $Ca^{2+}$ source and therefore have a lower $P_{ves}$, a higher likelihood to fuse in an asynchronous manner and their fusion is sensitive to EGTA treatment. A prominent example is the Calyx of Held, where during development the spatial arrangement is altered from a loose coupling regime in young animals toward a tight coupling regime in older animals release (Fedchyshyn & Wang, 2005; L.-Y. Wang, Neher, & Taschenberger, 2008). It has been shown that tight and loose coupling of SVs can function as regulatory elements to modify synaptic strength as a form of presynaptic plasticity (Ahmed & Siegelbaum, 2009; Vyleta & Jonas, 2014) (reviewed in Eggermann et al., 2011).

In summary, the interplay between the coupling modes has direct influence on the release mode of a synapse and on SV release probability.

## 2.5. Synaptic Vesicle Pools

In electron micrographs, morphological characteristics to distinguish SV are only based on the spatial localization of the vesicle relative to other structures at the synapse, like the plasma membrane or the electron-dense projection. In this context, SVs have been subdivided into the class of *docked SVs*, being attached to or located sufficiently close (<5 nm) to the plasma membrane, and the class of *tethered SVs*, where a connective linker of varying distances is observed to either the plasma membrane or the dense projection. The main portion of SVs however resides in the lumen of the axon terminal and is cross-linked to their respective SV neighbors (Fig. 7A). Synapsin has been identified as being crucial for this cross-linking and is found to have regulatory function on SV dynamics in the terminal (Bykhovskaia, 2011).

The term "docking" is purely based on morphological observations, which are identified by electron microscopy (EM). Recent advances in structure preservation of dynamic processes for EM suggest morphological correlates to the hitherto primarily physiologically defined SV pools (Watanabe, Liu, et al., 2013; Watanabe, Rost, et al., 2013). However, in general, SVs appear

morphologically indistinct in electron micrographs concerning their functional characteristics. The following distinction of SVs into functional pools was made based on physiological criteria, as functional heterogeneity has been observed in electrophysiological recordings and their different properties have led to the following classifications: In addition to the already mentioned *readily releasable pool (RRP)* of SVs, which is rapidly depleted during stimulation and contains the docked and primed SVs ready for fusion upon arrival of an AP, the further differentiation into *reserve pools* and *recycling pools (RP)* is widely accepted (Fig. 7A, B) (Alabi & Tsien, 2012; Denker & Rizzoli, 2010; Rizzoli & Betz, 2005). The *recycling pool (RP)* is continuously replenished during release and supplies SVs during moderate stimulation, while the reserve pool constitutes a depot of SVs which is accessed only during prolonged activity (Fig. 7A, B) (Haucke et al., 2011). At hippocampal synapses, all SVs which participate in release and/or recycling are grouped into the "total recycling pool" (TRP), while the SVs not participating in release are named "resting pool" (RtP) (Fig. 7B). Here it was shown that the number of docked SVs is decreased after evoked synaptic transmission. As already mentioned, the term “docked” SV originates from EM and describes the morphological arrangement of SVs at or close to the plasma membrane. Docking is a prerequisite for priming, the molecular requirement to finally achieve a fusion-competent SV, which is measured in RRP estimates in electrophysiological recordings. However, the number of docked SVs exceeds the number of SVs in the RRP; thus, “docking” is upstream of “priming” and not all docked SV are ready-releasable (Alabi & Tsien, 2012; Matthijs Verhage & Sørensen, 2008). Furthermore, it turned out that additional subdivisions of pools are necessary (Fowler & Staras, 2015; Schneggenburger et al., 2012). A new pool classification named superpool has been suggested in recent years, which defines a SV population that is dynamically shared at a high rate along axons between multiple presynaptic terminals (Fig. 7B) (Staras et al., 2010). The superpool is comprised of vesicles from the recycling pool as well as the resting pool in approximately even numbers (Fernandez-Alfonso & Ryan, 2008, reviewed in Fowler & Staras, 2015). However, its existence at the *Drosophila* larval NMJ, which is used as model synapse in this work, remains to be determined.

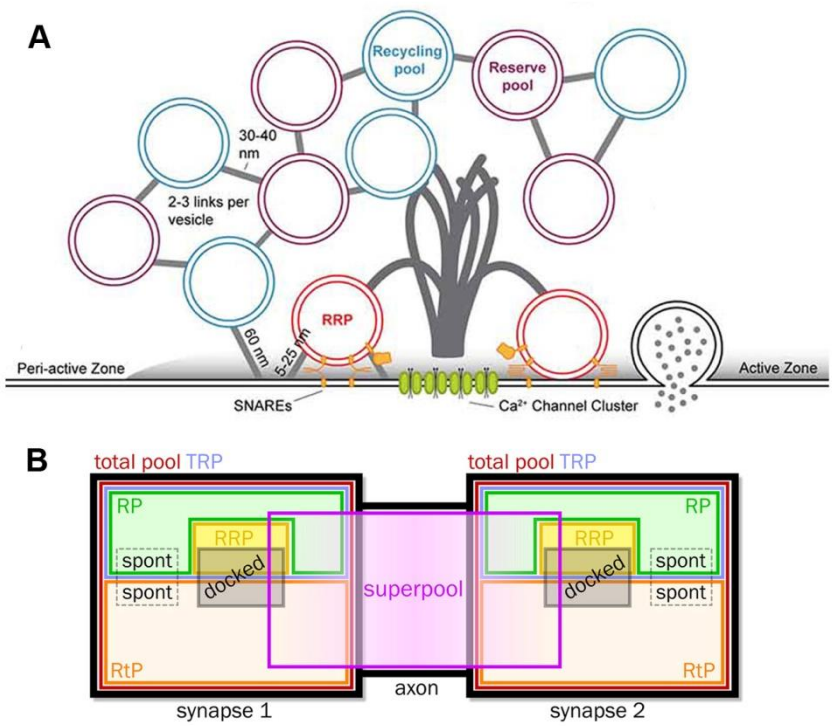


Figure 7 **Heterogeneous Release Properties of SV Lead to Their Classification in Distinct Pools.**
Diverse presynaptic terminals have a number of common structural characteristics visible in electron micrographs. The AZ membrane is delineated by its electron-dense lipid bilayer. Complex cytoskeletal filaments project from the AZ membrane into the presynaptic cytoplasm and are often visible as an electron-dense projection. SVs are 30–60 nm in diameter and organized into three functionally defined pools: the reserve pool (purple) (in hippocampal synapses named resting pool), recycling pool (blue), and readily releasable pool (RRP; red). SVs of the reserve and recycling pools are typically linked to one another by 2–3 thin proteinaceous tethers 30–40 nm in length, and occasionally linked to the AZ membrane by longer filaments of roughly 60 nm in length. The reserve and recycling pools are morphologically intermixed and therefore defined primarily by their mobility in functional assays. RRP vesicles are tethered or docked at the membrane in close proximity to clusters of voltage-gated calcium channels at the base of the dense projection. (B) Schematic picture of principal pool classifications and relationships. The pools shown are *total pool*, *total recycling pool* (TRP), *recycling pool* (RP), *resting pool* (RtP), *readily releasable pool* (RRP), *docked pool* and *superpool*. The *spontaneous pool* is indicated by dashed rectangles reflecting uncertainty in defining its place within existing pool structures. Approximate average magnitudes of pools are indicated by relative box sizes.
Figure and corresponding legend modified from Bruckner et al., 2015 (A) and Fowler & Staras, 2015 (B).

Furthermore, slow and fast fractions of the RRP (SRP and FRP, respectively) were identified in the Calyx of Held, a particularly large synapse in the auditory system in mammals, which allows simultaneous pre- and postsynaptic electrophysiological recordings. The subpopulations of the RRP are distinguished by their difference in release kinetics in response to a step-like voltage-clamp depolarization in the nerve terminal, which evoked release in a fast (*fast releasable pool, FRP*) and a slow (*slow releasable pool, SRP*) phase (Schneggenburger et al., 2012). The fast pool recovered slowly, while the slow pool had a fast recovery rate (Takeshi Sakaba & Neher, 2001). Two explanations are possible for the heterogeneous fusion likelihood of the RRP: i) the readily releasable vesicles are in different proximities to the $Ca^{2+}$ channels (positional model) or ii) the RRP contains two sets of vesicles, which differ in their priming state, and/or in their molecular

equipment (intrinsic model) (Schneggenburger et al., 2012). It was shown that the SRP can feed recovery of the FRP; in this phase the SRP is transiently decreased and thus might serve as an immediate reserve pool for the SRP (Lee et al., 2012). Combined with the positional model and the different recovery kinetics of the pools, the idea was proposed that the already docked SRP vesicles are first molecularly primed before they are moved laterally in closer proximity to the $Ca^{2+}$ channels (= positional priming), possibly in an Actin-dependent manner. However, until now no such movement of docked SV could be shown (Schneggenburger et al., 2012).

Extensive studies have contributed to increase the knowledge on the properties and prerequisites for fusion competence of SVs including their release probability $P_{ves}$ and their spatial position. However, the physical location of the release site and the requirements to define these slots would add valuable information towards understanding the release process. However, the determinants to define the physical release site remain enigmatic to date.

## 2.6. (M)Unc13

(Adapted from Böhme*, Hollmann* et al., under revision)

Unc13 was first described in *C. elegans*, where upon loss of the Diacylglycerol-binding protein Unc13 an uncoordinated phenotype was observed (Maruyama & Brenner, 1991). Mammals have five Munc13 (mammalian Unc13) genes of which Munc13-1, -2, and -3 encode proteins mainly expressed in the brain, while Munc13-4 and BAP3 are primarily found outside of the brain. Munc13-2 contains an alternative promotor which leads to the synthesis of the ubiquitously expressed isoform ubMunc13-2, additional to the brain-specific isoform bMunc13-2 (Augustin et al., 1999; Brose et al., 1995). The domain structure of Munc13 is evolutionarily highly conserved (Fig. 8).

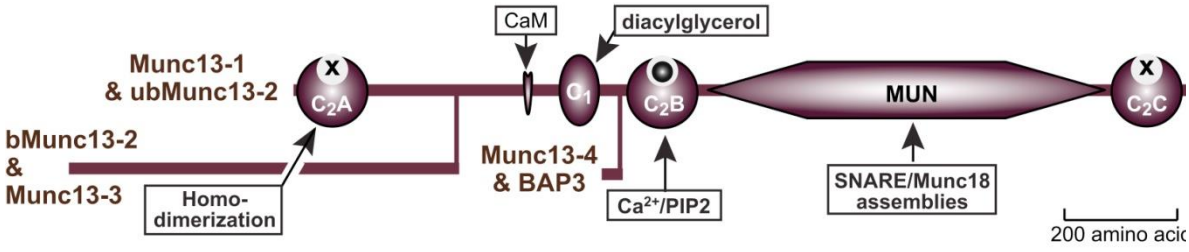


Figure 8 **Domain Structure of the Evolutionarily Conserved Core Active Zone Proteins (M)Unc13.**
Isoforms generated by alternative promoters and major splice variants are shown. Proteins and second messengers binding to specific sites are shown in boxes; domain designations are indicated by standard abbreviations. For C2 domains, $Ca^{2+}$-binding sites are indicated by a sphere and lack of $Ca^{2+}$-binding by an "X." Proteins and domains are drawn to scale, the asterisk indicate the position of the C terminus.
Figure modified from Südhof, 2012

In *Drosophila*, two isoforms are transcribed from a single Unc13 locus by alternative promotors (please see the online database Flybase (Attrill et al., 2015)). Hence, the isoforms differ within their N-terminal region but are identical at their C-terminal region, which includes the so-called C1, $C_2B$, MUN and $C_2C$ domains (please see Figure 12A, B in the results part). The C1 domain is common to both isoforms and mediates binding to Diacylglycerol (DAG). This DAG-binding was shown to induce the translocation of (M)Unc13s to the plasma membrane, influence vesicular release probability, linking C1 domain activation to a lowering of the energy barrier for SV fusion (Basu et al., 2005; Betz et al., 1998; Schotten et al., 2015). The central $C_2B$ domain is involved in $Ca^{2+}$ dependent Phospholipid binding and has been suggested to function in the recruitment of (M)Unc13s to the plasma membrane. Loss of function mutations of the $Ca^{2+}$ binding site of the $C_2B$ domain did not alter SV release upon single AP stimulation, but repressed release evoked by AP-trains, pointing to an involvement in presynaptic plasticity (Shin et al., 2010). Furthermore, both isoforms harbor the so-called MUN domain, which was shown to contain the minimal domain required for molecular priming (Basu et al., 2005; D. R. Stevens et al., 2005). In contrast to Unc13B, Unc13A also harbors a central $Ca^{2+}$ dependent Calmodulin (CaM) binding domain that was shown to be required for $Ca^{2+}$ dependent acceleration of RRP replenishment at mammalian synapses (Noa Lipstein et al., 2013).

## 2.7. Scope of This Thesis

The results and discussion of this thesis will examine the influence of several presynaptic AZ components on the **spatial arrangement of SVs at the AZ**. The major focus is on the investigation of Unc13, a protein already described to be relevant for docking and priming of SVs at the AZ. By means of isoform-specific mutagenesis, the distinct localization of the two Unc13 isoforms in *Drosophila* Unc13A and Unc13B is studied via two-color super-resolution STED microscopy. The resulting altered spatial arrangement of docked SVs at the AZ is investigated with EM, which upon loss of Unc13A are found to be reduced close to the T-Bar and hence, close to the $Ca^{2+}$ channels. The functional consequence of this SV re-arrangement is examined in detailed electrophysiological recordings. Here, high-frequency stimulation trains are utilized to estimate the RRP and the forward priming rate, which both are reduced in *unc13A*$^{Null}$ mutants. Furthermore, in $Ca^{2+}$ titration experiments a reduced SV release probability and $Ca^{2+}$ sensitivity is identified upon loss of Unc13A. The cause of these impairments is found in $Ca^{2+}$ buffering experiments to be an increased coupling distance between the readily-releasable SVs and the $Ca^{2+}$ source in *unc13A*$^{Null}$ mutants. Thus, **Unc13A is identified as the essential Unc13 isoform responsible for**

**tight coupling SV and $Ca^{2+}$ channels**, thereby ensuring fast and reliable transmitter release. However, Unc13B is discovered to have only a minor function in synaptic transmission. How does Unc13A fulfill its function in the spatial arrangement of release ready SVs? By the examination with two-color STED microscopy of an Unc13A transgene lacking the N-term, it becomes clear that **the N-term is essential to keep the protein in place at the AZ**. The proper localization of Unc13 determines sites of SV docking, which is revealed in EM. The functional consequences of this altered docked SV arrangement in *unc13A* mutants are unraveled in $Ca^{2+}$ buffering experiments to result in a highly increased asynchronous release rate. Together, the role of **Unc13 is identified to physically position docked SVs at the AZ, thereby ensuring tight coupling and determination of SV fusion sites**. In flash-freeze experiments, optogenetically stimulated SV fusion and subsequent HPF-conservation is utilized to **unravel the physical site of SV fusion** and following endocytosis in EM. Preliminary data are promising, as the number of endocytic compartments increases upon synaptic stimulation; the experiments are still ongoing. Furthermore, two **novel candidates**, namely PI4KIIIα and Rbcn3B, with a potential role in synapse function at the presynaptic AZ are identified in a loss of function RNAi screen and characterized utilizing immunohistochemical stainings, EM, electroretinography (ERG) in the adult eye and electrophysiological TEVC recordings at the larval NMJ. Both candidates are found to influence NMJ morphology and synaptic transmission. Finally, **the prerequisite for individual AZs to contribute to either spontaneous and/or evoked release is investigated at the level of single AZs.** $Ca^{2+}$ imaging experiments with the postsynaptically expressed membrane-anchored $Ca^{2+}$ sensor myrGCaMP5 are performed in *spn* mutants. Here, Spn is identified to not only have a regulatory role in the formation of new AZs, but also to be relevant for normal synaptic transmission.

## 2.8. The Aim in a Nutshell

- Study of the role Unc13 in SV docking and priming by *Drosophila* genetics, high-resolution light microscopy, electron microscopy and electrophysiological characterization in transmitter release.
    - Identification of the localization of Unc13 isoforms A and B at the *Drosophila* larval NMJ.
    - Investigation of a putative SV docking defect upon loss of Unc13A and its effect on SV coupling distances and $Ca^{2+}$ sensitivity.
    - Characterization of the role of Unc13N-term in the localization of Unc13.
    - Study possible rearrangement of docked SV upon loss of the Unc13 N-term and its effect on SV coupling distances.
- Characterization of the optogenetically induced SV fusion and endocytosis events in flash-freeze experiments on the ultrastructural level by electron microscopy.
- Characterization of novel components (Rbcn3B and PI4KIIIα) of the CAZ and their relevance for transmitter release.
    - Investigation of possible morphological alterations upon protein deficiency in a knock down experiment by light microscopy and electron microscopy.
    - Identification of a putative role in synaptic transmission by electrophysiological recording at the adult compound eye and the larval NMJ.
- Study different release modes (spontaneous and evoked release) on the level of single AZs by *in vivo* $Ca^{2+}$ imaging at the larval NMJ and investigation of a putative role of Spn in this process.

# 3. Materials and Methods

## 3.1. The *Drosophila* Neuromuscular Junction as a Model Synapse

Since the first mutation in *Drosophila melanogaster* was found 1910 by Thomas Hunt Morgan (Morgan, 1910) the fruit fly has been established as one of the best-studied model systems (Fig. 9A-C), especially concerning the multitude of possibilities for genetic modifications and introduction of mutations (Pandey & Nichols, 2011; St Johnston, 2002). After non-directed mutagenesis screens, where mutations were non-specifically introduced in the genome in varying amounts, the increasing number of genetically modified fly lines and technical possibilities allowed the directed genetic modification in the genome. The insertion of transposable P-elements and the invention of stock collections which made transgenic flies available for researchers from all over the world have made *Drosophila melanogaster* easily accessible to transgenesis. In particular, the introduction of the yeast GAL4-UAS expression into the *Drosophila* genome was a milestone, as it allows temporal and tissue specific protein expression (Brand & Perrimon, 1993).

While mammals have a very complex circuitry of nervous connections, the far less complex *Drosophila* model allows understanding the functional importance of molecules at sub-cellular level at synapses. Furthermore, while during evolution the genome of mammals has experienced genetic modifications leading to several paralogs of a gene, the *Drosophila* model organism allows the investigation of single genes, thereby unraveling the function of the gene products without the necessity of double-, triple or even quadruple-knockouts (e.g. Neurexin (Missler et al., 2003), or Rab3 (Schlüter et al., 2004)). Especially important and thanks to so-called balancer chromosomes, *Drosophila melanogaster* can even be propagated with mutations which lead to severe impairments or even lethality in early developmental stages, thereby allowing the identification and analysis of genes which e.g. are relevant for neuronal signal transduction (e.g. Unc13, see Results section).

Especially the larval neuromuscular junction (NMJ) harbors properties similar to mammalian central synapses and is a well-established and utile model synapse to study synaptic transmission, assembly and plasticity (Sigrist et al., 2003). At the NMJ, glutamatergic motoneurons project onto larval body wall muscles (Fig. 9C). The stereotypic bilaterally symmetric anatomy of motoneurons and muscles in segmented *Drosophila* larvae is useful for the comparison of identical synapses and allows orientation in the animals without difficulty (Fig. 9A). Beside the easy

visualization of its morphology with immunohistochemical stainings or EM, also *in vivo* studies of axonal transport or synapse assembly are possible (Owald et al., 2010). Additionally, functional readouts like electrophysiological recordings and $Ca^{2+}$-imaging can be performed (Peled & Isacoff, 2011). The special features of the NMJ model synapse combined with the multitude of available methods allow the description of the

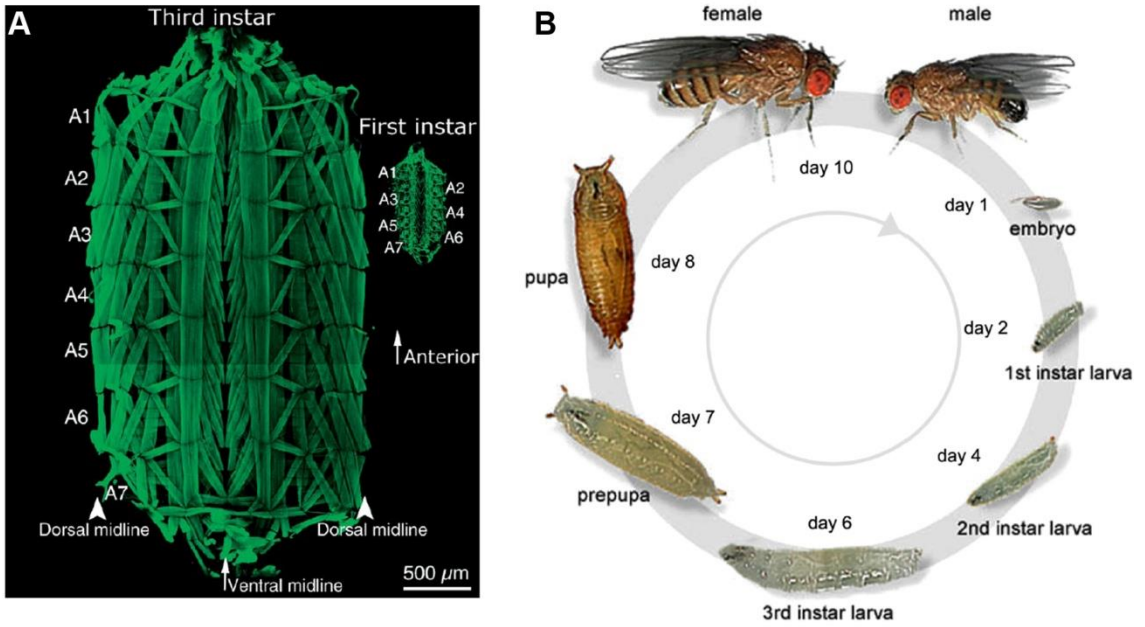


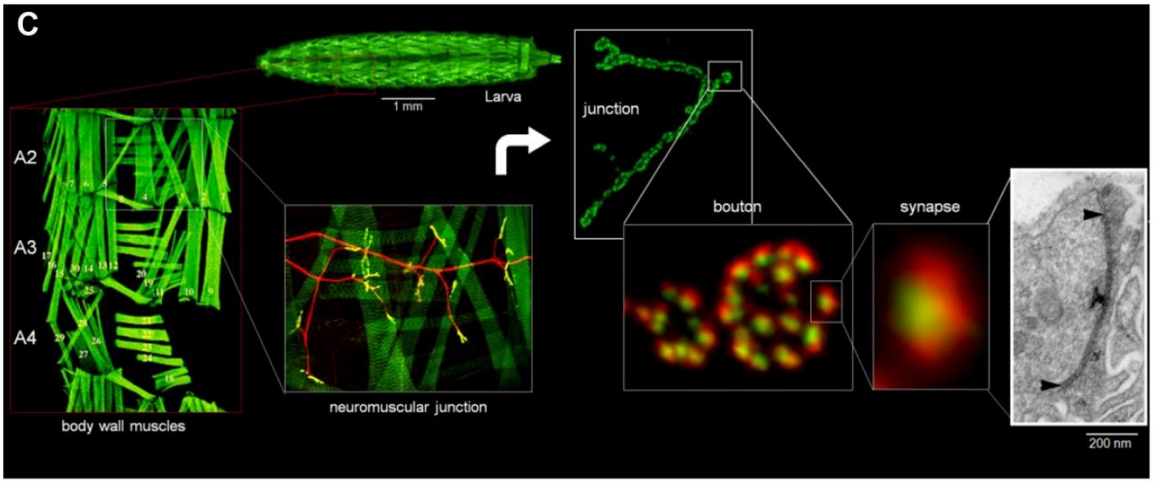


Figure 9 **The Neuromuscular Junction of *Drosophila melanogaster* as a Model Synapse.**
(A)The life cycle of the fruit fly *Drosophila melanogaster* takes 10 days at 25°C and can be subdivided into distinct developmental stages including the embryonic stage, three larval stages, followed by the prepupa stage which leads over to the pupal stage until the adult fly hatches. For all methods used in this paper, the larval neuromuscular junction (NMJ) as a model synapse was analyzed in 3rd instar larvae. Modified version from http://flymove.uni-muenster.de, taken from the PhD thesis of Matthias Siebert. (B) Third instar wandering stage (left) and young first instar (right) larval body wall muscle preparations labeled using FITC-conjugated phalloidin. A1–A7 denote abdominal segments 1 to 7. Up is anterior. In these preparations, the lateral muscles correspond to the dorsal musculature (arrowheads = dorsal midline), whereas the ventral muscles run along the midline separating the left and right hemisegments (arrow at the bottom of the preparation = ventral midline). Taken from "The fly neuromuscular junction", Gorczyca & Budnik, 2006. (C) Schematic representation of the *Drosophila* NMJ from the larva to the synapse, depicting the main structural features of this model system. The larval body wall muscles are labeled using FITC-conjugated phalloidin, the motoneuron (red, left middle panel) projects on to the larval body wall muscles where it forms the NMJ (in green upper right panel, stained with the presynaptic AZ marker BRP). The terminal globular axon

swellings are called boutons, and harbor several synapses consisting of a presynaptic AZ, which are the sites of transmitter release (green, middle right panel) and postsynaptic receptor field (red, middle right panel). In the electron micrograph of a synapse at the NMJ (right panel) the AZ length is marked by arrow heads, please note the parallel pre- and postsynaptic membrane separated by a strongly contrasted synaptic cleft. The dense projection called T-Bar can be easily identified at the AZ plasma membrane. The bouton is filled with synaptic vesicles. (Adapted from Gorczyca, Budnik, 2006 and Aberle et al., 2002). Designed by and taken from W. Fouquet's PhD thesis, 2008.

complete picture of a mutant phenotype (Bradley, Harris, & Jenner, 2006). A typical NMJ contains several hundred AZs (Atwood et al., 1993); at the NMJ of muscle 6/7 two axons innervate the muscle forming two classes of terminals. Their subtypes of boutons can be distinguished by their size and are grouped in Ib (b for “big”) and Is (s for “small”) boutons (Lnenicka & Keshishian, 2000). Besides the larval NMJ, neurotransmission is furthermore studied in the central nervous system of especially the olfactory and visual system, mainly in adult animals. Here, the circuitry of central neurons and the influence of mutations in specific neuronal cell types and synapses (e.g. in the Calyx of the mushroom body, involved in learning and memory) is investigated and their influence on learning and memory can be analyzed.

## 3.2. Larval Dissection for Electrophysiological Recordings, Immunohistochemistry and $Ca^{2+}$ Imaging

For immunohistochemistry, a rubber dissection pad was used, on which third-instar larvae were immobilized with fine insect pins (0.1x10 mm, Thorns, Göttingen, Germany). The larvae were covered with ice cold *Drosophila* hemolymph-like saline (HL-3) without Ca2+ (Stewart et al., 1994; 70 mM NaCl, 5 mM KCl, 20 mM MgCl2, 10 mM NaHCO3, 5 mM trehalose, 115 mM sucrose, 5 mM HEPES, pH adjusted to 7.2). In larval dissection for electrophysiological recordings or Ca-imaging at the NMJ, a piece of Sylgard (Sylgard 184 Silicone Elastomer, Dow Corning, Midland, Michigan, USA) was used instead of the rubber pad and HL-3 saline was freshly prepared at least every five days. The larvae were opened dorsally along the midline with dissection spring scissors, the epidermis was pinned down and the inner organs were removed with fine forceps (FST, Vancouver, Canada). For *in vivo* recording ($Ca^{2+}$ imaging and electrophysiological recordings) the CNS was especially carefully removed by cutting the nerves directly below the ventral ganglion to leave them intact before the fillet was directed to the respective recording. For immunohistochemistry, the larval fillets were fixed with 4% paraformaldehyde in phosphate-buffered saline (PBS) for 10 min and washed briefly with PBS containing 0.05% Triton X-100 (PBT). After blocking in 0.05% PBT supplemented with 5% normal goat serum (NGS, Sigma-Aldrich) for 30-45 min at room temperature, dissected larvae were incubated overnight at 4° C with the primary antibody in fresh blocking solution. Samples were then rinsed quickly for two

times with 0.05% PBT followed by three washing steps each lasting 20 minutes. Subsequently, the fillets were incubated with the fluorescent- conjugated secondary antibody in blocking solution for 3 h (room temperature). After rinsing twice and three washing steps, the larvae were mounted in Vectashield (Vector Laboratories, USA) on a glass slide.

## 3.3. Screening Tools

In an RNAi-based loss of function screen, novel candidates of the AZ were screened for a potential function in synaptic transmission. The following techniques were applied in this context: immunofluorescence staining at the larval NMJ (please find the staining procedure including all used antibodies in 3.4.2), wide field light microscopy, observation of adult fly mobility, and electroretinography.

### 3.3.1. Wide-field Microscopy Image Acquisition

Images were digitally captured using a high-resolution AxioVisionRed 4.6 CCD (Charge coupled device) camera mounted on a Zeiss Axiovert microscope equipped with a EC Plan-NEO FLUOR 40x 1.3 N.A. oil immersion objective. Images were acquired and analyzed using AxioVision software 4.6 (Release 4.8 June2009, Zeiss).

### 3.3.2. Confocal Laser Scanning Microscopy

A Leica TCS SP5 upright setup (Leica 63x 1.4 N.A. oil immersion objective) was used. Images of fixed samples were acquired at room temperature. In z-stacks of the NMJ the step size between single optical slices was 0.3 µm. Images were acquired from larval NMJs of muscles 6 and 7 or 4 using the Leica LCS AF software.

### 3.3.3. Electroretinography (ERG)

Recordings were performed following an established protocol (Wagh et al., 2006). In brief, anesthetized female flies were glued to a glass slide and their legs and wings were cut to reduce the noise level of the recording. Two electrodes filled with 3 M NaCl were used, one reference electrode and one recording electrode. The reference electrode was inserted into the fly's dorsal thorax; the recording electrode was placed on the eye of the fly. In a darkened room 10 light pulses/fly at 0.25 Hz were measured using Axoscope software 10.3 (Molecular Devices). 5-6 flies per genotype were recorded and data was analyzed with Clampfit 10.3 software (Molecular Devices).

## 3.4.Antibodies and Light Microscopy

### 3.4.1. In the Spinophilin Project

Partially taken from Muhammad et al., 2015:

For the investigation of Spn, Nc82 (1:100) and GluRIID (1:500) were used. Secondary antibodies were generally diluted 1:500. The sizes and surface densities of AZ cluster (visualized using $BRP^{Nc82}$) were quantified from maximal projections of confocal NMJ stacks. A Cy5-HRP antibody (23-175-021, Jackson ImmunoResearch, 1:250) was used to outline the shape of the NMJ. Control and mutant larvae were stained in the same vial. All images for synapse quantification from fixed samples were acquired using the same microscope settings (with 63x magnification and numerical aperture 1.4 oil immersion objective, Leica). AZ cluster analysis was done as described previously (Andlauer & Sigrist, 2012). AZ densitiy values were obtained by normalizing the total number of particles analyzed to the total synaptic area (pixel units) measured via HRP. Similarly, the absolute intensities of synaptic proteins per NMJ were normalized to the absolute intensity of synaptic HRP of the corresponding NMJ.

### 3.4.2. In the Unc13 Project

For the Unc13 project, the isoform-specific antibodies were generated as follows (from Böhme*, Hollmann*, et al., under revision; generated by Husam Babikir):

<u>Unc13A specific Antibody:</u>

The polyclonal antibody was raised in Guinea pig. The immunization of the animals was performed using a GST tagged fusion protein. The coding sequence corresponding to 384-494aa of Unc13A:

SVTSFPSSAVTAITKTRKLPKVLPTPLCKSSRHPITIAT-
DALSSSYTSDPLPEKSHRPAAKQLPKLPISLPQSNDRASLNSNWATPPAPDALPFNSFDHKSASSPTPTTTITK

The PCR was performed using the following primers:

Unc13A N-term FW 5'-CAAATTCACTCACAATTTCCC-3'

Unc13A N-term REV 5'-TACTCATCATTTTTTATTTTTTTT-3'

The PCR product was ligated to pGEX-6p1 (GST tag vector). The expression and purification of the target protein were conducted as mentioned above. After injection into guinea pig animals, several attempts to produce a 6×His tagged fusion protein of the same protein construct were not successful. Therefore, the GST tag of the GST tagged fusion protein was cleaved and the pure protein was used for the affinity purification of the AB containing serum which obtained from Selbaq.

Unc13B specific Antibody:

A rabbit polyclonal antibody was raised against the N-terminus of Unc13B with the following peptide sequence (941-1602 AA):

SNFHSFPLSHEQAQTTNQTEFVILEENLNYIYELSKNL-
PICSAYENKSIFDMKYEICDSNEIGKFSTVDEMLEWDQLNEPDKQNFSGKRLNSNLMP-
DLLTAQIPNSISKHNKNTSVNIEYVRQKENKGMDRRSIIEPNIYNGKSEDQICRPCLT-
DKLVFYPSSNSITDHNSSHDFNCLSQQDQTRIIKEFGSAHLNQDPT-
NYLDYTSGTYSKAPPEVLTHETNSSHLEFNHESESLFNSPNTSSYCKQKFVPGTSPAKPSKVWKRLNTILAD-
SYCKQKFVPGTSPAKPSKVWKRLNTILAD-
NLKLKRVSKFNRSLSLPGDVQSQGLQRQPRGQAGSCPFIHKRSNLAGSPVQLSKRIQKL-
PIRFIGRAKGVPFVRRSSSPDSAVSLDSAADKRFSSEKGLKKKTISSKMS-
GLMQKAKTYKRHSFVLRRGCNMSDSELEMPDFVSSGND-
NSSISTREILLNQSIEVEDEQEDFNYKNRCDSKSVLGGSIEKLNGNLTNNLFPIVGDLK-
KIQSPLPLAVLTEIPSYKDEYSNKSDSIKNSPIEMPKILLETAC-
NQELNLAHSDDDVDKNILANSAKDYVNAPTFSILKTVEDASEPTMTPLHTTTTTNSSLNV-
TSALWVTQQCLDLPNYPGWGSREDDDNRSQHSARTLSSSRRQSTED-
SIDTDDEYFYYELRQLEEQEKQRAHNSAIPSCER

The coding sequence was cloned from Pacman clone CH321-74A09 (BACPAC Resource Center BPRC, CA, USA) into pENTR/D-Topo (Invitrogen, CA, USA). The following primers were used:

Unc13B FW 5'-CACCATGGCTTCGAACTTTCACAGTTTCCC-3´

Unc13B REV 5'-AGTACTAGTTTATCGTTCACAAGATGGAATTGC-3´

Through Gateway reaction, the construct was shuttled into the bacterial expression vectors pDEST17(N-terminal 6xHis--tag) and expressed as corresponding fusion proteins. Rabbit antisera, obtained from Selbaq, were affinity purified with the same fusion protein.

## 3.5. Immunostaining

From Böhme* Hollmann* et al., under revision:

For the analysis of Unc13 and the loss-of-function candidate screen, the following primary antibodies were used: guinea-pig Unc13A (1:500; this study); rabbit Unc13B (1:1000; this study); rabbit $RBP^{C\text{-}term}$ (1:500; (Liu et al., 2011)) guinea-pig $RBP^{SH3\text{-}II+III}$ (1:500; this study); mouse GFP (3E6; 1:500, Life Technologies), rabbit GFP (1:500, Life Technologies), mouse GluRIIA (1:500, Developmental Studies Hybridoma Bank, University of Iowa, Iowa City, IA, USA), rabbit GluRIID (1:500, (Qin et al., 2005)), mouse Nc82 = anti-$BRP^{C\text{-}term}$ (1:100, Developmental Studies Hybridoma

Bank, University of Iowa, Iowa City, IA, USA); rabbit $BRP^{Last200}$ (1:1000; (Ullrich et al., 2015)). Except for staining against $Cac^{GFP}$, GluRIIA and Unc13A, where larvae were fixed for 5 min with ice-cold methanol, all fixations were performed for 10 min with 4 % paraformaldehyde (PFA) in 0.1 mM phosphate buffered saline (PBS). Secondary antibodies for standard immunostainings were used in the following concentrations: goat anti-HRP-Cy5 (1:250, Jackson ImmunoResearch, PA, USA); goat anti-rabbit-Cy3 (1:500, Jackson ImmunoResearch, PA, USA); goat anti-mouse-Cy3 (1:500, Jackson ImmunoResearch); goat anti-mouse Alexa-Fluor-488 (1:500, Life Technologies, CA, USA). Larvae were mounted in vectashield (Vector labs, CA, USA). Secondary antibodies for STED were used in the following concentrations: goat anti-mouse Atto590 (1:100); goat anti-rabbit Atto590 (1:100); goat anti-guinea pig star635 (1:100); goat anti-rabbit star635 (1:100); Atto590 (ATTO-TEC) and star635 (Abberior) coupled to respective IgGs (Dianova). For STED imaging, larvae were mounted in Mowiol (Max-Planck Institut for Biophysical Chemistry, Group of Stefan Hell).

## 3.6. Confocal Microscopy: Image Acquisition, Processing and Analysis

From Böhme* Hollmann* et al., under revision:

Confocal microscopy was performed with a Leica SP8 microscope (Leica Microsystems, Germany). STED microscopy was performed with a custom-built STED-microscope (see below). Images of fixed and live samples were acquired at room temperature. Confocal imaging of NMJs was done using a z step of 0.25 µm. The following objective was used: 63×1.4 NA oil immersion for NMJ confocal imaging. All confocal images were acquired using the LCS AF software (Leica Microsystems, Germany). Images from fixed samples were taken from 3rd instar larval NMJs (segments A2-A4). Images for figures were processed with ImageJ software to enhance brightness using the brightness/contrast function. Where necessary, images were smoothened (0.5 pixel Sigma radius) using the Gaussian blur function. Confocal stacks were processed with ImageJ software (http://rsbweb.nih.gov/ij/). Quantifications of AZ spot number, density and size (scored via BRP) were performed following an adjusted manual (Andlauer & Sigrist, 2012), briefly as follows. The signal of a HRP-Cy5 antibody was used as template for a mask, restricting the quantified area to the shape of the NMJ. The original confocal stacks were converted to maximal projections and after background subtraction; a mask of the synaptic area was created by applying a certain threshold to remove the irrelevant lower intensity pixels. The segmentation of single spots was done semi-automatically via the command “Find Maxima” embedded in the ImageJ software and by hand with the pencil tool and a line thickness of 1 pixel. To remove high fre-

quency noise, a Gaussian blur filter (0.5 pixel Sigma radius) was applied. The processed picture was then transformed into a binary mask using the same lower threshold value as in the first step. This binary mask was then projected onto the original unmodified image using the “min” operation from the ImageJ image calculator. The synapses in the resulting images were counted with the help of the “analyze particle” function with the threshold set to 1. The spot density was obtained by normalizing the total number of analyzed particles to the NMJ area measured via HRP. The mean intensity of synaptic proteins per NMJ was measured using the command “measure” giving the mean gray pixel value within the HRP mask. For colocalization analysis (Manders or Pearson correlation) the ImageJ plug-in “JACOP” (http://rsb.info.nih.gov/ij/plugins/track/jacop2.html) was used.

## 3.7. STED Microscopy

From Böhme*, Hollmann* et al., under revision:

STED images were recorded with a custom-built STED microscope as previously described in Muhammad et al., 2015. Here, two-color STED images were recorded on a custom-built STED-microscope (Göttfert et al., 2013), which combines two pairs of excitation laser beams of 595 nm and 640 nm wavelength with one STED fiber laser beam at 775 nm. All STED images were acquired using Imspector Software (Max Planck Innovation GmbH). STED images were processed using a linear deconvolution function integrated into Imspector Software (Max Planck Innovation GmbH). Regularization parameters ranged from 1e−09 to 1e−10. The point spread function (PSF) for deconvolution was generated by using a 2D Lorentz function with its half-width and half-length fitted to the half-width and half-length of each individual image. Images for figures were processed with ImageJ software to remove obvious background, enhance brightness/contrast and smoothened (1 pixel Sigma radius) using the Gauss blur function.

The measurements of BRP ring diameters were performed on deconvolved images. A line profile was laid across the middle of planar oriented BRP rings and the peak-to-peak distance measured. Subsequently the line was rotated 90 degrees, a second line profile was created and the peak-to-peak distance measured again. The average of both peak-to-peak distances gave the ring diameter.

## 3.8. Electrophysiology

Two electrode voltage clamp recordings at the larval NMJ were performed on male third instar larvae at muscle 6 of the abdominal segments 2 and 3 as previously described (Qin et al., 2005). Analyzed cells had initial membrane potentials between -45 and -70 mV and input cell resistances of ≥ 4 MΩ, using sharp intracellular electrodes filled with 3 M KCl with resistances between 8 and 20 MΩ. Excitatory evoked junctional currents (eEJCs) were evoked by placing the segmental nerve into a fire-polished suction electrode (10-15 µm inner diameter) and applying a brief (300µs) depolarizing voltage step between 3 and 8 V using a S48 Stimulator (Grass Technologies, Warwick, RI, USA). eEJCs were recorded at -60 mV. Miniature excitatory junctional currents (mEJCs) represent spontaneous fusion events and were recorded for 90 s at -80 mV. Signals were sampled with an Axoclamp 2B amplifier at either 5 kHz and low-pass filtered at 1 kHz or with a sampling rate of 10 kHz and filtered at 5 kHz. Holding currents never exceeded 10nA. 0.2 Hz stimulation protocols included 20 traces/cell, subsequent recordings of paired-pulse events, high frequency stimulation or recovery protocols followed after 30 s rest. Paired-pulse recordings consisted of 10 traces/interval/cell with a 4 s rest between the stimulations. The rise time and decay time constants (τ) were obtained from the averaged traces of one cell. The rise time was measured from 10 to 90 % of the maximum eEJC amplitude. The decay constant was calculated with a single exponential function, fit to the trace starting at 60% of the maximum amplitude back to baseline. The amplitude values of high frequency trains and recovery protocols were measured from the baseline before the onset of the train to the peak value of the EPSC. The recordings were analyzed with pClamp 10 (Molecular Devices, Sunnyvale, CA, USA). The exemplary traces in the figures are averaged traces unless otherwise noted, the stimulation artifact of eEJCs was removed for clarity.

### 3.8.1. Recording of Synaptic Recovery

The kinetic of recovery was recorded as described earlier (Hallermann et al., 2010). In brief, 100 stimuli were applied at 60 Hz followed by single stimulations at different time intervals after the train (in ms): 25, 50, 100, 200, 300, 500, 1000, 2000, 5000, 10000, 20000, 50000 and 100000. Only cells with reliable recruitment of both axons innervating muscle 6 and with recovery to at least 70% of their initial amplitude were included. The time constants of the fast and slow recovery component were obtained by fitting a single exponential curve to the average recovery kinetic of each genotype.

### 3.8.2. $Ca^{2+}$- Buffering with EGTA-AM and Bapta-AM (TEVC)

Partially from Böhme*, Hollmann* et al., under revision:

In an incubation experiment, EGTA-AM (Calbiochem, 50mM stock solution in DMSO) was dissolved in $Ca^{2+}$-free HL3 to a final concentration of 0.1 mM. The same volume of Pluronic F-127 (Molecular Probes, 20% (w/v) in DMSO) was added. As control, an equal amount of DMSO (0.2%) and Pluronic F-127 was dissolved in $Ca^{2+}$-free HL3. The dissected larva was incubated exactly 30 minutes at room temperature, then it was rinsed three times with HL3 containing 2.5mM $Ca^{2+}$ to remove residual EGTA-AM from the fillet before the recording was started. In two-electrode voltage clamp at -60 mV 100 APs of a 60Hz train were measured in HL3 with 2.5 mM $Ca^{2+}$, data was analyzed using pClamp 10 (Molecular Devices, Sunnyvale, CA, USA) and a custom-written MatLab (MathWorks, R2010b) script. Changes in the first amplitude of the train upon EGTA-AM incubation were compared to reveal potential genotype-specific changes in EGTA sensitivity.

In an EGTA-AM wash-in experiment, five initial amplitudes were recorded at 0.1 Hz before 0.2 mM EGTA-AM and Pluronic F-127 was added to the bath containing 2.5 mM $Ca^{2+}$. The cell was clamped at -60mV, recording lasted for 3000s, nerve stimulation continued with 0.1 Hz. The baseline amplitude was obtained by averaging the initial five amplitudes. The decay of the amplitudes upon addition of EGTA-AM was fitted in the range between wash-in and 1000 s with a single exponential fit in Igor Pro with the following formula:

$$f(x) = y_0 + (1 - y_0) * e^{-\frac{x - x_0}{\tau}}$$

where x is time, f(x) are normalized amplitudes, start at 1 and decay with a delay in time until the EGTA-AM has been washed in (which is taken into account with x0) with the constant τ down to plateau y0. τ is the reciprocal of the rate constant and its unit is equal to the X-axis units (= s).

All experiments were performed on male 3rd instar larval NMJs from animals raised on special food (Bloomington recipe) at 25°C. The eEJCs were sampled at 10 kHz and low-pass filtered at 5 kHz. The exemplary traces are averaged traces unless otherwise noted, the stimulation artifact of eEJCs was removed for clarity. The data are reported as mean ± SEM, n indicates the number of analyzed cells, P represents the significance according to the students t-Test unless otherwise noted.

With Bapta-AM (abcam Biochemicals, 100mM stock solution in DMSO) only incubation experiments with a final concentration of 0.1 mM and Pluronic F-127 were recorded. Recordings were performed in HL3 with 2.5mM $Ca^{2+}$, the procedure was exactly the same like with EGTA-AM (see above).

### 3.8.3. $Ca^{2+}$ Titration Experiment

From Böhme*, Hollmann*, et al., under revision:

$Ca^{2+}$ titration experiments were performed from an initial $Ca^{2+}$ concentration of 0.75 mM. The concentration was subsequently increased to 1.5, 3.0, 6.0, and 10 mM. At each $Ca^{2+}$concentration, a single eEJC was recorded, followed by 10 seconds rest. Following the 10 seconds rest, one paired pulse trace was recorded (10 ms ISI). The bath solution was then exchanged five times via pipetting and the process was repeated at the next $Ca^{2+}$concentration. Calcium-dependence of release data in individual cells were fit with a standard site-specific Hill equation ( $I = I_{max} * \frac{[Ca^{2+}]_{ex}{}^{h}}{K_D + [Ca^{2+}]_{ex}{}^{h}}$ )

where $[Ca^{2+}]_{ex}$ is the concentration of extracellular $Ca^{2+}$, I is the current, $I_{max}$ is the asymptotic current, h is the hill slope, and $K_D$ is the extracellular $Ca^{2+}$ concentration at which $I=0.5*I_{max}$. Amplitudes (I) were divided by $I_{max}$ in each cell, then averaged. Quantifications represent mean $K_D$ and h (slope) values of each individual cell fit with a site-specific Hill equation. Cells were excluded if the Hill equation could not be properly fit to the data (affected only 2 cells in *unc13A*$^{Null}$). The data are reported as mean ± s.e.m., n indicates the number of cells examined.

## 3.9. Electron Microscopy

### 3.9.1. Conventional Embedding at Room Temperature

3$^{rd}$ instar larvae (2-3 for one block) were dissected as described earlier, fixed with 4% Paraformaldehyde (PFA) and 0.5% Glutaraldehyde (GA) for 10 min. The fillets were kept on ice in 2% GA in 0.1 M sodium cacodylate buffer (NaCac) until the dissection was finished and subsequently fixed for additional 1h at RT. Three washing steps in NaCac buffer each lasting 5 min followed. With the last washing step the filets were transferred to snap-on lid vials. For 1 h the samples were post-fixed with 1% $OsO_4$ in 0,8% KFeCn on ice for 1h in the dark. After 1 h of washing with NaCac buffer on ice in the dark, three brief washings with Millipore water followed. The samples incubated for 1 h in 1% UrAc on ice in the dark, then the resin infiltration was accomplished beginning with a dehydrating Ethanol concentration gradient leading over to increasing EPON concentrations.

| | |
|---|---|
| 30% EtOH | 2 min |
| 50% EtOH | 2 min |
| 70% EtOH | 5 min |
| 95% EtOH | 2x 10 min |
| 100% EtOH | 3x 15 min |

| | | |
|---|---|---|
| Dehydration: | 100% EtOH/EPON 1:1 | 30 min |
| | 100% EtOH/EPON 1:1 | 90 min |
| | Pure Epon | overnight |

Infiltration:
Always prepared freshly

100% resin was changed once, embedding: muscle 6 and 7 of segment 2-5 were cut out with cannulae, a stack was built on an EPON dummy for high throughput. The blocks hardened over night at 60°C.

### 3.9.2. High Pressure Freeze / Freeze Substitution Embedding, with Optional Light Stimulation

Adapted from Böhme*, Hollmann*, et al., under revision:

HPF embedding was performed as described previously (Matkovic et al., 2013). In brief, about three to five *Drosophila* late second/early third instar larvae were placed in aluminum specimen carrier of 200-µm depth (type A; Leica, Germany), filled with yeast paste, and covered with a lid (specimen carrier typeB, Leica, Germany). Samples were frozen immediately in an HPF machine (HPM100; Leica, Germany). In flash-freeze experiments with a light stimulation before freezing, transparent half cylinders and a transparent Sapphiredisc (Leica, Germany) was used with a 200 µm spacer ring instead of the metal carrier type A. The HPM100 was operated externally by a custom-written program by Shigeki Watanabe (Watanabe, Liu, et al., 2013; Watanabe, Rost, et al., 2013), the start of the light stimulation at 480 nm from an LED (Schott LLS light source A20960.4 blue, Germany) and subsequent freezing with a chosen delay was started after a dark adaption period in the freezing chamber of at least 30s. Cryosubstitution was performed in an AFS (Leica, Germany) in anhydrous acetone with 1% EMD Millipore water, 1% glutaraldehyde, and 1% osmiumtetroxide. From -90°C for 10 h the temperature was slowly (5°C/h) increased to -20°C , the samples incubated for additional 12 h before being warmed (10°C/h) to 20°C (Fig. 10). The samples were washed with anhydrous acetone and incubated with 0.1% uranylacetate dissolved in anhydrous acetone for 1 h at RT. After washing, the samples were infiltrated with the plastic resin Epon in increasing concentrations. The first incubation step in 30% Epon/70% anhy-

drous acetone for 4 h was followed by 70% Epon/30% anhydrous acetone overnight. The samples were incubated twice in 100% Epon for 2 h, respectively, before being embedded.

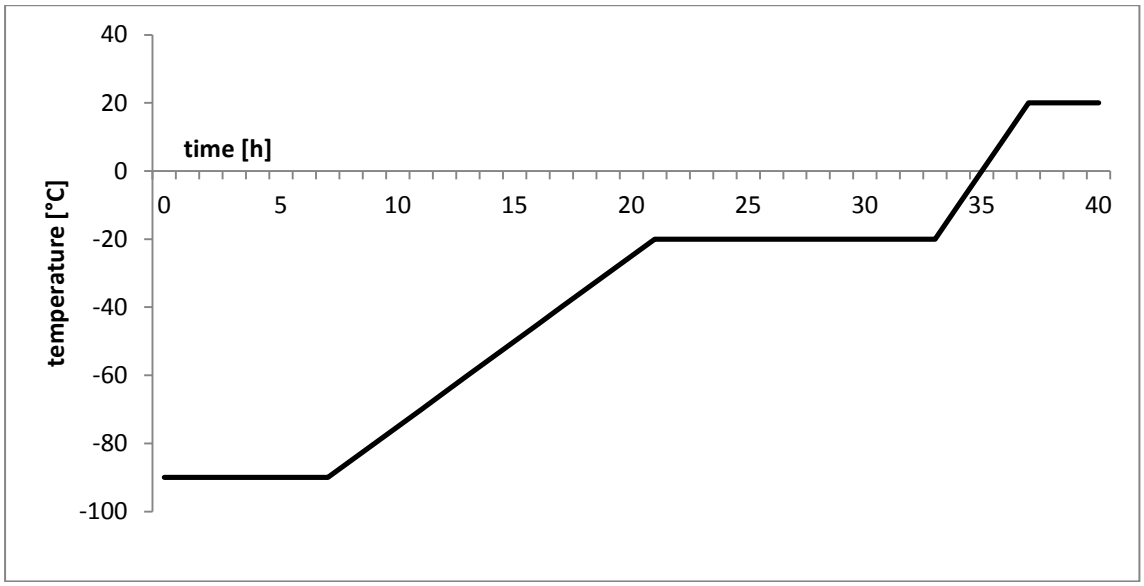


Figure 10 **Time Course of the Cryosubstitution Program Run in the AFS for HPF Embedding.**
The temperature was kept at -90°C for 10 h, followed by an increase with 5°C/h to -20°C, were the samples incubated for additional 12 h. In a final steep increase of the temperature (5°C/h), the samples are finally warmed to room temperature and processed further (for details please see text).

The Epon hardened at 60°C for at least 24 h. 60–65-nm sections were cut using an ultramicrotome (RMC Power Tome XL; Boeckeler or Reichert Ultracut S). Sections were collected on Formvar-coated 100 mesh grids. Sections were post-stained with 2% uranylacetate for 30 min and lead citrate for 3 min. Micrographs were acquired on an electron microscope (Tecnai Spirit; FEI or Zeiss 900A ).

### 3.9.3. Data Analysis

The analysis of the EM micrographs was done with ImageJ (http://imagej.nih.gov/ij). The micrographs were rotated (linear extrapolation) until the AZ membrane was horizontal. Synaptic vesicles in 300 nm radius from the T-Bar center, plasma membrane and the electron-dense T-bar were detected by eye and labeled manually. The nearest distance of the outer leaflet of SVs to the inner (cytosolic) leaflet of the plasma membrane was measured, as well as the SV outer leaflet distance to the inner leaflet of the plasma membrane at the T-bar pedestal center. Only SVs with direct contact to the plasma membrane were categorized as "docked". SV with contact to the T-bar were classified to be "tethered". The SV distances to the T-bar pedestal center were binned in 30 nm bins and the number of SV in a respective bin was counted and plotted. The same was done with 10 nm bins for the SV distance from the plasma membrane.

## 3.10. Calcium Imaging *in vivo*

Spontaneous and evoked transmitter release was analyzed in an optical assay utilizing the post-synaptically expressed $Ca^{2+}$ sensor GCaMP5G. With subsequent staining of the AZ marker BRP local activity could be assigned to single AZs after the alignment of the images. The following detailed descriptions of the procedure containing the sections 'GCaMP5 imaging' and 'data acquisition and analysis' is a direct excerpt from the publication by Muhammad et al., 2015:

### 3.10.1. GCaMP5 Imaging

Third instar larvae of both sexes expressing UAS-myrGCaMP5 (Melom et al., 2013) in the muscle were dissected in $Ca^{2+}$ free, ice-cold HL3. The motoneuron nerves were cut below the ventral nerve cord and the CNS was removed. The preparation was allowed to rest for 5-10 min in HL3 containing 1.5 mM $CaCl_2$ at RT. During this time, the motor nerve of the respective segment was sucked into a stimulation pipette filled with HL3 for later NMJ stimulation. Image sequences (spontaneous and evoked release) were acquired at 20 Hz with an Olympus BX51WI epifluorescence microscope with a 40x (NA 0.8) water immersion objective (Olympus, Tokio, Japan), equipped with a Lambda DG-4 light source (Sutter Instruments, Novato, CA, USA) and a Hamamatsu OrcaFlash 4.0 V2 camera (Hamamatsu Photonics K.K., Hamamatsu, Japan) (exposure time 0.05 s). The camera was operated in stream mode using HoKaWo software (vers. 2.9, Hamamatsu Germany). First, spontaneous activity in muscle 4 in segments A2 or A3 was recorded for 100 s. Then evoked release was stimulated 35 times by depolarizing the afferent motor nerve using voltage steps to 10 V. Each step lasted 300 µs and was applied at a frequency of 0.2 Hz with an S48 Stimulator (Grass Technologies, Warwick, RI, USA). The stimulator and camera were triggered using a Digidata 1440A (Axon CNS, Molecular Devices, Sunnyvale, CA, USA), running Clampex software (vers. 10.4, Molecular Devices, UK). The larval fillet was fixed immediately in PBS containing 4 % PFA immediately after the final stimulation was applied. Fillets were then stained for BRP (see above).

### 3.10.2. Data Acquisition and Analysis

Image sequences were processed using ImageJ (versions 1.48t and 1.48q). Slight drift between images was corrected with the "TurboReg" plug-in (http://bigwww.epfl.ch/thevenaz/turboreg/), which uses the "Rigid Body" transformation (Thévenaz et al., 1998) to register all images to the

first frame of the spontaneous recording. Additionally, maximal z-projections of post-hoc confocal images of the GCaMP5 fluorescence were aligned to this target frame using the “affine” transformation. The same transformation was also applied to the other channel with the BRP staining (Fig. 11). Single AZs were automatically identified through their intensity maxima and equally sized regions of interest (ROIs, 0.65 µm diameter) were placed around each maximum (Fig. 11A''', B'''). Integrated fluorescence intensity values from each ROI were read out from each frame to capture the temporal change in GCaMP5 fluorescence at a particular AZ. Each ROI was then moved to a region outside of the GCaMP5 signal to obtain a background intensity value, which was subtracted from the signal. Data were transferred to Matlab (Mathworks, vers. R2011a) for further analysis. Spikes were detected by analyzing the background corrected GCaMP5 intensity profiles using a custom-written script. Traces were filtered using a running average filter implemented in the Matlab function “filter” with a box size of four frames. Spikes were identified by detecting signals that exceeded the standard deviation of the signal by a factor of 4 for at least three consecutive frames. The following criteria were applied to prevent the same signal being counted several times at adjacent AZs: only the largest signal in recordings of spontaneous activity was considered if several AZs had simultaneous fluorescence peaks. Signals were only considered for the analysis of evoked episodes if they were temporally locked to the stimulation, with peak values occurring within 1 s after the stimulus. Spikes that coincided at different AZs were only considered if they were at least 2.5 µm apart, otherwise only the largest signal was considered. All signals matching these criteria were evaluated by visual inspection, and peaks that showed atypical rise and decay kinetics were rejected. A section of the local GCaMP5 fluorescence signal (2 s prior and 2 s after the maximal spike value) was selected to obtain the average GCaMP5 response and the baseline corrected by subtracting a line that was fitted to the fluorescence signal during the first and last second of this 4 s window. Traces were then averaged over all events from all AZs in one animal and, finally, averaged over all animals. The total number of spontaneous events per NMJ was divided by the number of analyzed AZs and the acquisition time in order to calculate the frequency of spontaneous events per AZ. The total number of AZs that showed activity at least once was divided by the total AZ number to obtain the fraction of active AZs. The release probability per AZ was calculated by dividing the total number of stimulus-locked, evoked events per NMJ by the number of AZs and stimuli. All values were then averaged over all animals. The BRP intensities per AZ were measured from confocal maximal projection images using the same ROIs that were used for reading out the GCaMP5 fluorescence (Fig. 11A''', B'''). The BRP intensities were then binned in ascending order in five bins containing the same number of AZs and the average BRP intensity as well as the av-

erage number of evoked events calculated per AZ. Binned data were then averaged over all animals of one group.

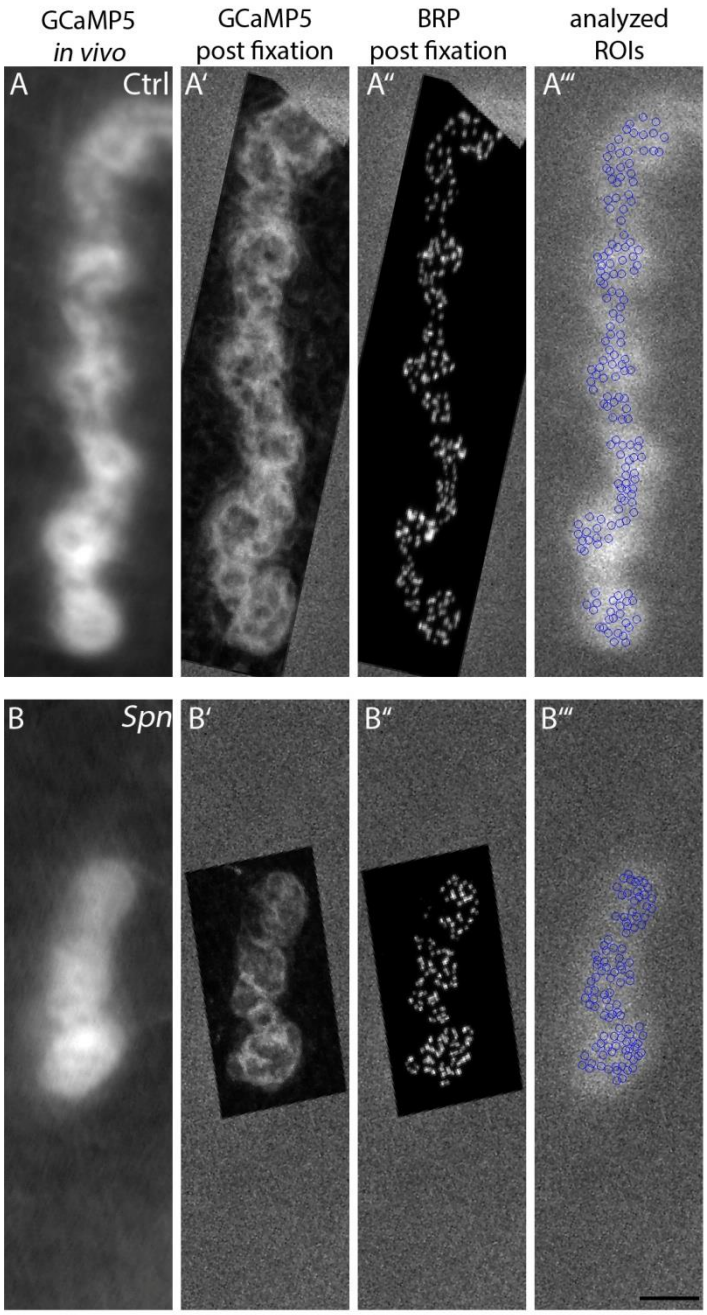


Figure 11 **Assignment of Single Active Zones Identified by post-hoc Staining Against Bruchpilot (BRP) to GCaMP5 Events at Control and Spn NMJs.**
related to Figure 31, Results part. (A, B) In vivo GCaMP5 signal, produced from live movies by an average projection of 2000 frames acquired during spontaneous activity. (A', B') GCaMP5 signal after fixation, shown is a Z-projection of confocal light microscopic scans. Individual areas of the confocal image were registered to the first frame of the *in vivo* GCaMP5 signal (see Methods). (A'', B'') The same registration transformation as for the confocal GCaMP5 images (A'', B'') was used to align individual active zones identified in confocal scans by staining against the presynaptic active zone marker BRP. (A''', B''') BRP staining was used to place uniformly sized regions of interest (ROIs) to read out GCaMP5 fluorescence over time. Images A', A'', A''' and B', B'', B''' are placed on top of the first frame acquired in the live $Ca^{2+}$- imaging experiment (exposure time 0.05s). Scale bar 5 µm.
This Figure is taken from Muhammad et al., 2015; data were obtained and analyzed by me and Dr. A. Walter.

Linear fits were performed in OriginPro 6G (vers. 8.0773) taking vertical and horizontal error bars into account. The function “Compare Datasets” was used to test whether the two datasets were significantly different from one another.

## 3.11. Genetics and Fly Lines

Fly-strains were reared under standard laboratory conditions (Sigrist et al., 2003) at 25°C on semi-defined medium (Bloomington recipe) unless noted differently. As background for generation of transgenes (Rainbow Genetics) w1118 strain was used. For genetic combinations standard (double) balancer stocks for the second and third chromosome were used, for fourth chromosome genetics the Balancer ci[D] and homozygous 3x P3 RFP was used.

For the biochemical screen and combinations with Unc13 alleles, the used GAL4-expressing stocks were previously described: elav$^{c155}$-GAL4 (Lin & Goodman, 1994), ok6-GAL4 (Aberle et al., 2002), mef2-GAL4, and GMR-GAL4. UAS-RNAi construct stocks were obtained from the VDRC (Dietzl et al., 2007), and transposon insertion and deficiency lines were requested from the Bloomington Stock center, Kyoto Stock collection and the Exelixis collection at Harvard University. Details concerning the Spinophilin mutations can be found in Karzan Muhammad's Ph.D. thesis (Muhammad, 2014) and the corresponding publication (Muhammad et al., 2015).

For the Unc13 project, the mutant alleles were generated as follows (from Böhme*, Hollmann*, et al., under revision):

### 3.11.1. Generation of *unc13A$^{Null}$* by Chemical Mutagenesis

The EMS screen was performed according to standard protocols. In brief, isogenic *w1118* males were mutagenized with 25 mM EMS solution and crossed to virgins carrying a fourth chromosomal balancer. For initial mapping, male F1 offspring were crossed with P84200 virgins, and candidate flies were tested for adult lethality. Genomic DNA was extracted from positive candidate flies, and PCR amplicons containing *unc13* exon clusters were double-strand sequenced to identify the mutations.

### 3.11.2. Generation of *unc13B$^{Null}$* and *ctrl*

*Unc13* genomic transgenes were generated by Red/ET Recombineering. For this purpose, the Unc13 P[acman] BAC CH321-60O10 clone containing the *Drosophila unc13* gene was obtained from the BACPAC Resources Center, CA, USA used as a template for all cloning strategies. Based on the P[acman] technology (Venken et al., 2006) and using Red/ET Recombineering in *E.coli* for modifying large DNA vector constructs (*GeneBridges Protocol*: Counter-Selection BAC Modification Kit, Version 3.2, January 2012), a genomic rescue construct encompassing the whole *Drosophila Unc13* locus including putative promotor regions was generated giving raise to '*ctrl*'. Based on this wild type construct, an Unc13 isoform B specific deletion construct (*unc13B$^{Null}$*) was generated by removing the first 1000 bp of the *unc13B* DNA sequence, causing a shift of the reading frame, which interrupts the translation of Unc13B by generating an early stop-codon.

The cloning strategy was performed according to the Counter-Selection BAC Modification Kit by Red®/ET® Recombination (Gene Bridges Protocol, No. K002, Version 3.2, January 2012). For the generation of transgenic flies both constructs were sent for DNA micro-injection in embryos to Rainbow Transgenic Flies, Inc, CA, USA(service type: B/D2, injected fly strain: Strain 24862; y[1] M{vas-int.Dm}vZH-2A w[*]; PBac{y[+]-attP-9A}VK00005) on LB agar.

For the Unc13 project, the following genotypes were used:
wild type: +/+ (*w1118*). *unc13A$^{Null}$: EMS7.5/P84200.*
*unc13B$^{Null}$: Del100BPacman/+;P84200/P84200.*
*ctrl: Unc13Pacman/+;P84200/P84200.*
Motoneuronally driven *UAS-Unc13A$^{C\text{-}term\text{-}GFP}$*: *Ok6-GAL4/+; UAS-Unc13A$^{C\text{-}term\text{-}GFP}$/+*.
Motoneuronally driven *UAS-Unc13B$^{C\text{-}term\text{-}GFP}$*: *Ok6-GAL4/+; UAS-Unc13B$^{C\text{-}term\text{-}GFP}$*/+.
Motoneuronal driven Cac$^{GFP}$: *Ok6*-GAL4*/UAS-Cac$^{GFP}$.*
Pan-neuronally driven cDNA to express *UAS-Unc13$^{full\ length}$* or *UAS-Unc13$^{\Delta N\text{-}term}$*, with and without GFP-tag: *elax-GAL4/+;; UAS-Unc13$^{FL}$/+; P84200/P84200* or
*elax-GAL4/+;; Unc13$^{\Delta N\text{-}term}$/+;P84200/P84200*, respectively.
Stocks were obtained from: *Ok6-Gal4* (Aberle et al., 2002); UAS-*brp-RNAi-B3,C8* (Wagh et al., 2006); *genomic CacGFP* (Matkovic et al., 2013); *UAS-Cac$^{GFP}$* (K. S. Y. Liu et al., 2011); *rab3$^{rup}$* (Graf et al., 2009); *P84200* was provided by the *Drosophila* Genetic Resource Center.

## 3.12. Statistics

Unless otherwise stated, the data was analyzed with Prism 5 Software (GraphPad, La Jolla, CA, USA). To compare two groups, either nonparametric Mann-Whitney U-tests or student's T-tests were used for all data sets. For comparison of more than two groups, nonparametric one-way analysis of variance (ANOVA) tests were used, followed by a Turkey's multiple comparison test. P values and n values are given in the figure legends or main text. Means are annotated ± SEM. Asterisks are used to denote significance: *, $P < 0.05$; **, $P < 0.01$; ***, $P < 0.001$; n.s. (not significant), $P > 0.05$).

# 4. Results

My investigations on SV release probability at the level of single AZs and its dependence on SV distribution included the establishment of flash-freeze experiments in *Drosophila* larvae, high-pressure freeze and conventional embeddings for electron microscopy and the obtainment of electron micrographs, electrophysiological recordings (electroretinography and two-electrode-voltage-clamp), generation of *Drosophila* transgenic organisms, immunofluorescence stainings and subsequent confocal laser scanning microscopy, and the establishment of *in vivo* $Ca^{2+}$ imaging at the larval NMJ.

The work was embedded in several collaborative projects. I included data from collaborators to provide a comprehensive and complete overview on the findings. In particularly, i) all STED microscopy was obtained by Mathias Böhme; ii) Karzan Muhammad started the work on Spinophilin and generated all mutant alleles of Spn; iii) the *in vivo* $Ca^{2+}$ imaging of Spn mutants was teamwork together with Alexander Walter.

In the Unc13 project I contributed the majority of the electrophysiological characterizations and the electron microscopic studies. The project was conducted together with Mathias Böhme (imaging), Suneel Reddy (generation of mutant alleles), Eric Reynolds (part of the electrophysiological recordings were obtained in teamwork), Christine Quentin, Tanja Matkovic and Dominique Dufour Bergeron (support in electron microscopy), Malou Mampell (generation of mutant alleles). Data from these collaborators are clearly labeled as such in the figure legends. My work on Spinophilin is part of a publication recently published in Nature Communications in Muhammad et al., 2015. A part of the Unc13 results are included in a manuscript currently under revision in Nature Neuroscience (Böhme*, Hollmann* ... et al., under revision), whose content in parts overlaps with my thesis.

## 4.1. Two Unc13 Isoforms Are Located at the Larval Neuromuscular Junction

A timed fusion of synaptic vesicles (SVs) in response to action potentials (APs) is required for sound synaptic communication. To couple SV release to electrical stimulation by APs, $Ca^{2+}$ ions entering the cell through voltage gated $Ca^{2+}$ channels activate the $Ca^{2+}$ sensor Synaptotagmin on the SV to trigger fusion (Rizo & Rosenmund, 2008). The efficacy of synaptic transmission largely depends on the distance between SVs and voltage gated Ca2+ channels. Close proximity is required for fast and immediate responses, which may require active localization of RRP SVs, a process referred to as positional priming (Eggermann et al., 2011; Lee et al., 2013; Wadel et al., 2007).

At AZs, an evolutionarily conserved set of large proteins is implicated in the spatial organization of synapse topology including RIM, (M)Unc13, Rim-binding protein (RBP), Liprin-α, and ELKS/Bruchpilot (BRP) proteins (Sudhof, 2012). Among these, ELKS/BRP-family proteins, RIMs and RBPs are required to ensure proper $Ca^{2+}$ channel-SV topology and their levels predict release at single AZs (Acuna et al., 2015; Kaeser et al., 2011; Kittel et al., 2006; Liu et al., 2011; Matz et al., 2010).

Here we show that a selective spatio-temporal organization of the two Unc13 isoforms existing in *Drosophila* establishes distinct sites of release. Unc13 is a well-described protein known to be involved in SV docking and priming (Augustin et al., 1999; Imig et al., 2014; Man et al., 2015; Varoqueaux et al., 2002). In *Drosophila*, the Unc13 locus has two different promoters which lead to the synthesis of two specific isoforms (Fig. 12A), Unc13A and Unc13B (Flybase (Attrill et al., 2015)). They share a common C-term containing the C1, $C_2B$ and $C_2C$ domain, and the Mun domain, which is relevant for the protein function in SV priming (please see introduction chapter 1.5 "(M)Unc13" for further information). However, due to the alternative promoter the N-terminal region differs between the two isoforms (Fig. 12A). To investigate a potential isoform-specific localization of the two isoforms at the synapse, N-term specific antibodies were raised to differentially label Unc13A and B (the respective epitope regions are marked in Fig. 12A). In confocal microscopy of immunohistochemically stained NMJs, a distinct, isoform-specific localization pattern was revealed (Fig. 12C, D), where Unc13A clearly co-localizes with the AZ marker BRP. In contrast, Unc13B localizes adjacent to or in between the BRP signals (Fig. 12D, arrows). Furthermore, isoform-specific mutant alleles were generated in order to investigate potential differences in localization and function between both isoforms. Two Unc13A deficient mutants evolved from a chemical mutagenesis screen (ethyl methanesulfonate; EMS), the sites of the resulting premature stop codons are labeled in Fig. 12A (EMS7.5, which from now on is called

*unc13A*$^{Null}$, and EMS7.96). However, no *unc13B* allele could be isolated this way, indicating that *unc13B* null mutant flies are vital. To generate an Unc13B-deficient mutant situation, the first 1000kb of the Unc13B specific exon were deleted. This transgene was re-inserted in the *unc13*$^{Null}$ mutant background; the deleted region is labeled in Fig. 12B and from now will be called *unc13B*$^{Null}$. As control for *unc13B*$^{Null}$, the whole Unc13 locus is re-expressed in the *unc13*$^{Null}$ mutant background and is from now on named *control (ctrl)* (Fig 12E, F). In immunohistochemical stainings the *control* showed an isoform-specific staining pattern of Unc13 comparable to wild type (Fig. 12E, F). In *unc13A*$^{Null}$ the signal of Unc13A is abolished and the single AZs labeled by BRP stainings appeared larger with their density over the NMJ terminal area being decreased (Fig. 12G). The Unc13B signal was unaffected by the loss of Unc13A (Fig. 12H). Vice versa, the loss Unc13B does not markedly alter the Unc13A signal (Fig. 12I, J). With these experiments, the specificity of the custom-made isoform-specific antibodies was confirmed. Two additional Unc13 transgenes were produced carrying a GFP-tag at the C-term of each respective isoform. When they were expressed specifically in motoneurons with the UAS-Gal4 system, both variants effectively reached the NMJ terminal and exhibited the already known isoform-specific localization pattern comparable to the distribution of endogenous Unc13 proteins (Fig. 12K, L). The arrows (Fig. 12L) point to Unc13B sites devoid of Brp label.

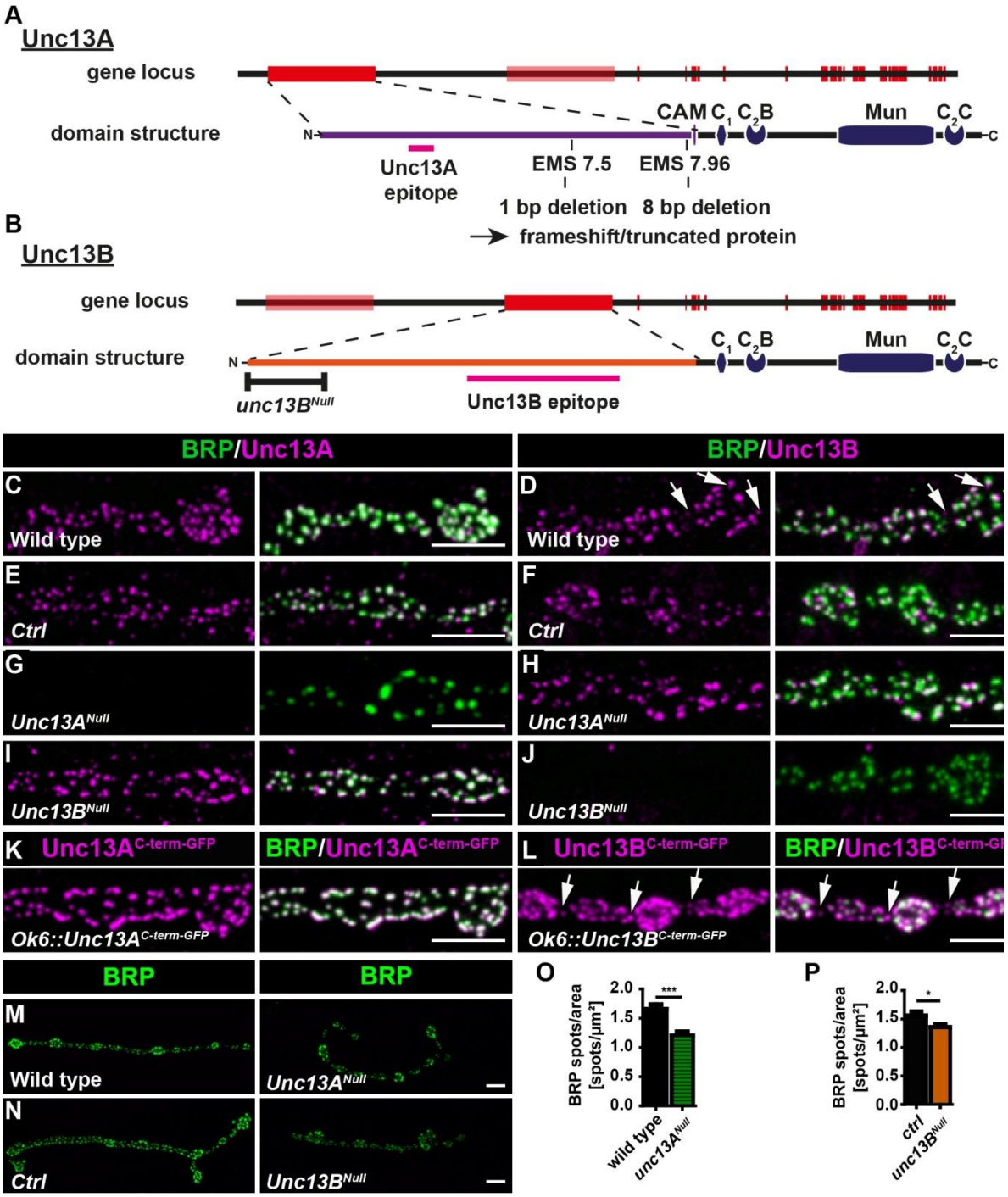


Figure 12 **Isoform-Specific Mutants of the Differentially Localizing Isoforms Unc13A and Unc13B at the Larval NMJ.** (A, B) Two Unc13 isoforms are expressed in the genome of *Drosophila melanogaster*, sharing a common C-term containing the C1, C2B, MUN and C2C domain; only the CAM domain (Calmodulin-binding site) is specific for Unc13A. The isoform-specific N-term has no predicted domains (purple in Unc13A, orange in Unc13B). The mutations which lead to the null-alleles of Unc13A and B which are analyzed in this work are labeled (in a: EMS7.5 is from now in called *unc13A*$^{Null}$, in b: the deleted promotor region of Unc13B leads to the *unc13B*$^{Null}$ situation). The epitope region of the isoform-specific Unc13 N-term antibodies are labeled in magenta. (C-N) Projected confocal stacks of NMJs (muscle 4) from segment A2-A4, labeled against BRP (BRPNc82, green) and Unc13A or Unc13B (magenta), respectively, in the indicated genotypes. (C) Immunostaining with an Unc13A specific antibody (magenta) revealed a strong colocalization with the AZ protein BRP (green) at wild type NMJs. (D) Immunostaining with an Unc13B specific antibody (magenta) labeled wild type NMJs but showed only partial overlap with BRP (green) and exhibited Unc13B positive signals devoid of BRP (arrows). (E,F) A genomic rescue construct containing the whole *Drosophila unc13* locus including putative promoter regions was generated that was expressed in the *unc13*$^{Null}$ background (*ctrl*). Unc13A and -B specific immunoreactivity was restored in *ctrl*. (G) Unc13A specific immunoreactivity was lost in *unc13A*$^{Null}$ and BRP spots appeared

overgrown. (H) Unc13B specific immunoreactivity was still present at *unc13A*$^{Null}$ NMJs. (I) Unc13A specific immunoreactivity was present in *unc13B*$^{Null}$. (J) Unc13B specific immunoreactivity was completely lost in *unc13B*$^{Null}$. (K,L) Unc13 transgenes with a GFP-tag at the C-term of each respective isoform reach reliably the nerve terminal and localize isoform-specifically. (M, N) Representative examples of whole NMJs at muscle 4 in Unc13 isoform-specific mutants. (O,P) The AZ density is significantly reduced in both mutants. (O) Quantification of BRP spots/µm²: wild type (19 NMJs): 1.658 ± 0.079; *unc13A*$^{Null}$ (23 NMJs): 1.207 ± 0.063. (P) Quantification of BRP spots/µm²: c*trl* (28 NMJs): 1.559 ± 0.070; *unc13B*$^{Null}$ (35 NMJs): 1.354 ± 0.055. Statistics: Mann-Whitney U test. Panels shows mean values and errors bars representing SEM. *, p ≤ 0.05; **, p ≤ 0.01; ***, p ≤ 0.001; ns, not significant, p > 0.05. Scale bar 5 µm.
This figure is designed by M. Böhme; data were obtained and analyzed by M. Böhme.

Both isoform-specific mutants reach larval stage, in contrast to *unc13*$^{Null}$ which is embryonically lethal (Aravamudan et al., 1999). Thus, both isoforms are obviously functionally relevant; their specific removal has consequences on the maturation of AZs at larval NMJs, as was found in the quantification of AZ densities in the respective mutant alleles (Fig. 12M-P). The AZ density was significantly reduced in both mutants, and the NMJ size was decreased (data not shown). However, only *unc13A*$^{Null}$ had an increased size of single AZs (Fig. 12G, M), while in *unc13B*$^{Null}$ individual AZs appeared normal (Fig. 12J, N).

### 4.1.1. Distinct Sub-Active Zone Localization of Unc13A and Unc13B

The voltage operated N/P/Q-type $Ca^{2+}$ channel α1 subunit Cacophony (Cac) is exclusively responsible for evoked release at NMJ AZs and clusters in the center of the BRP labeled AZ (Fouquet et al., 2009; Kawasaki et al., 2004; Liu et al., 2011). To analyze the endogenous sub-AZ distribution of both Unc13 isoforms in detail, we performed dual color super-resolution STED microscopy (with 35 nanometer lateral resolution for both channels). Both Unc13A and Unc13B formed discrete clusters only occupying a small part of the AZ area (about 300 nm diameter) and displayed a specific topography (Fig 13A-D). The immunofluorescence Unc13A signals were located adjacent to the RBP signals and the BRP signals which form a ring and were directed more towards the ring center (Fig. 13B, C, left panels). Unc13A tightly surrounded the $Ca^{2+}$-channels, which were labeled by GFP-tagged version of Cac (Fig 13D, left panel). In contrast, Unc13B signals were in a greater distance to the $Ca^{2+}$-channels as well as to the RBP signal (Fig. 13C, D, right panel) and were located at the outer edge of the BRP ring (Fig. 13B). To investigate whether the tight localization of BRP and Unc13A reflects a potential interdependence between the two proteins, RNAi-based knockdown of BRP (Wagh et al., 2006) in larval NMJs were analyzed. In fact, the loss of BRP apparently scaled with the loss of Unc13A (Fig. 13E). In the quantification, the reduction of Unc13A level (7.6 %) was almost as high as the reduction of BRP level (15.2 % left). In order to quantify the amount of co-localization, the Pearsson-coefficient was calculated, which is a measure of the linear correlation between two signals. It confirms a high amount of co-localization of the two proteins (Fig. 13F).

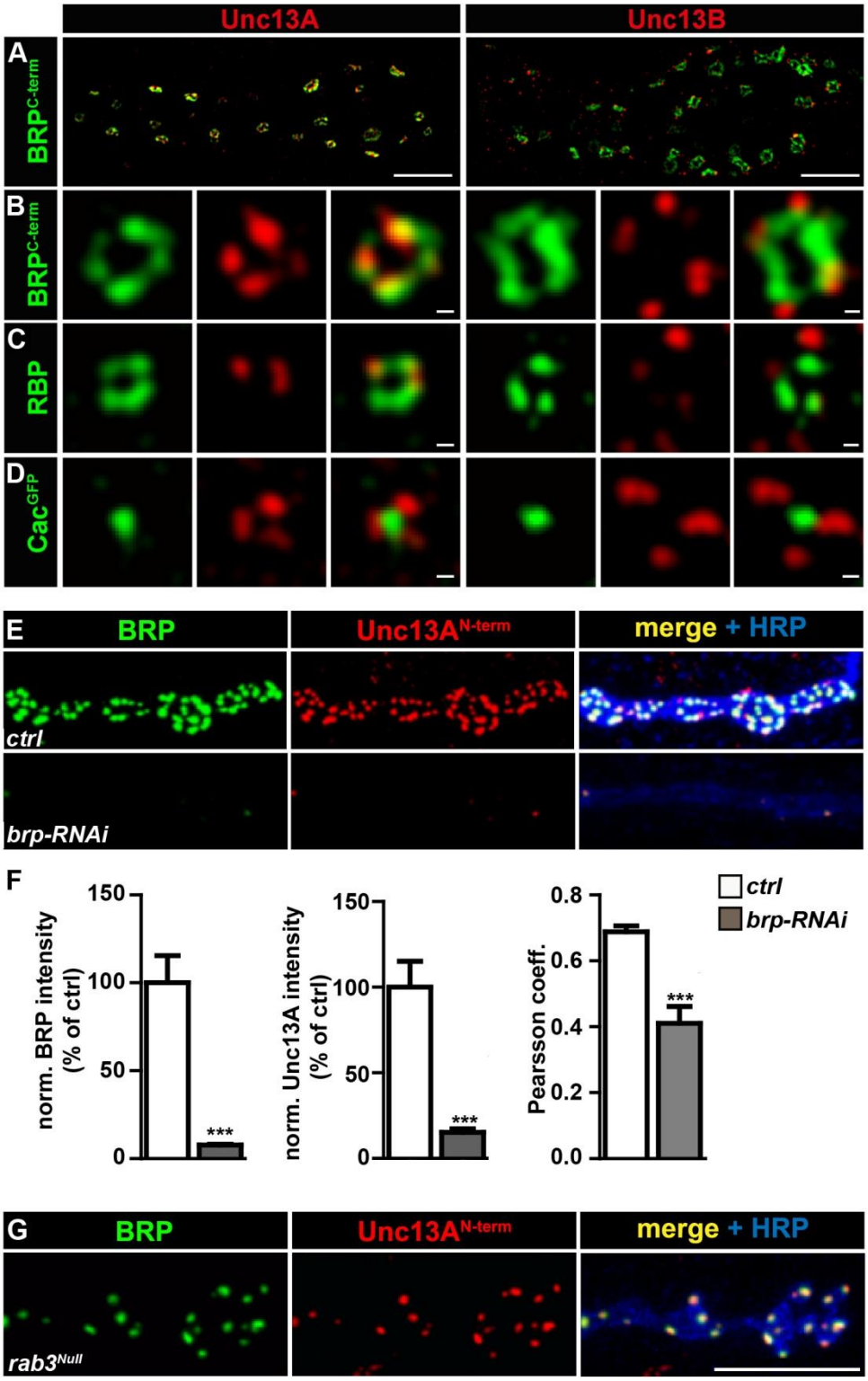


Figure 13 **In Super-Resolution Microscopy Using Two-Color STED Unc13A and Unc13B Exhibit a Distinct Sub-AZ Localization Pattern at the Larval NMJ.**
(A-D) Two-color STED images of synaptic boutons (A) or individual planar AZs (B-D) from 3rd instar larvae of the genotypes indicated stained with the indicated antibodies. (A) Unc13A (left panel) localized exclusively to the BRP positive signal, Unc13B (right panel) localized to the BRP positive signal but also showed immunoreactivity devoid of BRP. (B, C) Unc13A immunoreactivity localized to the inside or partly overlapping with the BRP signal (B, left panel) and in close proximity to the RBP signal, surrounding or overlapping with it (C, left panel). Unc13B immunoreactivity localized at the outer edge of the BRP signal (B, right panel) and further away from the RBP signal not contacting it (C, right panel). (D) The distance to $Ca^{2+}$ channels, labeled by the GFP-tagged subunit Cacophony, is clearly different between

the two Unc13 isoforms. (E) NMJs of muscle 4 in 3rd instar larvae of the genotypes indicated stained with the indicated antibodies. Loss of BRP led to massive decrease of Unc13A levels, quantified in (F) Fluorescence intensity measured over the whole NMJ (% of wild type). Quantification: mean BRP intensity in ctrl (n=14): 100.0 ± 15.41, in brp-RNAi (n=15): 7.639 ± 0.498. mean Unc13A intensity in ctrl (n=14): 100.0 ± 15.060, in brp-RNAi (n=15): 15.24 ± 1.916 (G) *rab*$^{Null}$ leads to large BRP-aggregates, leaving other AZ devoid of BRP. Unc13A invariably co-localized with the BRP aggregates. Scale bars: (A) 1.5 µm; (B,-D) 50 nm. Scale in A-D: 50 nm, scale in G 5 µm. Statistics: ANOVA test, followed by a Turkey's multiple comparison test. All panels show mean ± SEM; n.s., not significant; *, $p \leq 0.05$; **, $p \leq 0.01$; ***, $p \leq 0.001$.
This figure is designed by M. Böhme; data were obtained and analyzed by M. Böhme.

To verify the first finding that Unc13A localization depends on BRP, advantage was taken of the *rab3*$^{Null}$ phenotype of the AZs at the larval NMJ. Here, BRP accumulates at few sites, where it clusters to extraordinarily large presynaptic scaffold structures, leaving the rest of the AZs devoid of this crucial presynaptic component. Strikingly, in the *rab3*$^{Null}$ mutant NMJs with clearly observable BRP-"superclusters", Unc13A strictly and solely localized to AZs containing BRP clusters (Fig 13G). In summary, a high dependence between Unc13A and BRP is observed, indicating a tight interaction between the two proteins.

### 4.1.2. Unc13B is Not Relevant for Synaptic Transmission

To reliably couple SV fusion to $Ca^{2+}$ influx through VGCCs, a sufficiently close location of the SVs to the $Ca^{2+}$ source is important. The differential spatial distribution of the Unc13 isoform with Unc13B located more distantly to the $Ca^{2+}$ channels, raises the question to what degree Unc13B contributes to synaptic transmission.

Here, two-electrode voltage clamp (TEVC) recordings of 3rd instar larval muscle cells were performed. This allows the sampling of compound transmission over the whole NMJ terminal of spontaneous as well as evoked release events (for methodological details on TEVC recordings please see chapter 3.8 "Electrophysiology"). The recording of miniature excitatory junctional currents (mEJCs) represents spontaneous fusion events (representative traces in Fig. 14A). Whether the kinetics of the events are different between mutant and wild type cells can be assessed by the measurement of the time to peak, and the rise and decay time of the signal. The time to peak is only measured in the recordings of evoked excitatory junctional currents (eEJCs) and is the time between the point of stimulation and the point of the evoked amplitude peak. The rise time is the time the recorded signal needs to reach from 10% to 90% of the amplitude. The decay of the signal is represented in the time constant of a single exponential fit to the decreasing amplitude in the range from 60 % of the respective amplitude back to baseline. In TEVC recordings of 3$^{rd}$ instar larval muscle cells in *unc13B*$^{Null}$ mutants the mEJC and eEJC amplitude size and kinetics was unchanged at increasing $Ca^{2+}$ concentrations (Fig. 14A-K). Only a slight but significant reduction of the eEJC amplitude in *unc13B*$^{Null}$ was observed (Fig. 14H).

Changes in the synaptic vesicle release probability $P_{ves}$ can be detected by a shift in the $Ca^{2+}$ sensitivity of release which is tested by titrating the extracellular $Ca^{2+}$ concentration (Fernández-Chacón et al., 2001). This step-wise increase of the extracellular $Ca^{2+}$ concentration ($[Ca^{2+}]_{ex}$) allowed to investigate mutant-specific changes of the SV release probability, measured in paired pulse recordings with 10 ms inter-stimulus interval (ISI) (an exemplary paired pulse trace at $[Ca^{2+}]_{ex}$=1.5 mM is shown in Fig. 14L). If more transmitter was released in the second pulse compared to first pulse, release is termed to be "facilitated". A spreading of the $Ca^{2+}$ nanodomain within increasing number of APs is meant to be a major contribution to facilitation (Zucker & Regehr, 2002) likely leading to fusion of SVs which have not sensed $Ca^{2+}$ in the first pulse. Vice versa, it is called "depression" if the second amplitude is smaller than the first amplitude. The main cause for depression is deprivation of the readily-releasable pool (RRP) when the majority of release-ready synaptic vesicles fuse already with the first stimulus. This lack of readily releasable SVs leads to a reduction in the second pulse (for details on mechanisms which contribute to synaptic depression, please see chapter 1.2 "Short-Term Plasticity (STP), SV Release Probability ($P_r$ and $P_{ves}$) and Synaptic Strength" in the introduction). Thus, facilitation and depression are directly dependent on the concentration of extracellular $Ca^{2+}$, and measuring evoked release during a step-wise increase of the extracellular $Ca^{2+}$ concentration can give a detailed picture of the SV release probability at the synapse. However, no alteration in $P_{ves}$ was observed upon loss of Unc13B at any of the tested $Ca^{2+}$ concentrations (Fig. 14M).

The reduced synaptic transmission was not fully rescued by high external $Ca^{2+}$ concentration, there always remained a tendency towards reduced amplitudes in *unc13B*$^{Null}$ (Fig. 14N).

The Hill plot (Fig. 14O) relating the eEJC amplitudes to the respective $Ca^{2+}$ concentrations on a logarithmic scale, allows the read-out of the characteristic properties of the resulting sigmoidal curve. At the inflection point of the curve, the slope is a value for $Ca^{2+}$ cooperativity and its X-value represents the diffusion constant $K_D$ and is a measure for the $Ca^{2+}$ sensitivity of the reaction. No change in $Ca^{2+}$ cooperativity or sensitivity was found in *unc13B*$^{Null}$ (Fig. 14O-Q).

Thus, Unc13B plays a comparatively minor role in transmitter release at the larval NMJ.

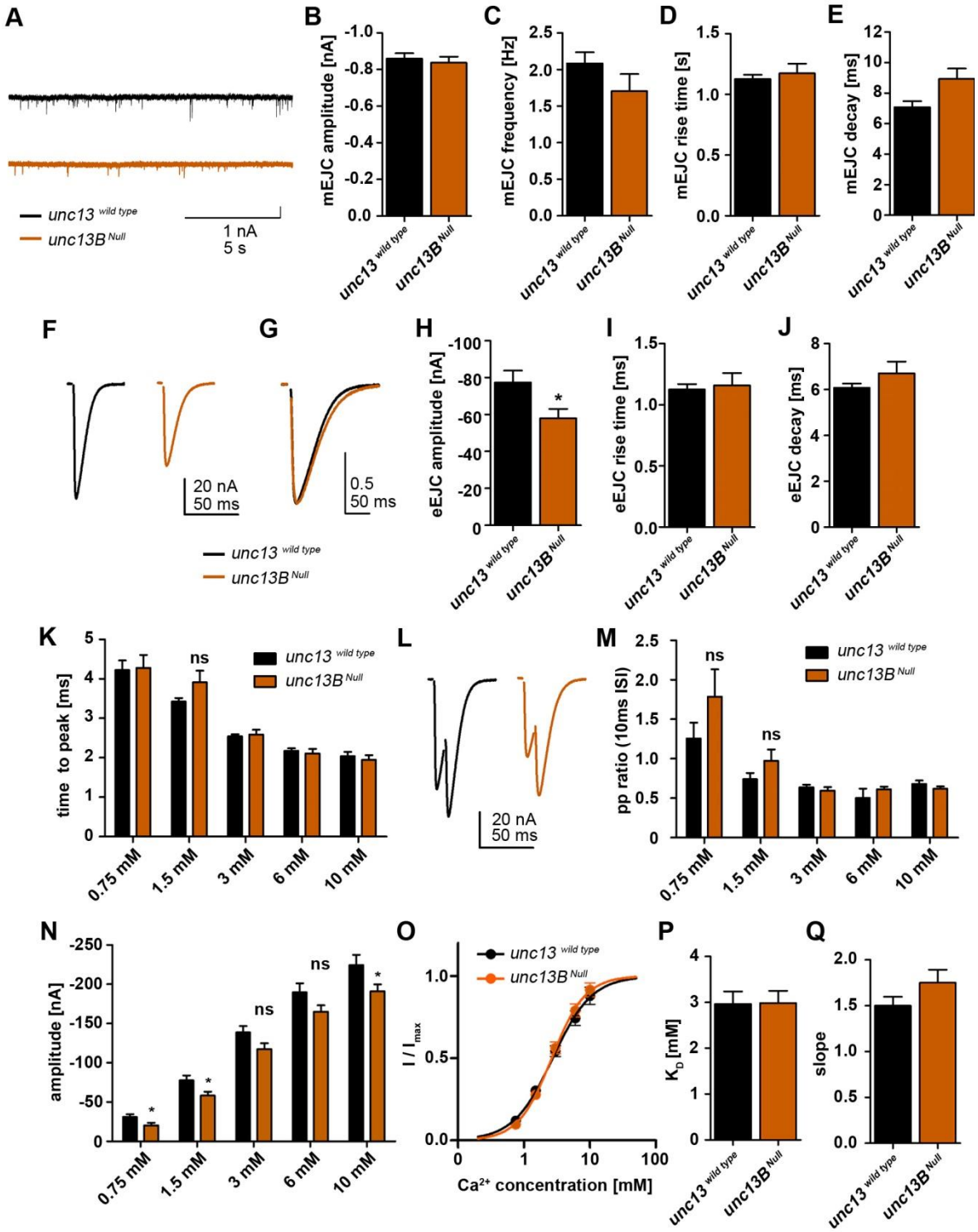


Figure 14 **Synaptic Transmission is Unaltered in *unc13B*$^{Null}$.**
(A-S) TEVC recordings at 3rd instar larval NMJ. (A) Representative mEJCs traces for wild type (black) and *unc13B*$^{Null}$ (orange). (B) *unc13B*$^{Null}$ exhibit no difference in mEJC amplitude size compared to wild type. Quantification: *unc13*$^{wild\ type}$ (n=14): -0.859±0.03 nA; *unc13B*$^{Null}$ (n=7): -0.837±0.03 nA. (C) The mEJC frequency is unaltered in *unc13B*$^{Null}$. Quantification: *unc13B*$^{wild\ type}$ (n=14): 2.08±0.15 Hz; *unc13B*$^{Null}$ (n=7): 1.70±0.23 Hz. (D, E) mEJC kinetics do not differ between wild type and *unc13B*$^{Null}$. Quantification mEJC rise time (D): *unc13B*$^{wild\ type}$ (n=14): 1.13±0.03 ms; *unc13B*$^{Null}$ (n=7): 1.17±0.08 ms. Quantification mEJC decay (E): *unc13B*$^{wild\ type}$ (n=14): 7.07±0.40 ms; *unc13B*$^{Null}$ (n=7): 8.93±0.68 ms. (F) Representative eEJC traces for control (black) and *unc13B*$^{Null}$ (orange). (G) Normalized amplitudes for control (black) and *unc13B*$^{Null}$ show no abnormalities. (H) eEJC amplitudes are decreased in *unc13B*$^{Null}$ compared to control. Quantification: *unc13B*$^{wild\ type}$ (n=12): -77.33 ± 6.383 nA; *unc13B*$^{Null}$ (n=12): -57.93 ± 5.026 nA. (I, J) The kinetics of the eEJC are unaltered in *unc13B*$^{Null}$. Quantification: eEJC rise time (I): *unc13B*$^{wild\ type}$ (n=12): 1.125 ± 0.044 ms;

*unc13B*$^{Null}$ (n=12): 1.158± 0.101 ms.; eEJC decay (J): *unc13B*$^{wild\ type}$ (n=12): 6.074 ± 0.181°ms; *unc13B*$^{Null}$ (n=11): 6.706 ± 0.511 ms. (K) Increasing $Ca^{2+}$ concentrations (in mM: 0.75, 1.5, 3, 6, 10) were washed into the bath solution and single eEJCs and paired pulse stimulations with 10 ms inter-stimulus interval were recorded. The time to peak is normal in *unc13B*$^{Null}$ at all tested $Ca^{2+}$ concentrations. The quantification can be found in Table 3 below. (L) Representative eEJC paired pulse traces for wild type (black) and *unc13B*$^{Null}$ (orange) with 10 ms interstimulus interval (ISI). (M) At various $Ca^{2+}$ concentrations there is no difference in short-term plasticity in *unc13B*$^{Null}$, tested with paired pulse recordings with 10 ms interstimulus interval (ISI). The quantification can be found in Table 3 below. (N) At all $Ca^{2+}$ concentration there is a clear tendency in *unc13B*$^{Null}$ to have deceased eEJC amplitudes. The quantification can be found in Table 3. (O-Q) $Ca^{2+}$-dependence of release analysis revealed neither changes in $Ca^{2+}$ requirement for release ($K_D$) in *unc13B*$^{Null}$ mutant synapses nor a change in the apparent $Ca^{2+}$ cooperativity of release (slope N). Please find the quantification in Table 3 below. The bath solution contained 1.5 mM $Ca^{2+}$ in (A-J, L), else as indicated. Statistics: Student's t-test except for panel (P, Q) where a Mann-Whitney U test was used. All panels show mean ± SEM; n.s., not significant; *, $p \leq 0.05$; **, $p \leq 0.01$; ***, $p \leq 0.001$.

**Table 1: Quantification of TEVC Recordings in *unc13B*$^{Null}$ at Various $Ca^{2+}$ Concentrations**

| | control (n) | mutant (n) | P | (test) |
|---|---|---|---|---|
| **eEJC time to peak (ms) in *unc13B*$^{Null}$ (Fig. 14K)** | | | | |
| **$[Ca^{2+}]_{ex}$ = 0.75 mM** | 4.225 ± 0.240 (12) | 4.275 ± 0.332 (12) | n.s. | (t- test) |
| **$[Ca^{2+}]_{ex}$ = 1.5 mM** | 3.425 ± 0.0888 (12) | 3.908 ± 0.297 (12) | n.s. | (t- test) |
| **$[Ca^{2+}]_{ex}$ =3 mM** | 2.542 ± 0.0528 (12) | 2.592 ± 0.119 (12) | n.s. | (t- test) |
| **$[Ca^{2+}]_{ex}$ =6 mM** | 2.175 ± 0.0664 (12) | 2.108 ± 0.114 (12) | n.s. | (t- test) |
| **$[Ca^{2+}]_{ex}$ =10 mM** | 2.042 ± 0.106 (12) | 1.950 ± 0.116 (12) | n.s. | (t- test) |
| **eEJC pp ratio (10ms ISI) in *unc13B*$^{Null}$ (Fig. 14M)** | | | | |
| **$[Ca^{2+}]_{ex}$ = 0.75 mM** | 1.255 ± 0.201 (12) | 1.787 ± 0.245 (12) | n.s. | (t- test) |
| **$[Ca^{2+}]_{ex}$ = 1.5 mM** | 0.741 ± 0.079 (12) | 0.974 ± 0.143 (12) | n.s. | (t- test) |
| **$[Ca^{2+}]_{ex}$ =3 mM** | 0.637 ± 0.034 (12) | 0.596 ± 0.044 (12) | n.s. | (t- test) |
| **$[Ca^{2+}]_{ex}$ =6 mM** | 0.503 ± 0.117 (12) | 0.614 ± 0.0316 (12) | n.s. | (t- test) |
| **$[Ca^{2+}]_{ex}$ =10 mM** | 0.680 ± 0.043 (12) | 0.619 ± 0.029 (12) | n.s. | (t- test) |
| **eEJC amplitude (nA) in *unc13B*$^{Null}$ (Fig. 14N)** | | | | |
| **$[Ca^{2+}]_{ex}$ = 0.75 mM** | -30.64 ± 3.643 (12) | -20.17 ± 3.176 (12) | ≤ 0.05* | (t- test) |
| **$[Ca^{2+}]_{ex}$ = 1.5 mM** | -77.33 ± 6.383 (12) | -57.93 ± 5.026 (12) | ≤ 0.05* | (t- test) |
| **$[Ca^{2+}]_{ex}$ =3 mM** | -138.3 ± 8.208 (12) | -117.3 ± 7.375 (12) | n.s. | (t- test) |
| **$[Ca^{2+}]_{ex}$ =6 mM** | -189.4 ± 11.54 (12) | -164.8 ± 8.270 (12) | n.s. | (t- test) |
| **$[Ca^{2+}]_{ex}$ =10 mM** | -224.1 ± 13.14 (12) | -190.9 ± 8.751 (12) | ≤ 0.05* | (t- test) |
| **$I/I_{Max}$ in *unc13B*$^{Null}$ (Fig. 14O)** | | | | |
| **$[Ca^{2+}]_{ex}$ = 0.75 mM** | 0.096 ± 0.015 (12) | 0.120 ± 0.014 (12) | n.s. | (t- test) |
| **$[Ca^{2+}]_{ex}$ = 1.5 mM** | 0.277 ± 0.024 (12) | 0.303 ± 0.025 (12) | n.s. | (t- test) |
| **$[Ca^{2+}]_{ex}$ =3 mM** | 0.562 ± 0 035 (12) | 0.542 ± 0.032 (12) | n.s. | (t- test) |
| **$[Ca^{2+}]_{ex}$ =6 mM** | 0.790 ± 0.039 (12) | 0.743 ± 0.045 (12) | n.s. | (t- test) |
| **$[Ca^{2+}]_{ex}$ =10 mM** | 0.915 ± 0.041 (12) | 0.879 ± 0.053 (12) | n.s. | (t- test) |
| **$K_D$ and slope in *unc13B*$^{Null}$ (Fig. 14P, Q)** values of fitted Hill coefficients | | | | |
| **$K_D$ (mM)** | 2.966 ± 0.273 (12) | 2.987 ± 0.265 (12) | n.s. | (Mann-Whitney U-test) |
| **slope** | 1.501 ± 0.096 (12) | 1.751 ± 0.140 (12) | n.s. | (Mann-Whitney U-test) |

### 4.1.3. SV Distribution Follows the Distinct Localization of Unc13 Isoforms

As already mentioned, Unc13 is a protein known to be involved in synaptic vesicle docking and priming (Augustin, et al., 1999; Imig et al., 2014; Man et al., 2015; Varoqueaux et al., 2002). Due to the specific localization pattern of Unc13 isoforms we started to speculate whether the different Unc13 isoforms promote this process at spatially distinct sites. To visualize whether SV

distribution and in particular a possible alteration in the SV docking sites, high-pressure freeze embedding (HPF) followed by freeze substitution (FS) was performed and directed to transmission electron microscopy (TEM, in the following called EM; for details concerning the method please see chapter 3.9.2 "High pressure freeze/ freeze substitution embedding"). The rapid cool-down of the tissue (20000K/s) in this technique has no fixation artifacts and allows to keeping the synaptic structures in their native state. Representative electron micrographs exemplify the altered distribution of docked SVs at Unc13A-deficient synapses compared to wild type controls (Fig. 15A, B). For clarification, the plasma membrane was highlighted in white, the electron-dense T-Bar was marked with light blue, SVs were encircled with pink while docked SVs were labeled with a black circle. Though the total number of SV per AZ was unchanged (Fig. 15C), the number of docked SVs per AZ was ~50% reduced (Fig. 15D). The T-Bar contains the scaffold proteins BRP and RBP, which are centered above the $Ca^{2+}$ channel clusters in the AZ (Fouquet et al., 2009; Kittel et al., 2006; K. S. Y. Liu et al., 2011). Hence, the distance between docked SVs and the center of the T-Bar was determined to analyze a potential locally specific docking deficit upon loss of Unc13A. Indeed, the minimal distance was found to be significantly increased in *unc13A*$^{Null}$ mutants (Fig. 15E). Consistently, the average SV distance to the T-Bar center was also significantly increased in *unc13A*$^{Null}$ (Fig. 15F). In immunofluorescence stainings, BRP-spots appeared larger in this situation (Fig. 12G). This could not be verified in EM. Here, the T-Bar pedestal width is, despite a small tendency, not significantly enlarged (Fig. 15G). However, it should be kept in mind for the labeling of BRP in STED that a C-terminal antibody was used, which binds to the cytosolic end of the elongated BRP scaffold protein located at "tips" of the T-Bar roof (Fouquet et al., 2009). Hence, an increased diameter of the pedestal in electron micrographs is not necessarily expected. Plotting the number of docked SVs in relation to their distance to the T-Bar in 30 nm “distance bins” reveals in wild type samples a clear preference of SVs to dock at about ~50 nm distance from the T-Bar center (Fig. 15H). The difference between wild type and *unc13A*$^{Null}$ is here shown as a dotted line and represents the Unc13A-specific docking positions. It peaks at ~50nm, which is in agreement with the localization of Unc13A relative to the BRP ring center of 60 nm determined by STED (Fig. 13A-D, quantification not shown). Consistent with Unc13A clusters organizing the docking of SVs at these positions, this preferential docking position at 50 nm was lost in *unc13A*$^{Null}$ AZs. Nonetheless, the distribution of the remaining, undocked SVs was unchanged (Fig. 5I). In summary, the loss of Unc13A has great impact specifically on the fraction of SVs normally positioned close to the T-Bar and thus close to the $Ca^{2+}$ channels.

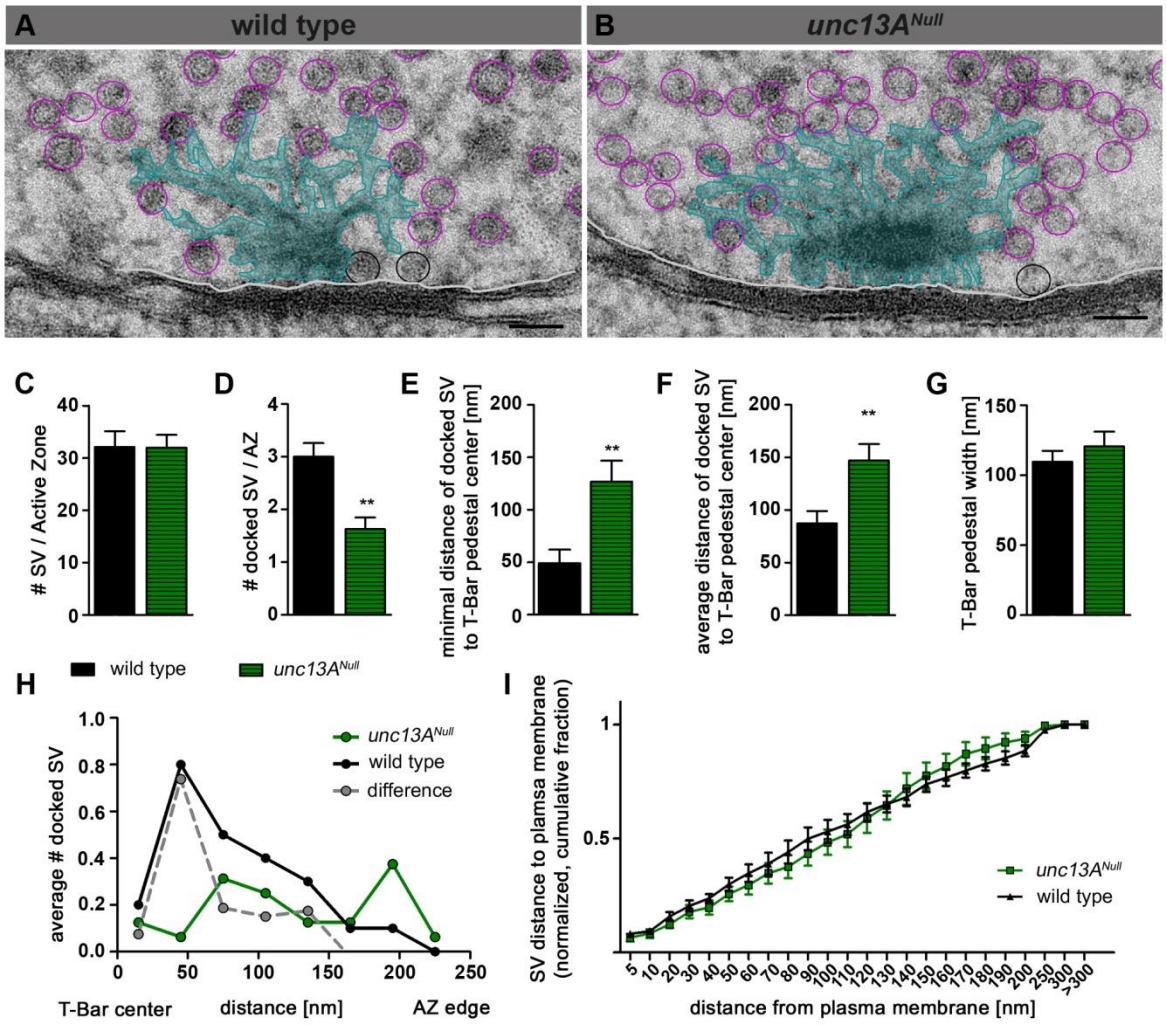


Figure 15 **The Enrichment of Docked Synaptic Vesicles at About 50 nm From the Active Zone Center Depends on Unc13A.**

(A,B) T-Bar in high-pressure-freeze (HPF) micrographs from wild type (A) and *unc13A*$^{Null}$ (B) NMJs. In *unc13A*$^{Null}$ SVs docked in close proximity to the T-Bar center were lost. (C) The average total number of SVs present in the region of individual AZs in a given EM section (counted in a radius of 300 nm around the T-Bar center) was not altered between the two groups. Quantification: wild type (n=9): 32.11±3.01 SV; *unc13A*$^{Null}$ (n=9): 32.00±2.43 SV. (D) The average number of docked SVs per section was significantly reduced *unc13A*$^{Null}$ (green) NMJs in comparison to wild type (black). Quantification: wild type (n=10): 3.0 ± 0.258 docked SV; *unc13A*$^{Null}$ (n=16): 1.625 ± 0.221 docked SV. (E) The minimal distance of docked SVs in the T-Bar center is strongly increased upon loss of Unc13A. Quantification: wild type (n=10): 49.10±12.94 nm; *unc13A*$^{Null}$ (n=15): 126.820.01 nm. (F) The average distance of docked SVs to the T-Bar center is significantly increased in *unc13A*$^{Null}$ compared to wild type. Quantification: wild type (n=10): 87.20±11.85 nm; *unc13A*$^{Null}$ (n=16): 147.0±15.71 nm. (G) No significant difference is found in the T-Bar pedestal width between wild type and *unc13A*$^{Null}$. Quantification: wild type (n=10): 109.5±7.95 nm; *unc13A*$^{Null}$ (n=16): 120.6±10.42 nm. (H) Docked SVs were binned with regard to their distance from the T-Bar center, and the average number of docked SV per bin was plotted. The number of docked SVs in close proximity to the T-Bar center where $Ca^{2+}$-channels are located is reduced in *unc13A*$^{Null}$ (green) compared to wild type (black). Subtracting the average vesicle distribution at *unc13A*$^{Null}$ AZs from wild type controls revealed Unc13A-specific docking positions, which peaked around 50 nm (grey dotted line). The values of the quantification can be found table 1. (I) The distribution of all SV at the AZ is unchanged. The SVs were normalized to the total number of SV at the AZ, binned with regard to their distance from the plasma membrane, and were plotted cumulatively. The values of the quantification can be found in table 1.

Statistics: Mann-Whitney U test. All panels show mean ± SEM; n.s., not significant; *, p ≤ 0.05; **, p ≤ 0.01; ***, p ≤ 0.001. Scale bar: 50 nm.

**Table 2 Quantification of the Synaptic Vesicles Distribution in High-Pressure Freeze Micrographs.**
The average number of docked SVs per AZ in relation to the distance from the T bar center (in 30 nm bins) (Fig. 15H) and the distances of all SVs to the plasma membrane (normalized cumulative fraction in 10nm in bins) (Fig. 15I) are given in the table.

| Distance from T-Bar center (30 nm bins); (Fig. 15H) | average number of docked SVs per bin, in wild type (n = 10) | average number of docked SVs per bin, in *unc13A*$^{Null}$ (n = 16) | Difference between control and mutant (wild type - *unc13A*$^{Null}$) |
|---|---|---|---|
| **0 - 30** | 0.200 | 0.125 | 0.075 |
| **31 - 60** | 0.800 | 0.063 | 0.737 |
| **61 - 90** | 0.500 | 0.313 | 0.187 |
| **91 - 120** | 0.400 | 0.250 | 0.150 |
| **121 - 150** | 0.300 | 0.125 | 0.175 |
| **151 - 180** | 0.100 | 0.125 | (-0.025) |
| **181 - 210** | 0.100 | 0.375 | (-0.275) |
| **211 - 240** | 0.000 | 0.063 | (-0.063) |

| Distance from plasma membrane (10 nm bins); (Fig. 15I) | average normalized fraction of SVs per bin, in wild type (n=9) | average normalized fraction of SVs per bin, in *unc13A*$^{Null}$ (n=9) |
|---|---|---|
| **0-10** | 0.0944 ± 0.01225 | 0.0836 ± 0.01836 |
| **11-20** | 0.1581 ± 0.01779 | 0.1242 ± 0.01562 |
| **21-30** | 0.2053 ± 0.02253 | 0.1797 ± 0.02749 |
| **31-40** | 0.2381 ± 0.01748 | 0.1976 ± 0.02904 |
| **41-50** | 0.2995 ± 0.02745 | 0.2571 ± 0.03065 |
| **51-60** | 0.3482 ± 0.03561 | 0.2963 ± 0.03945 |
| **61-70** | 0.3897 ± 0.04525 | 0.3475 ± 0.04176 |
| **71-80** | 0.4407 ± 0.04727 | 0.3763 ± 0.04738 |
| **81-90** | 0.4991 ± 0.04746 | 0.4334 ± 0.04965 |
| **91-100** | 0.5312 ± 0.04823 | 0.4839 ± 0.05229 |
| **101-110** | 0.5623 ± 0.04372 | 0.5197 ± 0.05385 |
| **111-120** | 0.6169 ± 0.03574 | 0.5893 ± 0.06064 |
| **121-130** | 0.6515 ± 0.03498 | 0.6460 ± 0.05785 |
| **131-140** | 0.6814 ± 0.03634 | 0.7182 ± 0.06527 |
| **141-150** | 0.7380 ± 0.03125 | 0.7747 ± 0.05521 |
| **151-160** | 0.7666 ± 0.03346 | 0.8159 ± 0.05275 |
| **161-170** | 0.7983 ± 0.02888 | 0.8713 ± 0.04801 |
| **171-180** | 0.8284 ± 0.02786 | 0.8948 ± 0.04508 |
| **181-190** | 0.8532 ± 0.02734 | 0.9216 ± 0.03732 |
| **191-200** | 0.8851 ± 0.02296 | 0.9379 ± 0.02875 |
| **201-250** | 0.9764 ± 0.01153 | 0.9928 ± 0.00676 |
| **251-300** | 1.0000 ± 0.00000 | 1.0000 ± 0.00000 |
| **>300** | 1.0000 ± 0.00000 | 1.0000 ± 0.00000 |

### 4.1.4. Unc13A is Critical for Synaptic Transmission

The next question we aimed to answer was whether the altered spatial arrangement of docked SVs influences synaptic transmission.

The analysis of mEJCs revealed significantly enlarged amplitudes in *unc13A*$^{Null}$ (Fig. 16A, B). In *unc13A*$^{Null}$ the kinetics of the mEJCs were not changed, the rise time and decay time of the signal were unaltered (Fig. 16C, D). However, the mEJC frequency was significantly higher upon loss of Unc13A (Fig. 16E). In the measurement of the amplitude size of evoked excitatory junctional

currents (eEJCs) (representative traces in Fig. 16F), *unc13A*$^{Null}$ mutant animals showed a dramatic reduction in amplitude size to less than 10% of the control values at 1.5 mM $Ca^{2+}$ in the bath solution (Fig. 16G). Furthermore, a significantly prolonged rise time of the eEJCs was found (Fig. 16H). The decay of the amplitudes remained unaltered (Fig. 16I). Notably, the input resistance was increased in *unc13A*$^{Null}$ muscle cells (Fig. 16J), a phenomenon already observed in other mutants with presynaptic transmission defects like *rbp*$^{Null}$ (data not published, personal communication with Elena Knoche). Why and how a strong presynaptic defect alters the resistance of the postsynaptic muscle cell was not further analyzed in this work, but would be an interesting question to follow in future experiments. The altered conductivity of the postsynaptic membrane is a mechanism likely to compensate the decreased synaptic currents and to allow for a more efficient muscle depolarization. Notably, *unc13B*$^{Null}$ cells had a normal input resistance (data not shown).

Previous analyses in several systems have identified Unc13 proteins as essential SV docking/priming factors with established functions in stabilization and replenishment of the RRP (Augustin, et al., 1999; Imig et al., 2014; Man et al., 2015; Varoqueaux et al., 2002). In line with this, fewer (~50%) SVs were docked in *unc13A*$^{Null}$ (Figure 15D). Recently the argument has been made that docking and priming are morphological and physiological correlates of the same molecular process (Imig et al., 2014). Accordingly, one may expect release (which scales with RRP size) to be similarly reduced. However, the reduction we observed at the NMJ upon Unc13A deletion was much larger than this (~90 %; figure 16G). Our data therefore argue that Unc13A-loss not only affects RRP size, but also the probability of exocytosis to single APs (release probability, $P_{ves}$). Changes in $P_{ves}$ can be detected by a shift in the $Ca^{2+}$ sensitivity of release which can be probed by monitoring evoked transmission while titrating the extracellular $Ca^{2+}$ concentration (Fernández-Chacón et al., 2001). Step-wise increase of the extracellular $Ca^{2+}$ concentration ($[Ca^{2+}]_{ex}$) clearly exemplifies the release deficit in *unc13A*$^{Null}$ mutant animals (Fig. 16K, green), the amplitudes were much smaller compared to wild type (black) at all tested concentrations. The overlaid normalized amplitudes at 1.5mM $[Ca^{2+}]_{ex}$ revealed a delay in the synaptic response (Fig. 16L), which is in line with the already observed increased rise time in *unc13A*$^{Null}$ mutants (Fig. 16H) and confirmed by the detailed analysis of the time to peak. The time to peak was prolonged in *unc13A*$^{Null}$ at all $Ca^{2+}$ concentrations (Fig. 16M). Please note that the eEJC in *unc13A*$^{Null}$ was so small at 0.75 mM $Ca^{2+}$ that no reliable value could be obtained for the time to peak at this $Ca^{2+}$ concentration (Fig. 6M). Interestingly, while the *unc13A*$^{Null}$ mutant time to peak converged to wild type values with increasing $Ca^{2+}$ concentrations, it never reached a plateau level

but keeps decreasing with each $[Ca^{2+}]_{ex}$-step. Contrarily, the wild type reached the minimal time to peak at 6 mM $Ca^{2+}$.

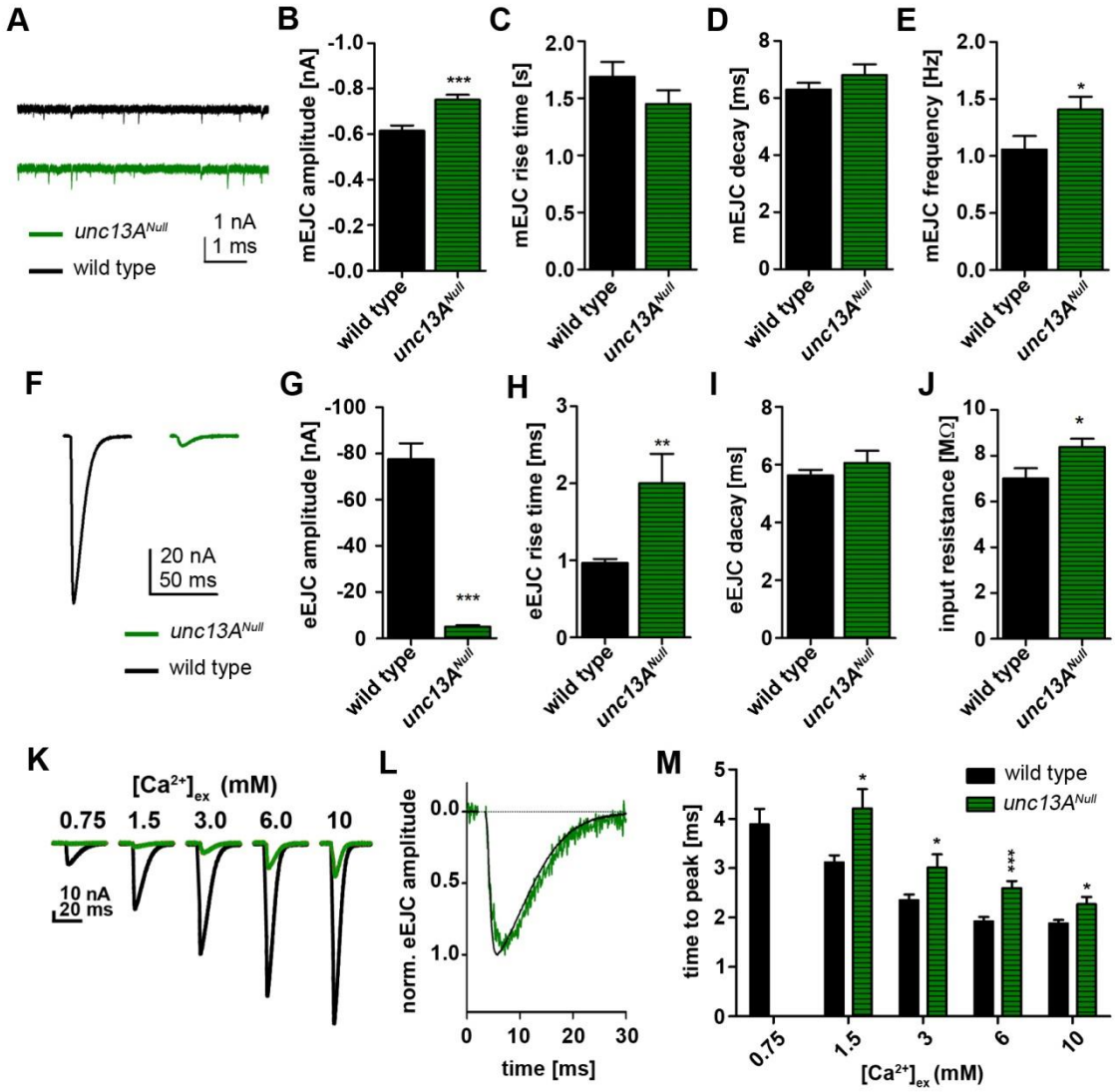


Figure 16 **Synaptic Transmission is Impaired in *unc13A$^{Null}$*.**
(A-S) TEVC recordings at 3rd instar larval NMJ. (A) Representative mEJCs traces for wild type (black) and *unc13A$^{Null}$* (green). (B) *unc13A$^{Null}$* exhibit significantly larger mEJC amplitudes compared to wild type. Quantification: wild type (n=12): -0.614±0.02 nA; *unc13A$^{Null}$* (n=11): -0.751±0.02 nA. (C, D) mEJC kinetics do not differ between wild type and *unc13A$^{Null}$*. Quantification mEJC rise time (C): wild type (n=12): 1.69±0.13 ms; *unc13A$^{Null}$* (n=11): 1.45±0.12 ms. Quantification mEJC decay (D): wild type (n=12): 6.30±0.23 ms; *unc13A$^{Null}$* (n=11): 6.80±0.38 ms. (E) The mEJC frequency is increased in *unc13A$^{Null}$*. Quantification: wild type (n=12): 1.06±0.12 Hz; *unc13A$^{Null}$* (n=11): 1.41±0.11 Hz. (G) Representative eEJC traces for wild type (black) and *unc13A$^{Null}$* (green). (I) eEJC amplitudes are dramatically decreased in *unc13A$^{Null}$* compared to wild type. Quantification: wild type (n=12): -77.46±6.954 nA; *unc13A$^{Null}$* (n=12): -4.879±0.768 nA. (H, I ) The eEJC rise time, which is the time it takes to reach from 10% to 90% of the eEJC amplitude, and eEJC decay, which is the time it takes from 60% of the eEJC amplitude back to baseline, is altered upon loss of Unc13A. (H) The eEJC rise time is doubled in *unc13A$^{Null}$* (green) relative to wild type (black). Quantification: wild type (n=12): 0.9667±0.05270 ms; *unc13A$^{Null}$* (n=9): 2.000±0.383 ms. (I) The eEJC decay is similar in wild type and *unc13A$^{Null}$*. Quantification: wild type (n=12): 5.627±0.196 ms; *unc13A$^{Null}$* (n=9): 6.058±0.425 ms. (J) The input resistance is increased in *unc13A$^{Null}$*. Quantification wild type (n=18): 7.000± 0.451 MΩ; *unc13A$^{Null}$* (n=21): 8.381± 0.360 MΩ. (K-M) Increasing $Ca^{2+}$ concentrations (in mM: 0.75, 1.5, 3, 6, 10) were washed into the bath solution and single eEJCs and paired pulse stimulations with 10 ms inter-stimulus interval were recorded. (K) Representative eEJC traces for wild type (black) and *unc13A$^{Null}$* (green) at various $Ca^{2+}$ concentrations clearly illustrate the impaired release in *unc13A$^{Null}$* synapses, independent of the extracellular $Ca^{2+}$ concentration. (L) Normalized amplitudes (at $[Ca^{2+}]_{ex}$=1.5mM) for wild type and *unc13A$^{Null}$* revealed delayed synaptic transmission in *unc13A$^{Null}$* in comparison to wild type. (M) At all tested $Ca^{2+}$ concentrations the time to peak, which is the time between the stimulus and the

minimum of the evoked amplitude, was significantly prolonged in *unc13A*$^{Null}$ (n=12 in each group). The quantification can be found in Table 2 below. The bath solution contained 1.5 mM $Ca^{2+}$ in (A-L), else as indicated. Statistics: Student's t-test except for panel Q, R and S where a Mann-Whitney U test was used. All panels show mean ± SEM; n.s., not significant; *, $p \leq 0.05$; **, $p \leq 0.01$; ***, $p \leq 0.001$.

### 4.1.5. Readily Releasable Pool and Forward Priming Rate Reduced in *unc13A*$^{Null}$.

As already mentioned, Unc13 proteins have been identified to be essential the stabilization and replenishment of the RRP (Augustin, et al., 1999; Imig et al., 2014; Man et al., 2015; Varoqueaux et al., 2002). Having observed a reduced number of docked SV in electron micrographs combined with a strong impairment in synaptic transmission, the question appears if a diminished RRP can be detected upon loss of Unc13A. Hence, a 60 Hz train protocol (100 actions potentials, with 2.5 mM $Ca^{2+}$ in the bath) was applied and a linear back-extrapolation of the plotted cumulative EPSCs versus stimulus number was used to determine the RRP. By this stimulation, the RRP should be efficiently emptied already during the first pulses (Millar et al., 2002; Pan & Zucker, 2009; Ralf Schneggenburger et al., 1999; C. F. Stevens & Williams, 2007). It is assumed that late in a stimulus train a steady state is reached, where the depletion rate of SVs is in balance with the refilling rate. Knowing that synaptic release is quantal and assuming furthermore that a miniature excitatory synaptic current (mESC) represents the spontaneous fusion of a single SV, the average mESC corresponds to one quantum. In the late phase of the train, the RRP is depleted and a steady-level is reached. Assuming that all SV fusions before the steady state level is reached belong to the RRP, the size of the RRP can be determined in the plot of the cumulative quantal content. Here, the RRP is equal to value of the Y-intercept of the linear fit to steady state values late in the train. The refilling rate of SVs during the train is represented by the slope of the linear fit (reviewed in Neher, 2015). In fact, a convergence of the last amplitudes of the train to a steady state level was observed (Fig. 17A).

Furthermore, the train recordings allow distinguishing between the asynchronous and synchronous component of release, which might be altered in *unc13A*$^{Null}$ (for detailed information concerning synchronous and asynchronous component of release, please see chapter 1.3 "Synaptic Transmission Modes: Synchronous, Asynchronous and Spontaneous Release"). The synchronous component is the transmitter release that occurs immediately after a stimulus. It is calculated from the amplitude size measured from a maximum in the train to the next minimum, which represents the direct and immediate transmitter release upon stimulation. The corresponding asynchronous component is measured from the minimum following that stimulus to baseline. The total amplitude is measured from the baseline to the minimum of the amplitude, hence it is the sum of the synchronous and asynchronous components of release. When all amplitudes of the train were normalized to the first amplitude and are plotted over time, a clear difference

between wild type and *unc13A*$^{Null}$ (Fig. 17B, C) was observed for the total amplitude as well as expected for the synchronous component. *unc13A*$^{Null}$ exhibited a strong facilitation during the first 10 APs of the train before a depression phase started which led over to the steady state phase (green curve). Contrarily, the wild type showed no facilitation, as expected in such a high external $Ca^{2+}$ the transmission was depressed as soon as the train began and entered quickly a steady state level (black curve). The cumulative plot of eEJC amplitudes confirmed the observation of an altered behavior during sustained release upon loss of Unc13A (Fig. 17D).

Notably, all train recordings in Fig. 17 were performed in 2.5 mM extracellular $Ca^{2+}$, while mEJC amplitudes were measured in 1.5 mM $Ca^{2+}$ (Fig. 16B). However, the mEJC amplitude size is $Ca^{2+}$ independent.

The RRP quantification (via linear back extrapolation of cumulatively plotted eEJC amplitudes, RRP size is read out in the Y-intercept) yielded in *unc13A*$^{Null}$ a value more than four-fold lower than in wild type. Notably, this ratio would be even more drastic when it is considered that the amplitudes would have been divided by an 1.2-fold increased mEJC size for *unc13A*$^{Null}$ (mEJCs in *unc13A*$^{Null}$ are ~20% larger compared to wild type, Fig. 16B) to obtain the quantal content. Undoubtedly, there is a significant decrease in the RRP in *unc13A*$^{Null}$ (Fig. 17E). Remarkably, also the forward priming rate is diminished in *unc13A*$^{Null}$ (Fig 17F), consistent with the already described important role of Unc13 in SV priming (Chen et al., 2013; Lipstein et al., 2013). Taken together, the RRP size is indeed drastically diminished upon loss of Unc13A, which is in line with the fewer (~50%) docked SVs in *unc13A*$^{Null}$ (Figure 16G). The reduction of RRP size and forward priming rate in *unc13A*$^{Null}$ reveals a specific role of isoform A of Unc13 in the process of SV priming at the larval NMJ AZs of *Drosophila*.

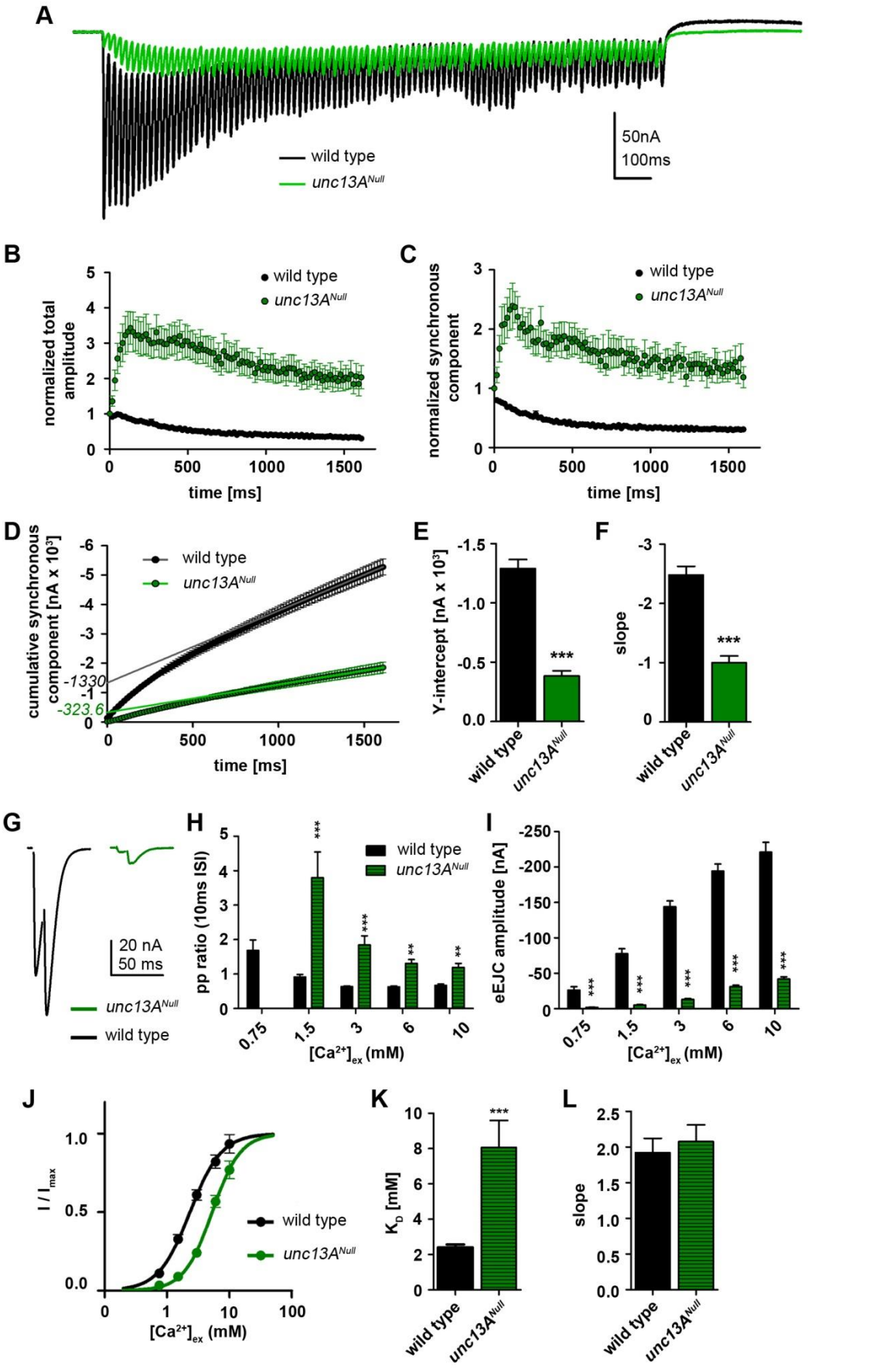


Figure 17 **The Readily Releasable Pool, the Forward Priming Rate and the $Ca^{2+}$ Sensitivity is Decreased in *unc13A*$^{Null}$.** (A) Representative average eEJC traces of 60 Hz train recordings with 100 APs in wild type (n=15, black) and *unc13A*$^{Null}$

(n=14, green). (B, C) The amplitudes of the train were normalized to the first amplitude and plotted over time. The total amplitude as well as only the synchronous component increase tremendously over time in *unc13A*$^{Null}$ (green), whereas the wild type (black) shows no facilitation at all. (D) The cumulative plot of synchronous amplitudes with a linear fit to the last 30 APs allows a backextrapolation of the readily releasable pool (Y-intercept of the linear fit). The RRP is reduced in *unc13A*$^{Null}$, also the forward priming rate of SVs during the train is reduced upon loss of the Unc13A (please compare the slope of the linear fit between the black and green curve). (E, F) The quantification of the linear fit to the cumulative plot yields a significantly reduced RRP and forward priming rate in *unc13A*$^{Null}$. (E) Quantification: Y-Intercept (wild type, n=15)= -1290±75.49 nA, Y-Intercept (*unc13A*$^{Null}$, n=10)= -383.2±42.96 nA. (F) Quantification: slope (wild type, n=15)= -2.479±0.1456, slope (*unc13A*$^{Null}$, n=10)= -0.9999± 0.1124. (G) Representative eEJC paired pulse traces for wild type (black) and *unc13A*$^{Null}$ (green) with 10 ms interstimulus interval (ISI). (H-L) Increasing $Ca^{2+}$ concentrations (in mM: 0.75, 1.5, 3, 6, 10) were washed into the bath solution and single eEJCs and paired pulse stimulations with 10 ms inter-stimulus interval were recorded. This set of experiments is marked with horizontal stripes in the bar graphs (H) The facilitation in short-term plasticity is significant in all tested $Ca^{2+}$ concentrations. Please note the missing value for 0.75 mM in *unc13A*$^{Null}$ because $eEJC_1$ amplitudes were generally close to zero. Please find the quantification in Table 2 below. (I) The mean eEJC amplitude in *unc13A*$^{Null}$ is significantly lower than in wild type at all tested extracellular $Ca^{2+}$ concentrations (n=12 in each group). Please find the quantification in Table 2 below. (J-L) $Ca^{2+}$-dependence of release analysis revealed an increased $Ca^{2+}$ requirement for release ($K_{D,}$ (K) ) in *unc13A*$^{Null}$ mutant synapses without changing the apparent $Ca^{2+}$ cooperativity of release (slope N, (L) ). Please find the quantification in Table 2 below.

Statistics: Mann-Whitney U test. All panels show mean ± SEM; n.s., not significant; *, $p \leq 0.05$; **, $p \leq 0.01$; ***, $p \leq 0.001$.

**Table 3: Quantification of TEVC Recordings in *unc13A*$^{Null}$ at Various $Ca^{2+}$ Concentrations**

| | control (n) | mutant (n) | P | (test) |
|---|---|---|---|---|
| **eEJC time to peak (ms) in *unc13A*$^{Null}$ (Fig. 16M)** | | | | |
| **$[Ca^{2+}]_{ex}$ = 0.75 mM** | 3.892 ± 0.309 (12) | 4.900 ± 0.760 (12) | n.s. | (t- test) |
| **$[Ca^{2+}]_{ex}$ = 1.5 mM** | 3.117 ± 0.142 (12) | 4.208 ± 0.394 (12) | ≤ 0.05* | (t- test) |
| **$[Ca^{2+}]_{ex}$ =3 mM** | 2.350 ± 0.120 (12) | 3.017 ± 0.263 (12) | ≤ 0.05* | (t- test) |
| **$[Ca^{2+}]_{ex}$ =6 mM** | 1.925 ± 0.0913 (12) | 2.600 ± 0.140 (12) | ≤0.001*** | (t- test) |
| **$[Ca^{2+}]_{ex}$ =10 mM** | 1.883 ± 0.0694 (12) | 2.275 ± 0.143 (12) | ≤ 0.05* | (t- test) |
| **eEJC pp ratio (10ms ISI) in *unc13A*$^{Null}$ (Fig. 17H)** | | | | |
| **$[Ca^{2+}]_{ex}$ = 0.75 mM** | 1.683 ± 0.308 (12) | -- | -- | -- |
| **$[Ca^{2+}]_{ex}$ = 1.5 mM** | 0.904 ± 0.065 (12) | 3.796 ± 0.748 (10) | ≤0.001*** | (t- test) |
| **$[Ca^{2+}]_{ex}$ =3 mM** | 0.633 ± 0.021 (12) | 1.846 ± 0.264 (10) | ≤0.001*** | (t- test) |
| **$[Ca^{2+}]_{ex}$ =6 mM** | 0.631 ± 0.023 (12) | 1.309 ± 0.116 (10) | ≤0.001*** | (t- test) |
| **$[Ca^{2+}]_{ex}$ =10 mM** | 0.674 ± 0.035 (12) | 1.192 ± 0.111 (10) | ≤0.001*** | (t- test) |
| **eEJC amplitude (nA) in *unc13A*$^{Null}$ (Fig. 17I)** | | | | |
| **$[Ca^{2+}]_{ex}$ = 0.75 mM** | -26.10 ± 4.89 (12) | -1.82 ± 0.17 (12) | ≤0.001*** | (t- test) |
| **$[Ca^{2+}]_{ex}$ = 1.5 mM** | -77.46 ± 6.95 (12) | -4.88 ± 0.77 (12) | ≤0.001*** | (t- test) |
| **$[Ca^{2+}]_{ex}$ =3 mM** | -143.90 ± 8.07 (12) | -13.07 ± 1.13 (12) | ≤0.001*** | (t- test) |
| **$[Ca^{2+}]_{ex}$ =6 mM** | -193.96 ± 10.04 (12) | -30.86 ± 2.12 (12) | ≤0.001*** | (t- test) |
| **$[Ca^{2+}]_{ex}$ =10 mM** | -220.72 ± 13.94 (12) | -41.78 ± 3.09 (12) | ≤0.001*** | (t- test) |
| **$I/I_{Max}$ in *unc13A*$^{Null}$ (Fig. 17J)** | | | | |
| **$[Ca^{2+}]_{ex}$ = 0.75 mM** | 0.110 ± 0.020 (12) | 0.033 ± 0.003 (10) | ≤0.01** | (t- test) |
| **$[Ca^{2+}]_{ex}$ = 1.5 mM** | 0.327 ± 0.029 (12) | 0.089 ± 0.014 (10) | ≤0.001*** | (t- test) |
| **$[Ca^{2+}]_{ex}$ =3 mM** | 0.608 ± 0.034 (12) | 0.240 ± 0.020 (10) | ≤0.001*** | (t- test) |
| **$[Ca^{2+}]_{ex}$ =6 mM** | 0.820 ± 0.042 (12) | 0.560 ± 0.039 (10) | ≤ 0.05* | (t- test) |
| **$[Ca^{2+}]_{ex}$ =10 mM** | 0.934 ± 0.058 (12) | 0.768 ± 0.056 (10) | ≤0.01** | (t- test) |
| **$K_D$ and slope in *Unc13A*$^{Null}$ (Fig. 17K, L)** values of fitted Hill coefficients | | | | |
| **$K_D$ (mM)** | 2.048 ± 0.160 (12) | 8.063 ± 1.537 (10) | ≤0.001*** | (Mann-Whitney U-test) |
| **slope** | 1.922 ± 0.2003 (12) | 2.079 ± 0.232 (10) | n.s. | (Mann-Whitney U-test) |

### 4.1.6. Loss of Unc13A Reduces The Release Probability $P_{ves}$

As mentioned before, loss of Unc13A not only affects RRP size, but presumably also the release probability $P_{ves}$. Changes in $P_{ves}$ can be detected by a shift in the $Ca^{2+}$ sensitivity of release which is tested by titrating the extracellular $Ca^{2+}$ concentration (Fernández-Chacón et al., 2001). An exemplary paired pulse trace at $[Ca^{2+}]_{ex}$=1.5mM is shown in Fig. 17G. Notably, 0.75 mM $[Ca^{2+}]_{ex}$ did not lead to recordable evoked synaptic transmission in *unc13A*$^{Null}$ (Fig. 17H). At all other $Ca^{2+}$ concentrations the release is significantly facilitated upon loss of Unc13A, indicating a drastically reduced $P_{ves}$. The highest facilitation was found at the physiological $Ca^{2+}$ concentration of 1.5 mM. Interestingly, the ratio of the second to the first pulse keeps decreasing in *unc13A*$^{Null}$ with increasing $Ca^{2+}$ concentration, whereas the maximal facilitation in wild type is already reached at 3 mM $Ca^{2+}$. The i) high rate of facilitation, the ii) increased time to peak (Fig. 16M), the iii) high variance in the paired pulse recording, and the iv) massively reduced evoked excitatory junctional currents (Fig. 16G) are an indication for severely impaired synaptic transmission and synaptic vesicle fusion upon loss of Unc13A.

The high variance in paired pulse recordings at low $[Ca^{2+}]_{ex}$ is expected, assuming a binomial release of SV at a limited number of release sites will at low $Ca^{2+}$ concentrations lead to a relatively high effect on amplitude size (Fig 17I). More precisely, the total amplitude is the sum of released quanta; the low number of total released quanta at low $[Ca^{2+}]_{ex}$ is strongly influenced by the variability of fusion likelihood of a single quantum.

In the Hill plot (Fig. 17J), eEJC amplitudes are plotted over to the respective $Ca^{2+}$ concentrations on a logarithmic scale. At the inflection point of the curve it allows the read-out of the $Ca^{2+}$ cooperativity (slope) and the $Ca^{2+}$ sensitivity of the reaction (X-value represents the diffusion constant $K_D$). The loss of Unc13A lead to significantly increased $K_D$ values (Fig. 17K). Hence, we conclude a shift in $Ca^{2+}$ sensitivity in *unc13A*$^{Null}$. The $Ca^{2+}$ cooperativity was unchanged, no difference was found concerning the slope of the curve (Fig. 17L). In summary, SV release probability and the kinetics of release are severely affected in the absence of Unc13A. Thus we conclude Unc13A is the major isoform involved in SV release and essential for normal synaptic transmission. For the altered $Ca^{2+}$ sensitivity two explanations are possible, i) there is a change in $Ca^{2+}$ sensitivity of the release apparatus (“biochemical”), or ii) there is a shift in the SV distance to the $Ca^{2+}$ source (“positional”); thus, release in *unc13A*$^{Null}$ mutants must operate from distant fusion sites and stationary synaptic $Ca^{2+}$ buffers like Calretinin and Calmodulin compete with the SVs $Ca^{2+}$ sensor Synaptotagmin for the $Ca^{2+}$ ions. The two possibilities are further investigated in the following experiments.

### 4.1.7. Unc13A Organizes Nanodomain Coupling at NMJ Terminals

To investigate the major role of Unc13A in transmitter release and its altered $Ca^{2+}$ sensitivity in more detail, $Ca^{2+}$ buffering experiments with EGTA were performed (Adler et al., 1991; reviewed in Eggermann et al., 2011). EGTA has a slow on-rate in $Ca^{2+}$ binding kinetics and tightly coupled SVs close to the $Ca^{2+}$ channels will not be affected by the $Ca^{2+}$ buffer, in contrast to loosely coupled SVs more distant to the $Ca^{2+}$ channels. This approach should provide information concerning the coupling distances between the $Ca^{2+}$ source and fusion-competent SVs and will unravel whether *unc13A*$^{Null}$ with a reduced number of docked SV close to the $Ca^{2+}$ channels account for the impaired transmitter release. We wanted to test the hypothesis whether the observed reduced $Ca^{2+}$ sensitivity (Hill plot, Fig. 16J, K) could be due to the loss of fusion-competent SV close to the T-Bar center (Fig. 15E, H). If residual release in *unc13A*$^{Null}$ mutants operated from a larger distance to the $Ca^{2+}$ channels *unc13A*$^{Null}$ should have higher EGTA sensitivity compared to wild type control. $Ca^{2+}$ chelators were used in the membrane-permeable acetoxymethyl ester (AM) form. They diffuse into the cell and enrich over time as intracellular esterases remove the lipophilic AM residue which prevents the now lipophobic molecules from leaving the intracellular space. Indeed, after 30 min of incubation in 0.1 mM EGTA-AM the evoked excitatory junctional current was reduced in a significantly higher amount in *unc13A*$^{Null}$ mutants compared to control (Fig. 18A-C). The EGTA affected the release at wild type synapses, indicating in general a rather loose coupling at the larval NMJ (Fig. 18A left panel, 18B). The ratio of amplitude size with and without EGTA was significantly different in *unc13A*$^{Null}$ (Fig. 18D).

To further test the hypothesis of looser $Ca^{2+}$ channel - SV coupling upon loss of Unc13A, EGTA-AM wash-in experiments were performed. Here, after baseline eEJCs were recorded, 0.2 mM EGTA-AM was applied to the bath solution under eEJCs continuously recording at 0.1 Hz stimulation frequency. EGTA diffuses into the cell and its concentration inside the cell increases over time (Kittel et al., 2006; Müller et al., 2012; Paul et al., 2015). The averaged eEJC traces clearly showed an accelerated reaction of eEJC amplitudes Unc13A-deficient NMJ to EGTA-AM (Fig. 18E), as the amplitudes declined much faster in *unc13A*$^{Null}$. Already 3 min after the EGTA-AM application the relative amplitude reduction differed significantly between *unc13A*$^{Null}$ mutants and wild type and continued to be significantly smaller than wild type eEJC over the whole duration of the recording (Fig. 18F, G). In this analysis, amplitude values were normalized to the corresponding baseline values of the same cell recorded before the EGTA-application. To quantify and compare the different decay behavior of the amplitude size over time, single-exponential curves were fitted to the values of amplitude sizes between 0-1000 s of the recording and the resulting time constants ($\tau$) were compared (Fig. 18G). The $\tau$-values significantly differed be-

tween wild type and *unc13A*$^{Null}$, with at each investigated time point the relative reduction on eEJCs in mutant synapses being significantly stronger and stayed smaller compared to wild type (Fig. 18G, H, I). Unc13A-deficient synapses decayed faster and thus were much more sensitive to even small EGTA-AM concentrations.

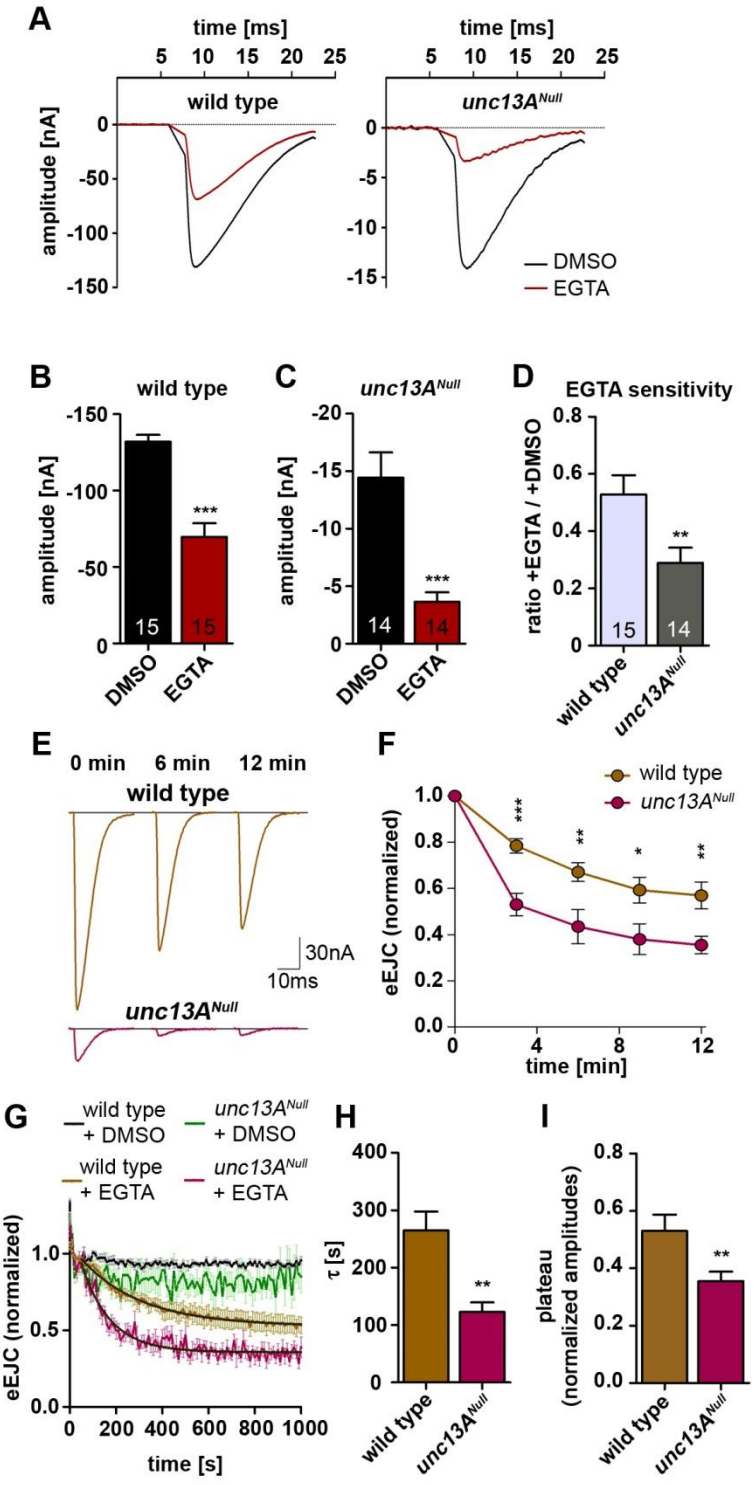


Figure 18 ***unc13A*$^{Null}$ Mutant Synapses Have an Increased EGTA-AM Sensitivity.** (A) 30 min incubation with the slow $Ca^{2+}$-buffer EGTA-AM (100µM) clearly reduced eEJCs amplitudes in both genotypes. Sample traces for wild type (left panel: black with DMSO, red with EGTA-AM) and *unc13A*$^{Null}$ (right panel: black with DMSO, red with EGTA-AM) show an increased EGTA-sensitivity for *unc13A*$^{Null}$ synapses. For clarity, the stimulation artifact was removed and replaced by a straight line. (B, C) A significant reduction of the eEJC amplitude after 30 min EGTA-AM incubation is observed in wild type (B) as well as *unc13A*$^{Null}$ (C) compared to only DMSO incubated cells, though the amplitude is decreased more drastically in *unc13A*$^{Null}$. Quantification: wild type (B) with DMSO (n=15): -131.8± 4.529 nA, with EGTA-AM (n=14): -69.67± 8.796 nA ; *unc13A*$^{Null}$ (C) with DMSO (n=14): -14.43±2.199 nA, with EGTA-AM (n=14): -3.620±0.8441 nA. (D) *unc13A*$^{Null}$ is more sensitive to EGTA-AM incubation compared to wild type. Quantification: wild type (n=15): 0.5286±0.06674; *unc13A*$^{Null}$ (n=14): 0.2891±0.05360. (E) A clear reduction in amplitude size can be observed over time at 3, 6 and 12 min after EGTA-AM application (200µM) to the bath. However, *unc13A*$^{Null}$ mutants (magenta) react more immediate to EGTA than wild type (gold). (F) The plot of the normalized amplitudes over time clearly shows that the rapid decline in amplitude size is significantly faster in *unc13A*$^{Null}$. Please find the quantification in Table 4 below. (G) A single exponential curve was fit to the decreasing normalized amplitudes upon EGTA application (*unc13A*$^{Null}$ magenta and wild type golden line) DMSO-treated control cells exhibit no significant run-down of amplitude size (*unc13A*$^{Null}$ green and wild type black line). (H) The quantification of the decay time induced by 200 µM EGTA-AM in the bath solution clearly reveals a higher EGTA sensitivity in *unc13A*$^{Null}$ compared to wild type. Single exponential fit in the range between 0-1000 s yields τ: wild type (n=10): 264.5±32.94 s; *unc13A*$^{Null}$ (n=10): 122.8±16.73 s. (I) Under the influence of 200 µM EGTA-AM the amplitude size converges towards a plateau. Here the fit clearly reveals a significant decrease of the plateau value in *unc13A*$^{Null}$ in comparison to wild type. Plateau: wild type (n=10): 0.530±0.057; *unc13A*$^{Null}$ (n=10): 0.354±0.033. Statistics: Student's t-test. All panels show mean ± SEM; n.s., not significant; *, p ≤ 0.05; **, p ≤ 0.01; ***, p ≤ 0.001. The bath solution contained 2.5mM $CaCl_2$.

**Table 4: Normalized eEJC Amplitudes at Various Time Points after EGTA-AM (200µM) Application to the extracellular solution.**

| | control (n) | mutant (n) | P | (test) |
|---|---|---|---|---|
| **Normalized residual amplitude in *unc13A*$^{Null}$ (Fig. 18F)** | | | | |
| **after 3 min** | 0.784 ± 0.031 (10) | 0.530 ± 0.048 (10) | ≤0.001*** | (t- test) |
| **after 6 min** | 0.671 ± 0.040 (10) | 0.434 ± 0.073 (10) | ≤ 0.05* | (t- test) |
| **after 9 min** | 0.592 ± 0.055 (10) | 0.379 ± 0.066 (10) | ≤ 0.05* | (t- test) |
| **after 12 min** | 0.569 ± 0.058 (10) | 0.354 ± 0.038 (10) | ≤0.01** | (t- test) |

I tested the possibility whether the observed effects could be due to differences in the $Ca^{2+}$ buffer concentration in the presynaptic terminal, caused by differences in loading with the membrane permeable chelators. However, it can be excluded that the altered sensitivity to EGTA-AM is due to differential loading with AM-esters between the two groups, because incubation with Bapta-AM, a $Ca^{2+}$-buffer with fast on-rates, leads to indistinguishable reduction of eEJC amplitudes regardless of the genotype (Fig. 19A-C). The sensitivity to Bapta-AM was not significantly different between wild type and *unc13A*$^{Null}$ (Fig. 19D). In conclusion, the shift in the $Ca^{2+}$ sensitivity (see Hill plot in Fig 17J, K) in *unc13A*$^{Null}$ is due to a shift in the SV distance to the $Ca^{2+}$ source. Thus, all data agree that Unc13A is necessary to establish tight spatial coupling between $Ca^{2+}$ channels and SVs.

The lack of docked SV close to the T-Bar center (Fig. 15E, H) goes along with a loss of fusion-competent SVs close to the $Ca^{2+}$ source (Fig. 18D, H, I). In other words, the Unc13A isoform in this system is crucial to allow for positional priming of SVs in the nanodomain range (<100 distance between fusion-competent SV and the $Ca^{2+}$ source (Eggermann et al., 2011)).

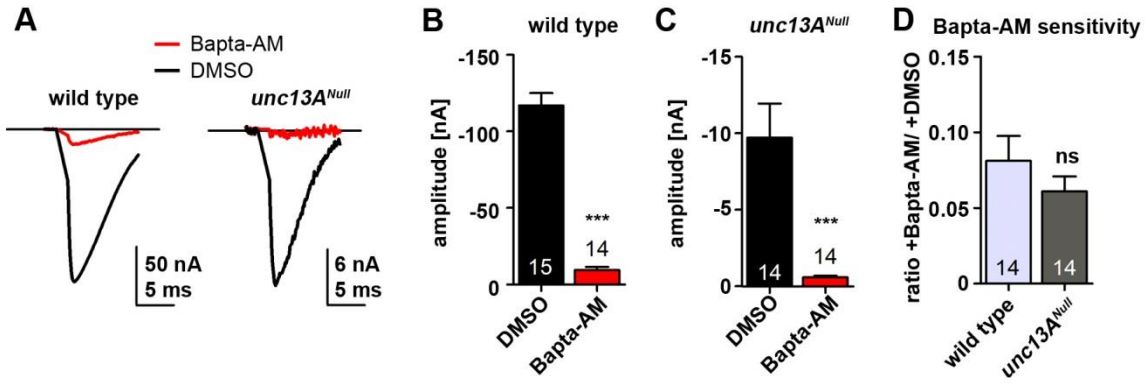


Figure 19 ***unc13A*$^{Null}$ Mutant Synapses and Wild Type Synapses Have a Comparable Sensitivity to Bapta-AM.**
(A) 30 min incubation with the fast $Ca^{2+}$- buffer Bapta-AM clearly reduced eEJCs amplitudes in both genotypes. Sample traces for wild type (left panel: black with DMSO, red with Bapta-AM) and *unc13A*$^{Null}$ (right panel: black with DMSO, red with Bapta-AM) exhibit similar Bapta-sensitivity for wild type and *unc13A*$^{Null}$ synapses. For clarity, the stimulation artifact was removed and replaced by a straight line. (B, C) The significant reduction of the eEJC amplitude after 30 min Bapta-AM incubation is similar in wild type (B) and *unc13A*$^{Null}$ (C) compared to DMSO incubated cells. Quantification: (B) wild type with DMSO (n=15): -116.9±8.033 nA, with Bapta-AM (n=14): -9.481±1.921 nA; (C) *unc13A*$^{Null}$ with DMSO (n=14): -9.707±2.224 nA, *unc13A*$^{Null}$ with Bapta-AM (n=14): -0.591±0.096 nA. (D) The Bapta sensitivity (Bapta/DMSO) does not differ between wild type and *unc13A*$^{Null}$. Quantification: wild type (n=14): 0.081 ± 0.016, *unc13A*$^{Null}$ (n=14): 0.060 ± 0.009. Statistics: Student's t-test All panels show mean ± SEM; n.s., not significant; *, p ≤ 0.05; **, p ≤ 0.01; ***, p ≤ 0.001. The bath solution contained 2.5mM $CaCl_2$.

## 4.2. Loss of the Unc13 N-term Mobilizes and Delocalizes Unc13

The localization of Unc13A is crucial to ensure the $Ca^{2+}$-SV topology necessary for a fast response upon the arrival of an AP. Though all catalytically relevant domains are located in the common C-Term shared by both Unc13 isoforms, the two isoforms serve functionally differentiated roles at the *Drosophila* larval NMJ which seem to depend on their specific localization. Hence, we analyzed how Unc13A fulfills its role in positional priming of SVs in detail. In yeast two-hybrid (Y2H) assays, it was found that the N-term of Unc13A binds to BRP and RBP, which possibly provides the necessary interactions with the AZ protein matrix to locate Unc13 molecules to their specific spots at the plasma membrane (data not shown). We conclude that the distinct localization is determined by the isoform-specific protein region located at the N-term. To identify the role of the Unc13A N-term and the functional importance of this location determining sequence, a cDNA based Unc13 transgene was generated lacking the N-term of the protein (Fig. 20A). The Unc13 N-term-deleted construct carried a GFP-tag at the C-terminus and was re-expressed with the UAS-Gal4-system in the *unc13*$^{Null}$ background (Unc13A$^{\Delta N\text{-term GFP}}$). For control, cDNA based full-length Unc13A with a C-terminal GFP-tag was re-expressed in the *unc13*$^{Null}$ background (Unc13A$^{FL\ GFP}$). The GFP-tagged Unc13 variants were compared with the same variants without tag in electrophysiological recordings. The GFP-tag did not interfere with the Unc13 function crucial for synaptic transmission (data not shown). Immunofluorescence stainings of the full-length Unc13A$^{FL\ GFP}$ revealed a wild type like distribution of the protein in control (Fig. 20B). In contrast, Unc13A$^{\Delta N\text{-term GFP}}$ exhibited no specific distribution or region-specific clustering. Instead, the truncated protein seemed to be ubiquitously distributed over the NMJ terminal surface (Fig. 20C). We compared the distribution of Unc13A$^{FL\ GFP}$ and Unc13A$^{\Delta N\text{-term GFP}}$ using the AZ-marker BRP and found that most BRP signal did in fact co-localize with Unc13A$^{\Delta N\text{-term GFP}}$ signal (Fig. 20D), which implies that AZs are not devoid of Unc13A$^{\Delta N\text{-term GFP}}$. The altered distribution of Unc13A$^{\Delta N\text{-term GFP}}$ became clear in the comparison of Unc13A$^{\Delta N\text{-term GFP}}$ distribution relative to BRP; most of Unc13A$^{FL\ GFP}$ signals co-localized with BRP, contrarily to Unc13A$^{\Delta N\text{-term GFP}}$ which is also localized everywhere else at the NMJ (Fig. 20E). We also noted that the overall amounts of Unc13A$^{\Delta N\text{-term GFP}}$ were increased when compared (Fig. 20F). In this context it should be emphasized that both constructs were expressed from the same chromosomal integration site and under identical conditions. The general increase in Unc13A$^{\Delta N\text{-term GFP}}$ levels at the NMJ could be a secondary effect of the unlimited ubiquitous localization of the Unc13 mutant. However, we speculate that degradation signals are

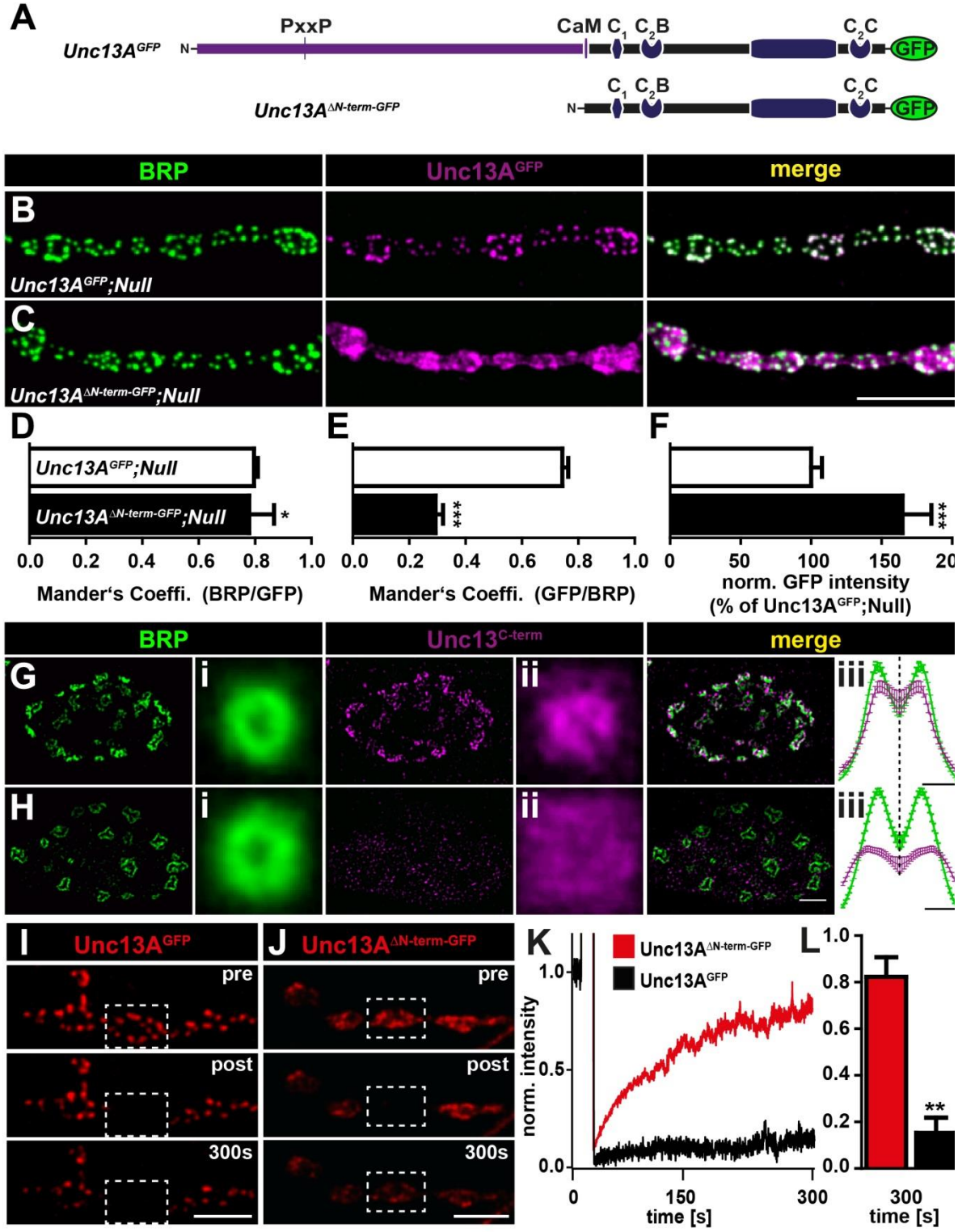


Figure 20 **The Loss of the Unc13 N-term Leads to an Altered Distribution and Mobilization of the Protein.**
(A) Sketch of Unc13A$^{GFP}$ and Unc13A$^{\Delta N\text{-term GFP}}$ domain structure. Unc13A$^{\Delta N\text{-term GFP}}$ contains the whole C-terminus besides the Calmodulin (CaM) binding site. (B,C) Muscle 4 NMJs of segment A2-4 from 3rd instar larvae of the indicated genotypes labeled with the BRP and GFP. Unc13A$^{\Delta N\text{-term GFP}}$ failed to localize specifically to the AZ but showed a distribution over the whole NMJ. (D,E) The Mander's overlap coefficient showed that at the confocal level Unc13A$^{\Delta N\text{-term GFP}}$ showed a similar overlap with BRP positive label as the control (E) but exhibit also a strong localization outside the BRP positive label (D) Quantification Mander's coefficient (BRP/GFP) in unc13A$^{GFP}$ (n=11): 0.796 ± 0.013, Unc13A$^{\Delta N\text{-term GFP}}$ (n=13): 0.7793 ± 0.088. (E) Quantification Mander's coefficient (GFP/BRP) in unc13A$^{GFP}$ (n=11): 0.7433 ± 0.020, Unc13A$^{\Delta N\text{-term GFP}}$ (n=13): 0.293 ± 0.026. (F) Normalized GFP intensity was more than 50% increased in Unc13A$^{\Delta N\text{-term GFP}}$

in comparison to the ctrl. GFP intensity was normalized to control and HRP intensity. Quantification in unc13A$^{GFP}$ (n=11): 100 ± 7.69, Unc13A$^{\Delta N\text{-term GFP}}$ (n=13): 164.9 ± 20.41. (G,H) Two-color STED image of synaptic boutons from 3rd instar larvae of the indicated genotypes stained with BRP and Unc13A$^{GFP}$. Also averaged AZs are shown for BRP (i), Unc13C-term (ii) as well the intensity distribution (iii). Unc13A$^{GFP}$ failed to localize to the AZ in Unc13A$^{\Delta N\text{-term GFP}}$ exhibiting a patchy structure distributed all over the bouton. Averaged AZs revealed that BRP ring sizes are increased in Unc13A$^{\Delta N\text{-term GFP}}$ (i and iii) and AZ specific localization of Unc13$^{GFP}$ was substantially reduced in Unc13A$^{\Delta N\text{-term GFP}}$ (compare purple line in Giii and Hiii). Still a weak accumulation can be observed in Unc13A$^{\Delta N\text{-term GFP}}$ (Hiii). (I-L) Short-term FRAP of Unc13AC-termGFP and Unc13A$^{\Delta N\text{-term GFP}}$. Dashed box shows bleached bouton before (pre) and directly after (post) the fluorescence bleaching. Fluorescence recovery was measured 300s after bleaching. (I) Bleached Unc13A$^{GFP}$ fluorescence did not recovery substantially within 300 s of acquisition. (J) Bleached Unc13A$^{\Delta N\text{-term GFP}}$ fluorescence recovered almost completely within 300 s of acquisition. (K) Quantification of fluorescence recovery within 300s after bleaching. (L) Unc13A$^{\Delta N\text{-term GFP}}$ showed a significantly stronger recovery within 300s. Quantification of fluorescence recovery (normalized intensity) in Unc13A$^{GFP}$ (n=6): 0.152 ± 0.064, Unc13A$^{\Delta N\text{-term GFP}}$ (n=11): 0.822 ± 0.082. Statistics: Mann-Whitney U-test. All panels show mean ± SEM; n.s., not significant; *, p ≤ 0.05; **, p ≤ 0.01; ***, p ≤ 0.001. Scale bar: (B,C) 10 µm; (G,H) 500 nm; (I,J) 5 µm.
This figure was designed by M. Böhme; data were obtained and analyzed by M. Böhme.

residing at the N-term of Unc13, and the deletion of this region might increase the stability of the protein.

Confocal imaging showed that the restriction of Unc13 to AZs is lost in the N-term deleted variant. To analyze the changes in Unc13 sub-AZ distribution of Unc13A$^{\Delta N\text{-term GFP}}$ in detail, we performed dual color super-resolution STED microscopy (Fig. 20G, H). Transgenic 3$^{rd}$ instar larvae were stained against BRP and the C-term of the GAL4-driven Unc13-GFP construct. Active zones in top-view were collected, averaged and a line profile was measured. The intensity peaks of Unc13A$^{FL\ GFP}$ signal matched with the BRP intensity signal, and confirmed the finding of Unc13A being localized slightly towards the BRP ring center (Fig. 20Gi-iii). However, the Unc13A$^{\Delta N\text{-term GFP}}$ signal had a broader distribution and exceeded the outer BRP ring edge (Fig. 20Hi-iii). Somewhat different from the impression derived from the confocal images, in STED pictures Unc13A$^{\Delta N\text{-term GFP}}$ was not randomly ubiquitously distributed but still had an increased density at AZs, which was still lower and less condensed in Unc13A$^{\Delta N\text{-term GFP}}$ compared to control. If the isoform-specific N-term of Unc13A determines the localization site of the protein, does the loss of the Unc13 N-term half lead to an increased mobility of Unc13? FRAP (fluorescence recovery after photobleaching) is a method to measure the mobility of a protein; the protein of interest is tagged with a fluophore. This fluophore signal is bleached in a particular area of the NMJ, and the recovery of the fluorescence is a measure for its mobility. For Unc13A$^{FL\ GFP}$, FRAP experiments showed that the control protein is stably anchored at the AZs, whereas the Unc13A$^{\Delta N\text{-term GFP}}$ is indeed highly mobile, as indicated by its fast recovery in FRAP (Fig. 20I, J). In conclusion, the N-term of Unc13 is important i) to restrict Unc13 localization to the sites of AZs and ii) to restrict the protein's mobility to the slots where it is functionally relevant.

### 4.2.1. Loss of the Unc13 N-term Affects Efficacy of Transmitter Release

The N-term of Unc13 is highly important for its cellular distribution. What is the functional consequence on synaptic transmission when depending on a largely delocalized and now highly mobile Unc13 variant? TEVC recordings in 3rd instar larval muscle cells at 1.5 mM extracellular $Ca^{2+}$ showed a clear reduction of evoked excitatory junctional current amplitudes (Fig. 21A,B). At the same time the kinetics of the eEJC amplitude were not measurably different in $Unc13A^{\Delta N\text{-term GFP}}$ (Fig. 21C, D). Also paired pulse ratios were not significantly changed, though there was a tendency towards facilitation in $Unc13A^{\Delta N\text{-term GFP}}$ in paired pulse recordings (Fig. 21E). Miniature excitatory junctional currents (Fig. 21F) were not altered in amplitude size (Fig. 21G) but were significantly increased in frequency (Fig. 21H).

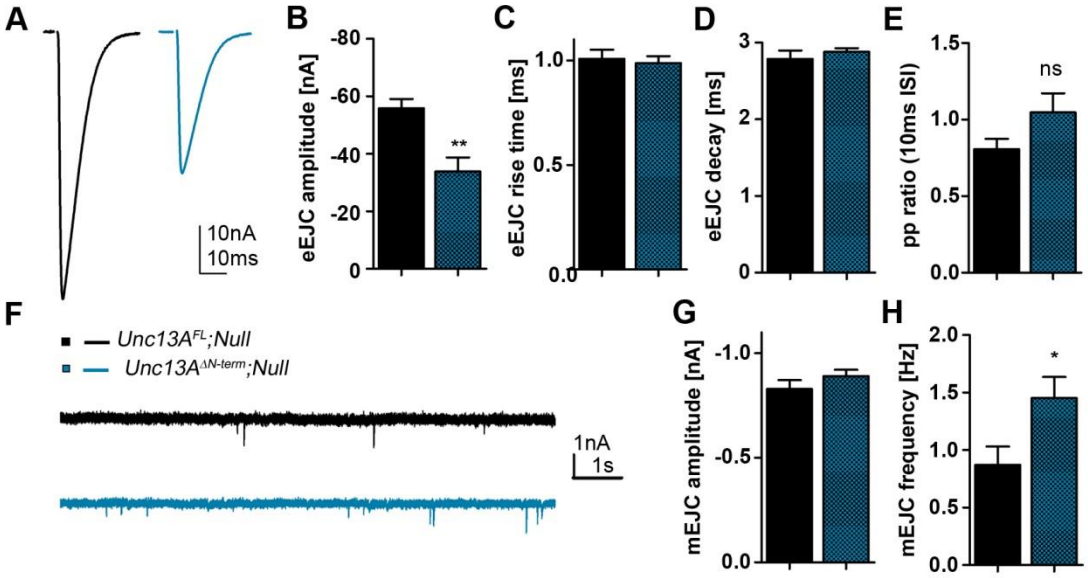


Figure 21 **The Loss of the N-term in Unc13A Leads to Reduced Synaptic Transmission.**
(A) Representative eEJC traces for control (black) and $Unc13A^{\Delta N\text{-term}}$ (petrol blue). (B) The eEJC amplitude is reduced in $Unc13A^{\Delta N\text{-term}}$ mutant synapses. Quantification: $Unc13A^{FL}$ (n=12): -55.75±3.302 nA, $Unc13A^{\Delta N\text{-term}}$ (n=12): -33.78±4.951 nA. (C, D) The kinetics of eEJCs are not altered upon loss of the N-term in Unc13. Quantification eEJC rise time (C): $Unc13A^{FL}$ (n=12): 1.008±0.04345 ms, $Unc13A^{\Delta N\text{-term}}$ (n=12): 0.9867±0.03399 ms; eEJC decay (D): $Unc13A^{FL}$ (n=12): 5.579±0.2175 ms, $Unc13A^{\Delta N\text{-term}}$ (n=12): 5.764±0.09289 ms. (E) The paired pulse ratio with 10 ms interstimulus interval shows a trend towards facilitation upon loss of the Unc13 N-term. Quantification: $Unc13A^{FL}$ (n=12): 0.8068± 0.06753, $Unc13A^{\Delta N\text{-term}}$ (n=12): 1.047±0.1248. (F) Representative mEJCs traces for wild type (black) and $Unc13A^{\Delta N\text{-term}}$ (petrol blue). (G) The mEJC amplitude is not altered in $Unc13A^{\Delta N\text{-term}}$. Quantification: $Unc13A^{FL}$ (n=10): -0.8287±0.04289 nA, $Unc13A^{\Delta N\text{-term}}$ (n=10): -0.8906± 0.03048 nA. (H) The mEJC frequency is significantly increased in $Unc13A^{\Delta N\text{-term}}$. Quantification: $Unc13A^{FL}$ (n=10): 0.8710± 0.1601 Hz, $Unc13A^{\Delta N\text{-term}}$ (n=10): 1.453± 0.1835 Hz. Statistics: Student's t-test. All panels show mean ± SEM; n.s., not significant; *, $p \leq 0.05$; **, $p \leq 0.01$; ***, $p \leq 0.001$. The bath solution contained 1.5mM $CaCl_2$.
These data were obtained by E. Reynolds.

In conclusion, the loss of the N-term in Unc13 has clear functional consequences on synaptic vesicle fusion; the normal Unc13 localization i) is relevant for normal evoked transmitter release, and it ii) is relevant to “clamp” fusion-competent SV to avoid spontaneous transmitter release.

### 4.2.2. Altered Synaptic Vesicle Distribution at Unc13 ΔN-term Driven Synapses

Will the delocalized Unc13A$^{\Delta N\text{-term}}$ result in an altered arrangement of docked SV on the ultrastructural level? High-pressure freezing and subsequent freeze substitution allows keeping the structures in a native state; with this technique, the SV distribution at AZs was analyzed, and the SVs in a radius of 300 nm around the T-Bar were counted (Fig. 22A, B). In Unc13A$^{\Delta N\text{-term}}$, the number of docked SVs per AZ was significantly increased, while the total number of SVs at the AZ was not altered (Fig. 22C, D). As indicated by STED analysis, the $Ca^{2+}$ channels are located in the membrane below the T-bar pedestal center (Fouquet et al., 2009; K. S. Y. Liu et al., 2011). The distance of the docked SVs to this point was measured, and surprisingly the minimal distance of docked SVs to the T-Bar pedestal center was significantly smaller in Unc13A$^{\Delta N\text{-term}}$ compared to control (Fig. 22E). The maximal distance was in Unc13A$^{\Delta N\text{-term}}$, besides a slight trend to be increased, not significantly different compared to control (Fig. 22F). In addition, the number of SVs touching the T-bar was not altered between the two groups (Fig. 22G). The T-Bar pedestal width was not different in Unc13A$^{\Delta N\text{-term}}$, but as already mentioned in chapter 4.1.3, the selection of the electron micrographs for the analysis might exclude small T-bars from the analysis due to the selection criteria. By plotting the docked synaptic vesicles relative to their distance from the T-Bar pedestal center the differences in distribution became obvious (Fig. 22I): in the control the majority of docked SVs were preferentially located either in ~50 nm distance to the T-Bar pedestal center, whereas a high fraction of docked SVs in Unc13A$^{\Delta N\text{-term}}$ located in distances smaller than 50 nm to the T-Bar, while the remaining docked SVs distributed more or less evenly over the length of the AZ. This raised the question whether only docked SVs are affected or the overall distribution of SVs might be changed at Unc13A$^{\Delta N\text{-term}}$ synapses. The synaptic vesicles in the respective distance to the plasma membrane were normalized to the total number of SVs per AZ to obtain the fraction of SVs localized in that distance bin and plotted (Fig. 22J). As already mentioned, the fraction of docked SVs was higher in Unc13A$^{\Delta N\text{-term}}$ compared to control while the total number of SVs per AZ did not differ; this led to a higher fraction of SVs >5nm from the plasma membrane in Unc13A$^{\Delta N\text{-term}}$. Besides this difference in the initial value the distribution of the SVs from the plasma membrane in the two groups turned out to be straight lines with comparable slope. This means the SVs are evenly distributed at the AZs in Unc13A$^{\Delta N\text{-term}}$ as well as Unc13A$^{FL}$.

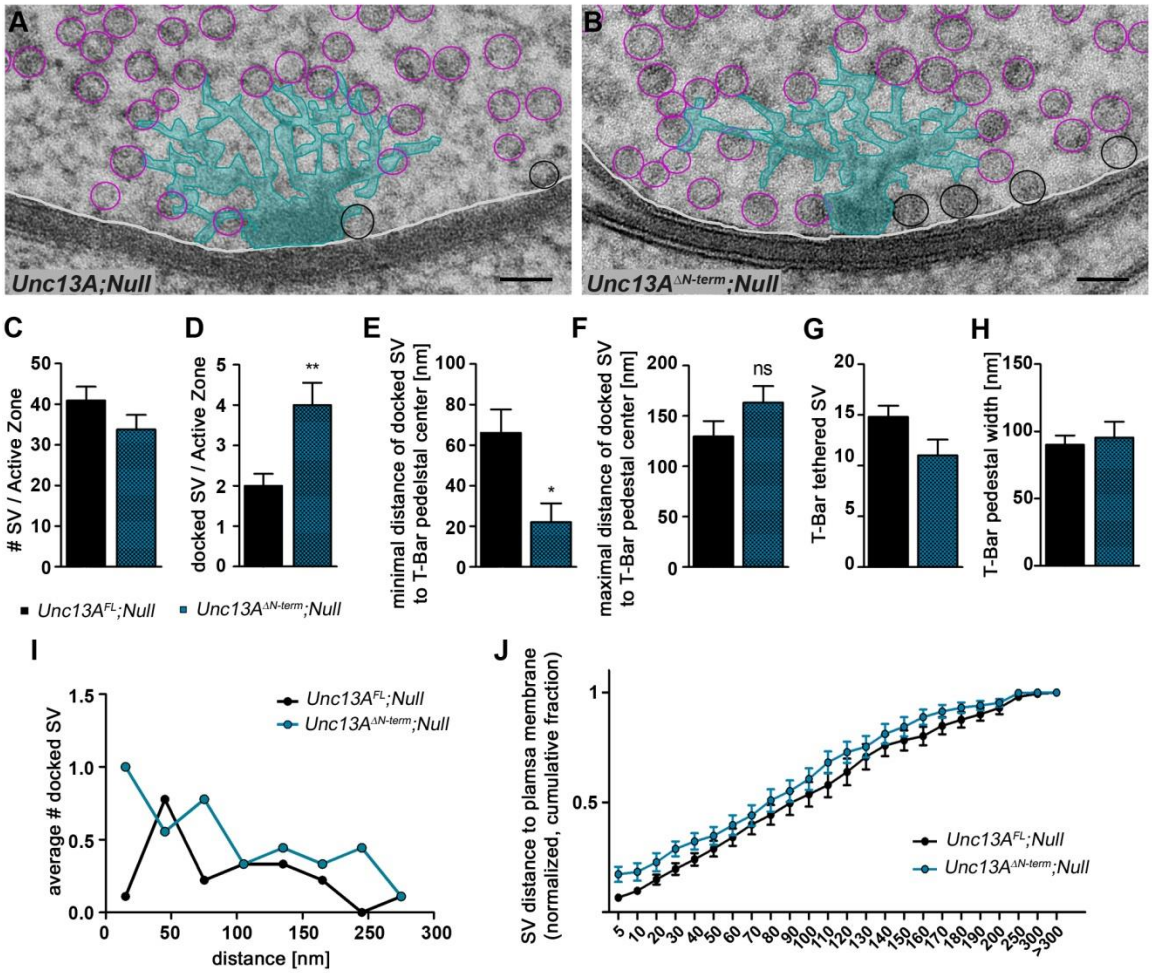


Figure 22 **The Number of Docked Synaptic Vesicles is Increased in Unc13A$^{\Delta N\text{-term}}$.**
(A,B) T-Bar high-pressure-freeze (HPF) micrographs from *Unc13A$^{FL}$* (A, full-length construct, control) and *Unc13A$^{\Delta N\text{-term}}$* (B) NMJs. In *Unc13A$^{\Delta N\text{-term}}$* the total amount of docked SV in doubled and SVs docked in close proximity to the T-Bar center is increased. (C) The total number of SV per AZ is unchanged in *Unc13A$^{\Delta N\text{-term}}$* (petrol blue) compared to control (black). Quantification: *Unc13A$^{FL}$* (n=10): 40.90±3.398 SVs, *Unc13A$^{\Delta N\text{-term}}$* (n=9): 33.78±3.582 SVs. (D) The number of docked SVs is doubled in *Unc13A$^{\Delta N\text{-term}}$*. Quantification: *Unc13A$^{FL}$* (n=10): 2.0± 0.2981 SVs, *Unc13A$^{\Delta N\text{-term}}$* (n=9): 4.0± 0.5528 SVs. (E) The SV are docked in closer proximity to the T-Bar in *Unc13A$^{\Delta N\text{-term}}$*. Quantification: *Unc13A$^{FL}$* (n=10): 66.10±11.52 nm, *Unc13A$^{\Delta N\text{-term}}$* (n=9): 22.00± 9.413 nm. (F) The maximal distance of docked SV in not significantly different between *Unc13A$^{\Delta N\text{-term}}$* and control. Quantification: *Unc13A$^{FL}$* (n=10): 129.5± 15.34 nm, *Unc13A$^{\Delta N\text{-term}}$* (n=9): 163.3± 16.27 nm. (G) The number of SV tethered to the T-Bar is not significantly changed in *Unc13A$^{\Delta N\text{-term}}$*. Quantification: *Unc13A$^{FL}$* (n=10): 14.80± 1.114 SVs, *Unc13A$^{\Delta N\text{-term}}$* (n=9): 11.00± 1.572 SVs. (H) In the electron micrographs, no change in T-Bar pedestal width was observed in *Unc13A$^{\Delta N\text{-term}}$*. Quantification: *Unc13A$^{FL}$* (n=10): 90.10± 6.924 nm, *Unc13A$^{\Delta N\text{-term}}$* (n=9): 95.44± 11.82 nm. (I) Docked SVs were binned with regard to their distance from the T-Bar center, and the average number of docked SV per bin was plotted. The number of docked SVs in close proximity to the T-Bar center where $Ca^{2+}$-channels are located is increased in *Unc13A$^{\Delta N\text{-term}}$* (petrol blue) compared to control (black). The values of the quantification can be found table 5. (J) Besides the different starting point of the curves due to the increased number of docked SV in the first bin, the distribution of all SV at the AZ is unchanged. The SVs were normalized to the total number of SV at the AZ, binned with regard to their distance from the plasma membrane, and were plotted cumulatively. The values of the quantification can be found table 5.
Statistics: t test. All panels show mean ± SEM; n.s., not significant; *, p ≤ 0.05; **, p ≤ 0.01; ***, p ≤ 0.001. Scale bar: 50 nm.

**Table 5 Quantification of the Synaptic Vesicles Distribution in High-Pressure Freeze Micrographs**. The average number of docked SVs per AZ in relation to the distance from the T bar center (Fig. 22I) and the distances of all SV to the plasma membrane (normalized cumulative fraction in 10nm in bins) (Fig. 22J) are given in the table.

| Distance from T-Bar center (30 nm bins); (Fig. 22I) | average number of docked SVs per bin, in Unc13A$^{FL}$ (n=10) | average number of docked SVs per bin, in Unc13A$^{\Delta N\text{-term}}$ (n=9) |
|---|---|---|
| **0 - 30** | 0.111 | 1.000 |
| **31 - 60** | 0.777 | 0.555 |
| **61 - 90** | 0.222 | 0.777 |
| **91 - 120** | 0.333 | 0.333 |
| **121 - 150** | 0.333 | 0.444 |
| **151 - 180** | 0.222 | 0.333 |
| **181 - 210** | 0.000 | 0.444 |
| **211 - 240** | 0.111 | 0.111 |
| | | |
| **Distance from plasma membrane (10 nm bins); (Fig. 22J)** | **average normalized fraction of SVs per bin, in Unc13A$^{FL}$ (n=10)** | **average normalized fraction of SVs per bin, in Unc13A$^{\Delta N\text{-term}}$ (n=9)** |
| **0-10** | 0.0976 ± 0.01232 | 0.1835 ± 0.03741 |
| **11-20** | 0.1486 ± 0.02105 | 0.2277 ± 0.03852 |
| **21-30** | 0.1969 ± 0.02514 | 0.2880 ± 0.03211 |
| **31-40** | 0.2410 ± 0.02686 | 0.3223 ± 0.03500 |
| **41-50** | 0.2891 ± 0.03374 | 0.3479 ± 0.03799 |
| **51-60** | 0.3415 ± 0.03750 | 0.3965 ± 0.04236 |
| **61-70** | 0.3988 ± 0.04200 | 0.4403 ± 0.04432 |
| **71-80** | 0.4433 ± 0.04262 | 0.5088 ± 0.04780 |
| **81-90** | 0.4961 ± 0.05072 | 0.5513 ± 0.04565 |
| **91-100** | 0.5369 ± 0.05282 | 0.6060 ± 0.04601 |
| **101-110** | 0.5787 ± 0.05208 | 0.6817 ± 0.04778 |
| **111-120** | 0.6386 ± 0.05732 | 0.7278 ± 0.04526 |
| **121-130** | 0.7075 ± 0.05444 | 0.7530 ± 0.04576 |
| **131-140** | 0.7587 ± 0.04605 | 0.8115 ± 0.04248 |
| **141-150** | 0.7823 ± 0.04372 | 0.8442 ± 0.04086 |
| **151-160** | 0.8016 ± 0.04006 | 0.8880 ± 0.03260 |
| **161-170** | 0.8487 ± 0.03675 | 0.9138 ± 0.02773 |
| **171-180** | 0.8755 ± 0.03371 | 0.9306 ± 0.02246 |
| **181-190** | 0.9010 ± 0.02828 | 0.9408 ± 0.01928 |
| **191-200** | 0.9295 ± 0.02672 | 0.9530 ± 0.01647 |
| **201-250** | 0.9803 ± 0.01347 | 0.9979 ± 0.00198 |
| **251-300** | 0.9942 ± 0.00547 | 1.0000 ± 0.00000 |
| **>300** | 1.0000 ± 0.00000 | 1.0000 ± 0.00000 |

Thus, the altered Unc13 localization due to loss of its N-term does not affect the distribution of the undocked SVs, but heavily changes the site of SV docking and doubles the number of docked SVs per AZ. Hence, the N-term of Unc13 is relevant to restrict docked SV to specific release sites at the synapse, including the maintenance of a minimal distance to the $Ca^{2+}$ channel cluster.

### 4.2.3. Unc13A$^{\Delta N\text{-term GFP}}$ has a Strong Asynchronous Component of Release

How does this altered distribution of docked SVs provoked by expressing an Unc13 N-term deficient mutant influence the likelihood of SV fusion? On the one hand, in Unc13A$^{\Delta N\text{-term GFP}}$ the MUN-domain, which is catalytically relevant for SV priming, is unaffected. On the other hand, the highly mobile Unc13A$^{\Delta N\text{-term GFP}}$ might not be able to keep readily releasable SVs long enough in sufficiently close proximity to the $Ca^{2+}$ channels to reach wild type-like amplitudes in TEVC recordings. How would the higher amount of docked SVs located close to the T-bar center influence release probability? To understand how the changed SV docking distances to the T-bar center influence the likelihood of SV fusion, EGTA experiments were performed. As described in *unc13A$^{Null}$* $Ca^{2+}$ buffering experiments, the use of EGTA allows the identification of changes in the physical distance of release-competent SVs relative to the $Ca^{2+}$ source. Like in Fig. 18, the dissected 3$^{rd}$ instar larvae were incubated in HL3 containing 0.1 mM EGTA-AM and Pluronic F-127 at RT for 30 min. Then a train with 100 pulses at 60 Hz was given; the resulting traces indicated several changes in the SV release modes and their potential position. As can be seen in the display of whole trains (Fig. 23A-C), first, a very striking and unexpected shift in the time to peak was observed in Unc13A$^{\Delta N\text{-term GFP}}$. This will be explained in detail in the next section by having a closer look on the 30$^{th}$ amplitude of the train, marked with an arrow in Fig.23A-C. Second, in the beginning of the train we observed a strong facilitation in Unc13A$^{\Delta N\text{-term GFP}}$ (Fig. 23B) which was abolished by EGTA incubation (Fig. 23A). Third, a positive current was observed in both Unc13A$^{FL\ GFP}$ and Unc13A$^{\Delta N\text{-term GFP}}$ under control (DMSO) condition, which is abolished by EGTA treatment. Fourth, the expected effect of EGTA in reducing the asynchronous release component and along this a reduction of the total amplitude size was found in both genotypes (Fig. 23A, C). Synchronous release is the result of immediate SV exocytosis triggered by an AP, while asynchronous release takes place with a longer, variable delay following an AP (Kaeser & Regehr, 2014). In a loose coupling regime, where SVs are in a higher distance to the $Ca^{2+}$ source and thus prone to fuse in an asynchronous manner, the slow $Ca^{2+}$ chelator EGTA will capture the $Ca^{2+}$ on its way from the source to the sensor. The tighter the coupling, the higher is the synchronous component of release and the lower is the EGTA sensitivity of the synapse (Eggermann et al., 2011). As already described in Fig. 17, the synchronous component is the amplitude size measured from a maximum in the train to the following minimum. The corresponding asynchronous component is measured from the minimum following that stimulus to baseline. The total amplitude is the sum of the synchronous and asynchronous component of release. In the first stimuli of the train, the total amplitudes increased strongly in Unc13A$^{\Delta N\text{-term GFP}}$ without EGTA-AM treatment (Fig. 23D). The corresponding paired pulse ratio was significantly higher in Unc13A$^{\Delta N\text{-term GFP}}$ compared to

Unc13A$^{FL\ GFP}$. This Unc13A$^{\Delta N\text{-}term\ GFP}$ -specific behavior was completely abolished by EGTA-AM (Fig. 23F, G). Thus, the facilitation is likely a result of increased asynchronous release, which in turn is the component of release being primarily affected by EGTA. To investigate the increased asynchronous release component we found for Unc13A$^{\Delta N\text{-}term\ GFP}$ in detail, the two release components were analyzed and plotted separately. Here, the amplitudes of the train were normalized to the first evoked amplitude to identify relative, genotype-specific effects on the respective release component (Fig. 23H-O). As expected, the asynchronous release component is 4-fold increased in Unc13A$^{\Delta N\text{-}term\ GFP}$, and the paired pulse ratio is significantly higher as well (Fig. 23H, I). Notably, EGTA-AM treatment reliably reduced this tremendous increase back to normal levels (Fig. 23J, K). The large error bars at the end of the train are possibly a consequence of EGTA consumption during stimulation, leading to reduced $Ca^{2+}$ buffering towards the last stimuli. Interestingly, also the synchronous release and the paired pulse ratio were slightly, but significantly higher in Unc13A$^{\Delta N\text{-}term\ GFP}$ when compared to Unc13A$^{FL\ GFP}$ (Fig. 23L, M). While in controls the synchronous component was not affected by the EGTA-AM at all (Fig. 23N green, compare to Fig. 23L black), the Unc13A$^{\Delta N\text{-}term\ GFP}$ specific increase was gone with the EGTA-AM treatment (Fig. 23N, O blue, compare to Fig. 23L, M red). In conclusion, also the synchronous components profit from ectopic SV docking.

To estimate the RRP, usually the amplitudes are divided by the mean mEJC amplitude of the respective genotype, cumulated and plotted. In a different series of measurements using 1.5 mM $Ca^{2+}$ the recording of mEJCs yielded no difference in amplitude size, the amount of transmitter released by a single fusion event is the same (Fig. 21G). It is reasonable to assume this does not change in higher external $Ca^{2+}$ (Kaeser & Regehr, 2014); thus, a cumulative plot of the eEJC amplitudes is already informative concerning the RRP size, as the eEJC amplitudes in both groups would anyway have been divided by the same value to obtain its quantal content. The RRP is estimated by a linear back-extrapolation in a cumulative plot (reviewed in Neher, 2015; Ralf Schneggenburger et al., 1999). Under untreated (DMSO-) condition, the loss of the Unc13 N-term decreased the readily releasable pool not significantly (Fig. 23P, please compare the Y-intercept of the linear fit to the black and red curve). EGTA-treatment led to a slightly reduced RRP in Unc13A$^{FL\ GFP}$, the Y-intercept of the back-extrapolation is smaller compared to untreated cells (Fig. 23P and Q, please compare the Y-intercept of the linear fit to the red (P) and green (Q) curve). Thus, the RRP seems to be at least in parts susceptible for EGTA-AM in Unc13A$^{FL\ GFP}$. The refilling of the releasable SVs during a stimulus train is increased by the $Ca^{2+}$ influx to the synaptic terminal. The elevated $Ca^{2+}$ concentration shifts the dynamic equilibrium between the reserve pool SVs and primed SVs towards an enhanced priming rate (reviewed in

Neher & Sakaba, 2008; L. Y. Wang & Kaczmarek, 1998). In untreated (DMSO) conditions, the SV refilling during the train was reduced in Unc13A$^{\Delta N\text{-term GFP}}$ compared to Unc13A$^{FL\ GFP}$ (Fig. 23P; the slope of the fitted line to the red values is more shallow than the slope of the fit to control values in black). Notably, EGTA-treatment affects the SV refilling kinetics only in Unc13A$^{FL\ GFP}$, the slope of untreated versus EGTA-treated in Unc13A$^{\Delta N\text{-term GFP}}$ was unchanged (Fig. 23Q). By plotting the quotient of synchronous to asynchronous release over time the already mentioned high amount of asynchronous release in Unc13A$^{\Delta N\text{-term GFP}}$ DMSO is clearly seen as a steep drop in the red curve (Fig. 23R), while the highest amount of synchronous release is found in Unc13A$^{FL\ GFP}$ with EGTA (green line).

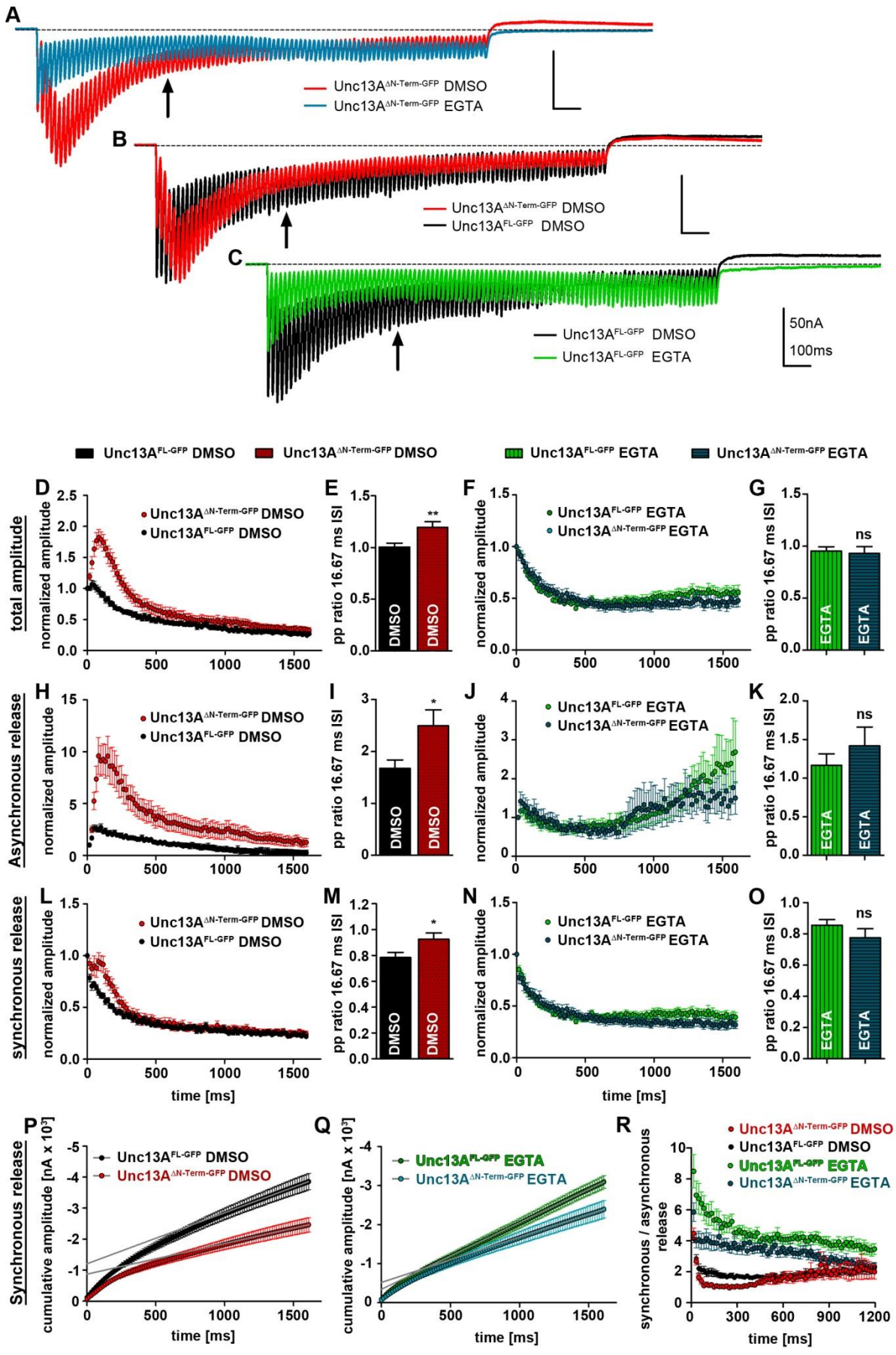


Figure 23 **Unc13A$^{\Delta N\text{-term}}$ has Augmented Asynchronous Release which is Abolished by EGTA Treatment.**

(A-C) Representative average eEJC traces of 60 Hz trains with 100 APs with DMSO (control) and EGTA-AM treatment in *Unc13A*$^{FL\ GFP}$ (full length construct, control; black and green line, respectively) and *Unc13A*$^{\Delta N\text{-}term\ GFP}$ (red and blue line, respectively). (D-O) All amplitudes in the train were normalized to the first amplitude and plotted over time. The paired pulse ratio of the respective genotype and treatment are right to the normalized amplitude plots. The color code is described in (A-C); the diagrams show distinct components of release: the total amplitude with DMSO (without EGTA-AM; D, E) and with EGTA-AM (F, G); the asynchronous component of release with DMSO (without EGTA-AM; H, I) and with EGTA-AM (J, K); and the synchronous component of release with DMSO (without EGTA-AM; L, M) and with EGTA-AM (N, O). The asynchronous component (H-K) is efficiently decreased by EGTA-AM treatment. However, the increasing error bars towards the end of the train in (J) suggests, that the $Ca^{2+}$ buffer might be consumed during the train, leading to reduction in $Ca^{2+}$ buffering efficiency. The quantifications can be found in Table 6 below. (P; Q) The cumulative plot of synchronous amplitudes shows an unchanged readily releasable pool (Y-intercept) upon EGTA treatment, the refilling of SVs during the train is reduced upon loss of the Unc13 N-term (please compare in (P) the slope of the linear fit between the black and red curve). Quantification: in (P) slope *Unc13A*$^{FL\ GFP}$ with DMSO (black) = -1.646 ± 0.5474, slope *Unc13A*$^{\Delta N\text{-}term\ GFP}$ with DMSO (red) = -0.9876±0.4923; Y-intercept *Unc13A*$^{FL\ GFP}$ with DMSO (black) = -1205±796.8 nA, Y-intercept *Unc13A*$^{\Delta N\text{-}term\ GFP}$ with DMSO (red) = -872±716.7 nA; in (Q) slope *Unc13A*$^{FL\ GFP}$ with EGTA (green) = -1.710 ± 0.2373, slope *Unc13A*$^{\Delta N\text{-}term\ GFP}$ with EGTA (blue) = -1.164 ± 0.3291; Y-intercept *Unc13A*$^{FL\ GFP}$ with EGTA (green) = -336.8±336.1 nA, Y-intercept *Unc13A*$^{\Delta N\text{-}term\ GFP}$ with EGTA (blue) = -512.8±446.0 nA. (R) The ratio of synchronous to asynchronous release clearly shows the reducing effect of EGTA-AM on asynchronous release by shifting the values to considerably higher values in the EGTA-treated groups. Statistics: t test. All panels show mean ± SEM; n.s., not significant; *, $p \leq 0.05$; **, $p \leq 0.01$; ***, $p \leq 0.001$. The bath solution contained 2.5mM $Ca^{2+}$.

**Table 6: Quantification of the Paired Pulse Ratio with 16,67ms Interstimulus Interval (ISI) in Unc13A$^{FL\ GFP}$ and Unc13A$^{\Delta N\text{-}term\ GFP}$, With DMSO and EGTA Treatment, Respectively.**

| **paired pulse ratio (16 ms ISI)** | | | | |
|---|---|---|---|---|
| | **control (n)** | **mutant (n)** | **P** | **(test)** |
| **total amplitude** | | | | |
| **DMSO (Fig. 23E)** | 1.004±0.0378 (13) | 1.196±0.0542 (13) | ≤0.01** | (t- test) |
| **EGTA-AM (Fig. 23G)** | 0.952±0.0411 (11) | 0.931±0.0640 (13) | n.s. | (t- test) |
| **asynchronous release** | | | | |
| **DMSO (Fig. 23I)** | 1.676±0.1615 (13) | 2.493±0.309 (12) | ≤ 0.05* | (t- test) |
| **EGTA-AM (Fig. 23K)** | 1.167±0.1478 (11) | 1.417±0.243 (13) | n.s. | (t- test) |
| **synchronous release** | | | | |
| **DMSO (Fig. 23M)** | 0.784±0.0382 (13) | 0.925±0.0488 (13) | ≤ 0.05* | (t- test) |
| **EGTA-AM (Fig. 23O)** | 0.854±0.0367 (11) | 0.774±0.0584 (13) | n.s. | (t- test) |
| **Cumulative synchronous release: Y-intercept of linear fit** | | | | |
| **DMSO (Fig. 23P)** | -1205.0±796.8 (13) | -872.0±716.7 (13) | n.s. | (t- test) |
| **EGTA-AM (Fig. 23Q)** | -336.8±336.1 (11) | -512.8±466.0 (13) | n.s. | (t- test) |

Notably, EGTA treatment alters the ratio of synchronous to asynchronous release in Unc13A$^{\Delta N\text{-}term\ GFP}$ massively (compare red and blue values), but also in Unc13A$^{FL\ GFP}$ the ratio is tremendously influenced by EGTA treatment (compare black and green values). In both cases, the reduction of the asynchronous component shifts the ratio to 3-fold higher values. In summary, the loss of the N-term of Unc13 leads to an increase in asynchronous release, which can be restored by EGTA treatment. The most likely conclusion is that the N-term of Unc13 is necessary to restrict the localization of Unc13 to specific sites in the cytomatrix at the AZ, and in consequence, the Unc13 N-term defines the sites of SV docking. This ensures the necessary coupling distance at the larval NMJ for stimulus-adapted transmitter release.

### 4.2.4. The N-term Of Unc13 Determines The Site of Synaptic Vesicle Fusion

Analysis of synaptic transmission revealed an increase in asynchronous release and altered spatial arrangement of docked SVs. We were curious whether this observation directly influences the release kinetics at Unc13 N-term deficient synapses. A magnification of the normalized first and 30$^{th}$ amplitude, which is labeled with arrow in Fig. 23A-C, clearly shows a genotype-specific alteration in the time-to-peak (Fig. 24A-F). In the first amplitude, the release was immediate and directly coupled to the stimulus in all genotypes (Fig. 24A-C). However, after the 30$^{th}$ stimulus the release was slightly delayed in the untreated (DMSO) Unc13A$^{FL\ GFP}$, but massively delayed in the untreated (DMSO) Unc13A$^{\Delta N\text{-term GFP}}$ (Fig. 24D). Incubation with EGTA reduced asynchronous release and restored the immediate release directly after the stimulus, to even higher levels than in untreated (DMSO) Unc13A$^{FL\ GFP}$ (Fig. 24E, F). This effect becomes even clearer in the comparison between untreated (DMSO) Unc13A$^{\Delta N\text{-term GFP}}$, and control and Unc13A$^{\Delta N\text{-term GFP}}$ incubated with EGTA (Fig. 24F), where the time to peak in Unc13A$^{\Delta N\text{-term GFP}}$ with EGTA treatment was just as fast as Unc13A$^{FL\ GFP}$ with EGTA. Any delay in the mutant concerning the time-to-peak was completely abrogated upon EGTA treatment. The quantification of the time-to-peak (Fig. 24G) showed no significant difference in the first stimulation upon EGTA-treatment, though there was a small but significant difference between untreated (DMSO) Unc13A$^{FL\ GFP}$ and Unc13A$^{\Delta N\text{-term GFP}}$ (upper panel). However, after the 30$^{th}$ stimulus (lower panel) a significant delay in the time-to-peak in untreated Unc13A$^{\Delta N\text{-term GFP}}$ compared to untreated Unc13A$^{FL\ GFP}$ was found, which could be restored to EGTA-treated Unc13A$^{FL\ GFP}$ levels with EGTA incubation. The $Ca^{2+}$ buffer led to a highly significant reduction of the time-to-peak in the Unc13A$^{\Delta N\text{-term GFP}}$ mutant resulting in a wild type-like performance. When the time to peak is plotted over the whole train (Fig. 24H), it becomes clear that the shift in the time-to-peak in Unc13A$^{\Delta N\text{-term GFP}}$ could be observed over almost the whole length of the train. This prolonged time-to-peak was completely restored by the EGTA-incubation over the whole train down to wild type levels. The EGTA forces synchronization of the release, which can overrun the Unc13A$^{\Delta N\text{-term GFP}}$ deficiency probably caused by its high mobility. The effect of EGTA in reducing asynchronous but not synchronous release also had clear impact on amplitude size after the first stimulus in untreated (DMSO) compared to treated Unc13A$^{FL\ GFP}$ cells (Fig. 24I, upper panel, compare black and green bar).

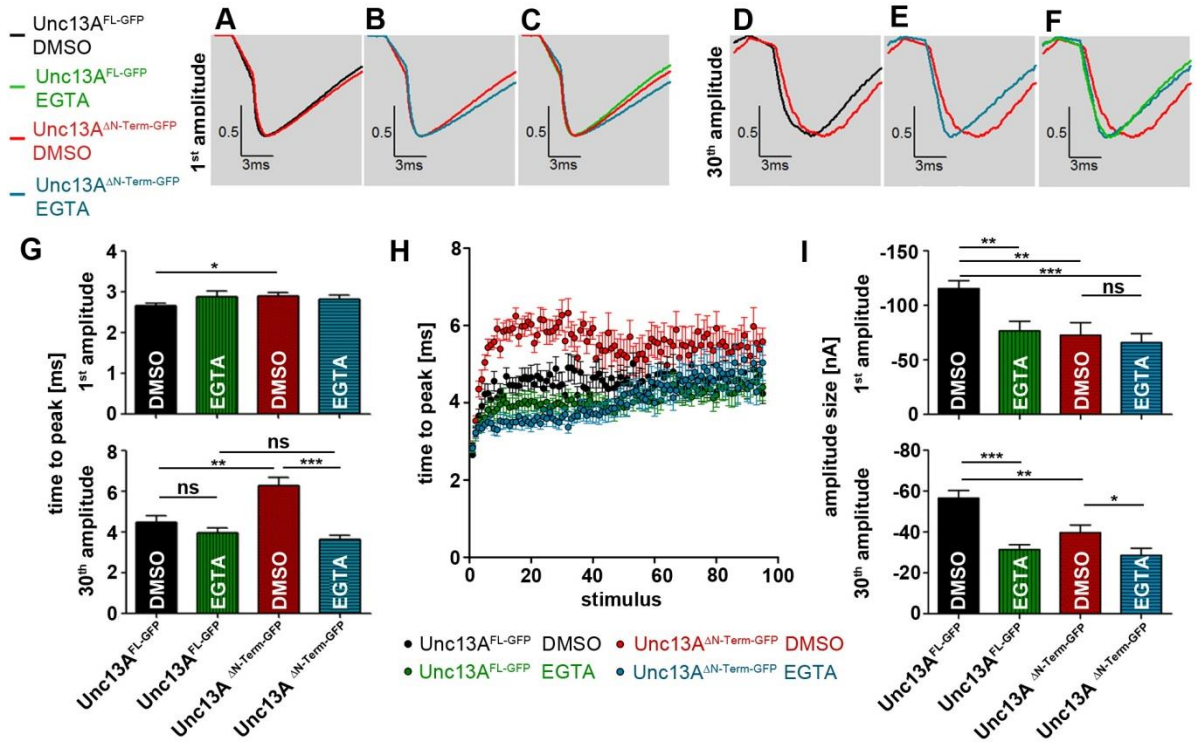


Figure 24 **The High Amount of Asynchronous Release Leads to a Pronounced Shift in the Time to Peak in *Unc13A*$^{\Delta N\text{-term GFP}}$ During the Train, Which can be Completely Abolished by EGTA-AM Treatment.**
(A-F) Representative average eEJC amplitudes of first stimulus (A-C) and the 30th stimulus (D-F) of the train with DMSO and EGTA-AM treatment in *Unc13A*$^{FL\ GFP}$ (full length construct, control; black and green line, respectively) and *Unc13A*$^{\Delta N\text{-term GFP}}$ (red and blue line, respectively). (G) The time to peak is only slightly increased in *Unc13A*$^{\Delta N\text{-term GFP}}$ without EGTA after the first stimulus (upper panel, compare black and red bar); after the 30th stimulus (lower panel), the time to peak is significantly increased in *Unc13A*$^{\Delta N\text{-term GFP}}$ without EGTA treatment compared to *Unc13A*$^{FL\ GFP}$ without EGTA (Compare black and red bar). Please note the rescue of the delayed time to peak by EGTA treatment (blue bar) to a level even faster than wild type (black bar). (H) The time to peak plotted over the whole duration of the train clearly shows the potential of EGTA to rescue the delay in the time to peak (compare red and blue dots). However, the $Ca^{2+}$ buffer seems to be consumed during the train, as the time to peak in *Unc13A*$^{\Delta N\text{-term GFP}}$ without EGTA (blue dots) starts to rise again towards the end of the train. Quantifications can be found in Table 7 below. (I) The amplitude size is significantly reduced in *Unc13A*$^{\Delta N\text{-term GFP}}$ compared to *Unc13A*$^{FL\ GFP}$ and cannot be reduced further by EGTA treatment (upper panel, compare red and blue bar); *Unc13A*$^{\Delta N\text{-term GFP}}$ is not sensitive to the $Ca^{2+}$ buffer EGTA after the first stimulus. However, after the 30th stimulus, EGTA treatment has a slightly decreasing effect on the eEJC amplitude size in *Unc13A*$^{\Delta N\text{-term GFP}}$ (lower panel). In *Unc13A*$^{FL\ GFP}$, EGTA is reliably reducing the eEJC amplitude size at any stimulus of the train (compare black and green bar). Quantifications can be found in Table 7 below. Statistics: t test. All panels show mean ± SEM; n.s., not significant; *, $p \leq 0.05$; **, $p \leq 0.01$; ***, $p \leq 0.001$. The bath solution contained 2.5mM $Ca^{2+}$.

**Table 7: Quantification of the Time to Peak and Size of the First eEJC Amplitude *Unc13A*$^{FL\ GFP}$ and *Unc13A*$^{\Delta N\text{-term GFP}}$ with DMSO and EGTA Treatment, Respectively.**

| time to peak (ms) (Fig. 24G) | DMSO | EGTA-AM | P | (test) |
|---|---|---|---|---|
| **1st eEJC** | | | | |
| *Unc13A*$^{FL\ GFP}$ | 2.654±0.0666 (13) | 2.864±0.1473 (11) | n.s. | (t- test) |
| *Unc13A*$^{\Delta N\text{-term GFP}}$ | 2.892±0.0843 (13) | 2.823±0.0878 (13) | n.s. | (t- test) |
| **30th eEJC** | | | | |
| *Unc13A*$^{FL\ GFP}$ | 4.477±0.3165 (13) | 3.936±0.2390 (11) | n.s. | (t- test) |
| *Unc13A*$^{\Delta N\text{-term GFP}}$ | 6.269±0.3921 (13) | 3.631±0.1889 (13) | ≤0.001*** | (t- test) |
| **amplitude size (nA) (Fig. 24I)** | | | | |
| **1st eEJC** | | | | |
| *Unc13A*$^{FL\ GFP}$ | -115.3±7.052 (13) | -76.38±8.949 (11) | ≤0.01** | (t- test) |
| *Unc13A*$^{\Delta N\text{-term GFP}}$ | -72.57±11.46 (13) | -65.72±8.236 (13) | n.s. | (t- test) |
| **30th eEJC** | | | | |
| *Unc13A*$^{FL\ GFP}$ | -56.48±3.773 (13) | -31.38±2.307 (11) | ≤0.001*** | (t- test) |
| *Unc13A*$^{\Delta N\text{-term GFP}}$ | -39.66±3.727 (13) | -28.57±3.457 (13) | ≤ 0.05* | (t- test) |

Surprisingly, EGTA had no significant effect on the size of the first amplitude in Unc13A$^{\Delta N\text{-term GFP}}$. Here, the first amplitude of untreated (DMSO) cells was significantly reduced compared to Unc13A$^{FL\ GFP}$ and was not further diminished by EGTA incubation. However, the amplitude size after the 30$^{th}$ stimulus was affected by EGTA in Unc13$^{FL\ GFP}$ as well as in Unc13A$^{\Delta N\text{-term GFP}}$ compared to untreated (DMSO) cells (Fig. 24I, lower panel). This suggests the high mobility of Unc13 lacking the N-term is probably unable to prime release-ready SV efficiently in a sufficiently small distance to the $Ca^{2+}$ source, which is in line with the insensitivity to EGTA, the small amplitude size in the first stimulus in Unc13A$^{\Delta N\text{-term GFP}}$ cells and the high amount of asynchronous release in Unc13A$^{\Delta N\text{-term GFP}}$.

The proteins found to be essential for SV fusion are the SNARE proteins, (M)Unc13 and (M)Unc18 (Ma et al., 2013). The SNARE protein in the plasma membrane Syntaxin-1A as well as (M)Unc18 are enriched at AZs, but their localization is not restricted to those sites. They are rather distributed over the whole neuronal membrane (C. Ma et al., 2013; Romero et al., 2008; Ullrich et al., 2015; Weimer et al., 2003). Thus, we conclude that Unc13 is the sole determinant to physically define the SV release sites.

## 4.3. In *brp$^{nude}$* the Synaptic Vesicle Refilling is Reduced, but Neither the Recovery Rate nor the Readily Releasable Pool is Altered

Unc13 is the major determinant for sites of docking and fusion of SVs at the plasma membrane. Its mutants show a severely altered distribution of docked synaptic vesicles and pronounced consequences in synaptic transmission. Another protein which influences the distribution of SV at AZs is BRP; upon loss of the last 17 amino acids at the C-term not the position of docked, but of T-Bar tethered SVs is changed. This allel of BRP called *brp$^{nude}$* (Ehmann et al., 2014; Hallermann et al., 2010). It has been shown that the T-Bar height and platform length is unchanged in *brp$^{nude}$*, also the total number of SV per bouton section was not altered. However, the T-Bar was bare of SVs, and the number of SV near the electron dense structure was significantly reduced (Hallermann et al., 2010). Furthermore, single eEJC amplitude were unaltered, but in short-term plasticity depression was observed in paired-pulse recordings and the recovery of the synaptic transmission at the NMJ was impaired. I was interested, if and how the altered location of the SV influence release kinetics in order to obtain a broader understanding how SV distribution at the AZ in general influences synaptic transmission. For the experiments, the *brp$^{nude}$* allel was brought in trans to the deficiency BSC29, as control served the heterozygous deficiency, to rule out a possible influence by the large deletion in BSC29. In Hallermann et al. (2010) 1 mM

external $Ca^{2+}$ concentration was applied to the bath solution. Here, 2.5 mM $Ca^{2+}$ was applied to the bath in order to reliably empty the RRP. Using the published concentration of 1 mM $[Ca^{2+}]_{ex}$ did not reliably deplete the readily releasable pool, which is a necessary precondition for e.g. the RRP size estimation by back-extrapolation in a cumulative plot (reviewed in Neher, 2015; Ralf Schneggenburger et al., 1999). In my recordings, single eEJCs were unchanged in *brp*$^{nude}$, (Fig. 25A), the amplitude size of the first eEJC of a train recording was not significantly different in *brp*$^{nude}$ compared to *control* (Fig. 25B, please note the first data point). However, in the course of trains the amplitude size was decreased in *brp*$^{nude}$, the paired-pulse ratio of the first two eEJCs of the train revealed a significant depression in *brp*$^{nude}$ compared to *control* (Fig. 25C). The parameters of single exponential fit to the decreasing amplitudes between 0 and 1000 s showed a slight but significant different in the decay (Fig. 25D, E). The significantly reduced plateau-value for *brp*$^{nude}$ reflects the reduced amplitudes during the train of the *brp*$^{nude}$ mutants (Fig. 25F). The lack of the last 17 amino acids in BRP seem to result in a deficit in maintaining release during sustained stimulation, probably due to a defect in the SV recruitment during the train. A possibly reduced refilling rate was read out in a cumulative plot of the train amplitudes (Fig. 25G), where the slope of a linear back-extrapolation reflects the refilling rate during the train, while the Y-intercept of the line represents the RRP size. Indeed, the forward priming rate is lower in *brp*$^{nude}$, the slope of the linear fit to the last 30 data points is significantly reduced in *brp*$^{nude}$. (Fig. 25H). Notably, the RRP has a comparable size in both groups, represented by the value of the Y-intercept of the linear fit (Fig. 25I). This is in line with i) previously published EM data, where no significant reduction in the number of docked SVs is reported (Hallermann et al., 2010), and ii) the unaltered amplitude size of single eEJCs in *brp*$^{nude}$ (Fig. 25A, B). Nonetheless, is it remarkable that the refilling, but not the RRP is different in *brp*$^{nude}$ compared to *control*, as one could assume a hampered forward priming rate generally impairs SV recruitment, placement and thus docking and priming. In a second experiment, the SV recruitment during recovery after synaptic depression was investigated, to check whether the SV recruitment in the recovery phase after a train stimulation is diminished as well. This was analyzed in a recovery protocol, where the SV recruitment to the RRP after the train is monitored over time. Single stimuli at increasing time intervals after the train (25ms, 50ms, 100ms, 200ms, 500ms, 1s, 2000, 5s, 10s, 20s, 50s, and 100s (Wu et al., 2005)) are given. The growing amplitude size with increasing interstimulus-intervals serves as an indicator for the recovery rate of the synapse. It was published that a biphasic recovery from depression was identified, consisting of a fast and a slow recovery component. For *brp*$^{nude}$, a decreased time constant for fast recovery was reported while the second, slow recovery component was unaltered (Ehmann et al., 2014; Hallermann et al., 2010). In

my recordings, however, the published values for synaptic recovery in *brp*$^{nude}$ could not be reproduced. Here, the time constants of the fast as well as the slow recovery component were comparable between both groups (Fig. 25J, K), though in *brp*$^{nude}$ the amplitude size in the small ISIs is still smaller than in the *control* (Fig. 25K). This is presumably the consequence of the smaller steady state amplitudes during train. In summary, *brp*$^{nude}$ compared to *control* exhibited a reduced forward priming rate, the SV recruitment after depression during the train was not diminished. Hence, the last 17 amino acids at the C-term of BRP are likely necessary to maintain the constant delivery of SV during sustained release.

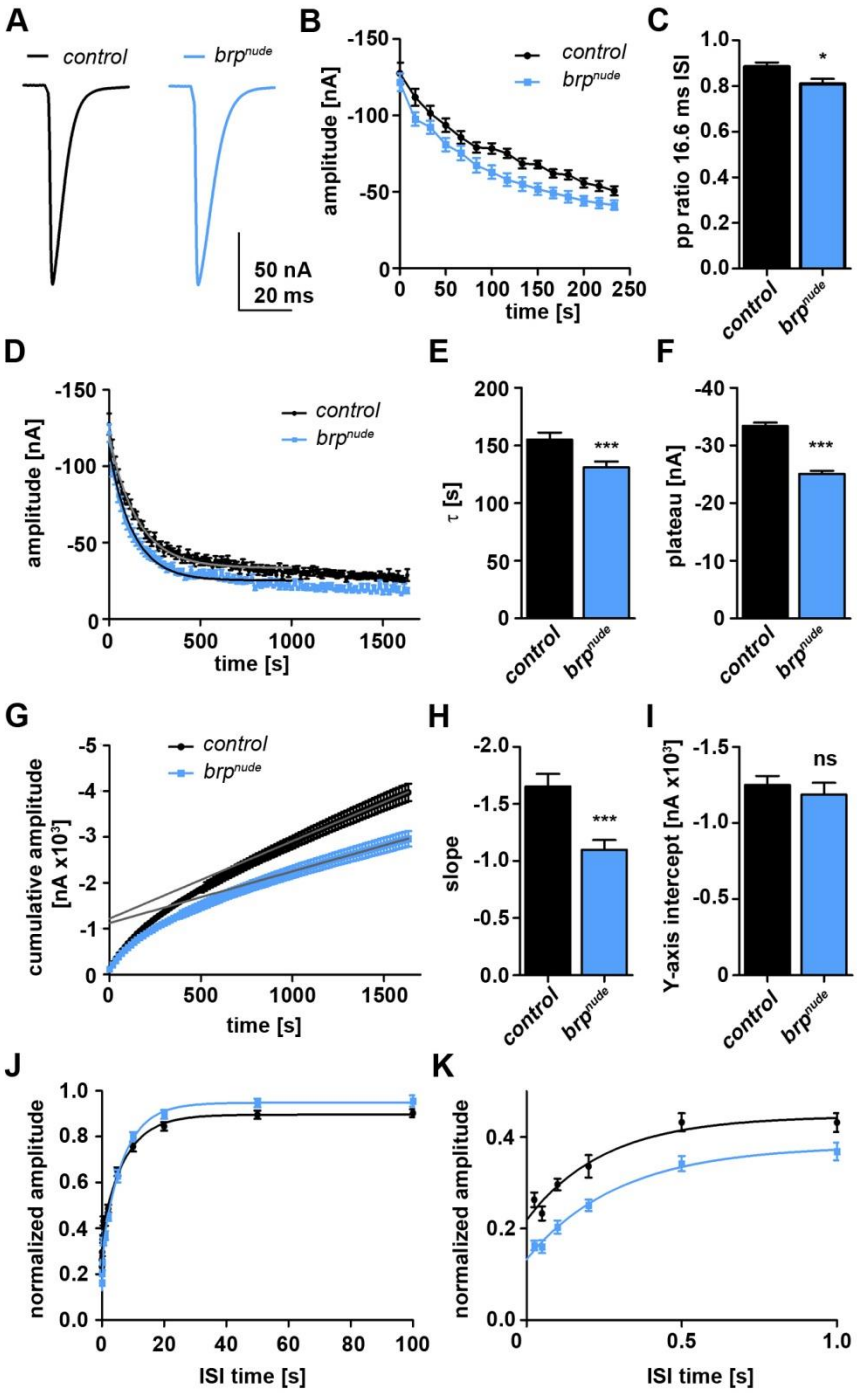


Figure 25 ***brp$^{nude}$* Shows a Deficit in Synaptic Vesicle Refilling During Sustained Release.**

(A) Representative eEJC traces for *control* (black) and *brp$^{nude}$* (light blue). (B) Display of the first 250 ms of a 60 Hz train with 100 stimuli shows a clear difference in rate of amplitude reduction between the two groups (*control*: black, *brp$^{nude}$* light blue). (C) *brp$^{nude}$* shows a depression in short-term plasticity, the paired pulse ratio between the first two amplitudes of the train was analyzed. (D) The decay in amplitude size during the train was fitted with a single exponential curve and is more drastic in *brp$^{nude}$* compared to *control* (*control*: black, *brp$^{nude}$* light blue). (E) The quantification of the decay time clearly reveals a faster run-down in *brp$^{nude}$* compared to *control. S*ingle exponential fit in the range between 0-1000 s yields τ: *control* (n=16): 154.9±6.228 s; *brp$^{nude}$* (n=16): 131.0±4.968 s. (F) The amplitude size converges towards a plateau. Here the single exponential fit clearly reveals a significant decrease of the plateau value in *brp$^{nude}$* in comparison to *control*. Plateau: *control* (n=16): -33.36±0.1514 nA ; *brp$^{nude}$* (n=16): -25.07±0.1283 nA. (G) The cumulative plot of synchronous amplitudes shows no change in the readily releasable pool (Y-intercept of the linear fit) in *brp$^{nude}$*, but the forward priming rate of SVs during the train is reduced (slope of the linear fit).

(H, I) Quantification of the linear fit to the cumulatively plotted amplitudes. (H) Slope of *brp$^{nude}$* (light blue) is significantly reduced compared to *control* (black). Quantification: slope (*control)*=-1.653± 0.1089, slope (*brp$^{nude}$*) = -1.099±0.0839. (I) Y-intercept of *control* (black) = -1248±59.37 nA, Y-intercept of *brp$^{nude}$* (light blue) = -1185±77.54 nA. (J, K) Recovery of the amplitude size after depression during the sustained release in the train. Two recovery components, a fast and a slow one, could be identified. There is no difference in both recovery components in *brp$^{nude}$*. Quantification (J) slow recovery, $\tau_{slow}$(*control*)= 5.376±0.437 s, $\tau_{slow}$(*brp$^{nude}$*)=5.343±1.351 s; (I) fast recovery, $\tau_{fast}$(*control*)=0.2508±0.0921 s, $\tau_{fast}$(*brp$^{nude}$*)= 0.2974±0.0802 s.

## 4.4. Towards the Ultrastructural Identification of SV Fusion Sites and Recycling Activity at Individual AZs

A strong indication for distinct release sites can be concluded from the Unc13 results, and motivated me to find and visualize the fusion sites on an ultrastructural level. Hence, flash-freeze experiments were performed, where the samples were vitrified and kept in their native state milliseconds after the induction of synaptic activity. The sites of SV fusion and following recycling events at AZs were investigated with electron microscopy. The experimental setup described in Watanabe, Liu, et al., 2013 and Watanabe, Rost, et al., 2013 combines an LED lamp with a high pressure freeze machine and allows optogenetic nerve stimulation and rapid subsequent high pressure freezing of the sample only milliseconds after the light stimulation. The experimental design was adjusted to freeze *all-trans* retinal fed *Drosophila* larvae, which is the co-factor for protein Channelrhodopsin (ChR), a light-inducible non-selective cation channel that is very sensitive to light stimulation at 480 nm wavelength. A UAS-construct with a variant of ChR2 with higher light sensitivity and slower desensitization called ChR-H134R (Pulver et al., 2009) is expressed in motoneurons with the driver-line ok6-Gal4. To confirm the functionality of the light-evoked nerve stimulation, two-electrode voltage clamp recordings at the 3$^{rd}$ instar larval NMJ were performed (Fig. 26). The light of a triggerable monochromatic LED light source with 480 nm wavelength was coupled into the microscope stand of the TEVC setup. Alternating electrically and light evoked amplitudes shows that light stimulation just as electrical stimulation lead to reproducible and reliable synaptic transmission (Fig. 26A). In a light power titration experiment the minimal necessary light power to evoke a junctional current was measured, to ensure the applied light power of the LED is sufficient to reliably evoke synaptic transmission (Fig. 26B). 3 mW/mm$^2$ is required to induce EJCs in 100% of the cells; in the HPF setup, the maximal light power of 4mW/mm$^2$ is applied, synaptic transmission will certainly be induced. In addition, light-evoked paired pulse recordings were possible (Fig. 26C). The amplitude size of light-evoked EJC is slightly but significantly smaller compared to electrically evoked EJC amplitudes (Fig.26D), while the decay and rise time of the amplitude (Fig. 26E and F) is unchanged. Thus, we can be sure that in the freezing chamber synaptic vesicle fusion will be induced before the larvae are rapidly frozen. In electron micrographs of non-stimulated NMJs, SVs can be observed to be docked to the plasma membrane (Fig. 27Ai, black arrow head), linked to the membrane with a filamentous structure (Fig. 27Ai, red arrow heads) or connected to the electron-dense T-bar at the larval NMJ (Fig. 27Ai, red arrows). In rare cases, large and clear vesicular structures can be found to be close to the T-bar or are even connected to it (Fig. 27Aii, arrow head). They resemble endocytic structures, and their presence might increase after light induced synaptic transmission and subse-

quent recycling. Upon light stimulation, large invaginations and large and clear vesicular structures can be frequently observed in the periactive zone (Fig. 27B, i-iii). Interestingly, they are devoid of Clathrin.

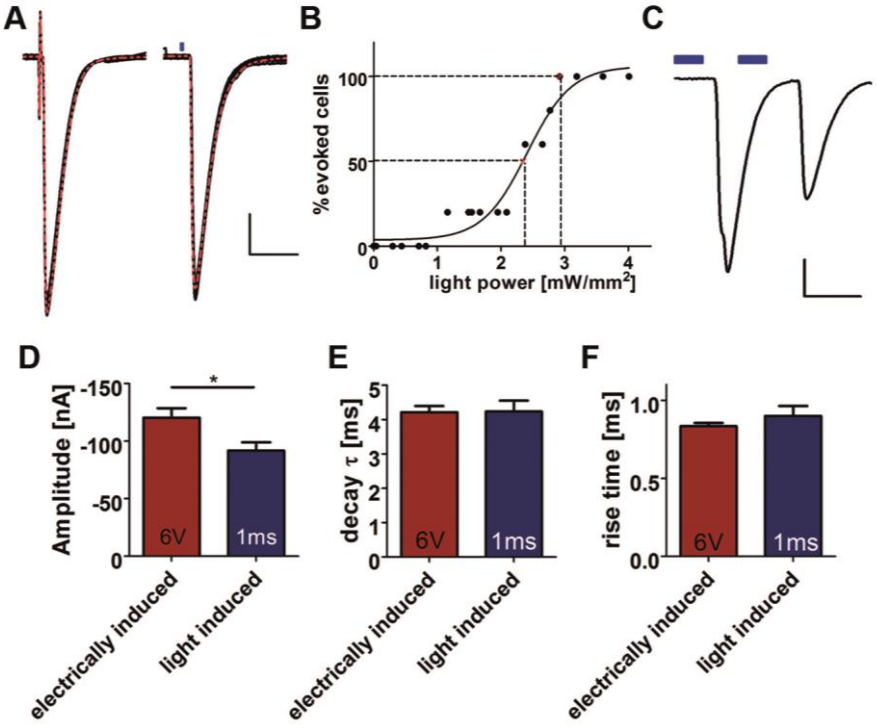


Figure 26 **Electrophysiological Properties of Light Induced eEJCs with ChR2-H134R.**
(A) Alternating electric (6V) and optic stimulation (1ms, 480nm) at 0.2Hz, recorded in the same cell (n=7). Electric stimulation can be identified by the stimulation artifact. Scale: 20 nA, 20ms (B) Light intensity ramp recording to identify the minimal necessary light intensity which reliably evokes synaptic transmission. At the intensity of 3 mW/mm2 100% of the cells are reacting to the light stimulus. Boltzmann sigmoidal fit. Dashed lines indicate 50% and 100% of cells responding to the light stimulus (n=5). (C) Representative trace of a paired pulse stimulation with 10 ms interstimulus interval (5ms light). The light-evoked amplitudes each refer to an individual light pulse. Scale: 10ms, 10nA. (D-F) Analysis of the eEJC traces corresponding to light and electrically induced amplitudes, concerning size (D) and kinetics of the amplitudes (E, F). No significant difference in decay (E) and rise time (F) between optically and electrically induced EJCs can be observed. Though the light-induced amplitude sizes differ from electrically induced amplitudes, the kinetics are comparable. Quantification: amplitude size electrical. stim. (n=10) =-120.2±8.306 nA, light stim. (n=10)=-91.51±7.362 nA; decay electrical. stim. (n=7)= 4.213±0.1823 ms, light stim. (n=7) 4.237±0.316 ms; rise time electrical. stim. (n=6) 0.833±0.021 ms, light stim. (n=6) 0.900±0.063 ms. All recordings were performed in HL3.1 with 1.5mM $Ca^{2+}$ in 3rd instar larvae raised on normal food containing 1mM all-Trans Retinal. Statistics: Mann-Whitney-U-Test. All panels show mean ± SEM; n.s., not significant; *, $p \leq 0.05$; **, $p \leq 0.01$; ***, $p \leq 0.001$.

This is in line with recent findings by Watanabe et al., who describe another ultrafast mode of endocytosis in *C. elegans* as well as in hippocampal cell culture (Watanabe, Liu, et al., 2013; Watanabe, Rost, et al., 2013). Nonetheless, Clathrin was found to be crucial in later steps of the recycling pathway (N. L. Kononenko & Haucke, 2015). With a stimulation protocol where extended light stimulation was applied, a massive increase in the number of large vesicular compartments could be observed (Fig. 27C, i and ii). This is an indication that the large clear compartments are indeed endocytic structures and are part of the membrane recycling pathway. However, despite of great efforts in the establishment and extensive usage of various stimulation protocols (e. g. light train with diverse stimulation lengths and /or delays before freezing,

single light pulses of different lengths and / or delays before freezing) it was not possible to capture SV exocytosis at the AZ.

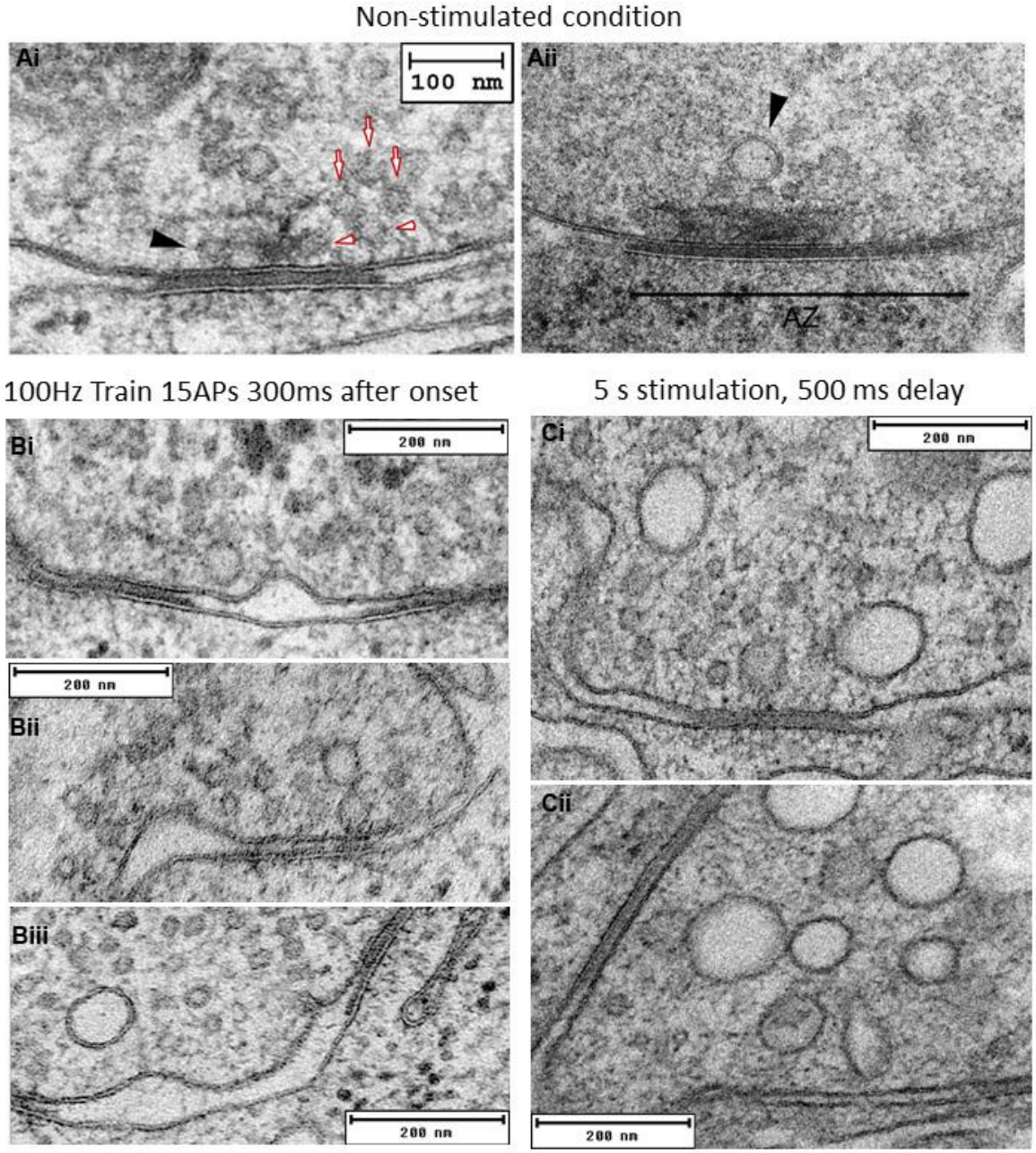


Figure 27 **Flash-Freeze Experiments Showing Optogenetically Induced Endocytic Events can be Observed in Electron Micrographs.**
High pressure freeze embedded NMJs of all-trans Retinal- fed animals expressing ChR2-H134R in motoneurons. (Ai) Without light stimulation, SVs (examples marked with red arrows) can be found in special positions where they are docked (black arrow head) or tethered to the plasma membrane (red arrow heads). (Aii) Occasionally, large and clear membrane compartments resembling endosomes (black arrowhead) can be found close to the T-Bar or near AZs. (Bi-iii) After optogenetic stimulation with 15 pulses at 100Hz and 150ms delay before freezing clear endosome-like membrane compartments together with large membrane invaginations adjacent to AZ are observed. Notably, neither the invaginations nor the clear membrane compartments are coated with Clathrin. (C) After prolonged and intense light stimulation, the number of clear membrane compartments is massively increased; often the endosome-like were observed to be close to AZs.

## 4.5. Identification of Novel Synaptic Proteins at the Active Zone

The light stimulated HPF embeddings for electron microscopy and especially the *in vivo* $Ca^{2+}$-imaging experiments demonstrate that the contribution of a single AZ to the total amount of transmitter release at the larval NMJ varies massively and can be very little at the level of an individual AZ. An extensive loss of function screen was conducted to identify novel players at the AZ influencing synaptic transmission. Though many proteins known to be important for transmitter release have been described (Südhof, 2012; Südhof, 2013), the cytomatrix at the AZ is a very complex and dense structure with a plethora of proteins of various functions. In order to discover yet unknown proteins which are essential for synaptic transmission, a novel method developed 2011 in the Sigrist lab for purification of exclusively presynaptic AZ-membrane and the attached cytomatrix was utilized (Depner et al., 2014). The enriched proteins of the AZs were directed to mass spectrometry analysis and resulted in a detailed list of proteins, amongst which already known proteins appeared on high ranks (sorted by abundance), like dSyd-1 on the fifth rank, Nrx1 on the 20th and RBP on the 22nd rank (see Table 8). Other proteins from ranks not lower than 200 and yet completely undescribed beside *in silico* domain predictions were selected for a RNAi-based loss-of-function screen employing the GAL4/UAS system for nervous system specific gene knock-down. UAS-RNAi-lines were ordered from the *Vienna Drosophila RNAi center* (VDRC), which offers different collections of lines expressing RNAi directed against most genes described in *Drosophila melanogaster*. Behavioral (larval and adult locomotion) and electrophysiological (electroretinography, ERG) high-throughput assays were utilized to investigate possible defects in synaptic transmission upon the knock-down of a candidate gene. Furthermore, the NMJ morphology was examined by fluorescence light microscopy. Candidates with phenotypic anomalies were analyzed in TEVC recordings at the larval NMJ and possible ultrastructural aberrations were investigated with electron microscopy. In the screen, the knock-down of the synaptic PI4-Kinase

**Table 8: List of Proteins Located at the *Drosophila* Active Zone, Sorted by Abundance in Mass Spectrometry Analysis.**

| # | Identified Proteins (785) | Name | CG-Number | Molecular Weight |
|---|---|---|---|---|
| 1 | **bruchpilot**, isoform G | **BRP** | CG42344 | 207 kDa |
| 2 | still life, isoform F | Sif | CG42344 | 295 kDa |
| 3 | alpha-spectrin | α-Spec | CG1977 | 278 kDa |
| 4 | beta spectrin | β-Spec | CG5870 | 266 kDa |
| 5 | RhoGAP100F, isoform C | **DSyd-1** | CG1976 | 197 kDa |
| 6 | FI02017p | CASK-RB | CG6703-RB | 101 kDa |
| 7 | ninaC long protein | ninaC | CG5125 | 174 kDa |
| 8 | CG42795, isoform A | | CG42795 | 359 kDa |
| 9 | CG34306 | | CG34306 | 406 kDa |
| 10 | Comatose | DNSF | CG1618 | 83 kDa |
| 11 | DNA fragmentation factor-related protein 2, isoform B | **Drep-2** | CG1975 | 58 kDa |
| 12 | stress-sensitive B, isoform A | sesB | CG16944 | 33 kDa |
| 13 | mind-meld, isoform D [ | mmd | CG42252 | 160 kDa |
| 14 | myosin heavy chain, isoform B | Mhc | CG17927 | 224 kDa |
| 15 | unc-13, isoform B | **dunc-13** | CG2999 | 360 kDa |
| 16 | Na pump alpha subunit, | Atpα | CG5670 | 111 kDa |
| 17 | actin 5C, isoform B | Act5C | CG4027 | 42 kDa |
| 18 | GH07902p | TM4SF | CG11303 | 25 kDa |
| 19 | plasma membrane calcium ATPase, isoform I | PMCA | CG42314 | 133 kDa |
| 20 | neurexin 1, isoform A | **Nrx1** | CG7050 | 199 kDa |
| 21 | hu li tai shao, isoform I | hts | CG9325 | 79 kDa |
| 22 | CG43073, isoform G | **RBP** | CG43073 | 191 kDa |

PI4KIIIα had a notable effect on synaptic transmission; furthermore a binding partner of Rab3 GEFs and GAPs called Rabconnectin-3B was identified to be relevant at the synapse.

### 4.5.1. The Role of Phosphatidylinositol-4 Kinase IIIα at the Synapse

Phosphatidylinositol-4-phosphate (PI(4)P) is a precursor for $PI(4,5)P_2$, which has an important role in synaptic vesicle fusion. Its effectors are CAPS (Jockusch et al., 2007), Unc13 (Shin et al., 2010; Südhof, 2012) and Synaptotagmin (Brose et al., 1992; Davletov & Südhof, 1993; Herrick et al., 2006; Park et al., 2015), which bind directly to $PI(4,5)P_2$ via PH-domains and have been reported to be crucial for SV fusion (Balakrishnan et al., 2015; Martin, 2015). Three PI4-Kinase genes have been annotated in the fly genome: four wheel drive (fwd; PI4KIIIβ) (Polevoy et al., 2009), CG2929 (PI4KIIα) (Raghu et al., 2009) and CG10260 (PI4KIIIα). The yeast homolog of PI4KIIIα, Stt4p, was shown to localize to patches on the plasma membrane where it is required for normal Actin cytoskeleton organization (Audhya et al., 2000). PI4KIIIα mutations have been reported to cause oocyte polarization defects, via a potential direct link between membrane composition and Hippo signaling. The Hippo signaling is mediating cell proliferation and apoptosis. Loss of PI4KIIIα might also have a Hippo-independent effect on Actin-based apical membrane structure (Yan et al., 2011). The product of PI4K catalyzed reaction is PI4P, which serves as substrate for the production of $PI(4,5)P_2$ in the plasma membrane (Di Paolo et al., 2004), which is functionally relevant for SV fusion at the AZ and endocytosis at the periactive zone (Haucke et al., 2011; Jahn & Fasshauer, 2012; Koch & Holt, 2012; Saheki & De Camilli, 2012).

In the RNAi-based knock-down screen I analyzed the NMJ morphology in immunofluorescence stainings, and the synaptic transmission in ERG recordings at the adult compound eye and in TEVC recordings at the larval NMJ. The knockdown of PI4KIIIα led to altered NMJ morphology, as can be seen in stainings against the presynaptic marker BRP and postsynaptic GluRIID-subunit (Fig. 28A, B). An increased amount of satellite boutons were found (white arrowheads), and the structure appeared generally irregular and misshapen. In ERG, the synaptic transmission at the eye was dramatically reduced in *PI4KIIIα knockdown (kd)* (Fig. 28 C). However, the conventional embedding for electron microscopy revealed no irregularities in larval NMJs at the ultrastructural level (Fig.28 D, E). The detailed analysis of synaptic transmission at the larval NMJ in TEVC revealed increased eEJC amplitudes in *PI4KIIIα kd* (Fig.28 F, G). In addition, the kinetics of the transmission were significantly altered, the rise time was increased while the decay was normal (Fig.28 H, I). The paired-pulse ratio as well as the mEJC analysis was not changed in *PI4KIIIα kd* (Fig.28 J-N). An explanation for the unexpected increase in eEJC amplitude and rise time could be an upregulation of an alternative precursor pathway in the production of $PI(4,5)P_2$, which

might overshoot upon knock-down of PI4KIIIα and lead to overcompensation of the lack in PI4K. However, this hypothesis is sheer speculation and needs to be tested in future experiments.

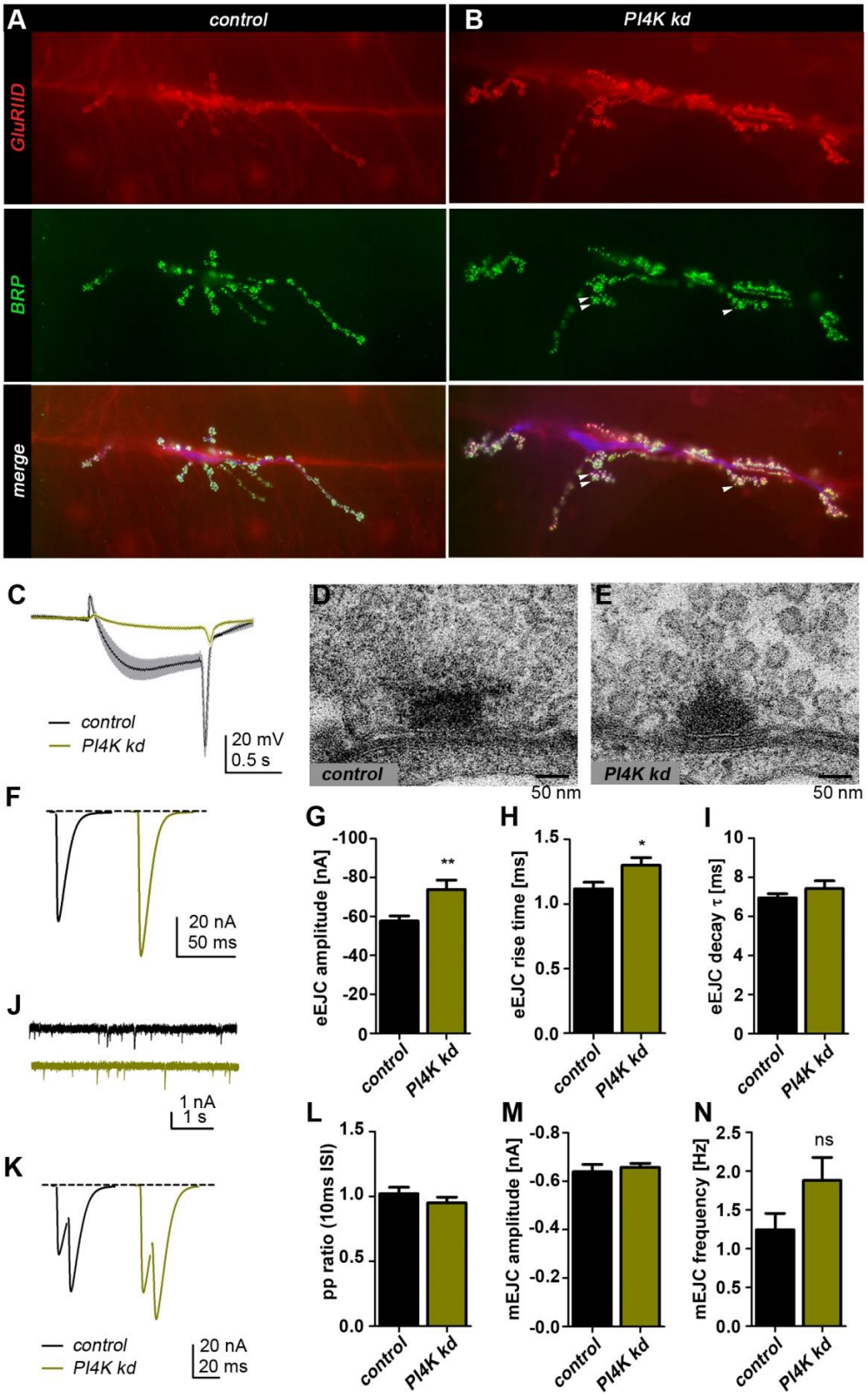


Figure 28 **RNAi-Based Knock-Down of PI4KIIIα.**
(A, B) In conventional epifluorescence microscopy, the knock-down of *PI4KIIIα* leads to an altered NMJ morphology, the genotypes indicated were stained with the indicated antibodies. (C) Flies lacking *PI4KIIIα* (knock-down) have a decreased synaptic transmission in the lamina (eye), measured in electroretinogram recordings which show a clear

reduction in the on- and off-transients of the trace. (D, E) Exemplary electron micrographs of *control* AZs and *PI4KIIIα kd* AZs show no abnormalities on the ultrastructural level. (F) Representative eEJC traces for *control* (black) and *PI4KIIIα kd* (light green). (G) The eEJC amplitude is increased upon reduction of PI4KIIIα. Quantification: *control* (n=12)= -57.63±2.595 nA, *PI4KIIIα kd* (n=9)= -73.82± 4.857 nA. (H) The eEJC rise time is prolonged in *PI4KIIIα kd*. Quantification: *control* (n=12)= 1.117± 0.05198 ms, *PI4KIIIα kd* (n=9)= 1.300± 0.05774 ms. (I) The decay of the amplitude is unchanged upon knock down of PI4KIIIα. Quantification: *control* (n=12)= 6.942± 0.2111 ms, *PI4KIIIα kd* (n=9)= 7.413± 0.4043 ms. (J) Representative mEJC traces for *control* (black) and *PI4KIIIα kd* (light green). (K) Representative paired pulse eEJC traces with 10 ms interstimulus interval (ISI) for *control* (black) and *PI4KIIIα kd* (light green). (L) The paired pulse ratio (10 ms ISI) is not altered in *PI4KIIIα kd* compared to *control.* Quantification: *control* (n=9)= 1.021± 0.049, *PI4KIIIα kd* (n=7)= 0.9354± 0.051. (M, N) mEJC amplitude size and frequency are not changed upon reduction of PI4KIIIα. Quantification mEJC amplitude (M): *control* (n=13)= -0.6385±0.0301 nA, *PI4KIIIα kd* (n=10)= -0.6570±0.0158 nA. Quantification mEJC frequency (N): *control* (n=10)= 1.243± 0.210 Hz, *PI4KIIIα kd* (n=10)= 1.881± 0.2959 Hz. All recordings were performed in HL3 with 1.5mM $Ca^{2+}$. Statistics: Mann-Whitney-U-Test. All panels show mean ± SEM; n.s., not significant; *, $p \leq 0.05$; **, $p \leq 0.01$; ***, $p \leq 0.001$.

### 4.5.2. The Role of Rabconnectin-3B at the Synapse

Rabconnectin-3B (Rbcn-3B) was found in the cell in a heterodimer with Rabconnectin-3A. The dimer was identified as binding partners of Rab3-GEF and Rab3-GAP in synaptic vesicle extracts of rat brain. The two proteins appear to form a stable complex, but the biochemical function of this complex remains unknown (Kawabe et al., 2003; Nagano et al., 2002). In the absence of Rbcn-3A and B, Notch and other membrane proteins accumulated in an aberrant late endosomal compartment. The observed endocytic defects in Rbcn-3A and B mutants were consistent with Rbcn-3 regulating V-ATPase activity, caused by defective Notch signaling. Rbcn-3 acts primarily through the regulation of V-ATPase function and thus reveal a functional connection between the vacuolar proton pump and Notch signaling (Yan et al., 2009). A specific role at the synapse is not described until now. Nonetheless, the knockdown of Rbcn-3B led to overgrown NMJs, which were completely unstructured and lost the typical "beads-on-a-string" morphology (Fig. 29A, B). *Rbcn-3B kd* had highly impaired synaptic transmission at the eye (Fig.29 C), though on the ultrastructural level no alterations were observed in electron micrographs of the NMJs after conventional embedding (Fig.29 D, E). TEVC recording at the larval NMJ showed however increased size and rise time of the amplitudes (Fig.29 F-H). The decay remained unaltered (Fig.29 I). Paired pulse recordings and mEJC analysis appeared normal (Fig.29 J-N). Why synaptic defects were observed particularly for Rbcn-3B, but not Rbcn-3A, remains enigmatic. Both proteins were found at the AZ and were part of the candidate list; however, a likely explanation could either be a different efficiency of the RNAi-knockdown, or that specifically Rbcn-3B is the functionally relevant part of the complex during interaction with Rab3-GEFs to fulfill its function at the synapse. Furthermore, it can only be speculated about the observation that *PI4KIIIα kd* as well as *Rbcn-3B kd* led to reduced synaptic transmission at the eye but increased eEJC amplitudes at the NMJ. The intensely analyzed model synapse at the NMJ and the synapses at the lamina in the eye are highly specialized types of synapses, serving obviously different functions in the nervous system. Different protein compositions and release behavior at different kind of synapses have been

reported earlier (reviewed in Eggermann et al., 2011), and loss of a specific protein at one type of synapse might have no or even the opposite consequence in another synapse type.

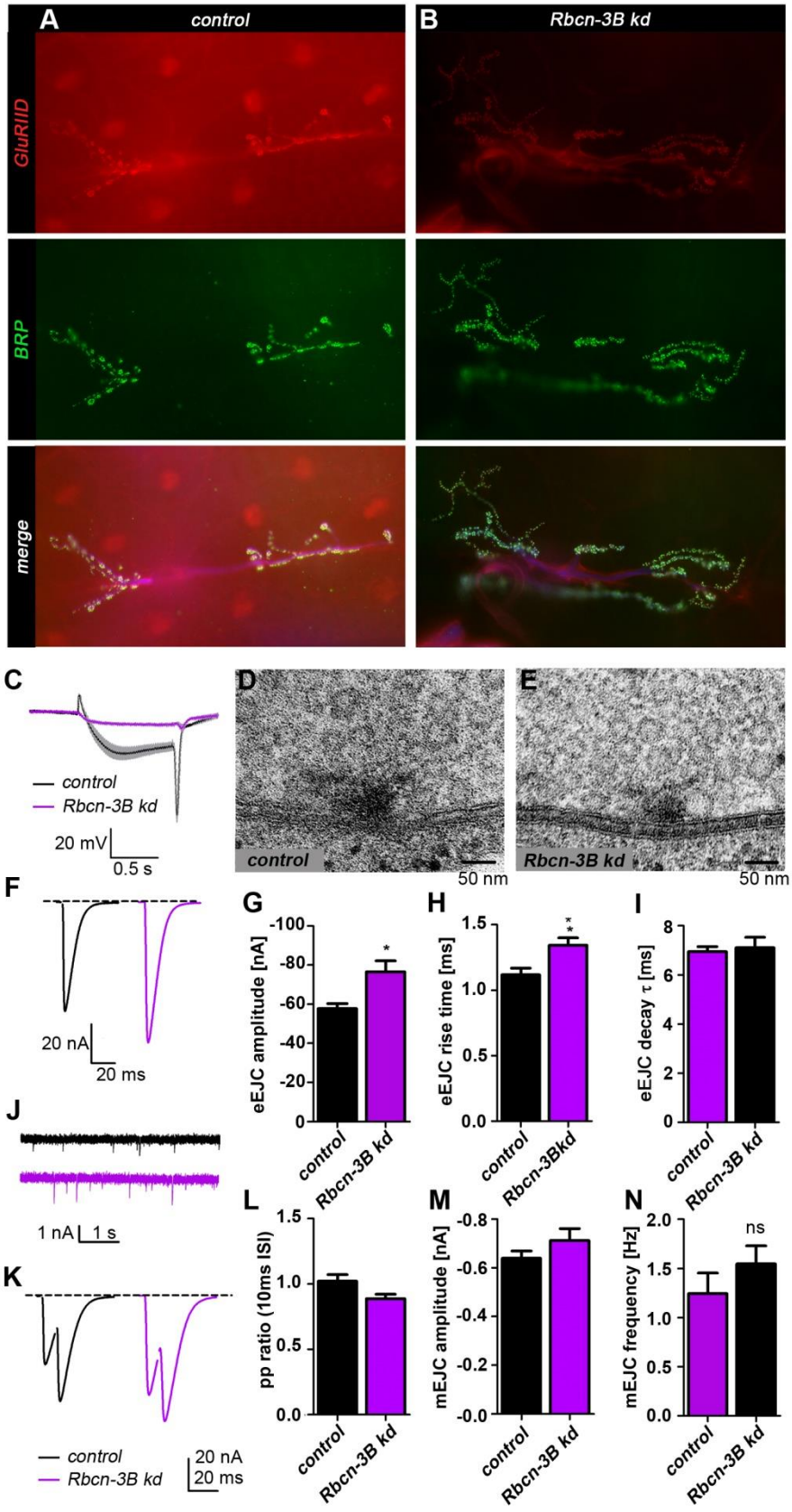


Figure 29 **RNAi-Based Knock-Down of Rabconnectin-3B.**
A, B) Knock-down of *Rbcn-3B* leads to an altered NMJ morphology, the genotypes indicated were stained with the indicated antibodies. (C) Flies lacking *Rbcn-3B* (knock-down) have a decreased synaptic transmission in the lamina (eye), measured in electroretinogram recordings which show a clear reduction in the on- and off-transients of the trace (*control*: black line, and *Rbcn-3B kd:* violet line). (D, E) Exemplary electron micrographs of *control* AZs and *Rbcn-3B kd* AZs show no abnormalities on the ultrastructural level. (F) Representative eEJC traces for *control* (black) and *Rbcn-3B kd* (violet). (G) The eEJC amplitude is increased upon reduction of Rbcn-3B. Quantification: *control* (n=12)= -57.63±2.595 nA, *Rbcn-3B kd* (n=7)= -73.82± 4.857 nA. H) The eEJC rise time is prolonged in *Rbcn-3B kd*. Quantification: *control* (n=12)= 1.117± 0.05198 ms, *Rbcn-3B kd* (n=7)= 1.343± 0.0571 ms. (I) The decay of the amplitude is unchanged upon knock down of Rbcn-3B. Quantification: *control* (n=12)= 6.942±0.2111 ms, *Rbcn-3B kd* (n=7)= 7.106±0.4240 ms. (J) Representative mEJC traces for *control* (black) and *Rbcn-3B kd* (violet). (K) Representative paired pulse eEJC traces with 10 ms interstimulus interval (ISI) for *control* (black) and *Rbcn-3B kd* (violet). (L) The paired pulse ratio (10 ms ISI) is not altered in *Rbcn-3B kd* compared

to *control.* Quantification: *control* (n=9)= 1.021± 0.049, *Rbcn-3B kd* (n=7)= 0.8872±0.03372. (M, N) mEJC amplitude size and frequency are not changed upon reduction of Rbcn-3B. Quantification mEJC amplitude (M): *control* (n=13)= -0.6385±0.0301 nA, *Rbcn-3B kd* (n=6)= -0.7117 ±0.0158 nA. Quantification mEJC frequency (N): *control* (n=10)= 1.243± 0.210 Hz, *Rbcn-3B kd* (n=6)= 1.547 ± 0.1833 Hz. All recordings were performed in HL3 with 1.5mM $Ca^{2+}$. Statistics: Mann-Whitney-U-Test. All panels show mean ± SEM; n.s., not significant; *, $p \leq 0.05$; **, $p \leq 0.01$; ***, $p \leq 0.001$.

## 4.6. Spinophilin Regulates Active Zone Number, Size, and Function

I could show that an altered spatial arrangement of SVs impairs the release probability at the larval NMJ. Another factor, which has been described as influencing the release probability at NMJs, is the local BRP level at individual AZs. The size of an AZ positively correlates with its release probability, whereas the frequency of spontaneous fusion events was reported to increase with a reduction in size, or more precisely with a reduced amount of BRP per AZ (Peled & Isacoff, 2011; Peled et al., 2014). In the Spinophilin (Spn) mutant, which was identified as a novel component at the AZs of larval NMJs (Muhammad et al., 2015), an increased number of AZs that were smaller in size was described. This rare morphological phenotype allowed the investigating whether the release probability at the level of single AZs was changed in Spn-deficient NMJs. To address this question, *in vivo* $Ca^{2+}$ imaging was performed in *spn* mutants via a postsynaptic expression of the membrane-bound $Ca^{2+}$ indicator myrGCaMP5 (Melom et al., 2013).

Spn was identified as a regulator in synaptogenesis (the formation of new AZs). The formation of new synapses is induced by Syd1 and Liprin-α (Fouquet et al., 2009; Owald et al., 2010). As an antagonist, Spn restricts the Syd1/Liprin-α signaling and keeps the number of evolving synapses limited to a normal level (Muhammad et al., 2015). In *spn* mutants, an immunofluorescence staining revealed that the number of AZ was significantly increased and AZs were smaller in size (Fig. 30). The AZs were labeled against BRP, while the postsynaptic compartment was labeled by staining against glutamate receptor 2D subunit (Fig. 30A-C). Though the NMJ size remained essentially unchanged (Fig. 30D), the loss of Spn increased the BRP-spot density (Fig. 30E, F). Also the intensity of the glutamate receptor field was increased (Fig. 30G), a phenomenon regularly observed in mutants with presynaptic release deficits. Electrophysiological recordings in *spn* mutants showed an increased rate in mEJCs (data not shown, for details see Muhammad et al., 2015), which is in line with the hitherto mentioned increase spontaneous release rate at AZs with a low amount of BRP (Peled & Isacoff, 2011; Peled et al., 2014).

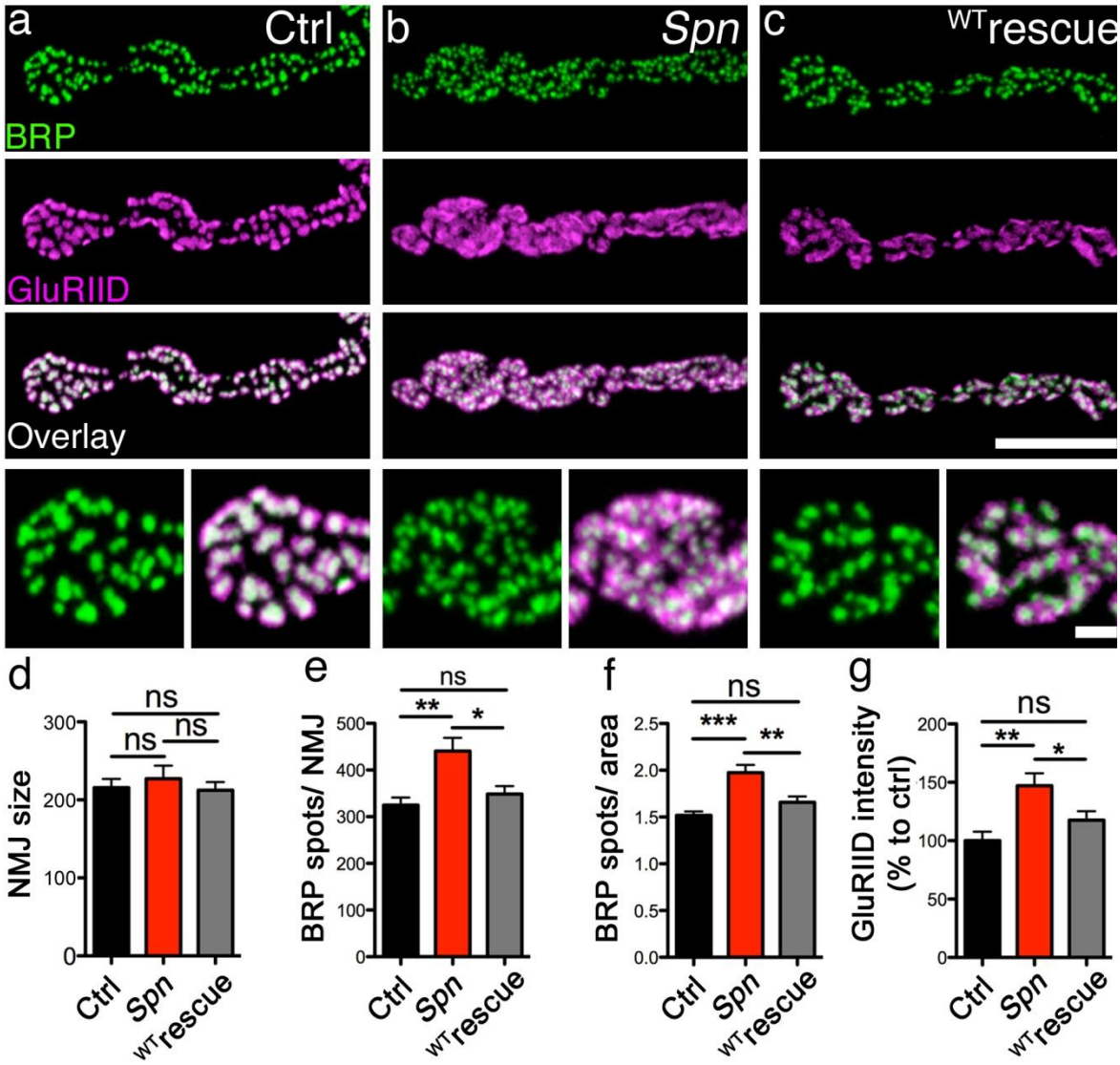


Figure 30 **Presynaptic Spn Limits NMJ Active Zone Numbers.**
(A-C) Projected confocal stacks of NMJs (muscle 4), labeled against BRP ($BRP^{Nc82}$, green) and GluRIID (magenta). (D) NMJ sizes measured using HRP labeling. (E) Numbers of AZ scaffolds per NMJ measured using $BRP^{Nc82}$ labeling (Ctrl: 324.8±16.29, n=14; *Spn*: 440.5±28.4 n=13; neuronal $^{WT}$Spn cDNA expression ($^{WT}$rescue): 348.4±17.45, n=14; Ctrl versus *Spn* P<0.01, (Ctrl versus $^{WT}$rescue: P>0.05, *Spn* versus $^{WT}$rescue: P<0.05). (F) AZ scaffold densities (spots per $\mu m^2$): $^{WT}$Spn cDNA expression (Ctrl: 1.5±0.04, n=14; *Spn*: 1.97±0.08, n=13; $^{WT}$rescue: 1.65±0.6, n=14; Ctrl versus *Spn* P<0.001; Ctrl versus $^{WT}$Spn rescue: P=0.05; *Spn* versus $^{WT}$rescue: P<0.01. (G) Integrated GluRIID intensity is increased in *Spn* (Ctrl: 100±7.6, n=14; *Spn*: 147.1±10.74, n=13; $^{WT}$rescue: 117.6±7.6, n=14; Ctrl versus *Spn*: P<0.01; Ctrl versus $^{WT}$rescue: P>0.05; *Spn* versus $^{WT}$rescue: P<0.05. All tests are Mann-Whitney U-test, values are mean±s.e.m., ns, not significant; *P≤0.05; **P≤0.01; ***P≤0.001. Scale bar, 10 or 1.5 µm in magnified images.
This Figure is taken from Muhammad et al., 2015; data were obtained and analyzed by K. Muhammad.

The myristoylated $Ca^{2+}$ sensor GCaMP5 was expressed at the post-synapse and spontaneous fusion events were recorded for 100s followed by recording of evoked fusion by giving 35 stimulations at 0.2 Hz. Subsequent fixation and staining of the larval filet against BRP allowed for the visualization of single AZs and thus for the analysis of the activity level at single AZ level (for details see Material and Methods, chapter 3.10). Indeed, the $Ca^{2+}$ imaging revealed an increased

overall rate of mEJCs, but on the single AZ level, the net fusion frequency per AZ was not altered. The higher number of AZs in the Spn-deficient animals is likely responsible for the higher spontaneous release rate rather than an increased individual release rate, as the frequency of spontaneous release and the number of AZs showing minis were unaltered (Fig. 31A, C). However, the release probability for evoked events was significantly reduced (Fig. 31B, D), though Spn-deficient synapses participated in both modes of release (spontaneous and evoked). Detailed analysis of the sub-type of release mode in AZs revealed that only the number of AZs participating exclusively in evoked release is significantly reduced in *spn* mutants (Fig. 31E). Thus, Spn is obviously relevant for normal synaptic transmission in evoked release. Now that indeed an altered release probability in evoked release was detected, the question remains whether this is due the reduced BRP levels at Spn-deficient synapses (Fig. 31B). The comparison of the synaptic BRP level to the respective release probability at individual AZs did in fact show a positive correlation; with increasing amount of BRP the release probability for evoked release increased, in control as well as in *spn* NMJs (Fig. 31F). However, this relationship differed between control and *spn*. Thus, the release probability at *spn* is not exclusively due to the reduced amount of BRP per AZ (please note the shift of the datapoints towards the Y-axis in *spn*). Rather, the loss of *spn* itself seems to have additional lowering effects on release probability. In conclusion, Spn is not only influencing the size and number of AZs, Spn is also functionally relevant for evoked neurotransmission by influencing the release probability of single AZs.

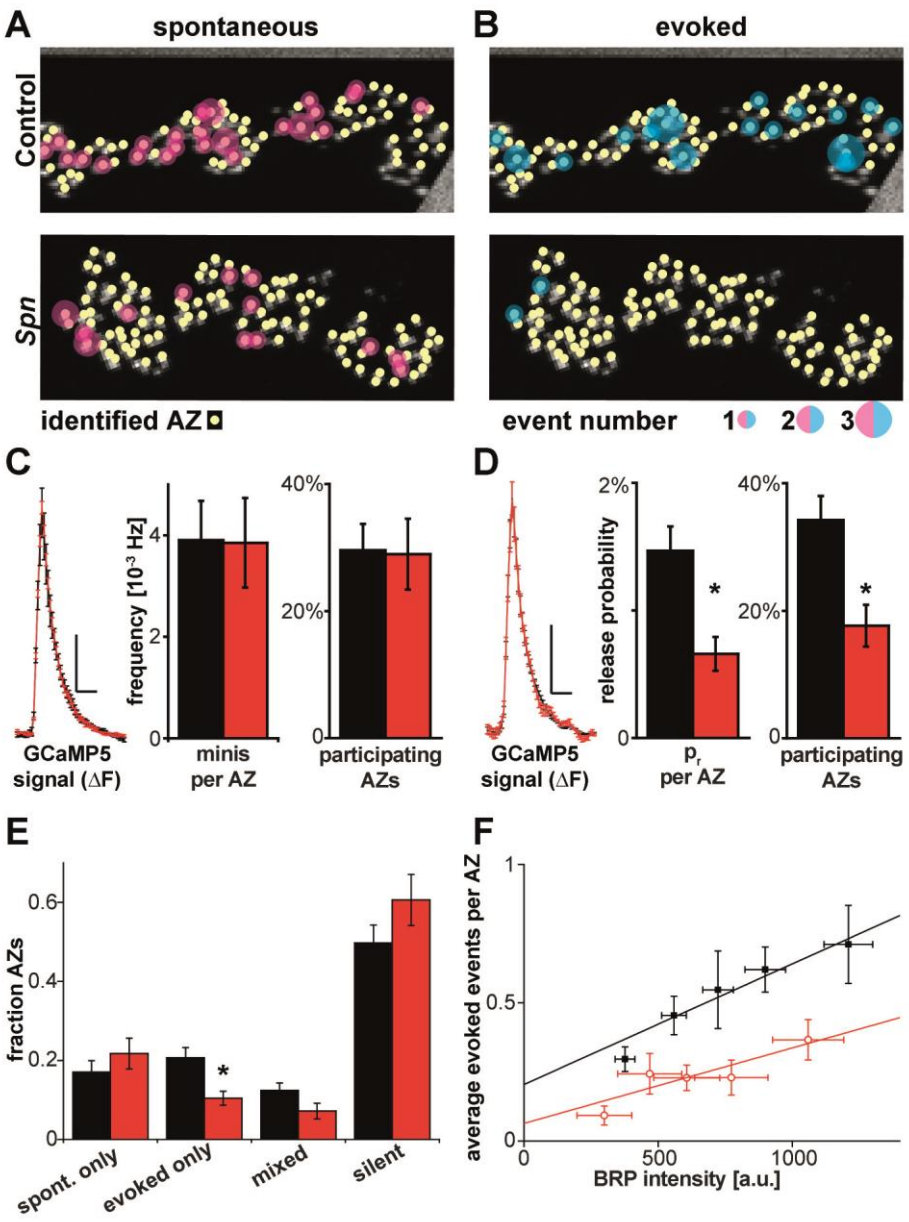


Figure 31 **Individual Spn AZs Show Normal Spontaneous Release, but Lower Probabilities for Action Potential-Induced (Evoked) Release.**
(A, B) Synaptic activity at control and *Spn* NMJs was first imaged for 100 s without stimulation. Subsequently, exocytosis was stimulated by 35 action potentials at 0.2 Hz. Images are montages of NMJ confocal scans showing staining for $BRP^{Nc82}$. Spontaneous and evoked activities indicated by magenta and cyan circles, sizes reflect the number of events per AZ. (C) Local average postsynaptic GCaMP5 signals at *Spn* and control AZs in response to spontaneous release events (left traces). Frequencies of spontaneous ('mini') events per AZ in *Spn* and controls very similar (centre bar graph), as is the fraction of AZs participating at least once in spontaneous activity (right bar graph). (D) Evoked release causes similar postsynaptic GCaMP5 signals at individual *Spn* and control AZs (left traces). The probability that an AZ shows release in response to a single action potential (pr) significantly reduced in *Spn* compared with controls (centre bar graph). The fraction of AZs responding at least once to stimulation also significantly reduced in *Spn* mutants AZs (right bar graph). (E) Categorization of AZs based on their activity pattern: (1) AZs exclusively active during spontaneous release (spont. only), (2) AZs exclusively responsive to AP stimulation (evoked only), (3) AZs releasing both modes at least once (mixed) or (4) AZs not responding (silent). The fraction of 'evoked only' AZs was significantly reduced at *Spn* NMJs. (F) Reduced pr at *Spn* AZs is not secondary to lower BRP levels. AZs were binned with regard to their local BRP intensity and the average number of evoked events was plotted against the average BRP intensities. Evoked events per AZ were correlated to local BRP levels in controls (black data points: experimental data, black line: linear fit, reduced $r^2$=0.92) and, to a lesser extent, at *Spn* AZs (red data points: experimental data, red line: linear fit, reduced $r^2$=0.69). Loss of *Spn* reduced evoked release more than expected by a mere reduction of BRP and both dependencies were best fit by different lines (F-test, P<0.05). Values are mean±s.e.m. Vertical/horizontal scale bars in c, d: 100 a.u./200 ms. Number of animals (n): Control: n=5, Spn: n=4. *P<0.05 in Mann–Whitney U-test.
The data for Figure 31 are published in Muhammad et al., 2015; data were obtained and analyzed by me and Dr. A. Walter.

## 4.7. The Main Findings in a Nutshell

- Unc13 isoforms A and B localize in a specific pattern at the *Drosophila* larval NMJ, with Unc13A closer to the AZ center (~ 60 nm) than Unc13B (~120 nm).
- The distribution of docked synaptic vesicles follows the location of Unc13.
- The Unc13 N-term is not relevant for SV docking, but it determines the position of Unc13 at the AZ.
- Spatial rearrangement of docked synaptic vesicles leads to severe impairment of release probability and thus synaptic transmission; positional priming is a major determinant of release probability at the larval NMJ.
- Unc13 determines the physical release site at the AZ exclusively.
- T-Bar-tethered synaptic vesicles serve as an immediate reserve pool to restore the readily- releasable pool under sustained release.
- The novel AZ components Rbcn3B and PI4KIIIα influence synaptic transmission.
- At the level of single AZs, the participation of individual AZs in spontaneous and evoked release is heterogeneously distributed, and the evoked release is dependent on the BRP level.
- Spinophilin is functionally relevant for evoked synaptic transmission and influences the release probability of individual AZs.

# 5. Discussion

## 5.1. The Spatial Arrangement of Synaptic Vesicles at the Synapse

The discussion may partially overlap with Böhme*, Hollmann*, et al., under revision.

Before neurotransmitter release can take place, specific reactions are necessary. The neuronal SNAREs Syntaxin, SNAP25 and VAMP2 (see Introduction) were shown to be required for docking, the physical localization of SVs to the AZ plasma membrane, and priming, the maturation of SVs into a readily releasable pool (RRP) (Imig et al., 2014; Jahn & Fasshauer, 2012; Walter et al., 2010). Prior to this process, a conformational change from closed to open Syntaxin is thought to be catalyzed by the essential priming factor Unc13, before all three neuronal SNAREs are engaged in establishing an RRP and enhancing vesicle replenishment following exocytosis (Aravamudan et al., 1999; Augustin, Rosenmund, et al., 1999; Imig et al., 2014; C. Ma et al., 2013; Man et al., 2015; Varoqueaux et al., 2002). Synaptic vesicle (SV) release is coupled to the arrival of action potentials (APs) via $Ca^{2+}$ influx through voltage-gated $Ca^{2+}$ channels (VGCCs), which in turn activate the $Ca^{2+}$ sensor Synaptotagmin on the SV to trigger fusion (Rizo & Rosenmund, 2008).

### 5.1.1. Unc13 Isoforms Specifically Influence Synaptic Vesicle Docking Sites and thus Synaptic Vesicle Release Probability

Among the evolutionarily conserved set of large scaffold proteins, ELKS/BRP-family proteins, RIMs and RBPs are needed to ensure proper $Ca^{2+}$ channel-SV topology and their levels predict release at single AZs (Acuna et al., 2015; Han, Kaeser, Südhof, & Schneggenburger, 2011; Kittel et al., 2006; Liu et al., 2011; Matz et al., 2010; Schneggenburger et al., 2012). Still, how the structural scaffold components tune the functionality of the release machinery remains largely enigmatic. Already in *C. elegans*, a reduced number of docked SVs close to the dense projection were observed upon loss of Unc13 (Weimer et al., 2006).

Here we provide evidence that these scaffold complexes operate as “molecular rulers” which confer a remarkable degree of order, and pattern the AZ composition. We find in high-resolution STED microscopy of AZs that both Unc13 isoforms were clearly physically segregated with differ-

ent distances to the $Ca^{2+}$ channel cluster. Unc13A clusters followed the location of BRP, suggesting a common building unit. The second isoform Unc13B located at distinct positions at the outer edge of the BRP ring, independent of BRP location (see Results, chapter 4.4.4). Strikingly, we found that the SV distribution followed this spatial organization, and that loss of Unc13A selectively reduced the number of docked SVs in the AZ center and thus close to $Ca^{2+}$ channels. This was shown in HPF embeddings of isoform-specific mutants for EM, where instant vitrification of the tissue allowed the resolution of SV populations on a nanometer scale.

However, the efficacy of synaptic transmission largely depends on the distance between SVs and VGCCs. Close proximity is called tight coupling and required for fast and immediate responses, which may require active localization of RRP SVs, a process referred to as positional priming (Eggermann et al., 2011; Lee et al., 2013; Wadel et al., 2007). To investigate the physiological relevance of Unc13A deficiency on SV release dynamics, *Unc13A*$^{Null}$ mutants were investigated. The presented data show that the functional consequences of the loss of Unc13A and the resulting altered spatial arrangement of docked SVs are tremendous: besides a reduced RRP size (see chapter 4.1.5), a massive increase in short-term facilitation and an increment of the time to peak were observed (see chapter 4.1.4 and chapter 4.1.6). The reason was identified in $Ca^{2+}$ buffering experiments with EGTA to be a decreased $Ca^{2+}$ dependence of release (see chapter 4.1.7). Either an altered coupling distance is the cause for the decreased $Ca^{2+}$ dependence of release (Lee et al., 2013), or molecular causes like a differential molecular equipment of the remaining SVs in Unc13A mutants, including Synaptotagmin-like $Ca^{2+}$ sensors with other $Ca^{2+}$ sensitivities, or a different number of SNARE complexes are possible (Acuna et al., 2015; Mohrmann et al., 2013; Sugita et al., 2002). However, no changes in the $Ca^{2+}$ cooperativity of the release machinery were detected (see chapter 4.1.6). Therefore, the "molecular equipment" explanation is highly unlikely, and suggests the altered spatial arrangement of the SVs upon loss of Unc13A leads to a change in the SV coupling distance and thus an altered positional priming. Thus, the Unc13 dependent process of docking and priming is mediated in an isoform-specific manner, in which Unc13A promotes the docking and priming of SVs closer to $Ca^{2+}$ channels than Unc13B.

However, not all observed physiological impairments, more precisely the reduced forward priming rate of SVs during in train recordings, are necessarily a direct consequence of the altered spatial arrangement of SVs due to loss of Unc13A. In contrast to Unc13B, the Unc13A isoform harbors a Calmodulin (CaM) binding site, which in mammals was reported to be involved in short-term plasticity and $Ca^{2+}$ dependent fast SV recruitment (Lipstein et al., 2012; Sakaba & Neher, 2001). Thus, not only the altered SV placement, but also the loss of the CaM interaction might contribute to the observed phenotype in *unc13A*$^{Null}$ mutants. The generation of Unc13

CaM-binding site mutants is completed; their electrophysiological characterization is in progress at the moment and preliminary data suggest a reduced forward priming rate to be the sole impairment in synaptic transmission upon loss of the CaM binding site. Thus, the refilling deficit in *unc13A*$^{Null}$ mutants seems to be at least partially caused by the loss of the CaM binding Unc13 isoform in *Unc13A*$^{Null}$. Hence, the characterization of Unc13 mutants with single mutations disrupting the CaM binding site will help to discern the physiological contribution of the two possible causes for altered synaptic transmission.

### 5.1.2. Parallel Release Pathways via the Two Unc13 Isoforms

The data presented here attribute Unc13B only a minor role in transmitter release under moderate stimulation. In its relatively distant localization to the $Ca^{2+}$ channels (see chapter 4.1.1) it is not involved in tight coupling of SVs. Interestingly, the contribution of both Unc13 isoforms (A and B) to the total amount of transmitter release do not add up to control levels (because the sum of the eEJC amplitude of *Unc13A*$^{Null}$ and *Unc13B*$^{Null}$ is lower than the wild type eEJC amplitude (see chapter 4.1.2 and chapter 4.1.4)). Thus, the SV fusion at the two sites does not contribute proportional to release. Rather, Unc13A is the major isoform relevant for transmitter release and the determinant for tight coupling of vesicles at larval NMJs.

Striking differences in short-term plasticity have been reported for mammalian Unc13 isoforms (Rosenmund et al., 2002), and fast and slow phases of release have recently been attributed to parallel release pathways operating at similar distances as the ones reported here in the calyx of Held of young rodents (56 nm and 135 nm;(Z. Chen et al., 2015)). Thus, it might warrant analyzing whether differences in the sub-active zone distribution of Munc13 isoforms contribute to these aspects of synapse diversity in the rodent brain. At mammalian synapses developmental changes in the coupling of SVs and $Ca^{2+}$ channels were described (Z. Chen et al., 2015; Nakamura et al., 2015; L.-Y. Wang et al., 2008), and differentially positioning Unc13 isoforms might be a major driving process to couple functional and structural maturation of AZs. To what degree modulation of this process might contribute to the functional diversification of synapses should be an interesting subject of future analysis.

A potential role of Unc13B in establishing a subtype of readily releasable vesicles is conceivable, where at Unc13B sites SVs could become molecularly primed and captured at the lateral AZ before they would be subsequently moved towards the $Ca^{2+}$ channels for positional priming at Unc13A sites where finally the SV fusion takes place in a fast and synchronous manner. This idea derives from the differentiation of the RRP into a fast (FRP) and slow (SRP) released subgroup of SVs, identified at the Calyx of Held, where SVs from the SRP were shown to replenish SVs of the

rapidly consumed FRP vesicles during sustained release (Lee et al., 2012; T Sakaba & Neher, 2001). Yet the necessary lateral movement of SVs towards the $Ca^{2+}$ channel cluster was never shown at any synapse type. Furthermore, mathematical modeling of the larval NMJ proposed a single reserve pool, which feeds one RRP without any further subdivision into FRP/SRP subpools (Hallermann et al., 2010). Nonetheless, the two sources for heterogeneous release probability of SVs in the RRP at the synapse, namely i) positional priming, and ii) differential molecular priming due to different molecular equipment of release-ready SV leading to heterogeneous efficiency of molecular priming ( Schneggenburger et al., 2012), are not mutually exclusive. Both were both shown to be present in the Calyx of Held (Wadel et al., 2007; Wölfel et al. , 2007).

Their existence and contribution to the heterogeneous release probability of RRP vesicles at the *Drosophila* NMJ are under investigation. With our study, we contribute the information that a spatial heterogeneity in SV placement determined by Unc13 isoforms is an important source for heterogenic release probability of the RRP at the larval NMJ.

Whether this positional priming explanation is the sole cause, or if additionally differential molecular priming contributes to the heterogeneous release probability remains an open question, which would be of great interest to investigate in future experiments. There are indications for two populations of RRP vesicles with differential SNARE protein number (Uytterhoeven et al., 2011; Wucherpfennig et al., 2003) suggesting differential molecular priming does exist at the *Drosophila* NMJ.

Furthermore, our data add valuable information to understand RRP dynamics: It is published that complete Unc13-deficiency leads to embryonic lethality in *Drosophila* (Aravamudan et al., 1999), while we find upon loss of isoform Unc13A (relevant for SV-$Ca^{2+}$ channel-coupling, see above) the larvae reach pupal stage, and a few escapers reach adulthood. As Unc13 is essential for SV fusion (Südhof, 2012; Südhof, 2013), it implicates SV fusion must take place at Unc13B release sites in *unc13A*$^{Null}$, with an increasing number of fusion events at the Unc13B sites under repetitive stimulation. Thus, we conclude two parallel, co-existing functional exocytosis pathways at mature synapses of the larval NMJ, differentially controlled by two Unc13 isoforms whose precise spatio-temporal positioning is a major denominator of AZ function (Fig. 32).

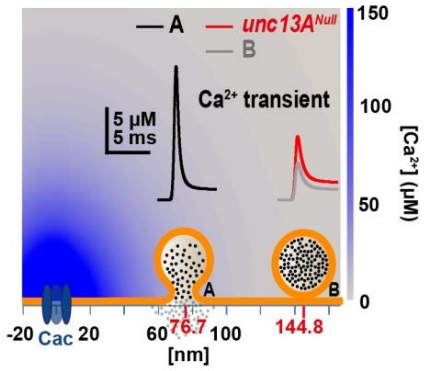


Figure 32 **Unc13 isoforms determine two distinct release sites at the NMJ.**
Release site model of two different pathways (A and B) with the postsynaptic response dependent on the distance of the SV to the $Ca^{2+}$ source (*Drosophila* VGCC at the NMJ Cac in blue). $Ca^{2+}$ transients at further distances (B site) from the $Ca^{2+}$ source (grey line) were smaller than at the A site (black line). $Ca^{2+}$ transients in *unc13A*$^{Null}$ (red line) were larger at the B site than in the wild type situation. Here, the color scale bar was cut off at 150 µM for better visualization, while the actual peak concentration reached values > 800 µM.
From Böhme*, Hollmann* et al., under revision.
Mathematical modeling by A. Grasskamp, designed by M. Böhme

Two possible scenarios for SV recruitment to the RRP are conceivable: i) The sites are refilled by the same reserve pool, and under prolonged stimulation they compete for SVs refilling (Hallermann et al., 2010), or ii) the SVs located at the Unc13A release site constitute the fast-releasable pool of the RRP (FRP), and SVs at the Unc13B release site are part of the slow releasable pool of the RRP (SRP) (Schneggenburger et al., 2012). If in the second scenario the SVs located at the Unc13B site would be feeding the release at the Unc13A site (Lee et al., 2012), a short-term depression would be expected in *unc13B*$^{Null}$ mutants during paired pulse recordings. However, a non-significant but strong tendency for short-term facilitation is observed, suggesting that a lack of Unc13B increases the availability of SVs for the Unc13A site, thereby indicating competition for SVs refilling. Thus, a refilling from a common reserve pool to both Unc13 release sites including potential competition during sustained release is the most likely scenario.
Further investigation on the question if the Unc13A and Unc13B release sites compete for SV refilling could be addressed by the recording of high frequency trains in transgenic larvae which overexpress Unc13B in wild type background. It would have to be necessary to rule out with high-resolution STED microscopy that the overexpressed Unc13B distributes over the whole AZ and would also occupy Unc13A release site. If this is not the case and Unc13B localizes solely to the release sites at the edge of the BRP ring, electrophysiological recordings of high frequency trains are expected to result in an increased asynchronous release component in addition to the normal release in Unc13B overexpression. Whether the two different release sites compete for RRP refilling from the same reserve pool could be discerned in cumulative plots of the train amplitudes; in this case, a reduced forward priming would be observed in the Unc13B overexpression.

### 5.1.3. The N-term of Unc13 Restricts Synaptic Vesicle Docking to Specific Sites

Positional priming mediated by the two Unc13 isoforms likely contributes profoundly to the observed phenotypes. Thus, we imply that the role of the N-terminus is to differentially target the

isoforms into specific zones of the AZ, which determines the striking functional differentiation of both isoforms.

Notably, recent work in *C. elegans* also characterized two Unc13 isoforms associated with two release types. Fast release is mediated by UNC13-L, whereas slow release required both UNC-13L and -S (Hu et al., 2013). The proximity of the UNC13-L isoform to $Ca^{2+}$ entry sites was mediated by the protein's N-terminal C2A-domain (not present in *Drosophila*) and was critical for accelerating neurotransmitter release, and for increasing and maintaining the probability of evoked release assayed by the fraction of AP- to sucrose-induced release (Zhou, Stawicki, Goncharov, & Jin, 2013). In contrast, the slow release form dominantly localized outside the very AZ regions (Hu et al., 2013). Thus, it would be interesting to investigate the sub-AZ distribution of *C. elegans* Unc13 isoforms and test whether the same scaffold complexes as in *Drosophila* mediate the localization of the different Unc13 isoforms.

Though the *Drosophila* Unc13 N-term does not include a C2A-domain like in *C. elegans* Unc13, the N-term nonetheless determines the location of the protein, while the C-term with the MUN-domain is relevant for the interaction with SVs. Deletion of the Unc13 N-term led to delocalized Unc13 at the NMJ terminal, the cluster-specific positions were lost in $Unc13^{\Delta N\text{-}Term}$ mutants (see chapter 4.2). Therefore, we conclude that the N-term of Unc13 is necessary to position the protein in its destined spot, and that these processes apparently involve the interaction with the protein scaffold at the CAZ. To identify the responsible protein-sequence, we investigated protein-protein-interactions in yeast-to-hybrid (Y2H) screens. In Y2H, the N-terminal PxxP motif was identified to be interacting with including $2^{nd}$ and $3^{rd}$ SH3 domain of RBP, but a local point mutation did not cause mislocalization (Data not shown; compare Böhme*, Hollmann* et al. , under revision). However, the localization of Unc13A was found to be dependent on multiple scaffold components including BRP, RBP and Liprin-α, suggesting several parallel interactions needed to enrich the respective Unc13 isoform in its specific "niche".

In summary, the loss of site-specific Unc13 clusters i) doubled the number of docked SVs, which ii) were no longer restricted to the above-mentioned specific sites. We conclude that the Unc13 N-term restricts the position of Unc13 to specific spots, thereby limiting the docking of SVs to these positions. The C-terminally located MUN-domain, which has been shown to be the minimal domain required for molecular priming (Basu et al., 2005; D. R. Stevens et al., 2005), is still intact. The mislocalization of the protein does not interfere with its ability to dock SVs at the AZ.

### 5.1.4. Unc13 Determines the Physical Release Slot

The findings presented in this work used N-terminally deleted Unc13 mutants to gain further information about the indispensability of proper Unc13 location for SV cycling. We could show in train recordings that the RRP was not significantly altered when delocalized Unc13 lacking the N-term was expressed, but the forward priming rate under prolonged stimulation was reduced (see chapter 4.2.3).

The refilling of releasable SVs during a stimulus train was increased by $Ca^{2+}$ influx to the synaptic terminal. The elevated $Ca^{2+}$ concentration shifts the dynamic equilibrium between the reserve pool SVs and primed SVs towards an enhanced priming rate (reviewed in Neher & Sakaba, 2008; L. Y. Wang & Kaczmarek, 1998). The $Ca^{2+}$ binding protein Calmodulin (CaM) has been described to mediate this process. As mentioned before, the binding of Unc13 to CaM was described to be crucial for the SV replenishment at the synapse (N. Lipstein et al., 2012; H. Liu et al., 2014; T Sakaba & Neher, 2001). Since the deletion of the Unc13 N-term included the CaM-binding site, it has to be determined whether the loss of CaM binding ability or the delocalization of the Unc13 lacking the N-term is the source for the observed transmission defects. The use of the $Ca^{2+}$ buffer EGTA allowed to testing for the $Ca^{2+}$ dependent component of SV refilling in train recordings. The EGTA-sensitivity of SV refilling in $Unc13A^{full\ length}$, but not $Unc13A^{\Delta N\text{-}term}$ suggests a requirement of the CaM binding site in the SV refilling during the train (see chapter 4.2.3). The characterization of a CaM-binding deficient Unc13 variant is still ongoing. Indeed, preliminary results suggest a reduced forward priming rate upon loss of CaM-binding ability.

Additionally, $Unc13A^{\Delta N\text{-}term}$ mutants were found to have an increased short-term facilitation which implies a reduced release probability $P_r$ ( Roy et al., 2014; Hallermann et al., 2010). In addition, the time to peak was significantly increased under repetitive stimulation (see chapter 4.2.4). These observations indicate that the building $Ca^{2+}$ nanodomain in a stimulation train triggers fusion of loosely coupled SV in a higher distance to the $Ca^{2+}$ source, likely in an asynchronous manner (Eggermann et al., 2011; Kaeser & Regehr, 2014). Alternatively, the recently proposed separate $Ca^{2+}$ sensor specifically involved in synaptic facilitation, Syt7, might be responsible for the altered release probability (Jackman et al., 2016). In *Drosophila*, the role of Syt7 is under investigation; as an alternative $Ca^{2+}$ sensor it seems unlikely to be involved in normal evoked transmission (personal communication). However, the investigation of a potential role for Syt7 specifically in synaptic facilitation will be an interesting task for future experiments.

The potential role of this asynchronous release was addressed in $Ca^{2+}$ buffering experiments with EGTA-AM in $Unc13A^{full\ length}$ and $Unc13A^{\Delta N\text{-}Term}$ mutants (see chapter 4.2.3). Asynchronous fusion is abolished by EGTA-treatment (Eggermann et al., 2011). In line with this, the short-term

facilitation in Unc13A$^{\Delta N\text{-}Term}$ was prohibited by EGTA treatment and the time to peak was at wild type levels after EGTA treatment of Unc13A$^{\Delta N\text{-}Term}$. Thus, the functionality of the Unc13A$^{\Delta N\text{-}term}$ can be restored by restricting the release close to the $Ca^{2+}$ channels. These findings strongly support the conclusion of an increased portion of loosely coupled SV in Unc13A$^{\Delta N\text{-}term}$. This phenomenon is explained by either i) an increased number of release sites with a lower release probability of a single SV at these sites, or ii) a small number of SVs with normal release probability and a silent docked pool. The first idea, however, is highly unlikely: Although a higher number of docked SV was observed in EM, the electrophysiological estimation of the RRP revealed no significant difference in the amount of readily-releasable vesicles (see chapter 4.2.2 and chapter 4.2.3). This apparent discrepancy can be explained by the discrimination criteria between the docked pool of SVs and the RRP. The two classes are not identical: docking is a morphological prerequisite for priming, and does not give information about the fusion competence of SVs. The term "dead end docking" was established to describe docked, but fusion-incompetent SV (Hugo et al., 2013; Verhage & Sørensen, 2008). The results obtained with N-term deficient Unc13 confirms our finding, that the proper spatial arrangement of docked SV is crucial for their fusion competence.

The release deficit in Unc13A$^{\Delta N\text{-}Term}$ seems to result from the high mobility of Unc13 leading to instable release sites. In the Calyx of Held, docked SVs were found to be located at a minimal distance to the $Ca^{2+}$ source. In mathematical modeling of this so-called exclusion zone, a 30 nm radius between fusion-competent SV and the $Ca^{2+}$ channels was found to match the recorded synaptic release best (Keller et al., 2015; Nakamura et al., 2015). However, although these models are based on recordings from Calyx of Held, and assume and discuss different topologies in $Ca^{2+}$ channel and SV arrangements, it is nonetheless possible that this exclusion zone is a universally existing phenomenon at synapses. Especially the location of Unc13A (~60 nm from the AZ center) and accordingly the SVs docking sites (~50 nm from the AZ center) at the larval NMJ suggest that an exclusion zone is maintained also in *Drosophila*. Assuming a required minimal distance at the larval NMJ, it becomes clear from electron micrographs that this exclusion zone is abolished upon loss of the Unc13 N-term (see chapter 4.2.2). In our studies, SVs are also located even closer to the $Ca^{2+}$ channels in Unc13A$^{\Delta N\text{-}term}$ mutants; in parallel, the portion of loosely coupled SVs is increased. The lower sensitivity to EGTA of the first amplitude in Unc13A$^{\Delta N\text{-}term}$ is likely due to the loss of the exclusion zone. This spatial arrangement possibly leads to tighter coupling and thus reduced sensitivity to EGTA in Unc13A$^{\Delta N\text{-}term}$ compared to control. This strengthens the likely function of Unc13 to be crucial to position the protein and in consequence the docked SVs to specific slots.

Notably, in the control Unc13A$^{full\ length}$ the synchronous release component was affected by EGTA, and the first amplitude of the stimulation train was reduced in Unc13$^{full\ length}$ (see chapter 4.2.3). This suggests that the coupling of SVs at motoneuronal terminals in *Drosophila* larvae is in general not especially tight.

Subsequent to the stimulation train, an outward current was observed, which was abolished under EGTA treatment (see chapter 4.2.3). Hence, the outward current is $Ca^{2+}$ dependent. Likely, a $Ca^{2+}$ dependent outwardly rectifying potassium channel is the source for the observed $Ca^{2+}$-dependent current. These $Ca^{2+}$ sensitive K-channels solely open under control condition with DMSO, while under EGTA treatment $Ca^{2+}$ is buffered, the $Ca^{2+}$ dependent channels remain closed and the membrane potential unaltered (Brown & Griffith, 1983; Meech, 1978).

In summary, we find Unc13 has not only a role upstream of SV docking, but rather it is the first molecule known to physically determine the release slot (Fig. 33). Unc18 and Syntaxin, the other two proteins of the CAZ essential for SV fusion, are known to be enriched but not exclusively localized to distinct sites at AZs. Rather, they are distributed over the whole neuronal membrane (C. Ma et al., 2013; Romero et al., 2008; Ullrich et al., 2015; Weimer et al., 2003). Thus, Unc13 is the hitherto only identified protein to physically determine the site of release.

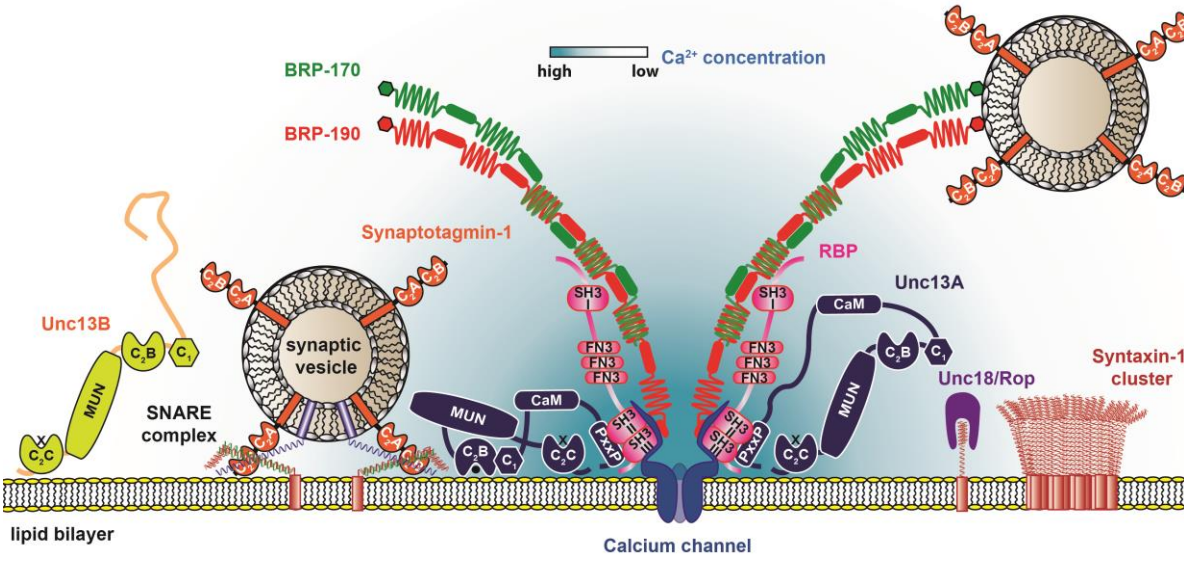


Figure 33 **Scheme of the arrangement of AZ components with the two Unc13 isoforms specifying release sites.** Unc13A (dark blue) is located close to the $Ca^{2+}$ channels (light blue, in the membrane), which are residing below BRP (Isoform 170 kDa green, isoform 190 kDa red) and RBP (pink). Unc13B (yellow) is residing in a larger distance to the $Ca^{2+}$ channels. Synaptotagmin-1 (orange) is in the SV membrane, while Syntaxin-1 (light red) in the plasma membrane is located in clusters in the periphery of the AZ, when it is not engaged in the formation of SNARE complexes. Unc18 (purple) is bound to Syntaxin-1 already in the closed conformation. The domain structure and various interactions between the AZ proteins were taken into account. Figure designed by M. Böhme

A direct visualization of release events and thus the fusion sites in flash-freeze experiments at *Drosophila* larval NMJ would be of high interest in this context, the experiments are still ongoing.

Flash-freeze experiments in other systems likely documented release events. For instance, in *C. elegans,* the main portion of docked SV is located close to the dense projection (<60 nm) (Watanabe et al., 2013; Weimer et al., 2006), which also is the main region where SV fusion was observed (Watanabe et al., 2013). In my experiments, I could show that a light-induced increase in synaptic activity led to plasma membrane invaginations adjacent to AZs 150 ms after the end of the stimulation, probably representing early stages of endocytosis (Koenig & Ikeda, 1996; Watanabe, Liu, et al., 2013; Watanabe, Rost, et al., 2013). I furthermore found that prolonged stimulation clearly increased the number of clear vesicular, likely endocytic compartments. The observation of release events and potential disturbances in this process in Unc13 mutants will be an interesting task for future experiments.

### 5.1.5. T-Bar Tethered Synaptic Vesicles Serve as Immediate Reserve Pool During Prolonged Stimulation

Several proteins are known to be important for the molecular integrity of the presynaptic machinery. BRP is such a member of the CAZ and an essential scaffold protein, critical for an intact AZ structure and $Ca^{2+}$ channel clustering in the presynaptic AZ membrane (Kittel et al., 2006; Wagh et al., 2006). The last 17 amino acids (aa) of the BRP C-term were shown to be involved in SV tethering to the T-Bar, the corresponding BRP allele was called $brp^{nude}$ due to the fully intact T-Bar structure bare of SVs. The altered SV distribution in $brp^{nude}$ mutants was accompanied by a reduced forward priming rate as well as a reduced SV recovery rate after synaptic depression (Ehmann et al., 2014; Hallermann et al., 2010).

To increase the knowledge about the role of SV distribution at the AZ and specifically its influence on SV refilling and release probability I subjected $brp^{nude}$ mutants to a detailed electrophysiological analysis. Though I could not reproduce the data of a reduced synaptic recovery rate after synaptic depression, a short-term depression was observed at the synapse, combined with a clear refilling deficit in the train (see chapter 4.3). Thus, the C-terminal last 17 aa and the attachment of SVs to the T-Bar seem to be relevant for a normal forward priming rate of SVs. However, the observations that the loss of the BRP C-term leads to depression in paired pulse recordings and that already the second stimulus of a 60 Hz train with 16.6 ms interstimulus interval has reduced synaptic transmission is surprising (see chapter 4.3). The SVs engaged in the early fusion events in a train recording or in paired pulse recording are considered to be part of the RRP, while the SV replenishment sets in later (Chen et al., 2013 and L. Y. Wang & Kaczmarek, 1998 measured the wild type calcium dependent recovery curve and fitted a double exponential with average time constants $\tau_1$ (fast time constant) of 116 ms and $\tau_2$ (slow time constant) of 3.6 s

at the Calyx of Held). The RRP was not reduced in *brp*$^{nude}$, so what might be the reason for the transmission deficit early in the train? A possible explanation for the short-term depression phenotype is found in Ehmann et al., 2015, where it is reported that the loss of the BRP C-term reduced the variability in the orientation of the cytosolic BRP C-term suggesting a rigid, immobile structure. Contrarily, in wild type the C-terminal end of BRP was versatilely oriented and covering a larger area of the BRP ring. The dynamic orientation of the BRP C-term is necessary to keep synaptic transmission at wild type levels at already moderate stimulation. The loss of this dynamic orientation does not influence the size of the RRP, but the $P_r$ of its content. This indicates a BRP dependent change in the ratio of a slow (SRP) and fast releasable (FRP) fraction of the RRP. As described before, a lateral movement of SVs of docked SV towards $Ca^{2+}$ channels in order to increase the release probability (positional priming) was not observed yet. However, in electron micrographs the BRP C-term was frequently found to be connected to docked SVs (see chapter 4.1.3 and chapter 4.2.2). In regard to the *brp*$^{nude}$ electrophysiology results (normal RRP size with a higher fraction of low $P_r$ vesicles) it is conceivable that the BRP C-term might mediate such a lateral movement of SVs towards the $Ca^{2+}$ source to increase the fraction of fast-releasable vesicles in the RRP. Yet this intriguing idea is yet speculative and remains to be elucidated.

It would have been interesting to compare the reduction of the forward priming rate in *brp*$^{nude}$ with the already published reduced number of tethered SVs, to examine whether these reductions are proportional. However, the EM data in the publication of Hallermann and colleagues (Hallermann, Kittel, et al., 2010) are not applicable for this purpose. The authors did not count the SV number with physical attachment to the T-Bar; instead, SVs per "shells" were analyzed i.e. SV numbers in half-circular distance bins around the T-Bar pedestal were quantified. Unfortunately, the distance bin quantification numbers are not published. Additionally, neither the smallest shell size was chosen adequately to the T-Bar size nor were the SV numbers per shell normalized to the T-Bar size. As the T-Bar size is variable, this however would have been important to estimate the number of T-Bar tethered SVs from the "shell data". Hence, a re-investigation of the electron microscopic phenotype, optimally with HPF embedded larvae, would be indispensable to compare the reduced refilling rate with the reduced number of T-Bar tethered vesicles.

A further interesting experiment will be the investigation of the $Ca^{2+}$ dependency of the refilling rate (Hosoi, Sakaba, & Neher, 2007; Schnee et al., 2011), more precisely whether and to what extent the $Ca^{2+}$ dependent SV recruitment is affected upon loss of the last 17 aa of BRP.

In our studies we observed several discrepancies in comparison to the published electrophysiology recordings of *brp*$^{nude}$: i) a decreased fast recovery rate was observed in *brp*$^{bude}$ in previous studies (Ehmann et al., 2014; Hallermann, Kittel, et al., 2010), while the fast recovery rate was not altered in my recordings; ii) instead of the applied $[Ca^{2+}]_{ex}$ of 1 mM and 1.5 mM in those previous studies, I had to increase the $Ca^{2+}$ concentration up to 2.5 mM in the bath solution to induce synaptic depression and thus reliable consumption of readily releasable vesicles in the train. Besides the central role of $Ca^{2+}$ to trigger SV fusion at the synapse, the $Ca^{2+}$ concentration has a regulatory function at most steps of the SV cycle (Eggermann et al., 2011; Hosoi et al., 2007; Neher & Sakaba, 2008; R Schneggenburger & Rosenmund, 2015; Südhof, 2012; L.-Y. Wang & Augustine, 2014). However, the exact cause for an almost two-fold higher $Ca^{2+}$ concentration needed here to obtain the required synaptic depression remains unsolved. This difference in $[Ca^{2+}]_{ex}$ may in turn account for the disagreeing observation concerning the unaltered fast recovery rate in my recordings. To obtain a decent estimation of the synaptic recovery rate, the RRP needs to be entirely emptied in the first few pulses of a train recording. If the RRP is not properly emptied due to low external $Ca^{2+}$ before the SV recruitment starts to refill readily releasable vesicles, the complicated interplay of synaptic depression and facilitation, $Ca^{2+}$ dependent SV refilling, and complex SV pool dynamics interleave and blend, and might lead to the observed disagreeing results.

## 5.2. Characterization of Proteins with a Putative Regulatory Function in Synaptic Transmission and Development

Though many proteins relevant for synaptic transmission have been described, the investigation and characterization of novel, yet unknown players in the synaptic vesicle cycle is a useful approach to understand the requirements and complex interplay of the underlying molecular processes. In an RNAi based loss-of-function screen, candidate genes with a putative function in synaptic transmission were analyzed. The adults were addressed to electroretinography, and the morphology and ultrastructure of the AZs at the larval NMJ were examined in light microscopy and electron microscopy. Furthermore, the synaptic transmission was investigated by TEVC upon RNAi knock down. Two candidates were found to be relevant for synaptic transmission, the Phosphatidylinositol-4-Kinase PI4KIIIα and Rabconnectin-3B (Rbcn-3B), which binds to Rab3 GEFs and GAPs.

### 5.2.1. Phosphatidylinositol-4-Kinase PI4KIIIα Affects Synaptic Transmission

Membrane lipids and their derivates are not only the building units of cellular membranes, but they have furthermore been found to have regulatory function in the SV cycle. Amongst them, the phosphoinositide variants are precisely distributed to limited plasma membrane regions where specific membrane dynamics take place, in particular sites of exo- and endocytosis. The regulation of membrane lipid composition in the coupling of exo- and endocytosis possibly serves as a homeostatic mechanism for the maintenance of stimulation-adequate neurotransmission (Puchkov & Haucke, 2013).

Phosphatidylinositol-4-phosphate (PI4P) serves as substrate for the production of $PI(4,5)P_2$ in the plasma membrane (Di Paolo et al., 2004), which is functionally relevant for SV fusion at the AZ and endocytosis at the periactive zone (Haucke et al., 2011; Jahn & Fasshauer, 2012; Koch & Holt, 2012; Saheki & De Camilli, 2012). At the AZ, Phosphatidylinositol-4-Kinase type III alpha (PI4KIIIα) was found in a large RNAi based knock down screen, where its reduction led to altered synapse morphology and transmission defect at the *Drosophila* adult compound eye in ERG recordings (see chapter 4.5.1). However, the following detailed electrophysiological and ultrastructural characterization unraveled ambiguous findings. ERG recordings upon PI4KIIIα knock down showed a clearly impaired synaptic transmission, whereas TEVC recording at the larval NMJ revealed an increased postsynaptic signal after stimulation. PI4P serves as a substrate to speed up exo- and endocytic coupling (Haucke et al., 2011). Therefore, a reduced level of PI4P would be expected to lead to a possibly decreased eEJC size and decreased recruitment rate of SVs during sustained release. However, there seems to be a synapse type specific difference between lamina synapses (whose synaptic transmission is recorded in ERG) in the adult eye and the NMJ.

These observations are intriguing, since the membrane lipids came into research focus in the recent years when their dynamics and regulation were identified as hitherto underestimated, yet crucial participants in every step of the SV cycle (Balakrishnan et al., 2015; Martin, 2015; Posor et al., 2015).

To understand the possible role of PI4KIIIα at the synapse, electrophysiological train stimulation of PI4KIIIα knock down larvae would be of interest to investigate the forward priming rate of SVs in the NMJ. Furthermore, a specific antibody for immunofluorescence stainings could help to solve the question if the protein is preferably expressed in specific synapse types. With these future experiments, the potential function of PI4KIIIα at the synapse could be identified.

### 5.2.2. Rabconnectin-3B Influences Synaptic Transmission

Rabconnectin-3B (Rbcn-3B) has been identified in SV extracts of rat brain, and it binds to Rab3-GEFs and Rab3-GAPs and forms heterodimers with Rbcn-3A (Nagano et al., 2002). Rbcn-3B has predicted GTPase activity and several WD40 repeats which are reported to serve as scaffold for protein-protein-interaction (Neer, Schmidt, Nambudripad, & Smith, 1994; Stirnimann, Petsalaki, Russell, & Müller, 2010). Rab3 was shown to be required for normal distribution of AZ components and AZ size at the larval NMJ (Graf et al., 2009). This makes Rbcn-3B a promising candidate in the search for regulators of synaptic transmission. Indeed, in our studies, Rbcn-3B was identified in an RNAi-based knock down screen to influence synaptic morphology (see chapter 4.5.2). Loss of Rbcn-3B led to reduced synaptic transmission in ERG recordings whereas TEVC recording at the larval NMJ revealed an increased postsynaptic signal after stimulation. The heterogeneous, synapse type dependent effects of Rbcn-3B knock down are however puzzling and lead to the question which of the published functions and predicted domains of Rbcn-3B could be the cause for the observed effect (Kawabe et al., 2003). The potential regulatory role of Rab3-GEF and Rab3-GAP in Rab3 signaling is neither the sole effect nor the main function for Rbcn-3B at the synapse, as the function of Rab3 in AZ spacing and distribution was shown to be independent of its GTPase activity (Chen et al., 2015). Thus, it remains enigmatic whether a potential function of Rbcn-3B in the regulation of Rab3-GEFs and Rab-GAPs is of relevance for synaptic development and transmission. However, Rbcn-3B was shown to regulate V-ATPase function and thus indirectly Notch signaling; loss of Rbcn-3B is embryonically lethal (Yan et al., 2009). Hence, a valuable information would be if the WD40 repeats in Rbcn-3B are the relevant regulatory domains and thereby the crucial organizational units in synapse development.

## 5.3. Spinophilin is Necessary for Evoked Release

Their number and distribution of AZs at the NMJ are regulated by a variety of presynaptic proteins and directly influence the amount of released neurotransmitter. Mutations in Synaptojanin (Dickman et al., 2006), Liprin (Kaufmann et al., 2002), Neurexin (Li et al., 2007), and Spectrin (Pielage et al., 2008) affect the size and spacing of the arrangement of AZs at the NMJ. Furthermore, similar to vertebrate central synapses, CAZ proteins at larval NMJs are distributed heterogeneously across the entire population of AZs, resulting in sites with varying release probability (S. Chen et al., 2015; Holderith et al., 2012; K. S. Y. Liu et al., 2011; Marrus et al., 2004; Peled & Isacoff, 2011). Also Spinophilin (Spn) was shown to influence the spatial organization and size of AZs at the NMJ by acting as an antagonist for Nrx/Syd-1 signaling during synaptogenesis (Fouquet et al., 2009; Muhammad et al., 2015; Owald et al., 2012). Nrx is located in the presyn-

aptic membrane and binds to Nlg, which resides in the postsynaptic membrane. This trans-synaptic interaction connects the pre- and postsynaptic compartment and serves as a regulatory module in synapse formation.

Here we showed that at mature synapses, Spn seems to serve additionally for the establishment of a correct release probability, independent of absolute AZ scaffold size. A postsynaptic expression of the membrane-attached $Ca^{2+}$ sensor GCaMP5 allowed the investigation if single AZs participate in spontaneous and/or evoked release and the analysis of the release probability $P_r$ at individual synapses in evoked release. The number of AZs engaged in spontaneous release was unaltered, while the loss of Spn led to a reduced number of AZs participating in evoked release, with a lower $P_r$ at single AZs (see chapter 4.6).

In line with our findings, it was already shown that a high BRP level at the presynaptic site correlates with a high release probability of this AZ (Peled & Isacoff, 2011). Our data clearly suggest that the release probability of single AZs in evoked release depends not on BRP levels, but additionally on the presence of further CAZ-components like Spn. In electrophysiological recordings, it was formerly only possible to display the compound transmission recorded over the whole NMJ, with no possibility to discern the contribution of individual AZs to the evoked postsynaptic signal.

Here, we present the first successful attempt to investigate the role of a CAZ member in the individual contribution of single AZ to synaptic transmission at the larval NMJ. With this powerful tool at hand, it would be of great interest to examine to what extent other proteins of the AZ potentially regulate the release probability on the single AZ level, and how this site-specific regulation contributes to the overall $P_r$. Given that the Spn/Nrx-1 interaction is conserved from *Drosophila* to rodents (Muhammad et al., 2015), addressing similar roles of presynaptic Spn in mammalian brain physiology and pathophysiology might be informative.

## 5.4. Conclusion

The results in this work allow conclusions concerning the role of Unc13 and BRP in the SV distribution at AZs. SV docking is dependent on Unc13, which seems to be the sole determinant of the physical release sites at the AZ. SV tethering and the distribution of T-Bar tethered SV is dependent on the BRP C-term, while the N-terminal half of BRP has an interaction site for Unc13A. Thus, BRP has an indirect but critical role in SV docking by interaction and localization of the essential docking factor Unc13A, and additionally a function upstream of SV docking in SV replenishment to the AZ mediated by the BRP C-term.

Furthermore, additional factors influencing synaptic transmission could be identified and characterized. Especially the heterogeneous release probability among individual AZs of the same NMJ and the dependence of evoked release on the presence of regulatory AZ proteins like Spinophilin are a major contribution towards the understanding of the different regulatory levels where release probability and thus synaptic strength can be adapted.

# 6. Appendix

## 6.1. The Cytomatrix at the AZ: Structure and Function of Key Components

Additional proteins at AZs which influence neurotransmitter release will be briefly described here. These proteins are involved in establishing a network for SV recruitment to and localization of $Ca^{2+}$-channels at release sites. Namely, five evolutionarily conserved proteins form the core of AZs: BRP/ELKS, RIM, RBP, Unc13, and liprin-α. Furthermore, Piccolo and Bassoon (two large homologous proteins) and Syd-1 are located at the AZ serving as scaffold or regulator in synapse formation, respectively. Notably, the proteins of the SV fusion machinery Syntaxin and SNAP-25 (t-SNARES) and Unc18 are not restricted to AZs but localize evenly distributed over the plasma membrane (reviewed in Südhof, 2012). Figure 34 contains a comprehensive list of proteins which have been found to be involved in AZ maturation or scaffolding, and SV fusion, tethering, docking, recruitment or recycling. The major components of this list are briefly described below.

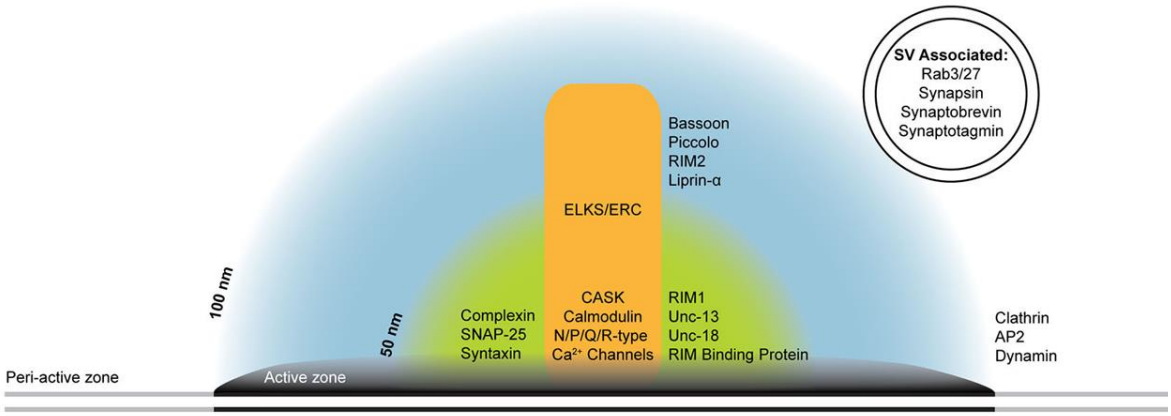


| Synaptic proteins | | Vertebrate and invertebrate gene names: Human | Fly | Worm | Function | Associated Neurological disorders | References |
|---|---|---|---|---|---|---|---|
| N/P/Q/R-$Ca^{2+}$ channel | $\alpha_1$ subunit | CACNA1A CACNA1B CACNA1E | Cacophony | UNC-2 | Pore-forming subunit of voltage-gated calcium channel | Episodic ataxia-typeII; Spinocerebellar ataxia typeVI Seizures; Juvenile myoclonic epilepsy; Cone dystrophy | Hillman *et al.*, 1991; Mori *et al.*, 1991; Dubel *et* 1992; Escayg *et al.*, 2000; Chu *et al.*, 2001; Jouvenceau *et al.*, 2001; Estevez *et al.*, 2003; Wycisk *et al.*, 2006; Chen *et al.*, 2007; Buraei a Yang, 2010; Catterall, 2010; Pietrobon *et al.*, 20 Dolphin, 2013; Simms and Zamponi, 2014 |
| | $\alpha_2\delta$ subunit | CACNA2D 1-4 | Straightjacket | UNC-36 | Auxiliary subunit of voltage-gated calcium channel | | |
| | β subunit | CACNB1-4 | Ca-β | CCB-1 | Auxiliary subunit of voltage-gated calcium channel | | |
| | γ subunit | CACNG1-8 | - | - | Auxiliary subunit of voltage-gated calcium channel | | |
| ELKS/ERC | | ERC1-2 | Bruchpilot | ELKS-1 | Glutamine, leucine, lysine, and serin-rich protein, formation of presynaptic cytomatrix | - | Ohtsuka *et al.*, 2002; Wang *et al.*, 2002; Wagh *et* 2006; Hida and Ohtsuka, 2010 |
| Complexin | | CPLX1-4 | Cpx | CPX-1 | Vesicle fusion, regulation of SNARE assembly | Parkinson's disease | Harrison and Eastwood, 1998; Reim *et al.*, 2001; Eastwood *et al.*, 2001; Basso *et al.*, 2003; Brose, Südhof, 2013b |
| Munc13 | | UNC13A-D | Unc-13 | UNC-13 | Mammalian homolog of *C. elegans* UNC-13, involved in SV docking/priming | - | Augustin *et al.*, 1999; James and Martin, 2013 |
| Munc-18 | | STXBP1-3 | Rop | UNC-18 | Mammalian homolog of C. elegans UNC-18, involved in SV exocytosis | Epileptic encephalopathy; Mental retardation and epilepsy | Hosono *et al.*, 1992; Toonen and Verhage, 2003; Weimer and Richmond, 2004; Saitsu *et al.*, 2008; Hamdan *et al.*, 2009 |
| SNAP-25 | | SNAP25 | Snap25 | RIC-4 | Synaptosomal-associated protein 25, involved in SV exocytosis | Schizophrenia; epilepsy; attention-deficit/hyperactivity disorder | Bark and Wilson, 1994; Lewis *et al.*, 2003; Faraon *al.*, 2005; Corradini *et al.*, 2009; Mohrmann *et al.*, |
| Syntaxin | | STX1A-B, STX2-8 | Syx1A | UNC-64 | Presynaptic membrane integrated SNARE proteins | Generalized epilepsy with febrile seizures plus-9 | Bennett *et al.*, 1992; Inoue *et al.*, 1992; Lerche *et* 2001; Weber *et al.*, 2008; Schubert *et al.*, 2014; S 2014 |
| RIM | | RIMS1-3 | Drim | UNC-10 | Rab3/27 interact molecule, involved in SV docking/priming | Cone-rod dystrophy | Wang *et al.*, 1997; Kniazeva *et al.*, 1999; Johnson 2003; Mittelstaedt *et al.*, 2010 |
| RIM binding protein | | RIMBP2 | Rbp | RIMB-1 | RIM binding protein, interaction with RIM and other synaptic proteins | - | Wang *et al.*, 2000; Südhof, 2013a |
| Rab3/27 | | RAB3A-C/ RAB27A | Rab3 | RAB-3 | Small G protein family, GDP/GTP exchange protein | - | Geppert and Südhof, 1998; Fischer von Mollard *e* 1991 |
| Synaptobrevin | | VAMP1-8 | nSyb | SNB-1 | SV associated SNARE proteins, involved in SV exocytosis | Spastic ataxia | Baumert *et al.*, 1989; Bourassa *et al.*, 2012; Shin, |
| Synapsin | | SYN1-3 | Synapsin | SNN-1 | SV-associated protein, component of filaments linking SVs | X-linked partial epilepsy with variable learning disabilities and behavioral disorders; autism | Greengard, 1988; Sudhof *et al.*, 1989; Bykhovska 2011; Fassio *et al.*, 2011 |
| Synaptotagmin | | SYT1 | Syt1 | SNT-1 | SV-associated protein, calcium sensor involved in SV exocytosis | Schizophrenia | Perin *et al.*, 1991; Laruelle and Abi-Dargham, 19 Dean, 2000; Südhof, 2013a; Südhof, 2013b |
| Bassoon | | BSN | - | - | Component of presynaptic cytomatrix, formation and stabilization of presynaptic active zone | - | tom Dieck *et al.*, 1998; Kononenko et al., 2013 |
| Liprin-α | | PPFIA1-4 | Liprin-α | SYD-2 | Member of the LAR protein tyrosine phosphatase-interacting protein (liprin) family, regulates synapse maturation | - | Serra-Pagès *et al.*, 1998; Spangler and Hoogenra 2007; |
| Piccolo | | PCLO | Fife | F45E4.3 | Regulation of SV clustering and exocytosis | Major depressive disorder; Bioplar disorder | Cases-Langhoff *et al.*, 1996; Wang *et al.*, 1999; Bochdanovits *el al.*, 2009; Sullivan *et al.*, 2009; Choi *et al.*, 2011; Gundelfinger and Feitová, 2012 |
| AP2 adaptor complex | | AP2A1, AP2B1 | AP-2α | DPY-23 | Adaptor proteins involved in clathrin-mediated endocytosis | - | Matsui and Kirchhausen, 1990; Traub, 2003 |
| Clathrin Complex | | CLTC CLTA/B | Chc Clc | CHC-1 - | Endocytic scaffolding | - | Pearse, 1976; Kirchhausen *et al.*, 2014 |
| Dynamin | | DNM1-3 | Shibire | DYN-1 | GTPase family, involved in SV endocytosis | Charcot-Marie-Tooth disease | Shpetner and Vallee, 1989; Bitoun *et al.*, 2005; Z and Vance, 2006; Fabrizi *et al.*, 2007; Gallardo *e* 2008; Ferguson and Pietro De Camilli, 2012 |

Figure 34 **A Highly Conserved Network of Proteins Organizes Presynaptic Function.**
Presynaptic proteins can be grouped into zones within the AZ based on studies of their location. Although the structural complexity of the presynapse is not illustrated (see Figure1), it can be generally divided into the dense projection (orange), an AZ-proximal zone extending to approximately 50 nm from the membrane (green), an AZ-distal zone extending to approximately 100 nm from the membrane (blue), the peri-active zone beyond the electron dense AZ

membrane (gray), and SVs that may transiently occupy any of the other zones. Presynaptic proteins discussed in this review are grouped according to their predominant localization and described in detail. For each molecule, conservation in multiple species is indicated with the gene name from humans, flies, and worms. Links between presynaptic proteins and human neurological disorders are summarized.
Figure and corresponding legend from Bruckner et al., 2015

BRP is the *Drosophila* homolog of ELKS (glutamine -E, leucine -L, lysine -K and serin -S, -rich protein)/ ERC (ELKS/Rab6-interacting/CAST=cytomatrix at the active zone-associated structural protein), a family of proteins which contains several coiled-coil domains and interact with $Ca^{2+}$ channels at synapses (Kittel et al., 2006; Kiyonaka et al., 2012; C. Liu et al., 2014). Vertebrates comprise two *erc* genes leading to the expression of several isoforms of which two are brain-specific (ERC2 and ERC1b). *Drosophila* has a single *brp* locus from which several isoforms are transcribed, among the two major isoforms with 190 kDa and 170 kDa, respectively (Matkovic et al., 2013). As already mentioned, the BRP N-term is homolog to vertebrate ERC, whereas the large coiled-coil regions at the C-term resemble the scaffolding proteins Bassoon and Piccolo, which are in *Drosophila* only partially conserved in the protein Fife (see below for details concerning Piccolo, Bassoon and Fife). BRP is an integral component of the electron-dense T-Bar at the AZ in *Drosophila* and promotes AZ assembly, $Ca^{2+}$ channel clustering and thereby indirectly also SV release (Kittel, 2006, Fouquet, 2009), and determines the size of the RRP (Matkovic et al., 2013). In vertebrates, the interaction of ERC with RIM1, Piccolo and Bassoon leads to a large complex at the synapse which also includes Unc13 (Hida & Ohtsuka, 2010). At inhibitory synapses, a potential role for ERC1 in the regulation of the RRP size was postulated (Kaeser et al., 2009), and ERC2 knockout mice have a reduced amount of $Ca^{2+}$ channels and smaller AZs at ribbon-type synapses of photoreceptors (Dieck et al., 2012).

RIM (Rab3-interacting molecule) is an evolutionary conserved scaffold protein at AZs that has a binding site for Rab3 (Koushika et al., 2001; Y. Wang et al., 1997). The brain comprises seven isoforms encoded in four genes, whereas *Drosophila* encodes a single RIM gene (Mittelstaedt et al., 2010; Y. Wang et al., 2002). RIM proteins bind $Ca^{2+}$-channels and recruit them to sites of release (Grabner et al., 2015; Han et al., 2015; Kaeser et al., 2011). Additionally, RIM proteins interact with Munc13 and facilitate SV docking, priming and tethering (Betz et al., 2001; Deng et al., 2011; Fernández-Busnadiego et al., 2013; Schoch et al., 2002). Loss of RIM in *Drosophila* as well as RIM1/2 double knockout in mice reduces neurotransmitter release, leads to reduced $Ca^{2+}$-influx into the presynaptic terminal and a reduced RRP (Han et al., 2011; Kaeser et al., 2011; Müller et al., 2012). In vertebrates, RIMs are scaffolding proteins that act as central organizers at the AZ which have binding sites for key components of the AZ including Unc13, ELKS/ERC, Bassoon/Piccolo, Liprin-α, $Ca^{2+}$ channels (X. Wang et al., 2009).

RBP (RIM-binding protein) binds to RIM as well as to $Ca^{2+}$ channels both in mammals and *Drosophila*. However, mammals have three *rbp* loci, whereas *Drosophila* has a single *rbp* gene (*drbp*). Nonetheless, all RBP proteins contain three SH3-domains and two to three contiguous fibronectin type III domains (Mittelstaedt & Schoch, 2007). In *Drosophila*, loss of DRBP leads to defective $Ca^{2+}$ channel distribution, impaired $Ca^{2+}$ influx, reduced SV docking, and defects in cytomatrix organization. Consistently, evoked fusion is severely impaired, whereas spontaneous fusion is unaltered ( Liu et al., 2011). RBP is a central part of a functional AZ cytomatrix not only in flies, but also in mammals (Acuna et al., 2015; Davydova et al., 2014) and is necessary for recruitment of release machinery components and proper localization of $Ca^{2+}$ channels at release sites to establish reliable synchronous SV fusion.

Rab3 is an evolutionary conserved small GTPase, which on the one hand was described to play a role in SV cycling (Nonet et al., 1997; Südhof, 2004). In *Drosophila* on the other hand Rab3 was shown to regulate the presynaptic distribution of AZ components. Here Rab3 deletion leads to fewer but significantly larger presynaptic AZs with enhanced release probability (Graf et al., 2009). Investigation with Rab3A, Rab3B, Rab3C, and Rab3D quadruple knockout mice revealed that Rab3 increases in the release probability of a subset of SV in the RRP (Schlüter et al., 2006). One explanation is that Rab3 recruits additional components of the release machinery at certain synapses to increase efficiency of release at those sites (Schlüter et al., 2006), consistent with the role of Rab3 in *Drosophila* where it is required for normal distribution of AZ components (Graf et al., 2009). Recently, it was found that GTP-binding is required for Rab3-localization to synapses and its function for distributing AZ components to release sites. However, the GTPase domain is unnecessary for this function, while membrane-attachment of the protein is essential. Whether AZ components are distributed via a mechanism which docks their transport vesicles at nascent release sites in a Rab3-dependent process remains to be determined (S. Chen et al., 2015; Shapira et al., 2003).

Piccolo (Pcl) and Bassoon (Bsn) are large scaffolding proteins at vertebrate synapses with a very similar structure containing N-terminally located zinc finger domains followed by coiled-coil domains. Though the loss of Pcl had no effect on synapse functionality or neuronal survival in cultured neurons and acute slices (Mukherjee et al., 2010), a partial knockout of Bsn disrupted the adhesion of the ribbon in photoreceptor synapses to the membrane and caused reduced neurotransmitter release (Altrock et al., 2003). The same effect was observed after *in vivo* knockdown of Piccolino, a Pcl splice variant selectively found in sensory ribbon synapses of the eye and ear (Regus-Leidig et al., 2013, 2014). It turned out Pcl and Bsn maintain synapse integrity by regulating protein ubiquitination and degradation (Waites et al., 2013 commented in N. Kononenko,

Pechstein, & Haucke, 2013). Furthermore, synaptic depression during high-frequency train recordings at the cerebellar mossy fiber boutons in Bsn-deficient mice were reported (Hallermann, Fejtova, et al., 2010). Thus, Bsn and Pcl seem to be involved in SV refilling at release sites by guiding SV from the backfield of the synapse to the AZ. The *Drosophila* homolog of Pcl is Fife, and its deletion causes detachment of T-Bars from the plasma membrane and a significant reduction of synaptic transmission (Bruckner et al., 2012).

$Ca^{2+}$ channels are oligomeric protein structures that consists of several subunits ($\alpha_1$, $\alpha_2\delta$, $\beta_{1-4}$, $\gamma$). The $\alpha_1$ subunit, however, is the major component of this family of ion-channels as it includes the four homologous I-IV domains which each contain six transmembrane α-helices forming the current-conducting pore (reviewed in Catterall et al., 2005). The other subunits have mainly regulatory functions. $Ca^{2+}$ channels are subdivided in the following classes according to their tissue-specific expression or pharmacological sensitivity to $Ca^{2+}$ channel blockers: L-, N-, P/Q- and R-type (Yamakage & Namiki, 2002). They are not structurally identical, but share high similarities. Their opening is triggered by membrane voltage changes which are induced by the arrival of an AP. In *Drosophila*, the voltage operated N/P/Q-type $Ca^{2+}$ channel α1 subunit Cacophony (Cac) is exclusively responsible for evoked release at NMJ AZs and clusters in the center of the BRP labeled AZ (Fouquet et al., 2009; Kawasaki et al., 2004; Liu et al., 2011).

Unc18 is an essential component of the core release machinery and absolutely required for SV fusion (M. Verhage et al., 2000). Unc18 is a member of the SM protein family and associates to assembled SNARE complexes and remains there for the whole fusion process (Dulubova et al., 2007). This interaction regulates stage-wise SNARE assembly by influencing the open-closed states in the t-SNARE complex (Dawidowski & Cafiso, 2016; L. Ma et al., 2015). The protein is highly conserved; the yeast homologue is Sec1p, in *Drosophila* the homologue is named Rop.

Liprin-α interacts with ELKS and RIM and is thus part of the already mentioned presynaptic complex which also includes Unc13 and RBP. The two variants Liprin-α and -β form heterodimers in vertebrates; however, the protein was mainly studied in *C. elegans* and *D. melanogaster*, where disruption of Liprin-α increased the size of AZs and impaired SV accumulation (Dai et al., 2006; Kaufmann et al., 2002). Furthermore, Liprin-α has been shown to initiate *de novo* synapse assembly in *Drosophila* together with Syd-1. Syd-1 is a RhoGAP and essential for synapse formation in invertebrates by retaining Liprin-α clusters at AZs and clustering of presynaptic Neurexin via a direct interaction at the sites where synapse are newly formed. Liprin-α, Syd-1, their interaction to Neurexin and its postsynaptic binding partner Neuroligin coordinate pre- with postsynaptic

assembly. The vertebrate homolog of Syd-1, mSYD1A, is relevant for SV docking and its loss leads to an impairment in synaptic transmission (Wentzel et al., 2013).

SNAREs: synaptobrevin, SNAP-25 and syntaxin-1 and their role in SV fusion are explained in detail in chapter 1.1.1. "SV fusion".

Spinophilin (Spn) is a conserved scaffold protein and the homologue of murine Neurabin II (Feng et al., 2000; Terry-Lorenzo et al., 2005). It harbors a binding site for the C-Term of Neurexin (Nrx-1) (Muhammad et al., 2015). The presynaptic Nrx-1 binds to post-synaptically localized Neuroligin (Nlg1), thereby bridging the synaptic cleft (Knight et al., 2011; Missler et al., 2012; Südhof, 2008). Nrx-1-Nlg1 signaling mediates early assembly processes of newly forming synaptic scaffolds, a process which is regulated by presynaptic Syd-1 (homologue of *C. elegans* Synapse-defective 1) (Owald et al., 2012). During the *de novo* formation of synapses Spn functions antagonistic to Syd-1. *syd-1* mutants, as well as *nrx-1* and *nlg1* mutants show a reduced number, but atypically large AZ. Contrarily, *spn* mutants exhibit an increased number of AZ, which are smaller in size. Thus, the trans-synaptic Nrx-1 –Nlg1 signaling is tightly regulated by Syd-1 and Spn (Muhammad et al., 2015). Additionally, Spn tunes presynaptic release of neurotransmitter (see chapter 4.6, "Spinophilin regulates active Zone number, size and function"). In summary, Spinophilin influences size and number of AZs during development as well as their functionality.

## 6.2. Abbreviations

| | |
|---|---|
| aa | amino acid |
| AMPAR | (α-amino-3-hydroxy-5-methyl-4-isoxazolepropionic acid receptor |
| AP | action potential |
| AZ | active zone |
| Bapta-AM | 1,2-bis(2-aminophenoxy)ethane -N,N,N‘,N‘-tetraacetic acid - acetoxymethyl ester |
| BLAST | Basic Local Alignment Search Tool |
| BRP | Bruchpilot |
| $Ca^{2+}$ | calcium ion |
| Cac | Cacophony |
| CaM | Calmodulin |
| CASK | calcium/calmodulin-dependent serine protein kinase |
| CAST | CAZ-associated Structural protein |
| CAZ | cytomatrix at the active zone |
| cDNA | complementary DNA |
| ChR | Channelrhodopsin |
| CNS | central nervous system |
| CSP | Cysteine-string protein |
| DAG | Diacylglycerol |
| DMSO | Dimethyl sulfoxide |
| DNA | deoxyribonucleic acid |
| eEPSC | evoked excitatory postsynaptic current |
| eEJC | evoked excitatory junctional current |
| EGTA-AM | ethylene glycol-bis(2-aminoethylether)-N,N,N‘,N‘-tetraacetic acid - acetoxymethyl ester |
| ELKS | glutamate (E), leucine (L), lysine (K), and serine (S) rich protein |
| EM | electron microscopy |
| EMS | Ethyl methanesulfonate |
| ERC | ELKS/Rab6-interacting protein/CAST |
| ERG | electroretinography |
| EST | expressed sequence tag |
| F-actin | filamentous Actin |
| FL | full length |

| | |
|---|---|
| FRAP | fluorescence recovery after photobleaching |
| FRP | fast-releasable pool |
| FS | freeze substitution |
| GAL4 | a yeast-specific transcription factor |
| GABA | gamma-Aminobutyric acid |
| GAP | GTPase-activating protein |
| GEF | Guanine nucleotide exchange factor |
| GFP | green fluorescent protein |
| GKAP | guanylate kinase-associated protein |
| GTP | Guanosine triphosphate |
| GluR | glutamate receptor |
| HL3 | hemolymph-like saline |
| HPF | high-pressure freeze |
| ISI | interstimulus interval |
| $K_D$ | Diffusion constant |
| kDa | kilodalton |
| K[on] | binding rate constant |
| LED | light emitting diode |
| LTD | long-term depression |
| LTP | long-term potentiation |
| LRRTM | leucine rich repeat transmembrane protein family |
| mEPSC | miniature excitatory postsynaptic current |
| mEJC | miniature excitatory junctional current |
| Nlg | Neuroligin |
| NMDAR | N-methyl-D-aspartate receptor |
| NMJ | neuromuscular junction |
| Nrx | Neurexin |
| NSF | N-ethylmaleimide-sensitive factor |
| n-Syb | neuronal Synaptobrevin |
| PCR | Polymerase Chain Reaction |
| PDZ | PSD-95, Dlg, and ZO-1/2 domain |
| PH | pleckstrin homology domain |
| PI4K | Phosphatidylinositol-4-Kinase |
| PI4P | Phosphatidylinositol-4-phosphate |

| | |
|---|---|
| pp ratio | paired pulse ratio |
| $P_r$ | release probability |
| PSD | post-synaptic density |
| PSF | point spread function |
| Rab | Ras-related in brain |
| Rbcn | Rabconnectin |
| RBP | Rim-binding-protein |
| RIM | Rab3-interacting-molecule |
| RNA | ribonucleic acid |
| RNAi | RNA interference |
| ROI | region of interest |
| Rop | Ras opposite |
| RP | recycling pool |
| RFP | red fluorescent protein |
| RRP | readily releasable pool |
| RtP | resting pool |
| SALM | synaptic cell adhesion-like molecule protein family |
| SEM | standard error of the mean |
| SH3 | Src homology 3 domain |
| Shank | SH3 and multiple ankyrin repeat domains protein |
| SNAP-25 | Synaptosomal-associated protein 25 |
| SNARE | soluble N-ethylmaleimide-sensitive factor attachment protein receptor |
| Spn | Spinophilin |
| SRP | slow releasable pool |
| STED | stimulated emission depletion microscopy |
| STP | short-term plasticity |
| SV | synaptic vesicle |
| Syb | Synaptobrevin |
| Syd | synapse defective mutants |
| SynCAM1 | Synaptic Cell Adhesion Molecule 1 |
| TEVC | two-electrode voltage clamp |
| TRP | total recycling pool |
| UAS | upstream activating sequence |
| unc | uncoordinated mutants |

| | |
|---|---|
| VAMP | vesicle-associated membrane protein |
| VGCC | voltage-gated $Ca^{2+}$ channel |
| Y2H | yeast-two-hybrid |

## 6.3. Figure Index

## 6.4. Acknowledgements

First, I would like to thank Prof. Dr. Stephan Sigrist, for the opportunity to conduct my PhD thesis in his lab, and his supervision and support.

I would like to express my gratitude to the 2nd reviewer of this PhD Thesis, Prof. Dr. Hans-Joachim Pflüger.

I am particularly grateful to Dr. Alexander Walter, for sharing his knowledge with me, for the productive discussions, and for the great teamwork and scientific guidance.

Special thanks to Dr. Harald Depner, Dr. Tanja Matkovic, Mathias Böhme, Dr. Astrid Petzoldt, Christine Quentin, Dr. Suneel Reddy, Dr. Karzan Muhammad, Dr. Stefanie Rosa, and Anastasia Stawrakakis for the support and teamwork.

Many thanks go to Dr. Shigeki Watanabe and AG Rosenmund, especially Berit Söhl-Kielczynski and Shu-Wen Chang, for the great support to establish the flash-freeze protocol in *Drosophila* larvae. In this context, many thanks go to Dr. Thorsten Mielke, Jörg Bürger, and Beatrix Fauler at the electron microscopy facility at the MPI for Molecular Genetics and to Dima Puchkov at the Leibniz-Institute for Molecular Pharmacology, for the teaching, help and support on countless hours at the EM.

Thanks to my students and colleagues Leandra Hahn, Janine Lützkendorf, Andreas Grasskamp, Karolin Holzwarth, and Dominique Dufour Bergeron – it was a pleasure to work with you.

Likewise, many thanks go to Malou Mampell, Eva Michael, Torsten Götz, Meida Jusyte, Sabine Hahn, Gabi Grüschow, Anthony McCarthy and Frau Stübner for our teamwork and the pleasant working atmosphere.

I thank Agnieszka Omodeo and Dr. Annemarie Hofmann, for their unconditional help in solving diverse questions concerning fly anatomy or FU administration challenges.

I thank the NeuroCure office and Antje Forströer for their great patience and constantly being the last resort in cases of big and small emergencies.

Furthermore, I would like to thank all lab members for the constant support. Last but not least, I appreciate the shared materials, chemicals and equipment, above all AG Haucke closely followed by AG Rosenmund, which substantially helped to conduct the work.

I wish to express my gratitude to my fiancé Daniel Beis, for the unconditional support, love and patience during the time of this PhD Thesis.

I am grateful to my parents and sister, their continuous and unrestricted support contributed importantly to the completion of this work.

## 6.5. Curriculum Vitae

The online version does not contain the CV due to data privacy protection.

Publications

- Matkovic et al., The Bruchpilot cytomatrix determines the size of the readily releasable pool of synaptic vesicles, JCB 2013
- Muhammad et al., Presynaptic spinophilin tunes neurexin signalling to control active zone architecture and function, Nat. Comm. 2015
- Böhme*, Beis* et al., Scaffold complexes differentially accumulate Unc13 isoforms to tune $Ca^{2+}$ channel-synaptic vesicle coupling within single active zones, Nat. Neurosc., 2016

## 6.6. References

Aberle, H., Haghighi, A. P., Fetter, R. D., McCabe, B. D., Magalhães, T. R., & Goodman, C. S. (2002). wishful thinking Encodes a BMP Type II Receptor that Regulates Synaptic Growth in Drosophila. *Neuron*, *33*(4), 545–558. http://doi.org/10.1016/S0896-6273(02)00589-5

Ackermann, F., Waites, C. L., & Garner, C. C. (2015). Presynaptic active zones in invertebrates and vertebrates. *EMBO Reports*, *16*(8), 1–16. http://doi.org/10.15252/embr.201540434

Acuna, C., Liu, X., Gonzalez, A., & Südhof, T. C. (2015). RIM-BPs Mediate Tight Coupling of Action Potentials to $Ca^{2+}$-Triggered Neurotransmitter Release. *Neuron*, *87*(6), 1234–1247. http://doi.org/10.1016/j.neuron.2015.08.027

Adler, E., Augustine, G., Duffy, S., & Charlton, M. (1991). Alien intracellular calcium chelators attenuate neurotransmitter release at the squid giant synapse. *The Journal of Neuroscience*, *11*(6), 1496–1507.

Ahmed, M. S., & Siegelbaum, S. A. (2009). Recruitment of N-Type Ca(2+) channels during LTP enhances low release efficacy of hippocampal CA1 perforant path synapses. *Neuron*, *63*(3), 372–85. http://doi.org/10.1016/j.neuron.2009.07.013

Alabi, A. A., & Tsien, R. W. (2012). Synaptic vesicle pools and dynamics. *Cold Spring Harbor Perspectives in Biology*, *4*(8). http://doi.org/10.1101/cshperspect.a013680

Alabi, A. A., & Tsien, R. W. (2013). Perspectives on Kiss-and-Run: Role in Exocytosis, Endocytosis, and Neurotransmission. *Annu. Rev. Physiol*, *75*, 393–422. http://doi.org/10.1146/annurev-physiol-020911-153305

Altrock, W. D., tom Dieck, S., Sokolov, M., Meyer, A. C., Sigler, A., Brakebusch, C., … Gundelfinger, E. D. (2003). Functional Inactivation of a Fraction of Excitatory Synapses in Mice Deficient for the Active Zone Protein Bassoon. *Neuron*, *37*(5), 787–800. http://doi.org/10.1016/S0896-6273(03)00088-6

Andlauer, T. F. M., & Sigrist, S. J. (2012). Quantitative analysis of Drosophila larval neuromuscular junction morphology. *Cold Spring Harbor Protocols*, *2012*(4), 490–3. http://doi.org/10.1101/pdb.prot068601

Aravamudan, B., Fergestad, T., Davis, W. S., Rodesch, C. K., & Broadie, K. (1999). Drosophila UNC-13 is essential for synaptic transmission. *Nature Neuroscience*, *2*(11), 965–71.

http://doi.org/10.1038/14764

Armitage, B. A., & Siegelbaum, S. A. (1998). Presynaptic Induction and Expression of Homosynaptic Depression at Aplysia Sensorimotor Neuron Synapses. *J. Neurosci.*, *18*(21), 8770–8779. Retrieved from http://www.jneurosci.org/content/18/21/8770.long

Atluri, P. P., & Regehr, W. G. (1998). Delayed Release of Neurotransmitter from Cerebellar Granule Cells. *J. Neurosci.*, *18*(20), 8214–8227. Retrieved from http://www.jneurosci.org/content/18/20/8214.long

Attrill, H., Falls, K., Goodman, J. L., Millburn, G. H., Antonazzo, G., Rey, A. J., & Marygold, S. J. (2015). FlyBase: establishing a Gene Group resource for Drosophila melanogaster. *Nucleic Acids Research*, *44*(D1), D786–92. http://doi.org/10.1093/nar/gkv1046

Atwood, H., Govind, C., & Wu, C. (1993). Differential ultrastructure of synaptic terminals on ventral longitudinal abdominal muscles in Drosophila larvae. *J Ournal of Neurobiology*, *24*(8), 1008–1024.

Audhya, A., Foti, M., & Emr, S. D. (2000). Distinct Roles for the Yeast Phosphatidylinositol 4-Kinases, Stt4p and Pik1p, in Secretion, Cell Growth, and Organelle Membrane Dynamics. *Molecular Biology of the Cell*, *11*(8), 2673–2689. http://doi.org/10.1091/mbc.11.8.2673

Augustin, I., Betz, A., Herrmann, C., Jo, T., & Brose, N. (1999). Differential expression of two novel Munc13 proteins in rat brain. *The Biochemical Journal*, *337 ( Pt 3*, 363–71. Retrieved from http://www.pubmedcentral.nih.gov/articlerender.fcgi?artid=1219986&tool=pmcentrez&rendertype=abstract

Augustin, I., Rosenmund, C., Südhof, T. C., & Brose, N. (1999). Munc13-1 is essential for fusion competence of glutamatergic synaptic vesicles. *Nature*, *400*, 457–461. http://doi.org/10.1038/22768

Balakrishnan, S. S., Basu, U., & Raghu, P. (2015). Phosphoinositide signalling in Drosophila. *Biochimica et Biophysica Acta - Molecular and Cell Biology of Lipids*, *1851*(6), 770–784. http://doi.org/10.1016/j.bbalip.2014.10.010

Banke, T. G., Bowie, D., Lee, H.-K., Huganir, R. L., Schousboe, A., & Traynelis, S. F. (2000). Control of GluR1 AMPA Receptor Function by cAMP-Dependent Protein Kinase. *J. Neurosci.*, *20*(1), 89–102. Retrieved from http://www.jneurosci.org/content/20/1/89.long

Basu, J., Shen, N., Dulubova, I., Lu, J., Guan, R., Guryev, O., … Rizo, J. (2005). A minimal domain responsible for Munc13 activity. *Nature Structural & Molecular Biology*, *12*(11), 1017–1018. http://doi.org/10.1038/nsmb1001

Bear, M., & Malenka, R. (1994). Synaptic plasticity: LTP and LTD. *Current Opinion in Neurobiology*, *4*(3), 389–399.

Betz, A., Ashery, U., Rickmann, M., Augustin, I., Neher, E., Südhof, T. C., … Brose, N. (1998). Munc13-1 Is a Presynaptic Phorbol Ester Receptor that Enhances Neurotransmitter Release. *Neuron*, *21*(1), 123–136. http://doi.org/10.1016/S0896-6273(00)80520-6

Betz, A., Thakur, P., Junge, H. J., Ashery, U., Rhee, J. S., Scheuss, V., … Brose, N. (2001). Functional interaction of the active zone proteins Munc13-1 and RIM1 in synaptic vesicle priming. *Neuron*, *30*(1), 183–196. http://doi.org/10.1016/S0896-6273(01)00272-0

Bradley, R., Harris, R., & Jenner, P. (2006). *The Fly Neuromuscular Junction*.

Brand, A., & Perrimon, N. (1993). Targeted gene expression as a means of altering cell fates and generating dominant phenotypes. *Development*, *118*(2), 401–415. Retrieved from http://dev.biologists.org/content/118/2/401.long

Brose, N., Hofmann, K., Hata, Y., & Sudhof, T. C. (1995). Mammalian Homologues of Caenorhabditis elegans unc-13 Gene Define Novel Family of C2-domain Proteins. *Journal of Biological Chemistry*, *270*(42), 25273–25280. http://doi.org/10.1074/jbc.270.42.25273

Brose, N., Petrenko, a G., Südhof, T. C., & Jahn, R. (1992). Synaptotagmin: a calcium sensor on the synaptic vesicle surface. *Science (New York, N.Y.)*, *256*(5059), 1021–1025. http://doi.org/10.1126/science.1589771

Brown, D. A., & Griffith, W. H. (1983). Calcium-activated outward current in voltage-clamped hippocampal neurones of the guinea-pig. *The Journal of Physiology*, *337*(1), 287–301. http://doi.org/10.1113/jphysiol.1983.sp014624

Bruckner, J. J., Gratz, S. J., Slind, J. K., Geske, R. R., Cummings, A. M., Galindo, S. E., … O'Connor-Giles, K. M. (2012). Fife, a Drosophila Piccolo-RIM homolog, promotes active zone organization and neurotransmitter release. *The Journal of Neuroscience : The Official Journal of the Society for Neuroscience*, *32*(48), 17048–58. http://doi.org/10.1523/JNEUROSCI.3267-12.2012

Bruckner, J. J., Zhan, H., & O'Connor-Giles, K. M. (2015). Advances in imaging ultrastructure yield

new insights into presynaptic biology. *Frontiers in Cellular Neuroscience*, *9*(May), 196. http://doi.org/10.3389/fncel.2015.00196

Bykhovskaia, M. (2011). Synapsin regulation of vesicle organization and functional pools. *Seminars in Cell & Developmental Biology*, *22*(4), 387–92. http://doi.org/10.1016/j.semcdb.2011.07.003

Catterall, W. a, Perez-Reyes, E., Snutch, T. P., & Striessnig, J. (2005). International Union of Pharmacology. XLVIII. Nomenclature and structure-function relationships of voltage-gated calcium channels. *Pharmacological Reviews*, *57*(4), 411–425. http://doi.org/10.1124/pr.57.4.5.units

Chen, S., Gendelman, H. K., Roche, J. P., Alsharif, P., & Graf, E. R. (2015). Mutational analysis of Rab3 function for controlling active zone protein composition at the Drosophila neuromuscular junction. *PLoS ONE*, *10*(8), 1–27. http://doi.org/10.1371/journal.pone.0136938

Chen, Z., Cooper, B., Kalla, S., Varoqueaux, F., & Young, S. M. (2013). The Munc13 proteins differentially regulate readily releasable pool dynamics and calcium-dependent recovery at a central synapse. *The Journal of Neuroscience : The Official Journal of the Society for Neuroscience*, *33*(19), 8336–51. http://doi.org/10.1523/JNEUROSCI.5128-12.2013

Chen, Z., Das, B., Nakamura, Y., DiGregorio, D. A., & Young, S. M. (2015). Ca2+ channel to synaptic vesicle distance accounts for the readily releasable pool kinetics at a functionally mature auditory synapse. *The Journal of Neuroscience : The Official Journal of the Society for Neuroscience*, *35*(5), 2083–100. http://doi.org/10.1523/JNEUROSCI.2753-14.2015

Choquet, D., & Triller, A. (2013). The dynamic synapse. *Neuron*, *80*(3), 691–703. http://doi.org/10.1016/j.neuron.2013.10.013

Cummings, D. D., Wilcox, K. S., & Dichter, M. A. (1996). Calcium-Dependent Paired-Pulse Facilitation of Miniature EPSC Frequency Accompanies Depression of EPSCs at Hippocampal Synapses in Culture. *J. Neurosci.*, *16*(17), 5312–5323. Retrieved from http://www.jneurosci.org/content/16/17/5312.long

Dai, Y., Taru, H., Deken, S. L., Grill, B., Ackley, B., Nonet, M. L., & Jin, Y. (2006). SYD-2 Liprin-alpha organizes presynaptic active zone formation through ELKS. *Nature Neuroscience*, *9*(12), 1479–87. http://doi.org/10.1038/nn1808

Davletov, B., & Südhof, T. (1993). A single C2 domain from synaptotagmin I is sufficient for high affinity Ca2+/phospholipid binding. *The Journal of Biological Chemistry*, *268*(35), 26386–90.

Davydova, D., Marini, C., King, C., Klueva, J., Bischof, F., Romorini, S., … Fejtova, A. (2014). Bassoon specifically controls presynaptic P/Q-type Ca(2+) channels via RIM-binding protein. *Neuron*, *82*(1), 181–94. http://doi.org/10.1016/j.neuron.2014.02.012

Dawidowski, D., & Cafiso, D. S. (2016). Munc18-1 and the Syntaxin-1 N Terminus Regulate Open-Closed States in a t-SNARE Complex. *Structure (London, England : 1993)*, *24*(3), 392–400. http://doi.org/10.1016/j.str.2016.01.005

Deák, F., Schoch, S., Liu, X., Südhof, T. C., & Kavalali, E. T. (2004). Synaptobrevin is essential for fast synaptic-vesicle endocytosis. *Nature Cell Biology*, *6*(11), 1102–8. http://doi.org/10.1038/ncb1185

Deák, F., Xu, Y., Chang, W.-P., Dulubova, I., Khvotchev, M., Liu, X., … Rizo, J. (2009). Munc18-1 binding to the neuronal SNARE complex controls synaptic vesicle priming. *The Journal of Cell Biology*, *184*(5), 751–64. http://doi.org/10.1083/jcb.200812026

del Castillo, J., & Katz, B. (1954). Quantal components of the end-plate potential. *The Journal of Physiology*, *124*(3), 560–573. http://doi.org/10.1113/jphysiol.1954.sp005129

Deng, L., Kaeser, P. S., Xu, W., & Südhof, T. C. (2011). RIM proteins activate vesicle priming by reversing autoinhibitory homodimerization of Munc13. *Neuron*, *69*(2), 317–31. http://doi.org/10.1016/j.neuron.2011.01.005

Denker, A., & Rizzoli, S. O. (2010). Synaptic vesicle pools: An update. *Frontiers in Synaptic Neuroscience*, *2*(OCT), 1–12. http://doi.org/10.3389/fnsyn.2010.00135

Depner, H., Lützkendorf, J., Babkir, H. A., Sigrist, S. J., & Holt, M. G. (2014). Differential centrifugation-based biochemical fractionation of the Drosophila adult CNS. *Nature Protocols*, *9*(12), 2796–808. http://doi.org/10.1038/nprot.2014.192

Di Paolo, G., Moskowitz, H. S., Gipson, K., Wenk, M. R., Voronov, S., Obayashi, M., … De Camilli, P. (2004). Impaired PtdIns(4,5)P2 synthesis in nerve terminals produces defects in synaptic vesicle trafficking. *Nature*, *431*(7007), 415–22. http://doi.org/10.1038/nature02896

Dickman, D. K., Lu, Z., Meinertzhagen, I. a., & Schwarz, T. L. (2006). Altered synaptic development and active zone spacing in endocytosis mutants. *Current Biology*, *16*(6), 591–598. http://doi.org/10.1016/j.cub.2006.02.058

Dietzl, G., Chen, D., Schnorrer, F., Su, K.-C., Barinova, Y., Fellner, M., … Dickson, B. J. (2007). A genome-wide transgenic RNAi library for conditional gene inactivation in Drosophila. *Nature*, *448*(7150), 151–6. http://doi.org/10.1038/nature05954

Dulubova, I., Khvotchev, M., Liu, S., Huryeva, I., Südhof, T. C., & Rizo, J. (2007). Munc18-1 binds directly to the neuronal SNARE complex. *Proceedings of the National Academy of Sciences of the United States of America*, *104*(8), 2697–702. http://doi.org/10.1073/pnas.0611318104

Dutta Roy, R., Stefan, M. I., & Rosenmund, C. (2014). Biophysical properties of presynaptic short-term plasticity in hippocampal neurons: insights from electrophysiology, imaging and mechanistic models. *Frontiers in Cellular Neuroscience*, *8*(May), 141. http://doi.org/10.3389/fncel.2014.00141

Eggermann, E., Bucurenciu, I., Goswami, S. P., & Jonas, P. (2011). Nanodomain coupling between Ca2+ channels and sensors of exocytosis at fast mammalian synapses. *Nature Reviews Neuroscience*, *13*(1), 7–21. http://doi.org/10.1038/nrn3125

Ehmann, N., van de Linde, S., Alon, A., Ljaschenko, D., Keung, X. Z., Holm, T., … Kittel, R. J. (2014). Quantitative super-resolution imaging of Bruchpilot distinguishes active zone states. *Nature Communications*, *5*, 1–12. http://doi.org/10.1038/ncomms5650

Fedchyshyn, M. J., & Wang, L.-Y. (2005). Developmental transformation of the release modality at the calyx of Held synapse. *The Journal of Neuroscience : The Official Journal of the Society for Neuroscience*, *25*(16), 4131–40. http://doi.org/10.1523/JNEUROSCI.0350-05.2005

Feng, J., Yan, Z., Ferreira, A., Tomizawa, K., Liauw, J. A., Zhuo, M., … Greengard, P. (2000). Spinophilin regulates the formation and function of dendritic spines. *Proceedings of the National Academy of Sciences of the United States of America*, *97*(16), 9287–92. Retrieved from http://www.pubmedcentral.nih.gov/articlerender.fcgi?artid=16860&tool=pmcentrez&rendertype=abstract

Fernandez-Alfonso, T., & Ryan, T. A. (2008). A heterogeneous “resting” pool of synaptic vesicles that is dynamically interchanged across boutons in mammalian CNS synapses. *Brain Cell Biology*, *36*(1-4), 87–100. http://doi.org/10.1007/s11068-008-9030-y

Fernández-Busnadiego, R., Asano, S., Oprisoreanu, A. M., Sakata, E., Doengi, M., Kochovski, Z., …

Lučić, V. (2013). Cryo-electron tomography reveals a critical role of RIM1 α in synaptic vesicle tethering. *Journal of Cell Biology*, *201*(5), 725–740. http://doi.org/10.1083/jcb.201206063

Fernández-Chacón, R., Königstorfer, a, Gerber, S. H., García, J., Matos, M. F., Stevens, C. F., … Südhof, T. C. (2001). Synaptotagmin I functions as a calcium regulator of release probability. *Nature*, *410*(6824), 41–49. http://doi.org/10.1038/35065004

Fouquet, W., Owald, D., Wichmann, C., Mertel, S., Depner, H., Dyba, M., … Sigrist, S. J. (2009). Maturation of active zone assembly by Drosophila Bruchpilot. *Journal of Cell Biology*, *186*(1), 129–145. http://doi.org/10.1083/jcb.200812150

Fowler, M. W., & Staras, K. (2015). Synaptic vesicle pools: Principles, properties and limitations. *Experimental Cell Research*, *335*(2), 150–156. http://doi.org/10.1016/j.yexcr.2015.03.007

Frank, C. A., Kennedy, M. J., Goold, C. P., Marek, K. W., & Davis, G. W. (2006). Mechanisms underlying the rapid induction and sustained expression of synaptic homeostasis. *Neuron*, *52*(4), 663–77. http://doi.org/10.1016/j.neuron.2006.09.029

Gad, H., Löw, P., Zotova, E., Brodin, L., & Shupliakov, O. (1998). Dissociation between Ca2+-Triggered Synaptic Vesicle Exocytosis and Clathrin-Mediated Endocytosis at a Central Synapse. *Neuron*, *21*(3), 607–616. http://doi.org/10.1016/S0896-6273(00)80570-X

Gerber, S. H., Rah, J.-C., Min, S.-W., Liu, X., de Wit, H., Dulubova, I., … Südhof, T. C. (2008). Conformational switch of syntaxin-1 controls synaptic vesicle fusion. *Science (New York, N.Y.)*, *321*(5895), 1507–10. http://doi.org/10.1126/science.1163174

Gorczyca, M., & Budnik, V. (2006). APPENDIX: ANATOMY OF THE LARVAL BODY WALL MUSCLES AND NMJS IN THE THIRD INSTAR LARVAL STAGE. In *The Fly Neuromuscular Junction* (pp. 367–373).

Goswami, S. P., Bucurenciu, I., & Jonas, P. (2012). Miniature IPSCs in hippocampal granule cells are triggered by voltage-gated Ca2+ channels via microdomain coupling. *The Journal of Neuroscience : The Official Journal of the Society for Neuroscience*, *32*(41), 14294–304. http://doi.org/10.1523/JNEUROSCI.6104-11.2012

Göttfert, F., Wurm, C. A., Mueller, V., Berning, S., Cordes, V. C., Honigmann, A., & Hell, S. W. (2013). Coaligned dual-channel STED nanoscopy and molecular diffusion analysis at 20 nm resolution. *Biophysical Journal*, *105*(1), L01–3. http://doi.org/10.1016/j.bpj.2013.05.029

Grabner, C. P., Gandini, M. A., Rehak, R., Le, Y., Zamponi, G. W., & Schmitz, F. (2015). RIM1/2-Mediated Facilitation of Cav1.4 Channel Opening Is Required for Ca2+-Stimulated Release in Mouse Rod Photoreceptors. *The Journal of Neuroscience : The Official Journal of the Society for Neuroscience*, *35*(38), 13133–47. http://doi.org/10.1523/JNEUROSCI.0658-15.2015

Graf, E. R., Daniels, R. W., Burgess, R. W., Schwarz, T. L., & DiAntonio, A. (2009). Rab3 Dynamically Controls Protein Composition at Active Zones. *Neuron*, *64*(5), 663–677. http://doi.org/10.1016/j.neuron.2009.11.002

Graf, E. R., Valakh, V., Wright, C. M., Wu, C., Liu, Z., Zhang, Y. Q., & DiAntonio, A. (2012). RIM promotes calcium channel accumulation at active zones of the Drosophila neuromuscular junction. *The Journal of Neuroscience : The Official Journal of the Society for Neuroscience*, *32*(47), 16586–96. http://doi.org/10.1523/JNEUROSCI.0965-12.2012

Hallermann, S., Fejtova, A., Schmidt, H., Weyhersmüller, A., Silver, R. A., Gundelfinger, E. D., & Eilers, J. (2010). Bassoon speeds vesicle reloading at a central excitatory synapse. *Neuron*, *68*(4), 710–23. http://doi.org/10.1016/j.neuron.2010.10.026

Hallermann, S., Heckmann, M., & Kittel, R. J. (2010). Mechanisms of short-term plasticity at neuromuscular active zones of Drosophila. *HFSP Journal*, *4*(2), 72–84. http://doi.org/10.2976/1.3338710

Hallermann, S., Kittel, R. J., Wichmann, C., Weyhersmüller, A., Fouquet, W., Mertel, S., … Heckmann, M. (2010). Naked dense bodies provoke depression. *The Journal of Neuroscience : The Official Journal of the Society for Neuroscience*, *30*(43), 14340–14345. http://doi.org/10.1523/JNEUROSCI.2495-10.2010

Han, Y., Babai, N., Kaeser, P., Südhof, T. C., & Schneggenburger, R. (2015). RIM1 and RIM2 redundantly determine Ca2+ channel density and readily releasable pool size at a large hindbrain synapse. *Journal of Neurophysiology*, *113*(1), 255–63. http://doi.org/10.1152/jn.00488.2014

Han, Y., Kaeser, P. S., Südhof, T. C., & Schneggenburger, R. (2011). RIM determines Ca2+ channel density and vesicle docking at the presynaptic active zone. *Neuron*, *69*(2), 304–316. http://doi.org/10.1016/j.neuron.2010.12.014

Haucke, V., Neher, E., & Sigrist, S. J. (2011). Protein scaffolds in the coupling of synaptic exocytosis and endocytosis. *Nature Reviews. Neuroscience*, *12*(3), 127–138.

http://doi.org/10.1038/nrn2948

Heerssen, H., Fetter, R. D., & Davis, G. W. (2008). Clathrin dependence of synaptic-vesicle formation at the Drosophila neuromuscular junction. *Current Biology : CB*, *18*(6), 401–9. http://doi.org/10.1016/j.cub.2008.02.055

Henkel, A. W., & Betz, W. J. (1995). Monitoring of Black Widow Spider Venom (BWSV) induced exo- and endocytosis in living frog motor nerve terminals with FM1-43. *Neuropharmacology*, *34*(11), 1397–1406. http://doi.org/10.1016/0028-3908(95)00126-Q

Herrick, D. Z., Sterbling, S., Rasch, K. A., Hinderliter, A., & Cafiso, D. S. (2006). Position of synaptotagmin I at the membrane interface: cooperative interactions of tandem C2 domains. *Biochemistry*, *45*(32), 9668–74. http://doi.org/10.1021/bi060874j

Hida, Y., & Ohtsuka, T. (2010). CAST and ELKS proteins: structural and functional determinants of the presynaptic active zone. *Journal of Biochemistry*, *148*(2), 131–7. http://doi.org/10.1093/jb/mvq065

Holderith, N., Lorincz, A., Katona, G., Rózsa, B., Kulik, A., Watanabe, M., & Nusser, Z. (2012). Release probability of hippocampal glutamatergic terminals scales with the size of the active zone. *Nature Neuroscience*, *15*(7), 988–997. http://doi.org/10.1038/nn.3137

Hosoi, N., Sakaba, T., & Neher, E. (2007). Quantitative analysis of calcium-dependent vesicle recruitment and its functional role at the calyx of Held synapse. *The Journal of Neuroscience : The Official Journal of the Society for Neuroscience*, *27*(52), 14286–14298. http://doi.org/10.1523/JNEUROSCI.4122-07.2007

Hu, Z., Tong, X. J., & Kaplan, J. M. (2013). UNC-13L, UNC-13S, and Tomosyn form a protein code for fast and slow neurotransmitter release in Caenorhabditis elegans. *eLife*, *2013*(2), 1–20. http://doi.org/10.7554/eLife.00967

Hugo, S., Dembla, E., Halimani, M., Matti, U., Rettig, J., & Becherer, U. (2013). Deciphering dead-end docking of large dense core vesicles in bovine chromaffin cells. *The Journal of Neuroscience : The Official Journal of the Society for Neuroscience*, *33*(43), 17123–37. http://doi.org/10.1523/JNEUROSCI.1589-13.2013

Huntwork, S., & Littleton, J. T. (2007). A complexin fusion clamp regulates spontaneous neurotransmitter release and synaptic growth. *Nature Neuroscience*, *10*(10), 1235–7. http://doi.org/10.1038/nn1980

Imig, C., Min, S.-W., Krinner, S., Arancillo, M., Rosenmund, C., Südhof, T. C., … Cooper, B. H. (2014). The Morphological and Molecular Nature of Synaptic Vesicle Priming at Presynaptic Active Zones. *Neuron*, *1*(Ldcv). http://doi.org/10.1016/j.neuron.2014.10.009

Jackman, S. L., Turecek, J., Belinsky, J. E., & Regehr, W. G. (2016). The calcium sensor synaptotagmin 7 is required for synaptic facilitation. *Nature*, *529*(7584), 88–91. http://doi.org/10.1038/nature16507

Jahn, R., & Fasshauer, D. (2012). Molecular machines governing exocytosis of synaptic vesicles. *Nature*, *490*(7419), 201–207. http://doi.org/10.1038/nature11320

Jockusch, W. J., Speidel, D., Sigler, A., S??rensen, J. B., Varoqueaux, F., Rhee, J. S., & Brose, N. (2007). CAPS-1 and CAPS-2 Are Essential Synaptic Vesicle Priming Proteins. *Cell*, *131*(4), 796–808. http://doi.org/10.1016/j.cell.2007.11.002

Kaeser, P. S., Deng, L., Chávez, A. E., Liu, X., Castillo, P. E., & Südhof, T. C. (2009). ELKS2alpha/CAST deletion selectively increases neurotransmitter release at inhibitory synapses. *Neuron*, *64*(2), 227–39. http://doi.org/10.1016/j.neuron.2009.09.019

Kaeser, P. S., Deng, L., Wang, Y., Dulubova, I., Liu, X., Rizo, J., & Südhof, T. C. (2011). RIM proteins tether Ca2+ channels to presynaptic active zones via a direct PDZ-domain interaction. *Cell*, *144*(2), 282–95. http://doi.org/10.1016/j.cell.2010.12.029

Kaeser, P. S., & Regehr, W. G. (2014). Molecular mechanisms for synchronous, asynchronous, and spontaneous neurotransmitter release. *Annual Review of Physiology*, *76*, 333–63. http://doi.org/10.1146/annurev-physiol-021113-170338

Katz, B., & Miledi, R. (1967). The timing of calcium action during neuromuscular transmission. *The Journal of Physiology*, *189*(3), 535–544. http://doi.org/10.1113/jphysiol.1967.sp008183

Kaufmann, N., DeProto, J., Ranjan, R., Wan, H., & Van Vactor, D. (2002). Drosophila liprin-α and the receptor phosphatase Dlar control synapse morphogenesis. *Neuron*, *34*(1), 27–38. http://doi.org/10.1016/S0896-6273(02)00643-8

Kawabe, H., Sakisaka, T., Yasumi, M., Shingai, T., Izumi, G., Nagano, F., … Takai, Y. (2003). A novel rabconnectin-3-binding protein that directly binds a GDP/GTP exchange protein for Rab3A small G protein implicated in Ca2+-dependent exocytosis of neurotransmitter. *Genes to Cells*, *8*(6), 537–546. http://doi.org/10.1046/j.1365-2443.2003.00655.x

Kawasaki, F., Zou, B., Xu, X., & Ordway, R. W. (2004). Active zone localization of presynaptic

calcium channels encoded by the cacophony locus of Drosophila. *The Journal of Neuroscience : The Official Journal of the Society for Neuroscience*, *24*(1), 282–5. http://doi.org/10.1523/JNEUROSCI.3553-03.2004

Keller, D., Babai, N., Kochubey, O., Han, Y., Markram, H., Schürmann, F., & Schneggenburger, R. (2015). An Exclusion Zone for Ca2+ Channels around Docked Vesicles Explains Release Control by Multiple Channels at a CNS Synapse. *PLoS Computational Biology*, *11*(5), e1004253. http://doi.org/10.1371/journal.pcbi.1004253

Khvotchev, M., Dulubova, I., Sun, J., Dai, H., Rizo, J., & Südhof, T. C. (2007). Dual modes of Munc18-1/SNARE interactions are coupled by functionally critical binding to syntaxin-1 N terminus. *The Journal of Neuroscience : The Official Journal of the Society for Neuroscience*, *27*(45), 12147–55. http://doi.org/10.1523/JNEUROSCI.3655-07.2007

Kittel, R. J., Wichmann, C., Rasse, T. M., Fouquet, W., Schmidt, M., Schmid, A., … Sigrist, S. J. (2006). Bruchpilot promotes active zone assembly, Ca2+ channel clustering, and vesicle release. *Science (New York, N.Y.)*, *312*(5776), 1051–1054. http://doi.org/10.1126/science.1126308

Kiyonaka, S., Nakajima, H., Takada, Y., Hida, Y., Yoshioka, T., Hagiwara, A., … Ohtsuka, T. (2012). Physical and functional interaction of the active zone protein CAST/ERC2 and the β-subunit of the voltage-dependent Ca2+ channel. *Journal of Biochemistry*, *152*(2), 149–159. http://doi.org/10.1093/jb/mvs054

Knight, D., Xie, W., & Boulianne, G. L. (2011). Neurexins and neuroligins: recent insights from invertebrates. *Molecular Neurobiology*, *44*(3), 426–40. http://doi.org/10.1007/s12035-011-8213-1

Koch, M., & Holt, M. (2012). Coupling exo- and endocytosis: An essential role for PIP 2 at the synapse. *Biochimica et Biophysica Acta - Molecular and Cell Biology of Lipids*, *1821*(8), 1114–1132. http://doi.org/10.1016/j.bbalip.2012.02.008

Koenig, J. H., & Ikeda, K. (1996). Synaptic vesicles have two distinct recycling pathways. *Journal of Cell Biology*, *135*(3), 797–808. http://doi.org/10.1083/jcb.135.3.797

Kombian, S. B., Hirasawa, M., Mouginot, D., Chen, X., & Pittman, Q. J. (2000). Short-Term Potentiation of Miniature Excitatory Synaptic Currents Causes Excitation of Supraoptic Neurons. *J Neurophysiol*, *83*(5), 2542–2553. Retrieved from http://jn.physiology.org/content/83/5/2542.long

Kononenko, N. L., & Haucke, V. (2015). Molecular Mechanisms of Presynaptic Membrane Retrieval and Synaptic Vesicle Reformation. *Neuron*, *85*(3), 484–496. http://doi.org/10.1016/j.neuron.2014.12.016

Kononenko, N., Pechstein, A., & Haucke, V. (2013). Synaptic requiem: a duet for Piccolo and Bassoon. *The EMBO Journal*, *32*(7), 920–2. http://doi.org/10.1038/emboj.2013.55

Körber, C., & Kuner, T. (2016). Molecular Machines Regulating the Release Probability of Synaptic Vesicles at the Active Zone. *Frontiers in Synaptic Neuroscience*, *8*(March), 5. http://doi.org/10.3389/fnsyn.2016.00005

Koushika, S. P., Richmond, J. E., Hadwiger, G., Weimer, R. M., Jorgensen, E. M., & Nonet, M. L. (2001). A post-docking role for active zone protein Rim. *Nature Neuroscience*, *4*(10), 997–1005. http://doi.org/10.1038/nn732

Kraushaar, U., & Jonas, P. (2000). Efficacy and Stability of Quantal GABA Release at a Hippocampal Interneuron-Principal Neuron Synapse. *J. Neurosci.*, *20*(15), 5594–5607. Retrieved from http://www.jneurosci.org/content/20/15/5594.long

Kuromi, H., Honda, A., & Kidokoro, Y. (2004). Ca2+ Influx through Distinct Routes Controls Exocytosis and Endocytosis at Drosophila Presynaptic Terminals. *Neuron*, *41*(1), 101–111. http://doi.org/10.1016/S0896-6273(03)00815-8

Kuromi, H., & Kidokoro, Y. (2002). Selective Replenishment of Two Vesicle Pools Depends on the Source of Ca2+ at the Drosophila Synapse. *Neuron*, *35*(2), 333–343. http://doi.org/10.1016/S0896-6273(02)00777-8

Kuromi, H., Ueno, K., & Kidokoro, Y. (2010). Two types of Ca2+ channel linked to two endocytic pathways coordinately maintain synaptic transmission at the Drosophila synapse. *The European Journal of Neuroscience*, *32*(3), 335–46. http://doi.org/10.1111/j.1460-9568.2010.07300.x

Lee, J. S., Ho, W.-K., & Lee, S.-H. (2012). Actin-dependent rapid recruitment of reluctant synaptic vesicles into a fast-releasing vesicle pool. *Proceedings of the National Academy of Sciences of the United States of America*, *109*(13), E765–74. http://doi.org/10.1073/pnas.1114072109

Lee, J. S., Ho, W.-K., Neher, E., & Lee, S.-H. (2013). Superpriming of synaptic vesicles after their recruitment to the readily releasable pool. *Proceedings of the National Academy of*

*Sciences of the United States of America*, *110*(37), 15079–84. http://doi.org/10.1073/pnas.1314427110

Li, J., Ashley, J., Budnik, V., & Bhat, M. A. (2007). Crucial role of Drosophila neurexin in proper active zone apposition to postsynaptic densities, synaptic growth, and synaptic transmission. *Neuron*, *55*(5), 741–55. http://doi.org/10.1016/j.neuron.2007.08.002

Lin, D. M., & Goodman, C. S. (1994). Ectopic and increased expression of fasciclin II alters motoneuron growth cone guidance. *Neuron*, *13*(3), 507–523. http://doi.org/10.1016/0896-6273(94)90022-1

Lipstein, N., Sakaba, T., Cooper, B. H., Lin, K.-H., Strenzke, N., Ashery, U., … Brose, N. (2013). Dynamic control of synaptic vesicle replenishment and short-term plasticity by Ca(2+)-calmodulin-Munc13-1 signaling. *Neuron*, *79*(1), 82–96. http://doi.org/10.1016/j.neuron.2013.05.011

Lipstein, N., Schaks, S., Dimova, K., Kalkhof, S., Ihling, C., Kolbel, K., … Jahn, O. (2012). Nonconserved Ca2+/Calmodulin Binding Sites in Munc13s Differentially Control Synaptic Short-Term Plasticity. *Molecular and Cellular Biology*, *32*(22), 4628–4641. http://doi.org/10.1128/MCB.00933-12

Liu, C., Bickford, L. S., Held, R. G., Nyitrai, H., Sudhof, T. C., & Kaeser, P. S. (2014). The active zone protein family ELKS supports Ca2+ influx at nerve terminals of inhibitory hippocampal neurons. *Journal of Neuroscience*, *34*(37), 12289–12303. http://doi.org/10.1523/JNEUROSCI.0999-14.2014

Liu, H., Bai, H., Hui, E., Yang, L., Evans, C. S., Wang, Z., … Chapman, E. R. (2014). Synaptotagmin 7 functions as a Ca 2 + -sensor for synaptic vesicle replenishment. *eLIFE*, 1–18. http://doi.org/10.7554/eLife.01524

Liu, K. S. Y., Siebert, M., Mertel, S., Knoche, E., Wegener, S., Wichmann, C., … Sigrist, S. J. (2011). RIM-Binding Protein, a Central Part of the Active Zone, Is Essential for Neurotransmitter Release. *Science*, *334*(6062), 1565–1569. http://doi.org/10.1126/science.1212991

Lnenicka, G., & Keshishian, H. (2000). Identified motor terminals in Drosophila larvae show distinct differences in morphology and physiology. *Journal of Neurobiology*, *43*(2), 186–197.

Ma, C., Su, L., Seven, A. B., Xu, Y., & Rizo, J. (2013). Reconstitution of the vital functions of

Munc18 and Munc13 in neurotransmitter release. *Science (New York, N.Y.)*, *339*(6118), 421–5. http://doi.org/10.1126/science.1230473

Ma, L., Rebane, A. A., Yang, G., Xi, Z., Kang, Y., Gao, Y., & Zhang, Y. (2015). Munc18-1-regulated stage-wise SNARE assembly underlying synaptic exocytosis. *eLife*, *4*. http://doi.org/10.7554/eLife.09580

MacGillavry, H. D., Kerr, J. M., & Blanpied, T. A. (2011). Lateral organization of the postsynaptic density. *Molecular and Cellular Neuroscience*, *48*(4), 321–331. http://doi.org/10.1016/j.mcn.2011.09.001

Man, K. N. M., Imig, C., Walter, A. M., Pinheiro, P. S., Stevens, D. R., Rettig, J., … Wojcik, S. M. (2015). Identification of a Munc13-sensitive step in chromaffin cell large dense-core vesicle exocytosis. *eLife*, *4*(NOVEMBER2015), 1–28. http://doi.org/10.7554/eLife.10635

Marrus, S. B., Portman, S. L., Allen, M. J., Moffat, K. G., & DiAntonio, A. (2004). Differential localization of glutamate receptor subunits at the Drosophila neuromuscular junction. *The Journal of Neuroscience : The Official Journal of the Society for Neuroscience*, *24*(6), 1406–15. http://doi.org/10.1523/JNEUROSCI.1575-03.2004

Martin, T. F. J. (2015). PI(4,5)$P_2$-binding effector proteins for vesicle exocytosis. *Biochimica et Biophysica Acta*, *1851*(6), 785–93. http://doi.org/10.1016/j.bbalip.2014.09.017

Maruyama, I. N., & Brenner, S. (1991). A phorbol ester/diacylglycerol-binding protein encoded by the unc-13 gene of Caenorhabditis elegans. *Proceedings of the National Academy of Sciences of the United States of America*, *88*(13), 5729–33. Retrieved from http://www.pubmedcentral.nih.gov/articlerender.fcgi?artid=51951&tool=pmcentrez&rendertype=abstract

Matkovic, T., Siebert, M., Knoche, E., Depner, H., Mertel, S., Owald, D., … Sigrist, S. J. (2013). The bruchpilot cytomatrix determines the size of the readily releasable pool of synaptic vesicles. *Journal of Cell Biology*, *202*(4), 667–683.

Matz, J., Gilyan, A., Kolar, A., McCarvill, T., & Krueger, S. R. (2010). Rapid structural alterations of the active zone lead to sustained changes in neurotransmitter release. *Proceedings of the National Academy of Sciences of the United States of America*, *107*(19), 8836–41. http://doi.org/10.1073/pnas.0906087107

McMahon, H. T., & Boucrot, E. (2011). Molecular mechanism and physiological functions of

clathrin-mediated endocytosis. *Nature Reviews. Molecular Cell Biology*, *12*(8), 517–33. http://doi.org/10.1038/nrm3151

Meech, R. W. (1978). Calcium-dependent potassium activation in nervous tissues. *Annual Review of Biophysics and Bioengineering*, *7*, 1–18. http://doi.org/10.1146/annurev.bb.07.060178.000245

Meinrenken, C. J., Borst, J. G. G., & Sakmann, B. (2002). Calcium secretion coupling at calyx of held governed by nonuniform channel-vesicle topography. *The Journal of Neuroscience : The Official Journal of the Society for Neuroscience*, *22*(5), 1648–1667. http://doi.org/22/5/1648 [pii]

Melom, J. E., Akbergenova, Y., Gavornik, J. P., & Littleton, J. T. (2013). Spontaneous and evoked release are independently regulated at individual active zones. *The Journal of Neuroscience : The Official Journal of the Society for Neuroscience*, *33*(44), 17253–63. http://doi.org/10.1523/JNEUROSCI.3334-13.2013

Millar, A. G., Bradacs, H., Charlton, M. P., & Atwood, H. L. (2002). Inverse Relationship between Release Probability and Readily Releasable Vesicles in Depressing and Facilitating Synapses. *J. Neurosci.*, *22*(22), 9661–9667. Retrieved from http://www.jneurosci.org/content/22/22/9661.abstract?ijkey=6f7fe4740b792ae30a14ad8843042c25862faeb3&keytype2=tf_ipsecsha

Missler, M., Südhof, T. C., & Biederer, T. (2012). Synaptic cell adhesion. *Cold Spring Harbor Perspectives in Biology*, *4*(4), a005694. http://doi.org/10.1101/cshperspect.a005694

Missler, M., Zhang, W., Rohlmann, A., Kattenstroth, G., Hammer, R. E., Gottmann, K., & Südhof, T. C. (2003). Alpha-neurexins couple Ca2+ channels to synaptic vesicle exocytosis. *Nature*, *423*(6943), 939–48. http://doi.org/10.1038/nature01755

Mittelstaedt, T., Alvaréz-Baron, E., & Schoch, S. (2010). RIM proteins and their role in synapse function. *Biological Chemistry*, *391*(6), 599–606. http://doi.org/10.1515/BC.2010.064

Mittelstaedt, T., & Schoch, S. (2007). Structure and evolution of RIM-BP genes: identification of a novel family member. *Gene*, *403*(1-2), 70–9. http://doi.org/10.1016/j.gene.2007.08.004

Mohrmann, R., de Wit, H., Connell, E., Pinheiro, P. S., Leese, C., Bruns, D., … Sørensen, J. B. (2013). Synaptotagmin interaction with SNAP-25 governs vesicle docking, priming, and fusion triggering. *The Journal of Neuroscience : The Official Journal of the Society for*

*Neuroscience*, *33*(36), 14417–30. http://doi.org/10.1523/JNEUROSCI.1236-13.2013

Morgan, T. H. (1910). Hybridization in a mutating period in Drosophila. *Proc. Soc. Exp. Biol.*, *7*, 160–161.

Muhammad, K. (2014). *Fine-tuning of Neurexin function in the control of presynaptic active zone organization*.

Muhammad, K., Reddy-Alla, S., Driller, J. H., Schreiner, D., Rey, U., Böhme, M. A., … Sigrist, S. J. (2015). Presynaptic spinophilin tunes neurexin signalling to control active zone architecture and function. *Nature Communications*, *6*, 8362. http://doi.org/10.1038/ncomms9362

Mukherjee, K., Yang, X., Gerber, S. H., Kwon, H.-B., Ho, A., Castillo, P. E., … Südhof, T. C. (2010). Piccolo and bassoon maintain synaptic vesicle clustering without directly participating in vesicle exocytosis. *Proceedings of the National Academy of Sciences of the United States of America*, *107*(14), 6504–9. http://doi.org/10.1073/pnas.1002307107

Müller, M., Liu, K. S. Y., Sigrist, S. J., & Davis, G. W. (2012). RIM controls homeostatic plasticity through modulation of the readily-releasable vesicle pool. *The Journal of Neuroscience : The Official Journal of the Society for Neuroscience*, *32*(47), 16574–85. http://doi.org/10.1523/JNEUROSCI.0981-12.2012

Nagano, F., Kawabe, H., Nakanishi, H., Shinohara, M., Deguchi-Tawarada, M., Takeuchi, M., … Takai, Y. (2002). Rabconnectin-3, a novel protein that binds both GDP/GTP exchange protein and GTPase-activating protein for Rab3 small G protein family. *Journal of Biological Chemistry*, *277*(12), 9629–9632. http://doi.org/10.1074/jbc.C100730200

Nakamura, Y., Harada, H., Kamasawa, N., Matsui, K., Rothman, J. S., Shigemoto, R., … Takahashi, T. (2015). Nanoscale Distribution of Presynaptic Ca2+ Channels and Its Impact on Vesicular Release during Development. *Neuron*, *85*(1), 145–159. http://doi.org/10.1016/j.neuron.2014.11.019

Neer, E. J., Schmidt, C. J., Nambudripad, R., & Smith, T. F. (1994). The ancient regulatory-protein family of WD-repeat proteins. *Nature*, *371*(6495), 297–300. http://doi.org/10.1038/371297a0

Neher, E. (2010). What is rate-limiting during sustained synaptic activity: Vesicle supply or the availability of release sites. *Frontiers in Synaptic Neuroscience*, *2*(SEP), 1–6. http://doi.org/10.3389/fnsyn.2010.00144

Neher, E. (2015). Merits and Limitations of Vesicle Pool Models in View of Heterogeneous Populations of Synaptic Vesicles. *Neuron*, *87*(6), 1131–1142. http://doi.org/10.1016/j.neuron.2015.08.038

Neher, E., & Sakaba, T. (2008). Multiple Roles of Calcium Ions in the Regulation of Neurotransmitter Release. *Neuron*, *59*(6), 861–872. http://doi.org/10.1016/j.neuron.2008.08.019

Nonet, M. L., Staunton, J. E., Kilgard, M. P., Fergestad, T., Hartwieg, E., Horvitz, H. R., … Meyer, B. J. (1997). Caenorhabditis elegans rab-3 Mutant Synapses Exhibit Impaired Function and Are Partially Depleted of Vesicles. *J. Neurosci.*, *17*(21), 8061–8073. Retrieved from http://www.jneurosci.org/content/17/21/8061.long

Owald, D., Fouquet, W., Schmidt, M., Wichmann, C., Mertel, S., Depner, H., … Sigrist, S. J. (2010). A Syd-1 homologue regulates pre- and postsynaptic maturation in Drosophila. *Journal of Cell Biology*, *188*(4), 565–579. http://doi.org/10.1083/jcb.200908055

Owald, D., Khorramshahi, O., Gupta, V. K., Banovic, D., Depner, H., Fouquet, W., … Sigrist, S. J. (2012). Cooperation of Syd-1 with Neurexin synchronizes pre- with postsynaptic assembly. *Nature Neuroscience*, *15*(9), 1219–1226. http://doi.org/10.1038/nn.3183

Pan, B., & Zucker, R. S. (2009). A general model of synaptic transmission and short-term plasticity. *Neuron*, *62*(4), 539–54. http://doi.org/10.1016/j.neuron.2009.03.025

Pandey, U. B., & Nichols, C. D. (2011). Human Disease Models in Drosophila melanogaster and the Role of the Fly in Therapeutic Drug Discovery. *Pharmacological Reviews*, *63*(2), 411–436. http://doi.org/10.1124/pr.110.003293

Park, Y., Seo, J. B., Fraind, A., Pérez-Lara, A., Yavuz, H., Han, K., … Jahn, R. (2015). Synaptotagmin-1 binds to PIP(2)-containing membrane but not to SNAREs at physiological ionic strength. *Nature Structural & Molecular Biology*, *22*(10), 815–23. http://doi.org/10.1038/nsmb.3097

Paul, M. M., Pauli, M., Ehmann, N., Hallermann, S., Sauer, M., Kittel, R. J., & Heckmann, M. (2015). Bruchpilot and Synaptotagmin collaborate to drive rapid glutamate release and active zone differentiation. *Frontiers in Cellular Neuroscience*, *9*(February), 1–12. http://doi.org/10.3389/fncel.2015.00029

Peled, E. S., & Isacoff, E. Y. (2011). Optical quantal analysis of synaptic transmission in wild-type and rab3-mutant Drosophila motor axons. *Nature Neuroscience*, *14*(4), 519–526.

http://doi.org/10.1038/nn.2767

Peled, E. S., Newman, Z. L., & Isacoff, E. Y. (2014). Evoked and spontaneous transmission favored by distinct sets of synapses. *Current Biology*, *24*(5), 484–493. http://doi.org/10.1016/j.cub.2014.01.022

Pielage, J., Cheng, L., Fetter, R. D., Carlton, P. M., Sedat, J. W., & Davis, G. W. (2008). A Presynaptic Giant Ankyrin Stabilizes the NMJ through Regulation of Presynaptic Microtubules and Transsynaptic Cell Adhesion. *Neuron*, *58*(2), 195–209. http://doi.org/10.1016/j.neuron.2008.02.017

Polevoy, G., Wei, H.-C., Wong, R., Szentpetery, Z., Kim, Y. J., Goldbach, P., … Brill, J. A. (2009). Dual roles for the Drosophila PI 4-kinase four wheel drive in localizing Rab11 during cytokinesis. *The Journal of Cell Biology*, *187*(6), 847–58. http://doi.org/10.1083/jcb.200908107

Posor, Y., Eichhorn-Gr??nig, M., & Haucke, V. (2015). Phosphoinositides in endocytosis. *Biochimica et Biophysica Acta - Molecular and Cell Biology of Lipids*, *1851*(6), 794–804. http://doi.org/10.1016/j.bbalip.2014.09.014

Puchkov, D., & Haucke, V. (2013). Greasing the synaptic vesicle cycle by membrane lipids. *Trends in Cell Biology*, *23*(10), 493–503. http://doi.org/10.1016/j.tcb.2013.05.002

Pulver, S. R., Pashkovski, S. L., Hornstein, N. J., Garrity, P. a, & Griffith, L. C. (2009). Temporal dynamics of neuronal activation by Channelrhodopsin-2 and TRPA1 determine behavioral output in Drosophila larvae. *Journal of Neurophysiology*, *101*(6), 3075–3088. http://doi.org/10.1152/jn.00071.2009

Qin, G., Schwarz, T., Kittel, R. J., Schmid, A., Rasse, T. M., Kappei, D., … Sigrist, S. J. (2005). Four different subunits are essential for expressing the synaptic glutamate receptor at neuromuscular junctions of Drosophila. *The Journal of Neuroscience : The Official Journal of the Society for Neuroscience*, *25*(12), 3209–3218. http://doi.org/10.1523/JNEUROSCI.4194-04.2005

Raghu, P., Coessens, E., Manifava, M., Georgiev, P., Pettitt, T., Wood, E., … Ktistakis, N. (2009). Rhabdomere biogenesis in Drosophila photoreceptors is acutely sensitive to phosphatidic acid levels. *Journal of Cell Biology*, *185*(1), 129–145. http://doi.org/10.1083/jcb.200807027

Regus-Leidig, H., Fuchs, M., Löhner, M., Leist, S. R., Leal-Ortiz, S., Chiodo, V. A., … Brandstätter, J.

H. (2014). In vivo knockdown of Piccolino disrupts presynaptic ribbon morphology in mouse photoreceptor synapses. *Frontiers in Cellular Neuroscience*, *8*, 259. http://doi.org/10.3389/fncel.2014.00259

Regus-Leidig, H., Ott, C., Löhner, M., Atorf, J., Fuchs, M., Sedmak, T., … Brandstätter, J. H. (2013). Identification and immunocytochemical characterization of Piccolino, a novel Piccolo splice variant selectively expressed at sensory ribbon synapses of the eye and ear. *PloS One*, *8*(8), e70373. http://doi.org/10.1371/journal.pone.0070373

Rizo, J., & Rosenmund, C. (2008). Synaptic vesicle fusion. *Nature Structural & Molecular Biology*, *15*(7), 665–74. Retrieved from http://www.pubmedcentral.nih.gov/articlerender.fcgi?artid=2519048&tool=pmcentrez&rendertype=abstract

Rizzoli, S. O., & Betz, W. J. (2005). Synaptic vesicle pools. *Nature Reviews. Neuroscience*, *6*(1), 57–69. http://doi.org/10.1038/nrn1583

Romero, E., Cha, G. H., Verstreken, P., Ly, C. V., Hughes, R. E., Bellen, H. J., & Botas, J. (2008). Suppression of Neurodegeneration and Increased Neurotransmission Caused by Expanded Full-Length Huntingtin Accumulating in the Cytoplasm. *Neuron*, *57*(1), 27–40. http://doi.org/10.1016/j.neuron.2007.11.025

Rosenmund, C., Sigler, A., Augustin, I., Reim, K., Brose, N., & Rhee, J. S. (2002). Differential control of vesicle priming and short-term plasticity by Munc13 isoforms. *Neuron*, *33*(3), 411–424. http://doi.org/10.1016/S0896-6273(02)00568-8

Saheki, Y., & De Camilli, P. (2012). Synaptic Vesicle Endocytosis. *Cold Spring Harbor Perspectives in Biology*, *4*(9), a005645–a005645. http://doi.org/10.1101/cshperspect.a005645

Sakaba, T., & Neher, E. (2001). Calmodulin mediates rapid recruitment of fast-releasing synaptic vesicles at a calyx-type synapse. *Neuron*, *32*(6), 1119–1131. http://doi.org/10.1016/S0896-6273(01)00543-8

Sakaba, T., & Neher, E. (2001). Quantitative relationship between transmitter release and calcium current at the calyx of held synapse. *The Journal of Neuroscience : The Official Journal of the Society for Neuroscience*, *21*(2), 462–76. Retrieved from http://www.jneurosci.org/content/21/2/462.abstract

Scannevin, R. H., & Huganir, R. L. (2000). Postsynaptic organization and regulation of excitatory

synapses. *Nature Reviews. Neuroscience*, *1*(2), 133–41. http://doi.org/10.1038/35039075

Schlüter, O. M., Basu, J., Südhof, T. C., & Rosenmund, C. (2006). Rab3 superprimes synaptic vesicles for release: implications for short-term synaptic plasticity. *The Journal of Neuroscience : The Official Journal of the Society for Neuroscience*, *26*(4), 1239–46. http://doi.org/10.1523/JNEUROSCI.3553-05.2006

Schlüter, O. M., Schmitz, F., Jahn, R., Rosenmund, C., & Südhof, T. C. (2004). A complete genetic analysis of neuronal Rab3 function. *The Journal of Neuroscience : The Official Journal of the Society for Neuroscience*, *24*(29), 6629–37. http://doi.org/10.1523/JNEUROSCI.1610-04.2004

Schnee, M. E., Santos-Sacchi, J., Castellano-Mu??oz, M., Kong, J. H., & Ricci, A. J. (2011). Calcium-Dependent Synaptic Vesicle Trafficking Underlies Indefatigable Release at the Hair Cell Afferent Fiber Synapse. *Neuron*, *70*(2), 326–338. http://doi.org/10.1016/j.neuron.2011.01.031

Schneggenburger, R., Han, Y., & Kochubey, O. (2012). Ca2+ channels and transmitter release at the active zone. *Cell Calcium*, *52*(3-4), 199–207. http://doi.org/10.1016/j.ceca.2012.04.011

Schneggenburger, R., Meyer, A. C., & Neher, E. (1999). Released Fraction and Total Size of a Pool of Immediately Available Transmitter Quanta at a Calyx Synapse. *Neuron*, *23*(2), 399–409. http://doi.org/10.1016/S0896-6273(00)80789-8

Schneggenburger, R., & Rosenmund, C. (2015). Molecular mechanisms governing Ca(2+) regulation of evoked and spontaneous release. *Nat Neurosci*, *18*(7), 935–941. http://doi.org/10.1038/nn.4044

Schneggenburger, R., Sakaba, T., & Neher, E. (2002). Vesicle pools and short-term synaptic depression: lessons from a large synapse. *Trends in Neurosciences*, *25*(4), 206–212. http://doi.org/10.1016/S0166-2236(02)02139-2

Schoch, S., Castillo, P. E., Jo, T., Mukherjee, K., Geppert, M., Wang, Y., … Südhof, T. C. (2002). RIM1alpha forms a protein scaffold for regulating neurotransmitter release at the active zone. *Nature*, *415*(6869), 321–6. http://doi.org/10.1038/415321a

Schotten, S., Meijer, M., Walter, A. M., Huson, V., Mamer, L., Kalogreades, L., … Cornelisse, L. N. (2015). Additive effects on the energy barrier for synaptic vesicle fusion cause supralinear effects on the vesicle fusion rate. *eLife*, *4*, e05531. http://doi.org/10.7554/eLife.05531

Shapira, M., Zhai, R. G., Dresbach, T., Bresler, T., Torres, V. I., Gundelfinger, E. D., … Garner, C. C. (2003). Unitary Assembly of Presynaptic Active Zones from Piccolo-Bassoon Transport Vesicles. *Neuron*, *38*(2), 237–252. http://doi.org/10.1016/S0896-6273(03)00207-1

Shin, O.-H., Lu, J., Rhee, J. S., Tomchick, D. R., Pang, Z. P., Wojcik, S. M., … Südhof, T. C. (2010). Munc13 C2B domain is an activity-dependent Ca2+ regulator of synaptic exocytosis. *Nature Structural & Molecular Biology*, *17*(3), 280–288. http://doi.org/10.1038/nsmb.1758

Sigrist, S. J., Reiff, D. F., Thiel, P. R., Steinert, J. R., & Schuster, C. M. (2003). Experience-dependent strengthening of Drosophila neuromuscular junctions. *The Journal of Neuroscience : The Official Journal of the Society for Neuroscience*, *23*(16), 6546–6556. http://doi.org/23/16/6546 [pii]

Söllner, T., Bennett, M. K., Whiteheart, S. W., Scheller, R. H., & Rothman, J. E. (1993). A protein assembly-disassembly pathway in vitro that may correspond to sequential steps of synaptic vesicle docking, activation, and fusion. *Cell*, *75*(3), 409–418. http://doi.org/10.1016/0092-8674(93)90376-2

St Johnston, D. (2002). The art and design of genetic screens: Drosophila melanogaster. *Nature Reviews. Genetics*, *3*(3), 176–88. http://doi.org/10.1038/nrg751

Stanley, E. F. (1993). Single calcium channels and acetylcholine release at a presynaptic nerve terminal. *Neuron*, *11*(6), 1007–1011. http://doi.org/10.1016/0896-6273(93)90214-C

Staras, K., Branco, T., Burden, J. J., Pozo, K., Darcy, K., Marra, V., … Goda, Y. (2010). A vesicle superpool spans multiple presynaptic terminals in hippocampal neurons. *Neuron*, *66*(1), 37–44. http://doi.org/10.1016/j.neuron.2010.03.020

Stevens, C. F., & Williams, J. H. (2007). Discharge of the readily releasable pool with action potentials at hippocampal synapses. *Journal of Neurophysiology*, *98*(6), 3221–9. http://doi.org/10.1152/jn.00857.2007

Stevens, D. R., Wu, Z.-X., Matti, U., Junge, H. J., Schirra, C., Becherer, U., … Rettig, J. (2005). Identification of the minimal protein domain required for priming activity of Munc13-1. *Current Biology : CB*, *15*(24), 2243–8. http://doi.org/10.1016/j.cub.2005.10.055

Stewart, B., Atwood, H., Renger, J., Wang, J., & Wu, C. (1994). Improved stability of Drosophila larval neuromuscular preparations in haemolymph-like physiological solutions. *Journal Comparative Physiology*, *175*(2), 179–191.

Stirnimann, C. U., Petsalaki, E., Russell, R. B., & Müller, C. W. (2010). WD40 proteins propel cellular networks. *Trends in Biochemical Sciences*, *35*(10), 565–74. http://doi.org/10.1016/j.tibs.2010.04.003

Sudhof, T. C. (2012). Review The Presynaptic Active Zone. *Neuron*, *75*(1), 11–25. http://doi.org/10.1016/j.neuron.2012.06.012

Südhof, T. C. (2004). the Synaptic Vesicle Cycle. *Annual Review of Neuroscience*, *27*(1), 509–547. http://doi.org/10.1146/annurev.neuro.26.041002.131412

Südhof, T. C. (2008). Neuroligins and neurexins link synaptic function to cognitive disease. *Nature*, *455*(7215), 903–11. http://doi.org/10.1038/nature07456

Südhof, T. C. (2012). Calcium control of neurotransmitter release. *Cold Spring Harbor Perspectives in Biology*, *4*(1). http://doi.org/10.1101/cshperspect.a011353

Südhof, T. C. (2013). Neurotransmitter release: The last millisecond in the life of a synaptic vesicle. *Neuron*, *80*(3), 675–690. http://doi.org/10.1016/j.neuron.2013.10.022

Sugita, S., Shin, O.-H., Han, W., Lao, Y., & Südhof, T. C. (2002). Synaptotagmins form a hierarchy of exocytotic Ca(2+) sensors with distinct Ca(2+) affinities. *The EMBO Journal*, *21*(3), 270–80. http://doi.org/10.1093/emboj/21.3.270

Sutton, M. A., Wall, N. R., Aakalu, G. N., & Schuman, E. M. (2004). Regulation of dendritic protein synthesis by miniature synaptic events. *Science (New York, N.Y.)*, *304*(5679), 1979–83. http://doi.org/10.1126/science.1096202

Takahashi, T. (2015). Strength and precision of neurotransmission at mammalian presynaptic terminals. *Proceedings of the Japan Academy. Series B, Physical and Biological Sciences*, *91*(7), 305–20. http://doi.org/10.2183/pjab.91.305

Taschenberger, H., & von Gersdorff, H. (2000). Fine-Tuning an Auditory Synapse for Speed and Fidelity: Developmental Changes in Presynaptic Waveform, EPSC Kinetics, and Synaptic Plasticity. *J. Neurosci.*, *20*(24), 9162–9173. Retrieved from http://www.jneurosci.org/content/20/24/9162.long

Terry-Lorenzo, R. T., Roadcap, D. W., Otsuka, T., Blanpied, T. A., Zamorano, P. L., Garner, C. C., … Ehlers, M. D. (2005). Neurabin/protein phosphatase-1 complex regulates dendritic spine morphogenesis and maturation. *Molecular Biology of the Cell*, *16*(5), 2349–62. http://doi.org/10.1091/mbc.E04-12-1054

Thévenaz, P., Ruttimann, U. E., & Unser, M. (1998). A pyramid approach to subpixel registration based on intensity. *IEEE Transactions on Image Processing : A Publication of the IEEE Signal Processing Society*, *7*(1), 27–41. http://doi.org/10.1109/83.650848

tom Dieck, S., Specht, D., Strenzke, N., Hida, Y., Krishnamoorthy, V., Schmidt, K.-F., … Moser, T. (2012). Deletion of the presynaptic scaffold CAST reduces active zone size in rod photoreceptors and impairs visual processing. *The Journal of Neuroscience : The Official Journal of the Society for Neuroscience*, *32*(35), 12192–203. http://doi.org/10.1523/JNEUROSCI.0752-12.2012

Ullrich, A., Böhme, M. A., Schöneberg, J., Depner, H., Sigrist, S. J., & Noé, F. (2015). Dynamical Organization of Syntaxin-1A at the Presynaptic Active Zone. *PLoS Computational Biology*, *11*(9), e1004407. http://doi.org/10.1371/journal.pcbi.1004407

Uytterhoeven, V., Kuenen, S., Kasprowicz, J., Miskiewicz, K., & Verstreken, P. (2011). Loss of Skywalker reveals synaptic endosomes as sorting stations for synaptic vesicle proteins. *Cell*, *145*(1), 117–132. http://doi.org/10.1016/j.cell.2011.02.039

Varoqueaux, F., Sigler, A., Rhee, J.-S., Brose, N., Enk, C., Reim, K., & Rosenmund, C. (2002). Total arrest of spontaneous and evoked synaptic transmission but normal synaptogenesis in the absence of Munc13-mediated vesicle priming. *Proceedings of the National Academy of Sciences of the United States of America*, *99*(13), 9037–42. http://doi.org/10.1073/pnas.122623799

Venken, K. J. T., He, Y., Hoskins, R. A., & Bellen, H. J. (2006). P[acman]: a BAC transgenic platform for targeted insertion of large DNA fragments in D. melanogaster. *Science (New York, N.Y.)*, *314*(5806), 1747–51. http://doi.org/10.1126/science.1134426

Verhage, M., Maia, A. S., Plomp, J. J., Brussaard, A. B., Heeroma, J. H., Vermeer, H., … Sudhof, T. C. (2000). Synaptic Assembly of the Brain in the Absence of Neurotransmitter Secretion. *Science*, *287*(5454), 864–869. http://doi.org/10.1126/science.287.5454.864

Verhage, M., & Sørensen, J. B. (2008). Vesicle docking in regulated exocytosis. *Traffic (Copenhagen, Denmark)*, *9*(9), 1414–24. http://doi.org/10.1111/j.1600-0854.2008.00759.x

Vyleta, N. P., & Jonas, P. (2014). Loose coupling between Ca2+ channels and release sensors at a plastic hippocampal synapse. *Science (New York, N.Y.)*, *343*(6171), 665–70. http://doi.org/10.1126/science.1244811

Wadel, K., Neher, E., & Sakaba, T. (2007). The Coupling between Synaptic Vesicles and Ca2+ Channels Determines Fast Neurotransmitter Release. *Neuron*, *53*(4), 563–575. http://doi.org/10.1016/j.neuron.2007.01.021

Wagh, D. a., Rasse, T. M., Asan, E., Hofbauer, A., Schwenkert, I., Dürrbeck, H., … Buchner, E. (2006). Bruchpilot, a protein with homology to ELKS/CAST, is required for structural integrity and function of synaptic active zones in Drosophila. *Neuron*, *49*(6), 833–844. http://doi.org/10.1016/j.neuron.2006.02.008

Waites, C. L., Leal-Ortiz, S. a, Okerlund, N., Dalke, H., Fejtova, A., Altrock, W. D., … Garner, C. C. (2013). Bassoon and Piccolo maintain synapse integrity by regulating protein ubiquitination and degradation. *The EMBO Journal*, *32*(7), 954–69. http://doi.org/10.1038/emboj.2013.27

Walter, A. M., Wiederhold, K., Bruns, D., Fasshauer, D., & Sørensen, J. B. (2010). Synaptobrevin N-terminally bound to syntaxin-SNAP-25 defines the primed vesicle state in regulated exocytosis. *The Journal of Cell Biology*, *188*(3), 401–13. http://doi.org/10.1083/jcb.200907018

Wang, L. Y., & Kaczmarek, L. K. (1998). High-frequency firing helps replenish the readily releasable pool of synaptic vesicles. *Nature*, *394*(6691), 384–8. http://doi.org/10.1038/28645

Wang, L.-Y., & Augustine, G. J. (2014). Presynaptic nanodomains: a tale of two synapses. *Frontiers in Cellular Neuroscience*, *8*(January), 455. http://doi.org/10.3389/fncel.2014.00455

Wang, L.-Y., Neher, E., & Taschenberger, H. (2008). Synaptic vesicles in mature calyx of Held synapses sense higher nanodomain calcium concentrations during action potential-evoked glutamate release. *The Journal of Neuroscience : The Official Journal of the Society for Neuroscience*, *28*(53), 14450–8. http://doi.org/10.1523/JNEUROSCI.4245-08.2008

Wang, X., Hu, B., Zieba, A., Neumann, N. G., Kasper-Sonnenberg, M., Honsbein, A., … Kilimann, M. W. (2009). A protein interaction node at the neurotransmitter release site: domains of Aczonin/Piccolo, Bassoon, CAST, and rim converge on the N-terminal domain of Munc13-1. *The Journal of Neuroscience : The Official Journal of the Society for Neuroscience*, *29*(40), 12584–96. http://doi.org/10.1523/JNEUROSCI.1255-09.2009

Wang, Y., Liu, X., Biederer, T., & Südhof, T. C. (2002). A family of RIM-binding proteins regulated by alternative splicing: Implications for the genesis of synaptic active zones. *Proceedings of*

*the National Academy of Sciences of the United States of America*, *99*(22), 14464–14469. http://doi.org/10.1073/pnas.182532999

Wang, Y., Okamoto, M., Schmitz, F., Hofmann, K., & Sudhof, T. C. (1997). Rim is a putative Rab3 effector in regulating synaptic-vesicle fusion, *388*(6642), 593–598.

Watanabe, S., Liu, Q., Davis, M. W., Hollopeter, G., Thomas, N., Jorgensen, N. B., & Jorgensen, E. M. (2013). Ultrafast endocytosis at Caenorhabditis elegans neuromuscular junctions. *eLife*, *2013*(2), 2–4. http://doi.org/10.7554/eLife.00723

Watanabe, S., Rost, B. R., Camacho-Pérez, M., Davis, M. W., Söhl-Kielczynski, B., Rosenmund, C., & Jorgensen, E. M. (2013). Ultrafast endocytosis at mouse hippocampal synapses. *Nature*, *504*(7479), 242–7. http://doi.org/10.1038/nature12809

Watanabe, S., Trimbuch, T., Camacho-Pérez, M., Rost, B. R., Brokowski, B., Söhl-Kielczynski, B., … Jorgensen, E. M. (2014). Clathrin regenerates synaptic vesicles from endosomes. *Nature*, *515*(7526), 228–33. http://doi.org/10.1038/nature13846

Weimer, R. M., Gracheva, E. O., Meyrignac, O., Miller, K. G., Richmond, J. E., & Bessereau, J. (2006). UNC-13 and UNC-10 / Rim Localize Synaptic Vesicles to Specific Membrane Domains. *Analysis*, *26*(31), 8040 – 8047. http://doi.org/10.1523/JNEUROSCI.2350-06.2006

Weimer, R. M., Richmond, J. E., Davis, W. S., Hadwiger, G., Nonet, M. L., & Jorgensen, E. M. (2003). Defects in synaptic vesicle docking in unc-18 mutants. *Nature Neuroscience*, *6*(10), 1023–30. http://doi.org/10.1038/nn1118

Williams, C., Chen, W., Lee, C.-H., Yaeger, D., Vyleta, N. P., & Smith, S. M. (2012). Coactivation of multiple tightly coupled calcium channels triggers spontaneous release of GABA. *Nature Neuroscience*, *15*(9), 1195–7. http://doi.org/10.1038/nn.3162

Wölfel, M., Lou, X., & Schneggenburger, R. (2007). A mechanism intrinsic to the vesicle fusion machinery determines fast and slow transmitter release at a large CNS synapse. *The Journal of Neuroscience : The Official Journal of the Society for Neuroscience*, *27*(12), 3198–210. http://doi.org/10.1523/JNEUROSCI.4471-06.2007

Wu, S., & Kelly, J. (1993). Response of neurons in the lateral superior olive and medial nucleus of the trapezoid body to repetitive stimulation: intracellular and extracellular recordings from mouse brain slice. *Hear Research*, *68*(2), 189–201.

Wu, Y., Kawasaki, F., & Ordway, R. W. (2005). Properties of short-term synaptic depression at

larval neuromuscular synapses in wild-type and temperature-sensitive paralytic mutants of Drosophila. *Journal of Neurophysiology*, *93*(5), 2396–2405. http://doi.org/10.1152/jn.01108.2004

Wucherpfennig, T., Wilsch-Bräuninger, M., & González-Gaitán, M. (2003). Role of Drosophila Rab5 during endosomal trafficking at the synapse and evoked neurotransmitter release. *Journal of Cell Biology*, *161*(3), 609–624. http://doi.org/10.1083/jcb.200211087

Xu, J., Pang, Z. P., Shin, O.-H., & Südhof, T. C. (2009). Synaptotagmin-1 functions as a Ca2+ sensor for spontaneous release. *Nature Neuroscience*, *12*(6), 759–66. http://doi.org/10.1038/nn.2320

Xu, J., & Wu, L.-G. (2005). The decrease in the presynaptic calcium current is a major cause of short-term depression at a calyx-type synapse. *Neuron*, *46*(4), 633–45. http://doi.org/10.1016/j.neuron.2005.03.024

Xu-Friedman, M. A., & Regehr, W. G. (1999). Presynaptic strontium dynamics and synaptic transmission. *Biophysical Journal*, *76*(4), 2029–42. http://doi.org/10.1016/S0006-3495(99)77360-1

Yamakage, M., & Namiki, A. (2002). Calcium channels--basic aspects of their structure, function and gene encoding; anesthetic action on the channels--a review. *Canadian Journal of Anaesthesia = Journal Canadien D'anesthesie*, *49*(2), 151–164. http://doi.org/10.1007/BF03020488

Yan, Y., Denef, N., & Schüpbach, T. (2009). The Vacuolar Proton Pump, V-ATPase, Is Required for Notch Signaling and Endosomal Trafficking in Drosophila. *Developmental Cell*, *17*(3), 387–402. http://doi.org/10.1016/j.devcel.2009.07.001

Yan, Y., Denef, N., Tang, C., & Schüpbach, T. (2011). Drosophila PI4KIIIalpha is required in follicle cells for oocyte polarization and Hippo signaling. *Development (Cambridge, England)*, *138*(9), 1697–1703. http://doi.org/10.1242/dev.059279

Zefirov, A. L., Abdrakhmanov, M. M., Mukhamedyarov, M. A., & Grigoryev, P. N. (2006). The role of extracellular calcium in exo- and endocytosis of synaptic vesicles at the frog motor nerve terminals. *Neuroscience*, *143*(4), 905–10. http://doi.org/10.1016/j.neuroscience.2006.08.025

Zhang, S., Xu, M., Miao, Q., Poo, M., & Zhang, X. (2009). Endocannabinoid-dependent

homeostatic regulation of inhibitory synapses by miniature excitatory synaptic activities. *The Journal of Neuroscience : The Official Journal of the Society for Neuroscience*, *29*(42), 13222–31. http://doi.org/10.1523/JNEUROSCI.1710-09.2009

Zhou, K., Stawicki, T. M., Goncharov, A., & Jin, Y. (2013). Position of UNC-13 in the active zone regulates synaptic vesicle release probability and release kinetics. *eLife*, *2*, e01180. http://doi.org/10.7554/eLife.01180

Zucker, R. S., & Regehr, W. G. (2002). Short-term synaptic plasticity. *Annual Review of Physiology*, *64*, 355–405.